

6)

STRUCTURAL STUDIES OF THE HYDROXYLASE COMPONENT OF
METHANE MONOOXYGENASE FROM *METHYLOCCOUS CAPSULATUS*
(BATH)

by

Amy Claire Rosenzweig

B. A., Chemistry
Amherst College
(1988)

Submitted to the Department of Chemistry
in partial fulfillment of
the requirements for the Degree of
Doctor of Philosophy

at the

MASSACHUSETTS INSTITUTE OF TECHNOLOGY

February, 1994

© Massachusetts Institute of Technology, 1994

Signature of Author _____
Department of Chemistry
February 2, 1994

Certified by _____
Stephen J. Lippard
Thesis Advisor


Accepted by _____
Glenn A. Berchtold, Chairman,
Departmental Committee on Graduate Students

MASSACHUSETTS INSTITUTE
OF TECHNOLOGY

MAR 21 1994

Stace

This doctoral thesis has been examined by a Committee of the Department of Chemistry as follows:



Professor Alan Davison, Committee Chairman

Professor Stephen J. Lippard, Thesis Supervisor
Arthur Amos Noyes Professor of Chemistry

Professor Joanne Stubbe

STRUCTURAL STUDIES OF THE HYDROXYLASE COMPONENT OF
METHANE MONOOXYGENASE FROM *METHYLOCCOUS CAPSULATUS*
(BATH)

by

Amy Claire Rosenzweig

Submitted to the Department of Chemistry on February 2, 1994 in partial fulfillment of the requirements for the Degree of Doctor of Philosophy in Chemistry

ABSTRACT

Chapter 1. The hydroxylase component of soluble methane monooxygenase catalyzes the oxidation of methane to methanol in methanotrophic bacteria. The hydroxylase is comprised of two copies each of three subunits, an $\alpha_2\beta_2\gamma_2$ polypeptide arrangement. The α subunit contains a dinuclear iron center similar to those in hemerythrin and the ribonucleotide reductase R2 protein. In this chapter, the structural information obtained by using methods other than X-ray crystallography are reviewed in terms of the recently determined X-ray structure.

Chapter 2. Methodologies for the fermentation of *Methylococcus capsulatus* (Bath) and the purification of the hydroxylase component of methane monooxygenase were established. The hydroxylases from both *M. capsulatus* (Bath) and *Methylosinus trichosporium* OB3b were purified to homogeneity, and large supplies of the *M. capsulatus* (Bath) enzyme were generated for physical studies. The gene for the α subunit of the hydroxylase was cloned, and expression in *E. coli* was attempted. Coupling protein expressed in *E. coli* was determined to be functional, and was successfully purified for use in spectroscopic experiments.

Chapter 3. The hydroxylase diiron center was characterized extensively by optical spectroscopy, EPR spectroscopy, electron spin echo envelope

modulation (ESEEM) spectroscopy, Mössbauer spectroscopy, and EXAFS spectroscopy. The optical spectrum and the EXAFS data indicated that the hydroxylase probably contains a bridging hydroxide rather than a bridging oxygen. The Mössbauer spectral parameters were consistent with the presence of a hydroxo bridge as well. An Fe...Fe distance of 3.4 Å was determined for the oxidized, Fe(III)Fe(III), and mixed valent, Fe(II)Fe(III), forms of the hydroxylase. The EXAFS data suggested that the two Fe atoms are ligated to a mixture of oxygen and nitrogen donors, with more oxygen than nitrogen donors. The ESEEM data revealed the presence of two histidine nitrogen ligands. A model for the diiron core was postulated based on the results of these experiments. The effects of the coupling protein, of 1-bromo-1-propene, and of N_3^- on the diiron center were also investigated. The coupling protein perturbed the EPR spectrum of the mixed valent hydroxylase, and produced small changes in the EXAFS spectrum. X-ray absorption edge data indicated that reduction to the fully reduced, Fe(II)Fe(II), state can occur in the presence of the coupling protein. Although 1-bromo-1-propene caused detectable changes in the EPR spectrum of the mixed valent hydroxylase, no Fe-Br interaction was observed in the EXAFS data, indicating that this substrate binds with the Br atom $> 5\text{Å}$ from the two Fe atoms. A weak optical band at 436 nm was observed in the presence of N_3^- , but definitive evidence for N_3^- binding to the diiron center was not obtained.

Chapter 4. Crystalline needles of the *M. capsulatus* (Bath) hydroxylase were obtained from solutions containing Li_2SO_4 , NH_4OAc , and PEG 4000. A seeding procedure was used to convert these crystalline needles to large single crystals, which diffracted to 1.8 Å resolution. The crystal lattice was orthorhombic, belonging to the space group $\text{P}2_12_12_1$, and the unit cell dimensions were 62.6 x 110.1 x 333.5 Å, with one $\alpha_2\beta_2\gamma_2$ dimer in the asymmetric unit. Data sets were collected both by using a conventional laboratory X-ray source and by using synchrotron radiation. The 2.2 Å native data set used for the structure determination was collected at the Photon Factory in Tsukuba, Japan. Several heavy atom derivatives were identified after extensive screening of heavy atom compounds, and multiple isomorphous replacement (MIR) electron density maps were generated. The heavy atom sites were used to locate a non-crystallographic twofold symmetry axis relating the two halves of the $\alpha_2\beta_2\gamma_2$ dimer. The MIR electron density

maps were then greatly improved by molecular averaging. The diiron center, the iron-coordinating helices in the α subunit, and a number of other helices, initially modeled as polyalanine chains, were located in the electron density. A strategy of partial structural phase combination was used, and after 28 cycles of model building, refinement, and phase combination, a model containing 512 of the 527 residues in the α subunit, 384 of the 389 residues in the β subunit, 162 of the 170 residues in the γ subunit, and ~850 water molecules was obtained. The R-value was 17.0% to 2.2 Å resolution with r.m.s. deviations from ideal bond distances and angles of 0.013 Å and 2.9°, respectively.

Chapter 5. The three-dimensional structure of the *M. capsulatus* (Bath) hydroxylase is presented. The hydroxylase is mostly helical with one region of beta hairpin structure in the α subunit. The α and β subunits possess the same fold, which is very similar to the fold of the ribonucleotide reductase R2 protein. The dimer interaction is formed primarily by the two β subunits. There is a wide canyon at the dimer interface and an opening at the center of the molecule. The hydroxylase dimer is shaped like a heart. There are many buried charged residues in the molecule, some of which form inter-subunit salt linkages. There are two diiron centers, one on each α subunit. The two Fe atoms are bridged by a carboxylate, Glu144, and two exogenous ligands, which were interpreted as a bridging hydroxide and a bridging acetate ion. In addition, each Fe is coordinated to the δ -N atom of a histidine residue, Fe1 to His147 and Fe2 to His246. Fe1 is coordinated to a water molecule and to a monodentate carboxylate, Glu114. The coordination of Fe2 is completed by two monodentate carboxylates, Glu209 and Glu243. The diiron center is located in a hydrophobic cavity, and several other cavities are apparent in the α subunit. Substrate and product might access the active site through these cavities. Possible mechanistic roles for two residues in the active site cavity, Cys151 and Thr213, are discussed. Finally, possible binding domains for the coupling protein and the reductase in the canyon formed by the two $\alpha\beta$ protomers are discussed.

Thesis Supervisor: Dr. Stephen J. Lippard

Title: Arthur Amos Noyes Professor of Chemistry

ACKNOWLEDGMENTS

My decision to go to graduate school resulted from my experience in Dave Dooley's laboratory at Amherst College. I wish to thank him for introducing me to the field of bioinorganic chemistry. He is an exemplary teacher and researcher, and has provided continuing support over the past 5 1/2 years.

At MIT, I joined the laboratory of Steve Lippard, from whom I have learned a great deal about research, education, writing, presentation, and management. He is completely devoted to excellence in research and to the education of his students. I wish to thank him for his constant encouragement and support. Although I have many people to thank, his guidance was at the core of all that has occurred during my graduate education.

Jim Bentsen initiated the MMO work in the laboratory, and I thank him for introducing me to the project. In the first several years, a number of students and postdocs provided assistance and encouragement in the lab, including Robert Beer, Petra Turowski, Ken Comess, Steve Bellon, Mike Keck, and Judith Burstyn. I owe a special thanks to the members of the MMO subgroup. I thank Kathy Liu, who came a year after me. We endured many horrific protein preparations together, inspiring the purchase of special worksuits. Thanks to Wayne Wu (and his goatee) for teaching me some molecular biology and to Thanos Salifoglou for help with fermentations and purifications. I also thank Axel Masschelein, David Coufal, and Ann Valentine. Many others in the Lippard lab have been helpful during the last few years of work: Steve Brown, Kingsley Taft, Dave Goldberg, Andrew Feig, Steve Watton, Jackie Acho, and Joanne Yun. I thank Jackie and Joanne for very important apparel assistance. I wish to thank Tricia Takahara for a huge amount of assistance with X-ray data collection at SSRL. I really appreciated her help, and we even had a tiny bit of fun on those grueling trips (long live

Ian). She and Mark also have provided me with great computer support over the past months.

We have had many collaborators on the MMO project. I thank Keith Hodgson, Britt Hedman, and Jane DeWitt for the EXAFS work. Jane carried out the EXAFS data analysis, and created the EXAFS figures in Chapter 3. I also thank Georgia Papaefthymiou for help acquiring the Mössbauer data in Chapter 3, and Chris Bender and Jack Peisach for the ESEEM data and analysis, also discussed in Chapter 3.

The X-ray structure determination (Chapters 4 and 5) could not have been successful without the help of a number of people. Chris Frederick introduced me to crystallography, and has been a great source of crystallographic education and support over the past 3 years. She generously allowed me to become a part of her group at the Dana Farber, and I have enjoyed working there a great deal (enough to stay on). I wish to thank John Genova for help with the X-ray equipment, and everyone in the Frederick-Liddington labs. I thank Amy Anderson Chang in particular for help with data collection at SSRL and at the Photon Factory. Her support over the past year is much appreciated. I also thank Henrique Silva for putting up with my massive consumption of disk space, incessant questions about the computers, and tampering with the printers, and George Planansky for computer advice. Jules Hendrix from Marresearch has been very important to the success of this project, and I thank him for fixing the imaging plates both at the Dana Farber and at SSRL. I thank Mike Soltis for assistance at SSRL and Noriyoshi Sakabe and Atsushi Nakagawa for assistance beyond the call of duty at the Photon Factory. Their repair of the detector at 3 a.m. is much appreciated. Finally, I wish to thank Pär Nordlund for teaching me so much about crystallography, and for being a great inspiration in the past year. The collaboration with him worked out better than I ever imagined.

I thank my parents Richard and Linda and my sister Jane for their ongoing support. Finally, the best result of my graduate school experience was meeting Ken Comess. I thank him for still wanting to be with me forever after witnessing and sharing all my neuroses over the past 5 1/2 years.

TABLE OF CONTENTS

Abstract	3
Acknowledgments.....	6
Table of Contents	8
List of Tables	13
List of Figures	15
 <u>Chapter 1.</u>	
Structural Analysis of a Non-Heme Iron-Oxo Hydroxylase	20
Introduction	21
Structural Information from Non X-Ray Crystallographic Methods	24
The holo hydroxylase and subunit interactions	24
Number and location of dinuclear iron centers.	26
The bridging ligands.	27
The non-bridging ligands.	29
Specific amino acid residues in the active site.	30
Interactions with the coupling protein and the reductase.	31
Structural Information from X-Ray Crystallography.	32
Brief history of the X-ray structure determination.	32
X-ray structure of the hydroxylase.	34
Conclusions and Unsolved Mysteries.	40
References.	43
 <u>Chapter 2.</u>	
Purification of the <i>Methylococcus capsulatus</i> (Bath) Methane Monooxygenase Proteins.	52
Introduction.	53
<i>M. capsulatus</i> fermentations	55

Experimental	55
Materials	55
Results and Discussion	59
Purification of the Hydroxylase	60
Experimental	60
Materials	60
Preparation of crude cell free extract	60
Column chromatography	61
Activity assays	62
Protein analytical procedures	63
Results and Discussion	64
Cloning, Expression, and Activity of the Coupling Protein and the α Subunit of the Hydroxylase	69
Experimental	69
Materials	69
Cloning of the α subunit	69
Expression of the α subunit	70
Expression, purification, and activity of the coupling protein	70
Results and Discussion	71
Expression of the α subunit	71
Expression and purification of the coupling protein	72
Conclusions	73
References	75

Chapter 3.

Spectroscopic Studies of the Hydroxylase	94
Introduction	95
Optical Spectroscopy	96
Experimental	96
Results and Discussion	97
Optical properties	97
Azide binding	97
Electron paramagnetic resonance (EPR) spectroscopy	99
Experimental	99
Materials	99

Sample preparations and EPR spectroscopy	99
Results and Discussion	100
Three oxidation states	100
Effects of nitric oxide	101
Effects of the coupling protein	102
Effects of 1-bromo-1-propene	103
Electron spin echo modulation (ESEEM) spectroscopy	103
Experimental	103
Materials	103
Sample preparations	103
ESEEM spectroscopy	104
Results and Discussion	104
Mössbauer Spectroscopy	107
Experimental	107
Materials	107
Sample preparation	107
Mössbauer spectroscopy	108
Results and Discussion	108
X-Ray Absorption Spectroscopy	109
Experimental	109
Materials	109
Sample preparations	109
EXAFS Data Collection, Reduction, and Analysis	111
Results and Discussion	112
Photoreduction of the oxidized hydroxylase	112
Uncomplexed oxidized, mixed valent, and reduced hydroxylase	113
First shell fit	114
Second Shell Fits	115
Complexes of mixed valent and reduced hydroxylase	116
First shell fits	118
Second shell fits	119
Edge spectra	119
Conclusions	121
References	123

Chapter 4.

X-Ray Crystallography of the Hydroxylase.....	170
Introduction.....	171
Crystallization.....	172
Experimental.....	172
Materials.....	172
Results and Discussion.....	173
Initial crystallization trials.....	173
Crystal seeding.....	175
Crystal analysis.....	176
Crystallization of the <i>M. trichosporium</i> hydroxylase.....	177
Preliminary X-Ray Analysis.....	178
Experimental.....	178
Results and Discussion.....	179
Unit cell.....	179
Space group determination and preliminary native data.....	179
Native Data Collection.....	181
Experimental.....	181
Results and Discussion.....	182
Heavy Atom Derivatives and Multiple Isomorphous Replacement (MIR)	
Phasing.....	183
Experimental.....	183
Results and Discussion.....	184
Initial soaks.....	184
Patterson analysis.....	185
Difference Fourier analysis.....	185
Native maps and non-crystallographic symmetry.....	186
Location of the diiron center.....	188
Higher resolution (3.0 Å) derivative data.....	188
Fixed phase refinement and further averaging.....	189
Model Building, Phase Combination, and Refinement.....	191
Partial structural phase combination.....	191
Molecular averaging.....	192
Sequence fitting.....	193

Water molecules and exogenous ligands	195
Final refinement statistics	196
References	197

Chapter 5.

The Three-Dimensional Structure of the Hydroxylase.	249
Introduction	250
The Overall Structure	250
Secondary structure of the α subunit.	250
Secondary structure of the β subunit	252
Secondary structure of the gamma subunit	253
The dimer	254
Heavy atom binding sites	255
Charged residues and subunit-subunit interactions	257
Water molecules	259
Crystal packing interactions	260
The iron center and the active site	260
Location of the diiron center	260
Coordination of the iron atoms	261
Access to and composition of the active site	264
The catalytic mechanism	266
Comparison to cytochromes P450	267
Component Interactions	268
Comparison to other diiron proteins	270
Conclusions	270
References	272
Biographical Sketch.	339

LIST OF TABLES

Table 3.1 EXAFS sample summary.	127
Table 4.1 Conditions which resulted in the formation of hydroxylase crystals.	199
Table 4.2 Data collection statistics for native data.	201
Table 4.3 R_{sym} for mmo142 native data set by resolution ranges.	202
Table 4.4 Completeness of mmo142 native data for different resolution ranges.	203
Table 4.5 Data collection statistics for derivative data.	204
Table 4.6 Heavy atom sites.	207
Table 4.7 Heavy atom sites used for determination of noncrystallographic symmetry operator NCS1.	212
Table 4.8 Heavy atom sites used for determination of noncrystallographic symmetry operator NCS2.	213
Table 4.9 Final phasing statistics.	214
Table 4.10 Refinement of the hydroxylase structure.	216
Table 4.11 Refinement statistics.	219
Table 5.1 Secondary structure elements in the alpha subunit.	275
Table 5.2 Tight turns.	278
Table 5.3 Secondary structure elements in the beta subunit.	283
Table 5.4 Secondary structure elements in the gamma subunit.	285

Table 5.5 Heavy atom binding sites in the PIP, TAMM, and EMTS derivatives.	286
Table 5.6 Buried charged residues in the alpha subunit.	288
Table 5.7 Buried charged residues in the beta subunit.	292
Table 5.8 Buried charged residues in the gamma subunit.	295
Table 5.9 Diiron center distances.	296
Table 5.10 Iron to ligand angles.	297

LIST OF FIGURES

Figure 1.1 The hydroxylase structure as determined by non-crystallographic experiments and by X-ray crystallographic analysis.	49
Figure 1.2 Models for the diiron core in the hydroxylase.	51
Figure 2.1 Flammability diagram for methane in an oxygen-nitrogen mixture at ambient temperature and pressure.	78
Figure 2.2 Fermentation kinetics for <i>M. capsulatus</i> growths.	80
Figure 2.3 HPLC elution profile of the hydroxylase after separation from the reductase and the coupling protein on DEAE cellulose.	83
Figure 2.4 SDS PAGE of the purified hydroxylase.	85
Figure 2.5 SDS PAGE of the highly purified hydroxylase.	87
Figure 2.6 SDS PAGE of the purified <i>M. trichosporium</i> hydroxylase.	89
Figure 2.7 SDS PAGE of α subunit expression experiment.	91
Figure 2.8 SDS PAGE of <i>E. coli</i> coupling protein purification.	93
Figure 3.1 Crystallographically characterized dinuclear iron proteins.	131
Figure 3.2 Optical spectrum of the hydroxylase.	133
Figure 3.3 Effects of N_3^- on the optical spectrum of the oxidized hydroxylase.	135
Figure 3.4 X-band EPR spectra of the hydroxylase.	137

Figure 3.5 EPR spectrum of the mixed valent hydroxylase in the presence of a 2-fold molar excess of coupling protein.	139
Figure 3.6 EPR spectrum of the mixed valent hydroxylase in the presence of excess 1-bromo-1-propene.	141
Figure 3.7 Three pulse ESE modulation and the cosine FT spectra of the hydroxylase at three g-values.	143
Figure 3.8 FT spectral simulations (at $g = 1.92$) of a single ^{14}N having a contact interactions of 5 MHz and 0.8 MHz.	145
Figure 3.9 Mössbauer spectra of the hydroxylase at 80 K and zero applied field.	147
Figure 3.10 Fe K X-ray absorption edge position of the diferric, photoreduced mixed valent, and diferrous hydroxylase.	149
Figure 3.11 EXAFS data of the hydroxylase and dinuclear iron model compounds.	151
Figure 3.12 Fourier transforms of the EXAFS data shown in Figure 3.11.	153
Figure 3.13 EXAFS data for the mixed valent (photoreduced) hydroxylase samples in the presence of coupling protein and 1-bromo-1-propene.	155
Figure 3.14 Fourier transforms of mixed valent hydroxylase EXAFS data shown in Figure 3.13.	157
Figure 3.15 EXAFS data for the fully reduced hydroxylase samples in the presence of coupling protein and 1-bromo-1propene.	159
Figure 3.16 Fourier transforms of the fully reduced hydroxylase EXAFS data shown in Figure 3.15.	161

Figure 3.17 Edge spectra of the mixed valent (photoreduced) hydroxylase samples in the presence of coupling protein and 1-bromo-1propene.	163
Figure 3.18 Edge spectra of the fully reduced hydroxylase samples in the presence of coupling protein and 1-bromo-1-propene.	165
Figure 3.19 Edge spectra of the mixed valent and fully reduced hydroxylase samples.	167
Figure 3.20 Model of the hydroxylase diiron center based on the spectroscopic data.	169
Figure 4.1 The diiron cores in the active site model of the hydroxylase and in the R2 protein of ribonucleotide reductase.	222
Figure 4.2 A crystal of the hydroxylase.	224
Figure 4.3 SDS PAGE of redissolved crystals used for activity assays.	226
Figure 4.4 Precession photograph of the h0l zone.	228
Figure 4.5 Diffraction pattern to 3.7 Å resolution.	230
Figure 4.6 Native MIR electron density map at 5 Å resolution.	232
Figure 4.7 Native averaged map at 5 Å resolution.	234
Figure 4.8 Structure solution and refinement protocol.	236
Figure 4.9 Electron density map at 2.2 Å resolution of residue 363 in the β subunit.	238
Figure 4.10 Ramachandran plot for all residues in both halves of the α ₂ β ₂ γ ₂ dimer.	240
Figure 4.11 Diagram showing the Ramachandran angles phi (φ) and psi (ψ). .	242

Figure 4.12 Main chain temperature factors for the α subunit.	244
Figure 4.13 Main chain temperature factors for the β subunit.	246
Figure 4.14 Main chain temperature factors for the γ subunit.	248
Figure 5.1 Structure of the hydroxylase.	300
Figure 5.2 Secondary structure of the α subunit.	302
Figure 5.3 Superposition of the α and β subunits and the R2 protein.	304
Figure 5.4 Schematic diagrams of an α helix and of Type I and II tight turns.	306
Figure 5.5 Secondary structure of the β subunit.	308
Figure 5.6 Secondary structure of the γ subunit.	310
Figure 5.7 Stereo views of the superposition of the C_{α} atom backbones of the three subunits from the two halves of the $\alpha_2\beta_2\gamma_2$ dimer.	312
Figure 5.8 The differences in the two halves of the $\alpha_2\beta_2\gamma_2$ dimer as a function of residue number.	314
Figure 5.9 Structures of heavy atom compounds PIP, TAMM, and EMTS.	318
Figure 5.10 A region of the $\alpha\beta$ subunit-subunit interface.	320
Figure 5.11 Crystal lattice packing of the hydroxylase molecules.	322
Figure 5.12 Final $2F_o - F_c$ electron density map and $F_o - F_c$ difference map of the diiron center at 2.2 Å resolution.	324
Figure 5.13 Schematic representation of the dinuclear iron center.	326

Figure 5.14 Hydrogen bonding interactions of the coordinated histidine ligands.	328
Figure 5.15 The active site.	330
Figure 5.16 Cavities present in the α subunit.	332
Figure 5.17 The difference Fourier electron density map for the EMTS derivative at Cys151.	334
Figure 5.18 Mechanism for methane hydroxylation involving Cys151.	336
Figure 5.19 Comparison of the amino acid sequence of the α subunit with the sequences of other proteins containing dinuclear iron centers.	338

Chapter 1

Structural Analysis of a Non-Heme Iron-Oxo Hydroxylase

Introduction

In 1981, the 2.2 Å crystal structure of hemerythrin, a non-heme dioxygen transport protein from marine invertebrates, revealed a triply bridged dimetallic center consisting of two iron atoms linked by an oxo bridge and two carboxylate ligands derived from glutamic acid residues in the protein.¹ Although the existence of the Fe-O-Fe unit was known in model complexes and had been proposed for hemerythrin based on spectroscopic and magnetic properties,² a triply bridged core including two carboxylate ligands in addition to the oxo bridge was unprecedented. In 1983, two model compounds containing this (μ -oxo)bis(μ -carboxylato) unit were successfully prepared, $[\text{Fe}_2\text{O}(\text{OAc})_2(\text{HB}(\text{pz})_3)_2]$,³ and $[\text{Fe}_2\text{O}(\text{OAc})_2(\text{TACN})_2]^{2+}$.⁴ These complexes mimicked the spectroscopic and magnetic properties of hemerythrin quite well, and a number of other compounds followed,⁵ showing that the (μ -oxo)bis(μ -carboxylato) diiron(III) core can assemble spontaneously in aqueous solution by using a variety of ligands.

Shortly thereafter, similar diiron cores in several other proteins, including the R2 protein of ribonucleotide reductase, which has recently been characterized by X-ray crystallography,^{6,7} purple acid phosphatases, and methane monooxygenase, were postulated based on spectroscopic investigations. In each of these proteins, the diiron core has a different function.⁸ In the R2 protein, the diiron(II) center reacts with dioxygen to generate a tyrosyl radical involved in the reduction of ribonucleoside diphosphates to deoxyribonucleotide diphosphates for DNA synthesis. In purple acid phosphatases, the diiron center is involved in phosphate ester hydrolysis, and in methane monooxygenase, the diiron center activates oxygen for incorporation into methane. Yet the physical properties of the dinuclear iron sites in these proteins and in the model compounds are very

similar. This ability of one unit to serve so many different functions drove us to expand our studies of iron oxo chemistry to include the biological systems as well as the model complexes, and in 1987, we began a research effort in our laboratory to study the soluble methane monooxygenase from the methanotrophic bacterium *Methylococcus capsulatus* (Bath).

Methanotrophic bacteria utilize methane as their sole source of carbon and energy,⁹ converting methane to methanol in the first step of their metabolic pathway (eq. 1). The existence of methanotrophic bacteria has been



documented since the beginning of the century,¹⁰ but it was not until the pioneering work of Whittenbury in the late 1960s and early 1970s^{11,12} that a large quantity of pure cultures of these bacteria was made available. In recent years, the role of methane in global warming,¹³ the need for more efficient use of methane as an energy source,¹⁴ and the potential use of methanotrophs for bioremediation of land^{15,16} and water^{17,18} has motivated study of these microorganisms as well as detailed studies of the enzyme system responsible for the conversion of methane to methanol, known as methane monooxygenase or MMO.

There are two forms of methane monooxygenase, a soluble and a particulate, membrane-bound enzyme. The expression of these two forms of the enzyme is regulated by copper concentrations in the environment.¹⁹ At high copper-to-biomass ratios, the particulate MMO activity predominates, and under conditions of low copper concentrations and high biomass, the soluble MMO is expressed exclusively. The particulate MMO from *M. capsulatus* (strain M) has been reported to consist of two proteins and to

contain copper ions.²⁰ The particulate MMO from *M. capsulatus* (Bath) has been solubilized, but was very unstable, and could not be resolved into individual components.²¹ Because the particulate MMO is so difficult to isolate, most attention has focused on the soluble form of the enzyme.

Soluble MMO from *M. capsulatus* (Bath), the first MMO system to be purified,²² consists of three proteins: a reductase (MW 38.6 kDa), also called protein C, a small coupling protein (MW 15.5 kDa), also called protein B, and a hydroxylase (MW 251 kDa), also called protein A. All three proteins are necessary for enzyme activity. The methane monooxygenase from *Methylosinus trichosporium* OB3b has also been purified,^{23,24} and is very similar to the *M. capsulatus* system. In addition, a MMO system consisting of the hydroxylase and the reductase, but lacking the coupling protein, has been isolated from *Methylobacterium* CRL-26.²⁵ The reductase, an iron-sulfur protein containing one 2Fe-2S cluster and one mole of FAD, transfers electrons to the hydroxylase.²⁶ The coupling protein is a small polypeptide with no metal or prosthetic group,²⁷ and has been implicated in several regulatory roles. The hydroxylase, which belongs to the growing class of functionally diverse iron oxo proteins mentioned above, is the site of methane oxidation, and is the key component in the enzyme system.

The hydroxylase (MW 251 kDa) is a multimeric protein, consisting of two copies each of three different subunits; the holoenzyme is $\alpha_2\beta_2\gamma_2$ (α , MW 60.6 kDa; β MW 45 kDa; γ , MW 19.8 kDa).²⁸ We began our investigations of the hydroxylase in a collaboration with Professor H. Dalton, who first reported the presence of a dinuclear iron center in the hydroxylase.²⁹ Our objectives were to establish the nature of the diiron center via spectroscopic methods and comparison to model compounds, to elucidate the role of the coupling protein, to determine the mechanism of the hydroxylation reaction,

and to characterize all three MMO components by X-ray crystallography. The collaboration enabled us to set up a program in our laboratory to purify the proteins, and we embarked on experiments to achieve our goals. In the past 6 years, significant progress has been achieved in all of these areas both in our laboratory and elsewhere. Most recently, we have solved the X-ray structure of the MMO hydroxylase at 2.2 Å resolution.³⁰

Our purpose in this Account is to review the structural studies of the hydroxylase carried out by ourselves and others in the context of the now known X-ray structure. Our structural investigations of the hydroxylase attempted to answer the following questions: (1) what is the structure of the holo enzyme and how do the three subunits interact, (2) how many diiron centers are present and which subunit(s) accommodate(s) the diiron centers, (3) what bridging ligands are present in the diiron center, (4) what nonbridging ligands are present in the diiron center, (5) what are the specific amino acid residues coordinated to and adjacent to the two iron atoms, and finally, (6) how does the hydroxylase interact with the other two MMO proteins. We begin this Account with a discussion of the spectroscopic and biochemical data obtained by using methodologies other than X-ray crystallography and the resulting models concerning each of these structural questions. We then discuss the X-ray structure determination briefly, and finally we describe the structure obtained from the X-ray analysis in terms of the models that resulted from the non X-ray crystallographic experiments.

Structural Information from Non X-Ray Crystallographic Methods

The holo hydroxylase and subunit interactions. In the first reported hydroxylase purification,²⁸ for the *M. capsulatus* hydroxylase, three subunits of molecular weights 54 kDa, 42 kDa, and 17 kDa were identified by SDS

PAGE, and were determined to be present in stoichiometric amounts by densitometric analysis. Since the total molecular weight was 210 kDa by gel filtration and 253 kDa by nondenaturing PAGE, it was concluded that there are two copies of each of the three subunits, an $\alpha_2\beta_2\gamma_2$ arrangement. Similar results were obtained for the *M. trichosporium* hydroxylase with a native molecular weight of 245 kDa by gel filtration and ultracentrifugation and subunit molecular weights of 54, 43, and 23 kDa.²⁴ In addition, the subunit structure of the *Methylobacterium* CRL-26 hydroxylase was determined to be $\alpha_2\beta_2\gamma_2$ with molecular weights of 55 kDa, 40 kDa, and 20 kDa for the subunits and a total molecular weight of 220 kDa.²⁵

The cloning of a 12 kb EcoR1 restriction fragment containing the genes for all three subunits and the reductase as well as two open reading frames, *orfX* and *orfY*, showed that the genes are contiguous in the *M. capsulatus* genome, forming an MMO operon.³¹ The sequences of the three subunits (α , *mmoX*; β , *mmoY*; γ , *mmoZ*) and of the reductase (*mmoC*) were identified,³² and one of the ORFs, *orfY* was subsequently identified as the gene for the coupling protein.^{33,34} The availability of these sequences was essential for the X-ray structure determination. The MMO genes for the *M. trichosporium* hydroxylase were also cloned,³⁵ and the two hydroxylases are homologous with 85% identity for the α subunit, 59% identity for the β subunit, and 49% identity for the γ subunit. There are slightly different numbers of amino acid residues in the α , β , and γ subunits from the two different hydroxylases, with 527, 389, and 170 residues respectively for the *M. capsulatus* hydroxylase, and 525, 394, and 169 for the *M. trichosporium* hydroxylase.

Very little information pertaining to the secondary structure of the hydroxylase was available. Based on alignments of the sequence of the α subunit with the ribonucleotide reductase R2 protein, it was suggested that

the diiron center is situated in a four helix bundle.³⁶ In addition, circular dichroism spectra of the *M. capsulatus* hydroxylase suggested a high helical content.³⁷ The only information about the arrangement of the three subunits was derived from chemical cross-linking experiments with the *M. trichosporium* hydroxylase.³⁸ Reaction of the hydroxylase with the covalent zero length cross-linking reagent 1-ethyl-3-(3-dimethylaminopropyl)-carbodiimide (EDC) resulted in several products, two of which were identified as attached α and β subunits and a dimer of β subunits. No cross-linking of the γ subunit was observed, even in the presence of the cross-linking catalyst *N*-hydroxysulfosuccinimide. Since EDC is a zero-length cross-linking reagent, the sites of attachment correspond to sites of inter-subunit salt bridges. The subunit arrangement inferred from these experiments is shown in Figure 1.1a.

Number and location of dinuclear iron centers. The presence of a dinuclear iron center similar to those found in hemerythrin and the R2 protein was first revealed by EPR studies on the *M. capsulatus* hydroxylase. In these experiments, dithionite reduced samples exhibited a $g < 2$ signal typical of an Fe(II)Fe(III) diiron center.²⁹ A similar signal with $g_{av} = 1.85$ was also observed for the *M. trichosporium* hydroxylase²⁴ and for the *Methylobacterium* CRL-26 and *Methylococcus* CRL-25 hydroxylases.³⁹ Upon further reduction to the Fe(II)Fe(II) state, another signal at $g = 15$ was observed for both the *M. trichosporium*²⁴ and *M. capsulatus*⁴⁰ hydroxylases. An Fe content of 2 Fe per $\alpha_2\beta_2\gamma_2$ hydroxylase dimer was initially reported for the *M. capsulatus* hydroxylase.²⁸ It was later stated that reconstitution of the apo hydroxylase resulted in increased specific activities and an Fe content of 3.3 Fe per protein.⁴¹ A value of 2.8 Fe per dimer was reported for the *Methylobacterium* CRL-26 protein.²⁵ For the *M. trichosporium* hydroxylase,

Fe contents of 4 Fe per hydroxylase molecule and higher specific activities were attributed to the use of Fe and cysteine in the purification buffers.²⁴ In our purifications of the *M. capsulatus* protein, we consistently observe close to 2 Fe per protein molecule, and derived no benefit from the inclusion of Fe and cysteine in the purification buffers.⁴⁰ In a very recent investigation, the *M. capsulatus* hydroxylase was depleted of Fe by using 3,4-dihydroxybenzaldehyde, and then reconstituted with Mn(II) ions. The incorporation of just two Mn(II) ions was quantitated by EPR spectroscopy, and it was concluded that the *M. capsulatus* hydroxylase contains just one diiron site.⁴²

Several lines of evidence suggested that the diiron center(s) was located on the α subunit. Reactions of the hydroxylase with ¹⁴C radiolabeled acetylene, a suicide substrate, resulted in incorporation of the radiolabel into the α subunit, suggesting that the α subunit contains the catalytically active center.⁴³ The EPR spectrum of the hydroxylase is perturbed by the addition of the coupling protein,³⁸ suggesting that it binds to the hydroxylase near the diiron center. Moreover, the cross-linking experiments yielded a covalent attachment between the α subunit and the coupling protein. The coupling protein did not cross-link to any other subunits.³⁸ Therefore, it seemed likely that the diiron center resides on the α subunit. Alternatively, the coupling protein could bind to the α subunit, but near a subunit-subunit interface, and still affect the diiron center if the diiron center were located on a different subunit.

The bridging ligands. The nature of the bridging ligands in the hydroxylase diiron core was investigated by a variety of spectroscopic techniques. Both the *M. capsulatus* and *M. trichosporium* hydroxylases are essentially colorless, with no optical bands beyond 300 nm.^{24,40} Oxo-bridged

proteins and model complexes typically exhibit absorption features in the 300-800 nm range.⁵ A peak at 410 nm was observed for the *Methylobacterium* CRL-26 hydroxylase,²⁵ but we have shown that such a feature is most likely due to a cytochrome impurity.⁴⁰ Hemerythrin and the R2 protein both exhibit resonance Raman bands attributable to an Fe-O-Fe symmetric stretch, but no such Raman feature was ever observed for the native hydroxylase. Moreover, preliminary EXAFS studies on the *M. capsulatus* and *M. trichosporium* hydroxylases indicated the absence of an oxo bridge. For these samples, which were photoreduced to the mixed valent oxidation state in the X-ray beam, no short Fe-O distance (~ 1.8 Å) typically associated with an Fe-O-Fe unit was observed.⁴⁴ The EXAFS data instead were similar to those for the hydroxo bridged model compound, $[\text{Fe}_2(\text{OH})(\text{OAc})_2(\text{HB}(\text{pz})_3)_2](\text{ClO}_4)$.⁴⁵ In a more detailed EXAFS study, Fe...Fe distances of 3.42 Å were determined for the both the diferric and mixed valent hydroxylases, a value long for a μ -oxo bridged diiron center, but consistent with the presence of hydroxide, monodentate carboxylate, or alkoxide bridges.⁴⁰ This value also indicated the presence of at least one additional bridging carboxylate ligand. Hemerythrin contains two bridging carboxylate ligands, and the same was expected for the R2 protein, but surprisingly, its X-ray structure revealed a single carboxylate bridge.⁶ An EXAFS study on the *Methylobacterium* CRL-26 hydroxylase yielded an Fe...Fe distance of 3.05 Å,³⁹ a discrepancy which we have attributed to differences in analysis protocol.⁴⁰ In this study, no evidence pertaining to the presence or absence of a short Fe-O distance was reported.

Antiferromagnetic coupling constants of $J = -32 \text{ cm}^{-1}$ for the *M. capsulatus* protein⁴⁰ and $J = -30 \text{ cm}^{-1}$ for the *M. trichosporium* protein³⁸ were also measured, where $H = -2JS_1 \cdot S_2$. These values are also consistent with the presence of hydroxo, carboxylato, or alkoxo bridges. A J value of -8 cm^{-1} has

recently been determined for the diferric *M. trichosporium* hydroxylase, which is unusual since diferric exchange interactions are usually stronger than mixed valent exchange interactions.⁴⁶ Finally, the Mössbauer spectroscopic parameters for both hydroxylases fall in between values for oxo and hydroxo bridged model compounds, suggesting the presence of a novel bridge.⁴⁰ From the accumulated data, we concluded that the hydroxylase did not contain an oxo bridge, but a hydroxo, alkoxo, or monodentate carboxylato bridge. The nature of the bridge in the diiron center was finally resolved by a proton ENDOR study of the mixed valent *M. capsulatus* hydroxylase.⁴⁷ A set of resonances with $A \sim 14 - 30$ MHz detected in the proton ENDOR spectrum were strikingly similar to resonances seen for semimet azidohemerythrin, and attributed to the hydroxo bridge in that protein. The hydroxylase resonances were therefore assigned to a bridging hydroxide. Since the EXAFS showed similar Fe...Fe distances for the mixed valent and oxidized hydroxylases, it was further concluded that a hydroxo bridge is probably present in the oxidized hydroxylase as well. Similar experiments yielded the same result for the *M. trichosporium* hydroxylase.⁴⁸

The non-bridging ligands. Some information about the nature of the nonbridging ligands in the diiron core was also obtained from spectroscopic experiments. According to the EXAFS data, the average first shell coordination consists of 5-6 oxygen or nitrogen ligands at distances of 2.04 Å for the diferric hydroxylase, 2.06-2.08 Å for the mixed valent hydroxylase, and 2.15 Å for the fully reduced hydroxylase. For the diferric R2 protein, which has just two coordinated histidines, the average first shell coordination distance is 2.04-2.06 Å, whereas for oxyhemerythrin, which has all histidine nitrogen ligands, the average first shell coordination distance is 2.15 Å.⁸ These values suggested that, like the R2 protein, the hydroxylase contains

more oxygen than nitrogen ligands. The presence of histidine nitrogen ligands in the mixed valent hydroxylase was further investigated by ESEEM and ENDOR spectroscopies. The ESEEM spectrum of the *M. capsulatus* hydroxylase revealed the presence of two types of nitrogens with a single nitrogen of each type coordinated to the Fe atoms.⁴⁹ In addition, ¹⁴N ENDOR spectroscopy demonstrated the presence of one or more coordinated histidines in the *M. trichosporium* hydroxylase.⁵⁰ Chemical modification of the oxidized *M. capsulatus* hydroxylase with diethylpyrocarbonate (DEPC), which reacts with histidine residues, showed that in the apo hydroxylase, 14 histidines were reactive, but in the iron-containing hydroxylase, only 12 histidines could be modified, suggesting that 2 histidines are ligated to the diiron center.³⁷ Finally, a coordinated water molecule or hydroxide was identified in the proton ENDOR spectrum of the mixed valent hydroxylase.⁴⁷ A model of the diiron center based on all the spectroscopic and biochemical data is shown in Figure 1.2a.

Specific amino acid residues in the active site. At this point, a working model of the diiron core structure had been developed, but no information about the specific amino acid residues present in the active site was yet available. Several alignments of the amino acid sequence of the α subunit of the hydroxylase, which was believed to contain the diiron center, and the amino acid sequence of the R2 subunit of ribonucleotide reductase were proposed.^{32,36} In the most detailed model,³⁶ the sequence of the α subunit was aligned with the iron coordinating four helix bundle of the R2 protein. This alignment suggested that Glu114, Glu144, His147, Glu209, Glu243, and His246 are coordinated to the iron atoms, and that other specific residues, including Ile239, Ile217, and Thr213, are present in the active site pocket. Notably, in the hydroxylase, a cysteine residue, Cys151, was postulated to

replace the functionally important tyrosyl radical site Tyr122 found in the R2 protein. Although this model could not provide exact details of coordination, the presence of 2 coordinated histidines and several oxygen ligands was consistent with the spectroscopic data. For the *M. trichosporium* hydroxylase, Glu209 is replaced by an aspartic acid residue. The information from the sequence alignment is incorporated into the active site model shown in Figure 1.2b.

Interactions with the coupling protein and the reductase. As mentioned above, the coupling protein perturbs the EPR spectrum of the mixed valent hydroxylase, and cross-links to the α subunit, suggesting that a binding domain for the coupling protein may exist on the α subunit. In addition, the EXAFS spectra of the mixed valent hydroxylase show slight differences in the presence of the coupling protein.⁵¹ The coupling protein regulates electron transfer by helping to tune the redox potentials of the diiron center in the hydroxylase.⁵² When coupling protein and reductase are present, but substrate is absent, electron transfer to the diiron center is completely inhibited, even at potentials as negative as -200 mV. The addition of substrate effects a drastic change, allowing reduction of the diiron center at potentials as high as 150 mV. In the presence of the coupling protein alone, reduction is inhibited, but does occur according to recent X-ray absorption edge data. These edge data also show that the coupling protein effects small changes in the coordination environment of the iron atoms.⁵¹

The coupling protein also affects the rate of substrate oxidation. For the substrate nitrobenzene, the rate constant for the formation of 4-nitrophenol was increased 30-fold in the presence of the coupling protein.⁵³ An effect on the regioselectivity of substrate oxidation by the coupling protein has been observed for the *M. trichosporium* system. For the substrates isopentane,

nitrobenzene, and propane, the coupling caused a significant change in product distribution.⁵⁴ Taken together, these data indicate that the coupling protein induces some sort of conformational change near the substrate binding site and diiron center. The coupling protein is therefore placed proximal to the α subunit in the model shown in Figure 1.1a.

The reductase neither affects the diiron center nor changes the rate and regioselectivity of substrate oxidation, and covalent attachment of the reductase and the β subunit was observed in the chemical cross-linking experiments.³⁸ If the binding domain for the reductase lies on the β subunit and the diiron center is located on the α subunit, it is unlikely, although not impossible, that the reductase would change the spectroscopic properties of the diiron center. Complexes between the reductase and the hydroxylase and the reductase and the coupling protein have been detected by fluorescence spectroscopy.³⁸ In the presence of the reductase, the tryptophan fluorescence of the hydroxylase is quenched by 86%, and the tryptophan fluorescence of the coupling protein is quenched by 78%. In addition, a shift in the fluorescence maximum is observed for the coupling protein complexed with the reductase. These observations suggest that the binding domains for the coupling protein and the reductase, despite residing on different subunits, are arranged in such a way that the coupling protein and reductase can interact (Figure 1.1a).

Structural Information from X-Ray Crystallography

Brief History of the X-ray structure determination. Since a complete structural characterization of the hydroxylase would ultimately require a three-dimensional X-ray analysis, we initiated attempts to crystallize the hydroxylase in mid-1990 in collaboration with Professor C. Frederick. After >1000 crystallization trials, we obtained thin crystalline plates that diffracted to

better than 2.2 Å resolution. We first observed diffraction in May 1991. The unit cell dimensions were 62.6 x 110.1 x 333.5 Å, and the crystals were orthorhombic, belonging to the space group $P2_12_12_1$.⁵⁵ The long cell dimension of 333.5 Å posed a frustrating problem in data collection because the Marresearch imaging plate detector available to us had limited spatial resolution, allowing collection of data to just 3.5 Å resolution. In addition, the thin crystal size rendered it difficult to collect good quality data by using a laboratory source. Both of these problems were overcome by the use of synchrotron radiation. We collected 3.0 Å native data and several partial heavy atom derivative data sets to 3.7 Å resolution at Stanford Synchrotron Radiation Laboratory (SSRL) in August 1992. The difference Patterson map for one of the heavy atom derivatives collected at Stanford, PIP, di- μ -iodobis(ethylenediamine)diplatinum(II), was solved, marking the first breakthrough in the structure determination. By using phases from the PIP derivative for difference Fourier maps, the heavy atom positions in several other derivatives were determined. These heavy atom sites led to the identification of a noncrystallographic twofold axis relating the two $\alpha\beta\gamma$ halves of the hydroxylase dimer. It was then possible to use molecular averaging to improve our native multiple isomorphous replacement (MIR) electron density maps. After averaging, our 3.5 Å maps revealed some secondary structure elements, but interpretation of the structure was not possible without higher resolution data.

In December 1992, with our collaborator Professor P. Nordlund, we traveled to the Photon Factory in Tsukuba, Japan, where, with the help of Professor N. Sakabe, we collected a 2.2 Å native data set by using a modified Weissenberg camera with imaging plates. In February 1993, we collected a number of 3.0 Å derivative data sets at SSRL, and these derivative data sets

and the 2.2 Å native data were used to calculate 3.0 Å native averaged maps of the hydroxylase, which were superior to the previous 3.5 Å maps. A hypothesis for the location of the diiron center was formulated from a native anomalous map and the presence of two mercury binding sites, which we postulated to be the cysteine residues near the diiron center (Cys151 and Cys211) predicted by a sequence alignment with the ribonucleotide reductase R2 protein.³⁶ Enough helices were evident in the map to build the iron coordinating four helix bundle into the electron density, thus locating part of the α subunit. We then pursued a strategy of partial structural phase combination, in which the MIR phases were gradually improved by the combination of phase information from a partial model. Eventually, the β and γ subunits were located, and their sequences fitted by using the heavy atom sites as markers for cysteine, histidine, or methionine residues. By the end of September 1993, we had a model which contained 512 of the 527 residues in the α subunit, 384 of the 389 residues in the β subunit, and 162 of the 170 residues in the γ subunit. There is no electron density for the first 15 residues in the α subunit, the first 6 residues in the β subunit, and the first residue and last 7 residues in the γ subunit.³⁰

X-ray structure of the hydroxylase. The X-ray structure of the holo hydroxylase confirms the presence of an $\alpha_2\beta_2\gamma_2$ polypeptide chain arrangement. The sequence fitting to the electron density for the α and γ subunits proceeded without problems once portions of the sequences were recognized. For the β subunit, however, we encountered some difficulty in fitting the last 30 residues in the C-terminus of the published sequence³¹ to the electron density map. Residue 363 was clearly a tryptophan residue, but the sequence had a glycine residue at this position. The addition of either one thymidine or one cytidine base at position 4227 in the *mmoY* gene sequence

resulted in an appropriate frameshift, changing the GGA codon for Gly to TGG, which codes for Trp. The derived amino acid sequence was consistent with the electron density map, and includes two more residues at the C-terminus, so that the β subunit now contains 389 rather than 387 residues (Trp 363-Ile-Glu-Asp-Tyr-Ala-Ser-Arg-Ile-Asp-Phe-Lys-Ala-Asp-Arg-Asp-Gln-Ile-Val-Lys-Ala-Val-Leu-Ala-Gly-Leu-Lys 389). The presence of an additional cytidine base at position 4227 has since been confirmed by sequencing.⁵⁶ When the new sequence is compared to that of the *M. trichosporium* β subunit, there are 11 identical residues in the C-terminal 30 residues, whereas with the incorrect sequence, only 4 residues were conserved between the two species.

The structure of the holo hydroxylase is shown in Figure 1.1b. The two $\alpha\beta$ protomers form a large heart, with the noncrystallographic twofold axis running down the center of the heart and an opening in the center of the molecule. The hydroxylase is primarily helical with just two small β hairpin structures in the α subunit. Whereas circular dichroism spectroscopic measurements indicated a large amount of helical structure,³⁷ no detailed information pertaining to the secondary structure of the hydroxylase could be obtained without an X-ray structure. Remarkably, 10 helices each of the α and β subunits have identical folds, although there is no detectable primary sequence homology. This feature of the structure was completely unexpected. Furthermore, the fold of the α and β subunits resembles the fold of the ribonucleotide reductase R2 protein, also a surprise. The sequence alignment did suggest that the diiron center was located in a four helix bundle as in the R2 protein,³⁶ but the extent of the similarity between the structures was not anticipated.

The interaction between the two protomers, which we have designated the A protomer and the B protomer, is primarily between the two β subunits. The $\beta\beta$ interface contains a several salt linkages, including $\beta_A\text{Arg122} - \beta_B\text{Glu115}/\beta_B\text{Glu116}$, $\beta_A\text{Glu115}-\beta_B\text{Arg118}/\beta_B\text{Arg122}$, and $\beta_A\text{Glu116} - \beta_B\text{Arg122}$. Most of these interactions occur at the opening in the center of the hydroxylase dimer. By contrast, there are no inter-subunit salt linkages between the two α subunits. There are also a number of interactions between the α and β subunits, including $\alpha\text{Glu230}-\beta\text{Arg9}$, $\alpha\text{Glu465}-\beta\text{Lys75}$, $\alpha\text{Lys185}-\beta\text{Asp68}$, and $\alpha\text{Lys75}-\beta\text{Asp188}$. The γ subunit does not participate in the dimer interaction, but is associated with the α and β subunits through the following salt bridges: $\alpha\text{Glu454}-\gamma\text{Arg156}$, $\alpha\text{Glu462}-\gamma\text{Arg143}$, $\alpha\text{Glu465}-\gamma\text{Arg44}$, $\beta\text{Asp61}-\gamma\text{Arg12}$, $\beta\text{Arg91}-\gamma\text{Glu61}$, and $\beta\text{Glu86}-\gamma\text{Arg115}$. The observation of a $\alpha\beta$ cross-linked product³⁸ is consistent with the X-ray structure, since the linkages $\alpha\text{Glu465}-\beta\text{Lys75}$, $\alpha\text{Lys185}-\beta\text{Asp68}$, and $\alpha\text{Lys65}-\beta\text{Asp188}$ are good candidates for cross-linking by EDC. The absence of cross-linked products involving the γ subunit could be due to the fact that all the inter-subunit salt bridges with the γ subunit involve arginine residues. Whereas lysine residues can form stable cross-linked products, arginine residues have a high pK_a , and are less likely to form a stable amide bond. A low yield $\beta\beta$ cross-linked product was observed, however,³⁸ and the interactions between the two β subunits also involve only arginine residues. The cross-linking experiments were carried out on the *M. trichosporium* hydroxylase, which could conceivably explain discrepancies between the cross-linking data and the X-ray structure if the two structures were different. This possibility seems highly unlikely, however, considering that every residue involved in inter-subunit interactions in the *M. capsulatus* hydroxylase is conserved in the *M. trichosporium* sequence.

The X-ray structure unambiguously shows that there are two diiron sites in the hydroxylase, one located on each α subunit, separated by 45 Å. The iron atoms in the hydroxylase structure are shown as spheres in Figure 1.1b. The two sites appear to be fully occupied.³⁰ The location of the diiron center is consistent with the chemical labeling and cross-linking experiments. As predicted by the alignment with the sequence of the R2 protein, the diiron center is positioned within a four helix bundle, which donates the coordinating amino acid residues. The presence of four Fe atoms supports quantitative results reported for the *M. trichosporium* hydroxylase,²⁴ but contradicts our measured values of 2 Fe atoms and the reported reconstitution of the apo hydroxylase with 2 Mn(II) atoms.⁴² It may be that we have crystallized 4 Fe protein from a mixture of apo and iron-depleted protein, and preliminary results in our laboratory indicate that an insoluble fraction of apo protein can be removed from hydroxylase samples resulting in a higher Fe content.⁵⁷ The fact that we sometimes measure Fe contents of close to 3 Fe per protein supports this hypothesis. We most often measure 2 Fe, however, which would suggest that there is always 50% apo protein present, a more regular value than would be expected for a random mixture of protein molecules with varying Fe contents. The reconstitution experiment with Mn(II)⁴² is perhaps the most difficult to explain. Presumably, both diiron sites are removed during preparation of the apo hydroxylase, and should be reconstituted with 4 Mn(II) ions.

The X-ray structure of the hydroxylase reveals three ligands bridging the two Fe atoms (Figure 1.2c). First, the two iron atoms are linked by one carboxylate ligand derived from the protein, Glu144. We have designated this carboxylate a "semi-bridging" ligand because the Fe-O distances for one of the Fe atoms, Fe2, of 2.5 Å and 2.7 Å in the two protomers, are longer than

normal coordinating distances. Although the carboxylate bridge was expected, this semi-bridging character was not anticipated from any of the spectroscopic studies. In addition, two exogenous bridging ligands were apparent in the $F_o - F_c$ difference Fourier maps. We have assigned one of these ligands as a hydroxo bridge. For this assignment, we relied on the proton ENDOR data⁴⁷ since we cannot distinguish between oxide, hydroxide, and water in the electron density map. Furthermore, the Fe...Fe distance is 3.4 Å in both protomers, which is consistent with a hydroxo bridge and agrees well with the EXAFS data for the both the diferric and mixed valent hydroxylases. A comparison of the EXAFS data and the X-ray structure raises an additional question. Since the EXAFS samples photoreduced to the mixed valent form in the X-ray beam, it is possible that the crystals may have photoreduced, since the data were collected by using synchrotron radiation. At present, we have no evidence supporting or disproving this possibility. We have assigned a second exogenous bridging ligand as an acetate ion since we used ammonium acetate in the crystallization buffers. We considered bicarbonate ion as an alternative assignment, but there are no hydrogen bonding interactions to this ligand, which would be expected for bicarbonate ion. This bridging acetate ligand was not predicted by spectroscopy, and may not be present in the native enzyme in cells. The position occupied by acetate in the X-ray structure may represent a site where the oxidized substrate, methoxide ion, is positioned before protonation and release from the active site.

The nonbridging ligands in the diiron center are comprised of those amino acid residues suggested in the alignment with the sequence of the R2 protein.³⁶ As shown in Figure 1.2c, Fe1 is coordinated to the δN atom of His147 and Fe2 is coordinated to the δN atom of His246. These ligands were predicted correctly by the ESEEM, ENDOR, and EXAFS experiments, and by

the sequence alignments. In addition, Fe1 is coordinated to one monodentate carboxylate, Glu114, and Fe2 is ligated to two monodentate carboxylates, Glu209 and Glu243. The presence of more oxygen than nitrogen ligands was suggested by the EXAFS analysis. The fact that all the nonbridging carboxylate ligands are monodentate was not previously determined. Finally, Fe1 is coordinated to a water molecule, a third exogenous ligand, as anticipated by the proton ENDOR data.⁴⁷ According to the ENDOR study, this ligand could be assigned as either a terminal water or hydroxide. The combination of a bridging hydroxide and a terminal water ligand renders the active site charge neutral, so we have chosen to assign this ligand as a water molecule. Other residues present in the active site, which had not been identified by spectroscopic or biochemical methods were also predicted accurately by the sequence alignment, including Cys151, and two aspartic acid residues, Asp242 and Asp143, which are hydrogen bonded to His147 and His246, respectively. The presence of Cys151 in the space occupied by the tyrosyl radical in the R2 protein suggests a redox role for this residue in the catalytic mechanism. One possible mechanism involving Cys151 has been described,⁵⁸ but currently, there is no experimental data which either supports or disproves such a mechanism.

Finally, the X-ray structure reveals possible binding sites for the coupling protein and the reductase, which are consistent with the cross-linking data, the fluorescence data, and the EXAFS and EPR spectral effects observed in the presence of the coupling protein. There is a wide canyon formed by the $\alpha\beta$ pairs in the dimer (Figure 1.1b). Two of the iron binding helices are exposed to this canyon, and could interact with the coupling protein, resulting in a conformational change near the active site. Two of the iron ligands, Glu209 and Glu243, are particularly well located to be affected by

this type of interaction. The changes observed in the EPR and EXAFS spectra of the hydroxylase could result in changes in the coordination of these ligands, perhaps in the form of carboxylate shifts.⁵⁹ Since optimal activity of the hydroxylase requires 2 moles of coupling protein,³⁸ it is probable that there are 2 binding domains for the coupling protein, located in the two canyons related by the noncrystallographic twofold axis. The canyon is large enough to accommodate the reductase as well, in the region closer to the β subunit. In addition, there are a number of tryptophan residues in the canyon, some of which are good candidates for quenching by reductase binding. For example, Trp31 on the α subunit and Trp43 on the β subunit are exposed to the surface, and are both located in a region that is probably too far from the active site to be the binding domain for the coupling protein.

Conclusions and Unsolved Mysteries

A variety of strategies were employed in the structural investigations of the hydroxylase which preceded the X-ray structure. In terms of the overall structure, the juxtaposition of the α and β subunits was correctly predicted by the chemical cross-linking experiments. The occurrence of only arginine salt bridges between the γ subunit and the α and β subunits may explain the lack of γ cross-linked products, but the $\beta\beta$ attachment is inconsistent with this argument. The structure also revealed an error in the published sequence of the β subunit,³² although X-ray crystallography is certainly not the most time-efficient method of amino acid sequencing. The conclusions about the binding of coupling protein and reductase deduced from the spectroscopic data and the cross-linking experiments are also consistent with the X-ray structure. Further investigations in this area, in the form of co-crystal structures and site-directed mutagenesis experiments, are clearly necessary.

The diiron center is located on the α subunit, as anticipated, and two iron centers are present in the hydroxylase, contrary to much of the quantitative work on the *M. capsulatus* hydroxylase. The reconstitution of apo *M. capsulatus* hydroxylase with 2 Mn(II) ions⁴² is particularly hard to reconcile with the structure.

The spectroscopic techniques used to characterize the diiron core proved to be reliable, correctly indicating the presence of a hydroxo bridge, 2 coordinated histidine residues, and several carboxylate ligands. The proton ENDOR study provided key information which was used in our assignments of the bridging hydroxide and terminal water molecule. The number of bridging carboxylates was not predetermined by spectroscopy, and the one bridging carboxylate revealed in the structure has actually been termed "semi-bridging," a feature that has not been observed in the other crystallographically characterized diiron proteins. The bridging acetate ligand was unexpected, and we suspect that this ligand is a result of the crystallization buffer. The binding of exogenous anions such as fluoride,⁶⁰ azide,⁴² and phenoxide⁶¹ to the oxidized hydroxylase has been reported. If the acetate is derived from the crystallization buffers, another bridging ligand may be present in the native oxidized hydroxylase. One possibility is a second hydroxo bridge, but the Fe...Fe distance of 3.4 Å from both the EXAFS analysis and the crystal structure is too long to be consistent with the presence of 2 hydroxo bridges. The true oxidation state of the diiron center in the structure constitutes an additional unknown. If the crystals had been photoreduced to the mixed valent state, the active site would have a net negative charge. For the EXAFS samples, the time of photoreduction was variable and depended on the synchrotron ring current. For example, an absorption edge shift of 0.8 eV occurred after 21 hours exposure to the X-ray beam at 30-58 mA, but after

injection to 90 mA, a 1 eV shift occurred in 11 hours. It is therefore difficult to determine whether the crystal used at the Photon Factory could have photoreduced.

Finally, the model derived from the sequence homology with the ribonucleotide reductase R2 protein accurately predicted many of the features of the active site, including the identities of the coordinating residues and other residues in the vicinity of the diiron center. The role of the active site cysteine residue, Cys151, clearly merits further experimental investigation. Recently, several other proteins including stearoyl ACP desaturase,⁶² ruberythrin,⁶³ phenol hydroxylase,⁶⁴ and toluene-4-monooxygenase⁶⁵ have been shown to contain Glu-X-X-His sequences, similar to the sequences in the hydroxylase and the R2 protein which provide the iron ligands. Models based on these homologies may prove invaluable in future structure determinations of these proteins, provided that excessive model bias is avoided.

In conclusion, although there is no substitute for the level of detail inherent in an X-ray structure determination, a combination of spectroscopic, biochemical, and more speculative techniques correctly predicted much of the hydroxylase active site structure. Other aspects of the structure, such as the striking similarity between the folds of the α and β subunits, were completely new revelations. Several recurrent issues including the number of iron atoms and the acetate ligand must now be addressed. In addition, the detailed information contained in the structure continually suggests an exciting array of new experiments which will help us to further understand this amazing and complex multicomponent enzyme system.

References

- (1) Stenkamp, R. E.; Siecker, L. C.; Jensen, L. H. *Nature* **1981**, *291*, 262-264.
- (2) Murray, K. S. *Coord. Chem. Rev.* **1974**, *12*, 1-35.
- (3) Armstrong, W. H.; Lippard, S. J. *J. Am. Chem. Soc.* **1983**, *105*, 4837-4838.
- (4) Wieghardt, K.; Pohl, K.; Gebert, W. *Angew. Chem. Int. Ed. Engl.* **1983**, *22*, 727.
- (5) Que, L., Jr.; True, A. E. *Prog. Inorg. Chem.* **1990**, *38*, 97-200.
- (6) Nordlund, P.; Sjöberg, B.-M.; Eklund, H. *Nature* **1990**, *345*, 593-598.
- (7) Nordlund, P.; Eklund, H. *J. Mol. Biol.* **1993**, *231*, 123-164.
- (8) Vincent, J. B.; Olivier-Lilley, G. L.; Averill, B. A. *Chem. Rev.* **1990**, *90*, 1447-1467.
- (9) Anthony, C. *The Biochemistry of Methylotrophs*; Academic Press: New York, 1982, p 296-379.
- (10) Whittenbury, R.; Dalton, H. In *The Prokaryotes*; M. P. Starr, H. Stolp, H. G. Truper, A. Balowes and H. G. Schlegel, Ed.; Springer-Verlag: Berlin, 1981.
- (11) Whittenbury, R.; Phillips, K. C.; Wilkinson, J. F. *J. Gen. Microbiol.* **1970**, *61*, 205-218.
- (12) Whittenbury, R.; Davies, S. I.; Davey, J. F. *J. Gen. Microbiol.* **1970**, *61*, 219-226.
- (13) Lelieveld, J.; Crutzen, P. J.; Brühl, C. *Chemosphere* **1993**, *26*, 739-768.
- (14) Periana, R. A.; Taube, D. J.; Evitt, E. R.; Löffler, D. G.; Wentrcek, P. R.; Voss, G.; Masuda, T. *Science* **1993**, *259*, 340-343.
- (15) Lindstrom, J. E.; Prince, R. C.; Clark, J. C.; Grossman, M. J.; Yeager, T. R.; Braddock, J. F.; Brown, E. J. *Appl. Environ. Microbiol.* **1991**, *57*, 2514-2522.
- (16) Pritchard, P. H.; Costa, C. F. *Environ. Sci. Technol.* **1991**, *25*, 372-379.
- (17) Green, J.; Dalton, H. *J. Biol. Chem.* **1989**, *264*, 17698-17703.

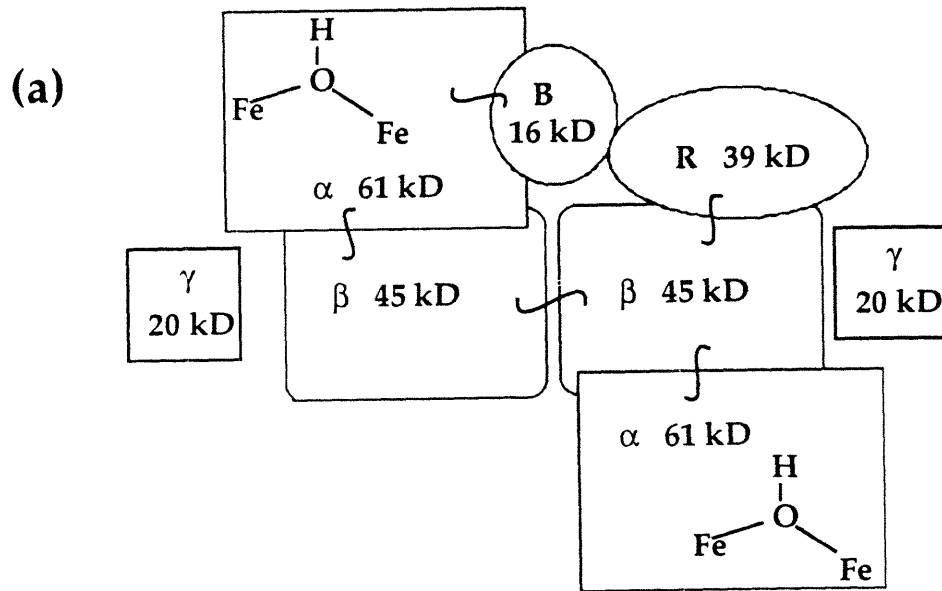
- (18) Fox, B. G.; Borneman, J. G.; Wackett, L. P.; Lipscomb, J. D. *Biochemistry* **1990**, *29*, 6419-6427.
- (19) Hanson, R. S.; Netrusov, A. I.; Tsuji, K. In *The Procaryotes*; A. Balows, H. G. Truper, M. Dworkin and K. Schliefer, Ed.; Springer-Verlag: Berlin, 1991; pp 2350-2364.
- (20) Akent'eva, N. F.; Gvozdev, R. I. *Biokhimiya* **1988**, *53*, 91-96.
- (21) Smith, D. D. S.; Dalton, H. *Eur. J. Biochem.* **1989**, *182*, 667-671.
- (22) Colby, J.; Dalton, H. *Biochem. J.* **1978**, *171*, 461-468.
- (23) Fox, B. G.; Lipscomb, J. D. *Biochem. Biophys. Res. Comm.* **1988**, *154*, 165-170.
- (24) Fox, B. G.; Froland, W. A.; Dege, J. E.; Lipscomb, J. D. *J. Biol. Chem.* **1989**, *264*, 10023-10033.
- (25) Patel, R. N.; Savas, J. C. *J. Bacteriol.* **1987**, *169*, 2313-2317.
- (26) Lund, J.; Dalton, H. *Eur. J. Biochem.* **1985**, *147*, 291-296.
- (27) Green, J.; Dalton, H. *J. Biol. Chem.* **1985**, *260*, 15795-15801.
- (28) Woodland, M. P.; Dalton, H. *J. Biol. Chem.* **1984**, *259*, 53-59.
- (29) Woodland, M. P.; Patil, D. S.; Cammack, R.; Dalton, H. *Biochim. Biophys. Acta* **1986**, *873*, 237-242.
- (30) Rosenzweig, A. C.; Frederick, C. A.; Lippard, S. J.; Nordlund, P. *Nature* **1993**, *366*, 537-543.
- (31) Stainthorpe, A. C.; Murrell, J. C.; Salmond, G. P. C.; Dalton, H.; Lees, V. *Arch. Microbiol.* **1989**, *152*, 154-159.
- (32) Stainthorpe, A. C.; Lees, V.; Salmond, G. P. C.; Dalton, H.; Murrell, J. C. *Gene* **1990**, *91*, 27-34.
- (33) Pilkington, S. J.; Salmond, G. P. C.; Murrell, J. C.; Dalton, H. *FEMS Microbiol. Lett.* **1990**, *72*, 345-348.

- (34) Rosenzweig, A. C.; Feng, X.; Lippard, S. J. In *IUCCP Symposium on Applications of Enzyme Biotechnology*; J. W. Kelly and T. O. Baldwin, Ed.; Plenum Press: New York, 1991.
- (35) Cardy, D. L. N.; Salmond, G. P. C.; Murrell, J. C. *Mol. Microbiol.* **1991**, *5*, 335-342.
- (36) Nordlund, P.; Dalton, H.; Eklund, H. *FEBS Lett.* **1992**, *307*, 257-262.
- (37) Smith, D.; Dalton, H. *Eur. J. Biochem.* **1992**, *210*, 629-633.
- (38) Fox, B. G.; Liu, Y.; Dege, J. E.; Lipscomb, J. D. *J. Biol. Chem.* **1991**, *266*, 540-550.
- (39) Prince, R. C.; George, G. N.; Savas, J. C.; Cramer, S. P.; Patel, R. N. *Biochim. Biophys. Acta* **1988**, *952*, 220-229.
- (40) DeWitt, J. G.; Bentsen, J. G.; Rosenzweig, A. C.; Hedman, B.; Green, J.; Pilkington, S.; Papaefthymiou, G. C.; Dalton, H.; Hodgson, K. O.; Lippard, S. J. *J. Am. Chem. Soc.* **1991**, *113*, 9219-9235.
- (41) Green, J.; Dalton, H. *J. Biol. Chem.* **1988**, *263*, 17561-17565.
- (42) Atta, M.; Fontecave, M.; Wilkins, P. C.; Dalton, H. *Eur. J. Biochem.* **1993**, *217*, 217-223.
- (43) Prior, S. D.; Dalton, H. *FEMS Microbiol. Lett.* **1985**, *29*, 105-109.
- (44) Ericson, A.; Hedman, B.; Hodgson, K. O.; Green, J.; Dalton, H.; Bentsen, J. G.; Beer, R. H.; Lippard, S. J. *J. Am. Chem. Soc.* **1988**, *110*, 2330.
- (45) Armstrong, W. H.; Lippard, S. J. *J. Am. Chem. Soc.* **1984**, *106*, 4632-4633.
- (46) Fox, B. G.; Hendrich, M. P.; Surerus, K. K.; Andersson, K. K.; Froland, W. A.; Lipscomb, J. D.; Münck, E. *J. Am. Chem. Soc.* **1993**, *115*, 3688-3701.
- (47) DeRose, V.; Liu, K. E.; Lippard, S. J.; Hoffman, B. *J. Am. Chem. Soc.* **1993**, *115*, 6440-6441.
- (48) Thomann, H.; Bernardo, M.; McCormick, J. M.; Pulver, S.; Andersson, K. K.; Lipscomb, J. D.; Solomon, E. I. *J. Am. Chem. Soc.* **1993**, *115*, 8881-8882.

- (49) Bender, C.; Rosenzweig, A. C.; Lippard, S. J.; Peisach, J., manuscript in preparation.
- (50) Hendrich, M. P.; Fox, B. G.; Andersson, K. K.; Debrunner, P. G.; Lipscomb, J. D. *J. Biol. Chem.* **1992**, *267*, 261-269.
- (51) DeWitt, J. G.; Rosenzweig, A. C.; Hedman, B.; Lippard, S. J.; Hodgson, K. O., manuscript in preparation.
- (52) Liu, K. E.; Lippard, S. J. *J. Biol. Chem.* **1991**, *266*, 12836-12839.
- (53) Liu, K. E.; Feig, A. L.; Goldberg, D. P.; Watton, S. P.; Lippard, S. J. In *The Activation of Dioxygen and Homogeneous Catalytic Oxidation*; D. H. R. Barton, A. E. Martell and D. Sawyer, Ed.; Plenum Press: New York, 1993.
- (54) Froland, W. A.; Andersson, K. K.; Lee, S.-K.; Lie, Y.; Lipscomb, J. D. *J. Biol. Chem.* **1992**, *267*, 17588-17597.
- (55) Rosenzweig, A. C.; Frederick, C. A.; Lippard, S. J. *J. Mol. Biol.* **1992**, *227*, 283-285.
- (56) Coufal, D. E.; Lippard, S. J., unpublished results.
- (57) Valentine, A. M.; Lippard, S. J., unpublished results.
- (58) Feig, A. L.; Lippard, S. J., in press.
- (59) Rardin, R. L.; Tolman, W. B.; Lippard, S. J. *New. J. Chem.* **1991**, *15*, 417-430.
- (60) Hamman, S.; Atta, M.; Ehrenberg, A.; Wilkins, P.; Dalton, H.; Beguin, C.; Fontecave, M. *Biochem. Biophys. Res. Commun.* **1993**, *195*, 594-599.
- (61) Andersson, K. K.; Elgren, T. E.; L. Que, J.; Lipscomb, J. D. *J. Am. Chem. Soc.* **1992**, *114*, 8711-8713.
- (62) Fox, B. G.; Shanklin, J.; Somerville, C.; Münck, E. *Proc. Natl. Acad. Sci. USA* **1993**, *90*, 2486-2490.
- (63) Kurtz, D. M., Jr.; Pickril, B. C. *Biochem. Biophys. Res. Comm.* **1991**, *181*, 337-341.

- (64) Nordlund, I.; Powlowski, J.; Shingler, V. *J. Bacteriol.* **1990**, *172*, 6826-6833.
- (65) Yen, K. M.; Karl, M. R.; Blatt, L. M.; Simon, M. J.; Winter, R. B.; Fausset, P. R.; Lu, H. S.; Harcourt, A. A.; Chen, K. K. *J. Bacteriol.* **1991**, *173*, 5315-5327.

Figure 1.1 a, Model of the hydroxylase based on the results of chemical crosslinking and spectroscopic experiments. b, The holo hydroxylase shown with the twofold axis running vertically. The α subunits are shown in red, the β subunits in blue, and the γ subunits in violet. The iron atoms are represented as yellow spheres.



(b)

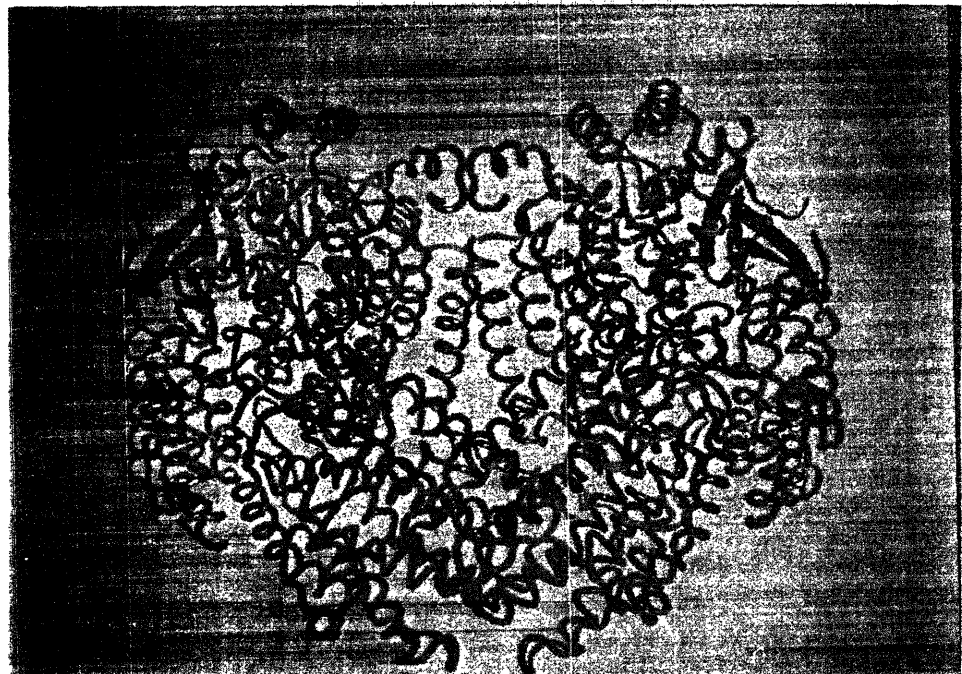
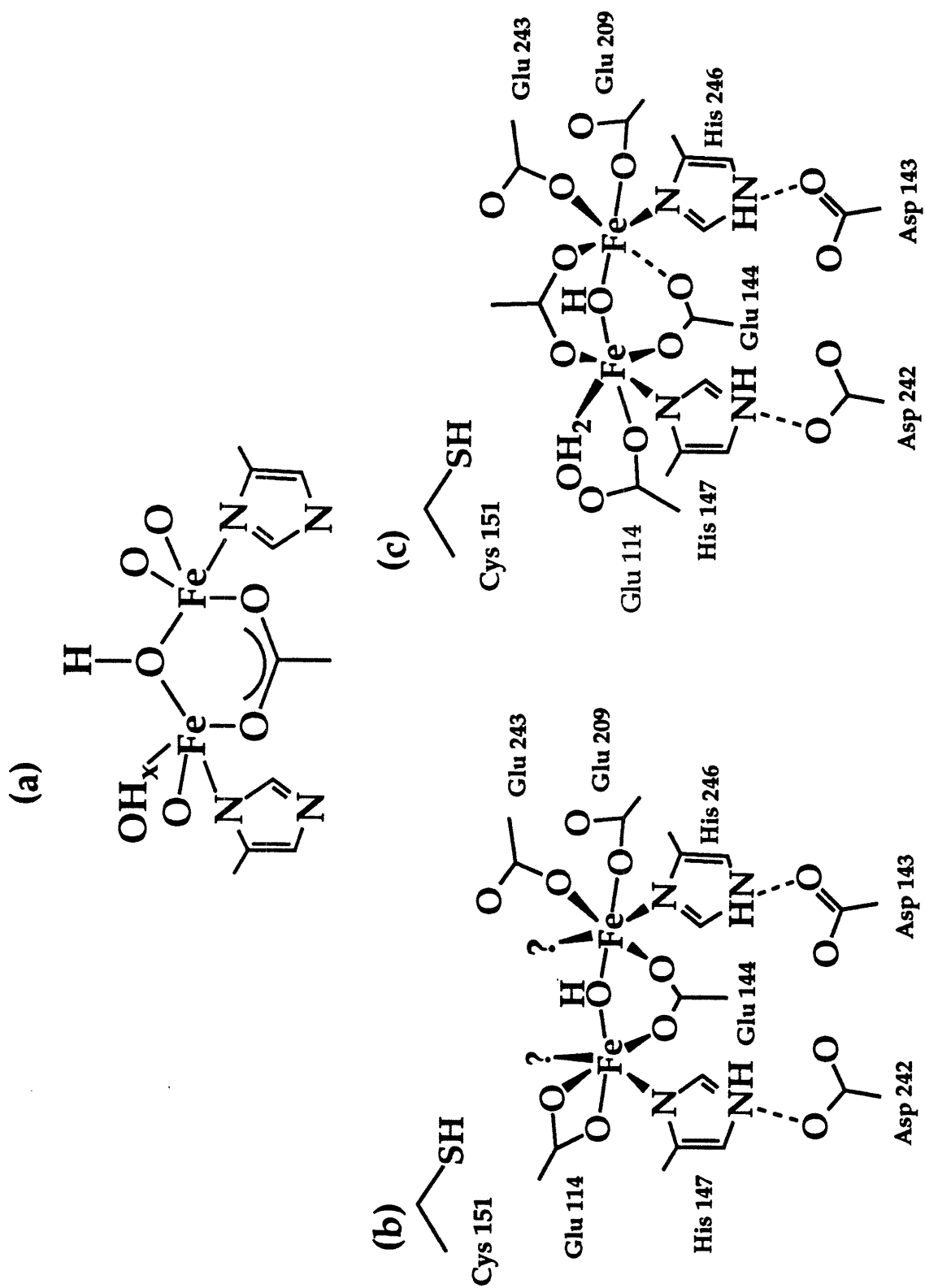


Figure 1.2 a, Spectroscopic model for the diiron core in the hydroxylase. b, Model of the diiron core in the hydroxylase based on spectroscopic data and sequence homology with the R2 protein of ribonucleotide reductase. c, The diiron core in the hydroxylase as revealed by the 2.2 Å X-ray structure.



Chapter 2

Purification of the *Methylococcus capsulatus* (Bath) Methane Monooxygenase
Proteins

I. Introduction

A focus of research in the Lippard group and elsewhere in the past decade has been the preparation and characterization of small inorganic model compounds which mimic the active sites in iron-oxo proteins such as hemerythrin, the R2 protein of ribonucleotide reductase, and methane monooxygenase. Methane monooxygenase, which is the least well characterized of these proteins, catalyzes the first step in the metabolic pathway of methanotrophic bacteria (eq. 1).



Methanotrophic bacteria, which are divided into three classes (Type I, Type II, and Type X) based on membrane morphologies and metabolic pathways for carbon incorporation¹, utilize methane as their sole source of carbon and energy. There are two forms of methane monooxygenase, a soluble enzyme and a particulate, membrane-bound enzyme. The particulate enzyme is expressed at high copper-to-biomass concentrations, and the soluble enzyme predominates at low copper concentrations. Particulate MMOs from both *Methylococcus capsulatus* (Strain M)² and *Methylococcus capsulatus* (Bath)³ have been isolated, but are not very stable. The soluble enzymes are more stable, and therefore have been the focus of most MMO research.

The soluble MMO enzyme system from the Type X methanotroph *Methylococcus capsulatus* (Bath), which was isolated from the warm springs at Bath, England, is comprised of three proteins: a reductase (MW 38.6 kDa), also called protein C, a small coupling protein (MW 15.5 kDa), also called protein B,

and a hydroxylase (MW 251 kDa), also called protein A. All three proteins are necessary for enzyme activity. The methane monooxygenase from the Type II organism *Methylosinus trichosporium* OB3b has also been purified,^{4,5} and is very similar to the *M. capsulatus* system. In addition, MMO has been isolated from *Methylobacterium* CRL-26, and contains the reductase and the hydroxylase, but purportedly lacks the coupling protein.⁶ The reductase is an iron-sulfur protein containing one 2Fe-2S cluster and one mole of FAD, and transfers electrons to the hydroxylase.⁷ The coupling protein (protein B),⁸ which lacks a metal or prosthetic group, regulates several aspects of the hydroxylation reaction. The hydroxylase is the site of methane oxidation. The hydroxylase is a multimeric protein, consisting of two copies each of three different subunits; the holoenzyme is $\alpha_2\beta_2\gamma_2$ (α , MW 60.6 kDa; β MW 45 kDa; γ , MW 19.8 kDa). Methane oxidation occurs at a dinuclear iron center, the presence of which was first indicated by the observation of an EPR signal at $g < 2$,⁹ similar to the signal observed for the mixed valent Fe(II)Fe(III) form of hemerythrin.

In the past 6 years, research efforts in the Lippard laboratory have expanded to include studies of methane monooxygenase in addition to iron-oxo model chemistry. A collaboration with Howard Dalton (University of Warwick, U.K.) to study the soluble methane monooxygenase from *M. capsulatus* (Bath) was initiated in 1987 by Jim Bentsen, a postdoctoral associate in the laboratory. Initial X-ray absorption and electron paramagnetic resonance spectroscopic studies of the hydroxylase were carried out by Jim Bentsen by using purified protein obtained from Dalton. An adequate supply of pure protein to carry out a variety of planned spectroscopic and biochemical experiments was not forthcoming, however. In order to ensure productive and reliable research on the MMO hydroxylase, it was decided that cultivation of the organism and purification of the MMO proteins should be established at MIT, independent of

Dalton. As the first graduate student to work on methane monooxygenase, my initial project was the development of reliable protocols for fermentation and protein purification at MIT. Methodologies for the growth of *M. capsulatus* and the purification of the hydroxylase protein are described in this chapter. In addition, the expression, from a plasmid harboring the genes, of the α subunit and coupling protein in *E. coli* and the purification of coupling protein from *E. coli* are described.

II. *M. capsulatus* Fermentations

Experimental

Materials. KNO_3 , Mg_2SO_4 , CaCl_2 , Na_2MoO_4 , $\text{ZnSO}_4 \cdot 7\text{H}_2\text{O}$, $\text{MnCl}_2 \cdot 4\text{H}_2\text{O}$, H_3BO_4 , $\text{CoCl}_2 \cdot 6\text{H}_2\text{O}$, $\text{CuSO}_4 \cdot 5\text{H}_2\text{O}$, $\text{NiCl}_2 \cdot 6\text{H}_2\text{O}$, $\text{FeSO}_4 \cdot \text{H}_2\text{O}$, EDTA, and MgCl_2 were obtained from Mallinckrodt. Commercial and technical grade methane was obtained from Air Products, and $\text{O}_2:\text{CO}_2$ gas mixtures were obtained from Matheson. Ultrapure HNO_3 , HCl , and NaOH were obtained from Baker, and Tris (Tris = tris[hydroxymethyl]aminomethane), sodium thioglycolate, and phenylmethyl sulfonyl fluoride (PMSF) were purchased from Sigma. DNase I was obtained from Boehringer Mannheim. The ^{57}Fe foil was purchased from U. S. Services, Inc., Summit, N. J.

Initially, *M. capsulatus* cell cultures obtained from Dalton were maintained in 50 ml cultures in an incubator shaker at 45 °C and 100 rpm. The cells were subcultured every three weeks, and a library of frozen cultures was kept in the -80 °C freezer as well as in the liquid nitrogen dewar. The cell medium is a 2x nitrate salt medium containing 0.2% w/v KNO_3 , 0.1% Mg_2SO_4 , 0.01% CaCl_2 , 0.1 ml/l stock FeEDTA (0.1 M in H_2O), 0.5 ml/l stock Na_2MoO_4 (0.5 g/L), 10 ml/L stock phosphate buffer (0.4 M pH 6.8), and 1 ml/l trace elements solution.¹⁰ The trace elements solution contains per 1 l of distilled water: 400 mg $\text{ZnSO}_4 \cdot 7\text{H}_2\text{O}$,

20 mg $\text{MnCl}_2 \cdot 4\text{H}_2\text{O}$, 10 mg H_3BO_4 , 50 mg $\text{CoCl}_2 \cdot 6\text{H}_2\text{O}$, 200 mg $\text{CuSO}_4 \cdot 5\text{H}_2\text{O}$, 10 mg $\text{NiCl}_2 \cdot 6\text{H}_2\text{O}$, 500 mg $\text{FeSO}_4 \cdot \text{H}_2\text{O}$, 250 mg EDTA. This medium is always used for large scale fermentations.

The first *M. capsulatus* growth (growth I) was a batch fermentation. A 10 l fermenter (New Brunswick Scientific, Co.) in the Orme-Johnson laboratory was inoculated with four 50 ml cultures of *M. capsulatus* which had been maintained for one week in the incubator shaker. Dissolved dioxygen was monitored with a probe containing a lead anode and a platinum cathode covered by a stretched membrane. Continuous agitation at 400 rpm ensured efficient O_2 transfer. The temperature was maintained at 45 °C. The pH controller consisted of an electrode and a peristaltic pump connected to a sterile bottle containing 1 M HCl. Whenever the pH exceeded the setpoint of 7.2, the acid pump automatically added HCl to the fermenter. Initial flows were 40 ml/min CH_4 and 150 ml/min $\text{O}_2:\text{CO}_2$ (95:5%). Samples were withdrawn from a sampling port with a 60 ml syringe. Every 12 hours, a sample was withdrawn to measure the optical density at 540 nm. When the OD reached 2.98, the O_2 source was switched from $\text{O}_2:\text{CO}_2$ (95:5%) to normal compressed air, and the flows were increased to 50 ml/min CH_4 and 200 ml/min air. Gas flows were carefully regulated to avoid flammability limits, which are shown in Figure 2.1.¹¹ *Within certain concentration limits, mixtures of CH_4 and O_2 are flammable, and a flame will self-propagate after ignition. Therefore, extreme caution must be exerted both to control the gas flows and to remove any possible source of ignition from the fermenter area.* Examination of the cells under a microscope did not reveal any rod-shaped pseudomonads, which are a likely contaminant from the air.

When the OD reached 12.78, the cells were harvested at 25 °C by using a Pennwalt tubular bowl centrifuge which permits 10 l of cells to be spun down within 20 minutes. The cell paste (75 g) was suspended in 400 ml of 20 mM NaP

buffer pH 7.0 and centrifuged at 8 K for 20 min at 4 °C. The cells were then resuspended in 400 ml of 20 mM Tris pH 7.0 containing 5 mM sodium thioglycolate, 0.01 mg/ml DNase 1, 1 mM phenylmethyl sulfonyl fluoride (PMSF), and 5 mM MgCl₂. After cracking on a French press (1100 psig) at 4 °C, the resuspended cells were centrifuged at 14,000 rpm for 20 min at 4 °C. The supernatant was immediately frozen in liquid nitrogen and stored at -80 °C. In all subsequent growths, the cell paste was directly frozen in liquid nitrogen, and the cells were cracked at the time of purification.

In order to obtain large quantities of cell paste, the second *M. capsulatus* fermentation was carried out in continuous culture (growth II). In a continuous culture, fresh nutrients are supplied continuously while simultaneously withdrawing cells. This method permits the growth to continue in a steady state for long periods of time.¹² In an attempt to improve the specific activity of the hydroxylase obtained from the cells, the concentration of FeEDTA was increased 8-fold from 10 μM to 80 μM, the concentration used for the *M. trichosporium* fermentations.⁵ The 10 l fermenter was inoculated with four 50 ml cultures, and dissolved O₂ and pH were monitored as described above. The temperature was maintained at 45 °C. Initial gas flows were 40 ml/min CH₄ and 150 ml/min O₂:CO₂ (95:5%). At an OD of 2.16, the O₂ source was switched to normal compressed air, and the flows were increased to 200 ml/min CH₄ and 750 ml/min O₂, a factor of four greater than the maximum flows in the first growth. At OD 5.9, the agitation was raised to 600 rpm, effecting a significant increase in OD. Continuous culture was initiated at OD 8.06, during the exponential growth phase. The continuous culture apparatus consisted of two peristaltic pumps, one connected to a 20 l vessel of media and the other connected to an outlet from the fermenter. These pumps were activated by a level probe in the fermenter vessel. The cells were harvested in four separate batches by using the Pennwalt

centrifuge. A total of 245 g of cell paste was harvested, washed with 20 mM NaP buffer pH 7.0, centrifuged for 20 min at 8 K, and frozen in liquid nitrogen.

Another batch growth (growth III) was carried out by using an ^{57}Fe containing medium in order to prepare samples for Mössbauer spectroscopy. The ^{57}Fe foil (95.2%, 7 mg) was dissolved in 0.5 ml of 1 M ultrapure HNO_3 . After adding 0.5 ml H_2O with 80 mg Na_2EDTA and 4.1 mg NaOH , the solution was stirred overnight. This solution replaced the stock FeEDTA solution usually used in the growth. In addition, a trace elements solution without Fe was prepared. The fermentation was carried out by following the procedure used for the first batch growth. At OD 2.98, the O_2 source was changed to compressed air, the gas flows were raised to 50 ml/min CH_4 and 200 ml/min O_2 , and the agitation was increased to 600 rpm. The cells were harvested at OD 8.96 and the 50 g of cell paste obtained were washed with 20 mM sodium phosphate (NaP) buffer pH 7.0, and frozen in liquid nitrogen.

Additional *M. capsulatus* fermentations were carried out by using a Chemap Type S 20 l fermenter (Lippard laboratory) equipped with a pH electrode, a dissolved oxygen probe, an *in situ* sterilization system, and a steam sterilizable harvest valve. It is possible to grow 15 l of cells in this fermenter whereas only 10 l growths are feasible in the New Brunswick Scientific fermenter in the Orme-Johnson laboratory. The first two *M. capsulatus* growths (growths IV and V) in the new fermenter were batch fermentations, and all subsequent growths were carried out by using a modified continuous culture procedure. In the initial continuous culture fermentation in the New Brunswick Scientific fermenter, it was difficult to maintain a constant OD, and it was only feasible to harvest the cells every 12 hours. Therefore, cells were continuously removed from the fermenter and kept at 4 °C until harvest. This method was modified according to the protocol described for the *M. trichosporium* fermentations.¹³ A

15 l culture is permitted to grow to approximately OD 8. At this point, 13 l of cells are drained from the fermenter and harvested. The fermenter is refilled with 13 l of fresh media by using a peristaltic pump, and the growth is continued. Each growth is about two days in duration, and the continuous culture can be continued for weeks if a reasonable level of sterility is maintained. A total of 8 cycles (~500 g of cell paste) were carried out according to this procedure, with help from Kathy Liu and Wayne Wu. Finally, a fermentation of the *M. trichosporium* organism has been successfully carried out by Thanos Salifoglou.

Results and Discussion

The fermentation kinetics for growths I-V are shown in Figure 2.2. Each plot shows both the OD₅₄₀ as a function of time and the log(OD₅₄₀) as a function of time. The exponential growth phase is defined by a straight line on the log(OD₅₄₀) versus time plot.¹² In growth I, the cells (75 g) were harvested at OD 12.78 in accordance with previous protocols for the *M. capsulatus*. According to the growth curve, however, this OD represents stationary phase rather than exponential growth phase. Therefore, in growths III, IV, and V, the cells were harvested at lower OD values of 8.96, 8.46, and 8.00, respectively. The yields for these growths were 50 g for growth III, 65 g for growth IV and 62 g for growth V. The lag time until exponential phase was long in growth IV because of low gas flows. In the first continuous culture fermentation (growth II, Figure 2.2b), a constant OD was maintained by draining small volumes of cells from the fermenter and continuously adding small volumes of fresh media. Although 245 g of wet cell paste were obtained in this growth, problems with maintaining the OD and with efficiently harvesting the cells led to a modification of the procedure in which 13 l of cells are harvested at once, and the remaining 2 l are used as the inoculum for the next growth. This procedure for continuous culture

is more efficient, more consistent, and less cumbersome than the original method. The first trial of this procedure resulted in ~500 g of cells after 8 cycles. Thanos Salifoglou later carried out multiple fermentations in this fashion. The fermentation procedures have been further modified and improved by Thanos, and complete guidelines for fermentation, including maintenance of the *M. capsulatus* cell stocks and growth of *M. trichosporium* have been compiled.

III. Purification of the Hydroxylase

Experimental

Materials. MOPS (MOPS = 3-[N-morpholino]propanesulfonic acid), sodium thioglycolate, NADH, PMSF, ascorbic acid, DEAE cellulose, and TEAE cellulose were purchased from Sigma. DNase I was obtained from Boehringer Mannheim and MgCl₂ from Mallinckrodt. DEAE Sepharose, Q Sepharose, and Sephacryl S-300 column resins were obtained from Pharmacia. Propylene gas and propylene oxide for activity assays were obtained from Matheson and from Aldrich, respectively. Ferrozine, [3-(2-pyridyl)-5,6-bis(4-phenyl-sulfonic acid) - 1,2,4-triazine] and Fe atomic absorption standard solutions were purchased from Sigma. Ammonium acetate was obtained from Mallinckrodt. Ultrapure HNO₃ was obtained from Baker. Coomassie Brilliant Blue G-250 dye for the Bradford assay was obtained from Bio-Rad.

Preparation of crude cell free extract. *M. capsulatus* cell paste from fermentations was stored at -80 °C and thawed immediately before purification. Typically, the cell paste (25 g) was resuspended in 25 mM MOPS pH 7.0 containing 5 mM sodium thioglycolate, 0.01 mg/ml DNase I, 1 mM PMSF, and 5 mM MgCl₂. The cells were lysed on a French press at 1100 psig, and the lysate was centrifuged at 100,000 x g for 90 min to produce a clear, cell-free extract.

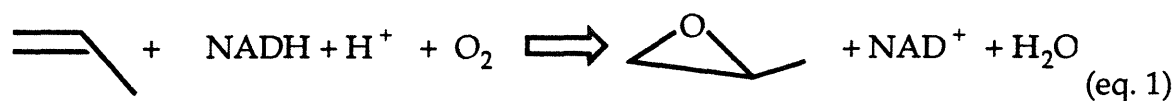
Crude extracts of the *M. trichosporium* proteins were prepared in the same way except that the lysate was diluted twofold before centrifugation.

Column chromatography. Initial purifications were carried out according to the published protocol for the *M. capsulatus* hydroxylase.^{14,15} All column chromatography with the exception of high pressure liquid chromatography (HPLC) was carried out at 4 °C. The crude extract was loaded onto a DEAE cellulose column (3 x 7 cm) equilibrated in 25 mM MOPS pH 7.0, containing 5 mM sodium thioglycolate, which was found to be necessary to stabilize the reductase. The hydroxylase, reductase, and coupling protein were then separated by a stepwise NaCl gradient. The hydroxylase was eluted in the absence of NaCl, the coupling protein was eluted with 0.2 M NaCl, and the reductase was eluted with 0.5 M NaCl. Alternatively, both the coupling protein and the reductase were eluted with 0.5 M NaCl to obtain a crude mixture of the two components for use in activity assays. The hydroxylase was then further purified by HPLC at 25 °C on a Pharmacia TSK G3000SWG gel filtration column (2.15 x 60 cm) equilibrated in 50 mM MOPS pH 7.0 containing 0.1 M NaCl, which was essential to achieve optimal resolution. The HPLC purification was carried out in 2 ml injections at room temperature at a flow rate of 3 ml/min. The HPLC purified hydroxylase was then concentrated to ~5 mg/ml in an Amicon ultrafiltration device, frozen in liquid nitrogen, and stored at -80 °C.

The HPLC step was eventually replaced by two conventional liquid chromatography columns, DEAE Sepharose (a weak anion exchanger) and Sephacryl S-300. The DEAE Sepharose was then replaced by Q Sepharose (a strong anion exchanger) because a loss of activity was observed on the DEAE Sepharose column. Following the DEAE cellulose column, the crude hydroxylase fraction was applied to the Q Sepharose column (2.5 x 8.5 cm) equilibrated in 25 mM MOPS pH 7.0 containing 0.05 mM NaCl. The hydroxylase

was eluted with a 0.05 - 0.35 M linear NaCl gradient (500 ml) with a flow rate of 1 ml/min. The hydroxylase eluted at approximately 0.15 M NaCl, and was concentrated to 5-10 ml (~20-30 mg/ml) by using Centriprep 30 concentration devices (Amicon). The hydroxylase was then loaded onto a Sephacryl S-300 gel filtration column (2.5 x 100) and eluted overnight at a flow rate of 0.6 ml/min. After this column, the purified hydroxylase was frozen in liquid nitrogen and stored at -80 °C. Several additional purification steps were tested in an attempt to obtain ultra pure hydroxylase for crystallizations, including isoelectric focusing with a Bio Rad Rotofor device and fast pressure liquid chromatography (FPLC) by using a Mono Q (anion exchange) column. The *M. trichosporium* hydroxylase was purified according to the published protocol, which includes $\text{Fe}(\text{NH}_4)_2(\text{SO}_4)_2 \cdot 6\text{H}_2\text{O}$ and cysteine in the buffers.¹³

Activity assays. Methane monooxygenase activity was assayed via the conversion of propylene to propylene oxide (eq. 1). The reaction was carried out in a 5 ml flask sealed with a Suba seal stopper. Propylene oxide formation was



monitored by using a HP5890A gas chromatograph with a 6 ft. glass column (O.D. 4.0 mm) packed with Porapak Q. The standard was 2 mM propylene oxide in H_2O . NADH contaminated with 4.3% ethanol was purified by ether extraction (5x) from 20 mM potassium phosphate (KP) buffer pH 7.0. Ether was removed by vacuum, and the purified NADH was analyzed for ether and ethanol by gas chromatography. The NADH was then diluted to 100 mM and stored in 1 ml aliquots at -20 °C. In a typical assay, at least 2 mg of hydroxylase were combined with a crude mixture of coupling protein and reductase, which was obtained by

column chromatography on DEAE cellulose. Air in the flask (2 ml) was replaced with 2 ml propylene oxide, and the reaction mixture was incubated for 15 seconds in a 45 °C shaker bath before adding 50 μl of NADH to initiate the reaction. After a 3 min incubation, 5 μl were withdrawn and analyzed by gas chromatography.

Protein analytical procedures. Iron content was determined by complexation with ferrozine.^{16,17} In each assay, 10 μl of ultrapure HNO_3 were added to a 100 μl sample. The sample was then boiled for 15 min and centrifuged. After removing the supernatant and diluting with H_2O to a total volume of 440 μl , 20 μl of 75 mM ascorbic acid, 20 μl of 10 mM ferrozine, and 20 μl of ammonium acetate were added. An Fe atomic absorption standard solution (1010 $\mu\text{g}/\text{ml}$) was used as a standard. The Fe content in nmoles was determined by absorbance at 562 nm minus a blank versus a standard curve.

Protein content was determined by the Bradford assay¹⁸ which is based on the binding of Coomassie Brilliant Blue G-250 dye to protein. Binding of the dye shifts its absorption maximum from 470 to 595 nm. By monitoring the increase in absorbance at 595 nm, the protein concentration can be measured. An extinction coefficient at 280 nm (ϵ_{280}) for the hydroxylase was determined by lyophilizing 0.4 ml of concentrated protein to obtain 38.2 mg of dried powder. An equal amount of MOPS buffer was also lyophilized to a dry weight of 2.6 mg. An ϵ_{280} of 788,400 $\text{M}^{-1}\text{cm}^{-1}$ was calculated by using Beer's law ($A = A_{280\text{measured}}$, $c = 3.44 \times 10^{-4}$ M, $l = 1$ cm). An ϵ_{280} of 567,200 $\text{M}^{-1}\text{cm}^{-1}$ can be calculated from the protein sequence.¹⁹ Because the measured ϵ_{280} is higher than the calculated value, the difference cannot be attributed to H_2O in the lyophilized sample. The measured value of ϵ_{280} may instead be due to the presence of absorbing species at 280 nm other than tyrosine, tryptophan, and cysteine residues. The diiron center in the hydroxylase may contribute to the ϵ_{280} . Carboxylate or phosphate

→ Fe transitions at 260 nm ($\epsilon = 38,500 \text{ M}^{-1}\text{cm}^{-1}$) have been suggested for several hydroxo-bridged model compounds.²⁰ These types of absorbances could contribute to the ϵ_{280} measured for the hydroxylase.

Protein concentrations and ϵ_{280} values for the hydroxylases from both *M. capsulatus* and *M. trichosporium* were also determined by amino acid analysis on samples submitted to the Molecular Biology Core Facility at the Dana Farber Cancer Institute. In these experiments, samples with a known absorbance at 280 nm were analyzed for protein concentration. For the *M. capsulatus* hydroxylase, an average ϵ_{280} of $435,000 \text{ M}^{-1} \text{ cm}^{-1}$ was calculated based on 5 analyzed samples. Only one sample of the *M. trichosporium* hydroxylase was analyzed, and an ϵ_{280} of $375,000 \text{ M}^{-1} \text{ cm}^{-1}$ was obtained. The obtained ϵ_{280} s of $435,000 \text{ M}^{-1} \text{ cm}^{-1}$ for the *M. capsulatus* hydroxylase and $375,000 \text{ M}^{-1} \text{ cm}^{-1}$ for the *M. trichosporium* hydroxylase are more consistent with the values calculated from the sequences, $567,200 \text{ M}^{-1} \text{ cm}^{-1}$ for the *M. capsulatus* protein and $466,820 \text{ M}^{-1} \text{ cm}^{-1}$ for the *M. trichosporium* protein. If some of the tyrosine, tryptophan, and cysteine residues are buried, the ϵ_{280} will be less than that predicted by the sequence. This ϵ_{280} for the *M. capsulatus* hydroxylase of $435,000 \text{ M}^{-1} \text{ cm}^{-1}$ may be the most accurate, and was used frequently in protein concentration determinations. Protein purity was determined by denaturing polyacrylamide gel electrophoresis.

Results and Discussion

The initial hydroxylase purifications consisted of separation of the three proteins on DEAE cellulose followed by purification of the hydroxylase by HPLC gel filtration chromatography. The elution profile for the HPLC purification is shown in Figure 2.3. Several unknown proteins are eluted first, followed by methanol dehydrogenase, the hydroxylase, and cytochromes. Methanol dehydrogenase was identified by its absorption spectrum, which exhibited a

peak at 345 nm and a shoulder at 400 nm, features typical of the PQQ (pyrrolo-quinoline quinone) cofactor.²¹ Similarly, the presence of cytochromes was confirmed by an absorption band at 410 nm. Hydroxylase purified by this procedure exhibited specific activities (SPA) of 100-300 mU/mg (1 mU = 1 μ mole product/min) and Fe contents of 1.5-3.0 Fe per protein molecule. The addition of 200 mM $\text{Fe}(\text{NH}_4)_2(\text{SO}_4)_2 \cdot 6\text{H}_2\text{O}$ and 2 mM cysteine to the buffers at various stages of the purification was investigated as a means of improving activity and Fe content, since significantly higher specific activities and Fe contents (4 Fe per protein molecule) are reported for the *M. trichosporium* hydroxylase, purified in the presence of $\text{Fe}(\text{NH}_4)_2(\text{SO}_4)_2 \cdot 6\text{H}_2\text{O}$ and cysteine^{5,13}. The addition of Fe and cysteine to the purification buffers had little effect on activity and Fe content, however, and only complicated the purification scheme since these buffers are unstable when exposed to dioxygen.

The HPLC purification was unsatisfactory for several reasons. First, purification by 2 ml injections was inefficient. In addition, the purification was carried out at room temperature instead of at 4 °C, which may have caused Fe loss. In the DEAE cellulose step, a large amount of the coupling protein elutes with the hydroxylase, and some coupling protein remains associated with the hydroxylase after the HPLC purification. Finally, the hydroxylase could not be completely resolved from methanol dehydrogenase (Figure 2.3). These problems were solved by modifying the purification procedure to include two more column chromatography steps. The HPLC step is replaced by anion exchange on Q Sepharose and gel filtration on Sephacryl S-300, which is also used in the protocol described for the *M. trichosporium* hydroxylase.^{5,13} The use of Fe and cysteine was also investigated with these columns, and again, no benefit was derived from their inclusion. Since methanol dehydrogenase elutes from the Q Sepharose column with no salt, and the hydroxylase adheres to the column, the

resolution problem observed in the HPLC purification was eliminated. In addition, the coupling protein remained bound to the Q Sepharose column after the hydroxylase is eluted.

After the Q Sepharose column, the hydroxylase is essentially pure, with just a few contaminating proteins (Figure 2.4, lanes 2 and 3), which are removed by gel filtration on Sephacryl S-300. Specific activities after the Q Sepharose column are typically 100-150 mU/mg, and increase to 200-300 mU/mg after the Sephacryl S-300 column. The hydroxylase purified by this procedure is fairly pure as shown by SDS polyacrylamide gel electrophoresis (Figure 2.4, lanes 4-6), and 200-250 mg of purified hydroxylase are usually obtained from 25 g of cell paste. Interestingly, hydroxylase purified by both methods is significantly more stable than originally suggested. Although it has been reported that the *M. capsulatus* (Bath) hydroxylase loses 80% of its activity after 4 hours at 4 °C,⁴ it was observed that the hydroxylase retained 95% of its activity after storage overnight at 4 °C and 55% of its activity after storage at 4 °C for 8 days.

Although the hydroxylase purified by chromatography on DEAE cellulose, Q Sepharose, and Sephacryl S-300 was sufficiently pure for spectroscopic studies, ultrapurification was carried out for crystallization experiments. Preparative isoelectric focusing by using a Rotofor device was attempted, but the hydroxylase did not focus well, and precipitated in the apparatus as the pH gradient was formed. Hydroxylase already purified by anion exchange on Q Sepharose and gel filtration on Sephacryl S-300 was further purified on TEAE cellulose or by using a Mono Q FPLC column. Neither of these strong anion exchangers significantly improved protein purity, as judged by SDS polyacrylamide gel electrophoresis. When crude hydroxylase separated from coupling protein and the reductase by DEAE cellulose chromatography was purified on the Mono Q column followed by gel filtration HPLC, a purer

preparation did result (Figure 2.5, lanes 4 and 5). This preparation exhibited a very low specific activity (20 mU/mg), however. A purer preparation was thus obtained by employing the same amount and type of purification steps, but in a different sequence. It may be that the use of FPLC and HPLC, both of which can be carried out quite rapidly, prevented some proteolytic degradation which occurs in the usual purification scheme. Despite the low specific activity, this protein was used in crystallization trials, and did produce somewhat cleaner preparations of crystalline needles. The best crystals were ultimately obtained by seeding procedures with hydroxylase purified by the usual procedure, however (see Chapter 4).

The *M. trichosporium* hydroxylase was also purified. In this purification, 200 mg of pure hydroxylase were obtained from 200 g of cell paste. The specific activity was 100 mU/mg, and the Fe content was 2.2 Fe per protein molecule. One reason for the low specific activity may be the use of reductase and coupling protein from *M. capsulatus* in the activity assay. The effects of cross-reacting the proteins from the two types of organisms on activity have not been investigated in detail. In addition, Fe contents of 4 Fe per protein molecule are reported for the *M. trichosporium* hydroxylase,⁵ and it is unclear why only 2.2 Fe were detected in this preparation. Nevertheless, the purified protein did exhibit activity, and was reasonably pure by SDS-PAGE (Figure 2.6), and therefore was used for crystallization trials.

The specific activity measured for the *M. capsulatus* hydroxylase is consistently 100-300 mU/mg, which is lower than that reported for the *M. trichosporium* protein (1500 mU/mg).¹³ In addition, Fe contents of 2 Fe per protein molecule are typically measured for the *M. capsulatus* protein whereas 4 Fe per protein molecule are reported for the *M. trichosporium* protein. The highest specific activity measured for the *M. capsulatus* hydroxylase was 550

mU/mg by using HPLC purified hydroxylase and a large excess of a concentrated mixture of the coupling protein and reductase. There are several possible explanations for these differences. The lack of highly purified reductase and coupling protein may have prevented optimization of the activity assay. The use of purified coupling protein and reductase, however, have never resulted in activities as high as those reported for the *M. trichosporium* hydroxylase.¹⁵ The lower Fe content for the *M. capsulatus* protein could be due to errors in the iron and protein concentrations. The ferrozine assay is extremely reproducible, but the Bradford assay for protein concentrations is not very accurate. When the Fe content is determined by using the ferrozine assay and the ϵ_{280} of 435,000 M⁻¹ cm⁻¹ from amino acid analysis, 2 Fe per protein molecule are consistently measured. Therefore, the lower iron content could account for the lower activity.

The X-ray structure of the *M. capsulatus* hydroxylase reveals, however, the presence of two dinuclear Fe centers (see Chapter 5), indicating that the *M. capsulatus* protein does contain 4 Fe atoms per protein molecule. It may be that 4 Fe protein was selectively crystallized from a mixture containing apo (iron-free) and/or iron-depleted protein. This type of a protein mixture would be consistent with both the X-ray structure and the analytical measurements. Furthermore, preliminary results indicate that apo protein can be removed from the purified hydroxylase by centrifugation, resulting in a 4 Fe preparation.²² This 4 Fe preparation may exhibit a higher specific activity, but the activity may still not be comparable to that reported for the *M. trichosporium* protein. The different activities may then be due to intrinsic differences between the two hydroxylases. For example, the *M. capsulatus* protein functions at 45 °C while the *M. trichosporium* functions at 30 °C, and is not stable at 45 °C. Moreover, the primary sequences of the two proteins do differ, with 85% identity for the α subunit, but only 59% and 49% for the β and γ subunits, respectively.

IV. Cloning, Expression, and Activity of the Coupling Protein and the α Subunit of the Hydroxylase

Experimental

Materials. IPTG (isopropylthio- β -D-galactoside) was purchased from Sigma. The restriction enzyme Hind III was obtained from New England Biolabs, and the restriction enzyme Bam HI was obtained from Boehringer Mannheim. Materials for DNA sequencing were obtained from United States Biochemical. MOPS, sodium thioglycolate, PMSF, 6-aminocaproic acid, benzamidine hydrochloride, and Sephadex G-50 were purchased from Sigma. DNase I was obtained from Boehringer Mannheim. DEAE Sepharose was purchased from Pharmacia.

Cloning of the α subunit. The gene for the α subunit of the hydroxylase and the gene for the coupling protein were isolated by Wayne Wu by using the polymerase chain reaction (PCR).²³ The α gene was gel purified and ligated into the Hind III restriction site in the vector Bluescript SKII+. Ligations were carried out with approximately a 2:1 molar ratio of α DNA to Bluescript vector for 16 hours at 16°C, and ligation mixtures were used to transform competent *E. coli* cells according to standard procedures.²⁴ The cells were then plated onto LB/AMP plates (50 μ g ampicillin per 1 ml Luria broth). Putative clones were identified visually by the color of the bacterial colonies. The Bluescript SKII+ vector carries part of the *lac* operon from *E. coli* which codes for the amino terminal fragment of β -galactosidase. A polycloning site is incorporated into the β -galactosidase gene. In the presence of IPTG, the β -galactosidase gene is induced, and a biologically active fragment of β -galactosidase is synthesized. When bacteria carrying the β -galactosidase gene are plated on media containing IPTG and the chromogenic substrate X-gal (5-bromo-4-chloro-3-indolyl- β -D-

galactoside), blue colonies appear due to the X-gal. The bacterial colonies carrying recombinant plasmids appear white rather than blue in the presence of X-gal, and can easily be identified. After several attempts at ligation and transformation, white colonies were obtained, and minipreparations of DNA were carried out by the boiling-lysis method.²⁴ According to restriction enzyme analysis with Hind III, at least 7 of the putative clones contained the α gene. Large scale plasmid preparations were carried out on three of these clones, named $\alpha 1(3)$, $\alpha 2(8)$, and $\alpha 2(10)$, by using the Qiagen system,²⁵ and the clones were partially sequenced by using the Sanger dideoxy-mediated chain termination method.²⁶

Expression of the α subunit. The α gene was removed from the vector Bluescript SKII+ by digestion with Hind III, gel purified, and ligated into the Hind III restriction site in the expression vector pKK223-3.²⁷ Ligation mixtures were used to transform competent JM105 cells, which were then plated onto LB/AMP plates. Multiple minipreparations were carried out by the boiling lysis method,²⁴ and clones were identified by digestion with Hind III. The orientation of the α insert in these clones was determined by restriction enzyme analysis with BamHI (Boehringer Mannheim). The expression experiments were carried out as follows. Cell cultures were grown in LB/AMP to an optical density at 600 nm of 0.7, and then IPTG was added to a 1 mM final concentration. A 1 ml aliquot of cells was taken immediately after induction, microcentrifuged, and the pellet was stored at -20 °C. After 2 hours, another 1 ml aliquot was taken, and the two pellets were boiled in SDS sample buffer for 5 minutes. These samples were then analyzed on an 8% SDS polyacrylamide gel. Clones containing the insert in the incorrect orientation were used as negative controls.

Expression, purification, and Activity of the coupling protein. The cloning and sequencing of the genes for the coupling protein and the γ subunit were

performed by procedures identical to those described for the α subunit, and are detailed elsewhere.²³ In a typical expression experiment, cells were grown to an optical density at 600 nm of 0.7, at which point IPTG was added to a 1 mM final concentration. After 2 hours, the cells were harvested by centrifugation for 20 min at 5000 rpm, and the pellets were resuspended in 25 mM MOPS pH 7.0 containing 5 mM sodium thioglycolate, 5 mM MgCl₂, 0.01 mg/ml DNase I, and 1 mM each of three protease inhibitors, PMSF, 6-aminocaproic acid, and benzamidine hydrochloride. PMSF was later eliminated, since it is not soluble in water, and thus requires the introduction of small amounts of EtOH, which interferes with activity assays. Cells were lysed by using a French press at 1100 psig, and the resulting crude extract was centrifuged at 40,000 rpm for 20 min. Further purification was carried out by column chromatography on Sephadex G50 (2.5 x 40 cm) and DEAE Sepharose (2.5 x 15 cm, 0.0-0.3 M NaCl gradient), and by HPLC on a Pharmacia TSK G3000SWG gel filtration column (2.5 x 60 cm). All columns were equilibrated in 25 mM MOPS pH 7.0 containing 1 mM of each protease inhibitor. Activity assays were performed as described above by using propylene as a substrate. Purified hydroxylase and partially purified reductase were used in the assays. Owing to the limited supply of reductase, a maximized specific activity for the coupling protein could only be measured for the final pure coupling protein. Protein concentrations were determined by using the Bradford assay.

Results and Discussion

Expression of the α subunit. Several attempts were made to express the α subunit. A representative gel is shown in Figure 2.7. Lanes 3-6 show the cell pellets from two different positive clones, which have been designated α 8-35 and α 8-112, immediately after IPTG induction (t=0) and 2 hours after induction (t=2).

The experiment was simultaneously carried out on two clones which contained the α insert in the wrong orientation, clones $\alpha 8-64$ and $\alpha 8-136$ (Lanes 7-10). If lanes 4 and 6 are compared to lanes 8 and 10, little or no expression of the α subunit is apparent. If the α subunit is expressed at all, it is present at very low levels. If the α subunit is very unstable, it may be expressed and then immediately degraded, but more frequent sampling did not reveal any sign of transient expression. The addition of Fe to the growth media has been reported to increase levels of expression of other Fe-containing proteins,²⁸ but the addition of 100 mg/ml $\text{FeSO}_4 \cdot 7\text{H}_2\text{O}$ did not result in obvious expression of the α subunit. The α subunit may not be stable in the absence of the other subunits, and may be more easily expressed along with the β subunit or with the β and γ subunits, or with the other subunits and the coupling protein. In addition, there are many other expression systems which may be more suited to obtaining the α subunit. If the α subunit were also very sensitive to proteolysis, the low (or nonexistent) level of expression of α observed in experiments identical to those carried out for the coupling protein and the γ subunit may be improved by the addition of stabilizers or by the use of a protease deficient cell strain.

Expression and purification of the coupling protein. The genes for the coupling protein and for the γ subunit of the hydroxylase were cloned into the expression vector pKK223-3²⁷ by Wayne Wu, and expression of the two proteins was demonstrated. This work was continued in order to determine whether the expressed coupling protein was functional and to obtain large amounts of pure, active coupling protein for use in spectroscopic studies of the hydroxylase such as EPR and EXAFS, as well as for crystallization of protein complexes. The SDS gel from a representative coupling protein purification is shown in Figure 2.8. A high level of expression of coupling protein and of the γ subunit is obtained. The γ subunit appears to become proteolyzed after the cells are lysed, suggesting that

this subunit may be unstable in the absence of the α and β subunits. After purification by column chromatography on Sephadex G50 and on DEAE Sepharose, the coupling protein was essentially pure except for a few high molecular weight impurities, which were removed by HPLC. The DEAE Sepharose step was later modified to include washing the column with buffer containing 0.15 M NaCl and gradient elution with 0.15 - 0.35 M NaCl (the coupling protein elutes at approximately 0.2 M NaCl), which eliminated the impurities and the need for a third purification step. Further improvements in the purity were observed by substituting Q Sepharose (a strong anion exchanger) for DEAE Sepharose in the second purification step. Some proteolysis of the coupling protein is observed, similar to that reported by Dalton.²⁹ This proteolysis can be minimized by carrying out the purification rapidly in the presence of protease inhibitors. Approximately 30 mg of pure coupling protein can be obtained from 2.5 l of cells, and the coupling protein comprises ~5-10% of the total protein in the crude extract.

A maximum SPA for pure coupling protein was measured by varying the amounts of hydroxylase and reductase in the assay mixture until the amount of propylene oxide produced was maximized. The measured SPA of 12,000 mU/mg (1 U = 1 μ mole product/ min) is consistent with the SPAs for the reported for the coupling proteins from *M. capsulatus* (13,376 mU/mg)¹⁵ and from *M. trichosporium* (11,200 mU/mg).¹³ The activity was measured by using partially purified reductase, however, and should be optimized with highly purified reductase.

IV. Conclusions

The fermentation and purification work described in this chapter were essential for establishing an independent research program for the study of the

soluble methane monooxygenase from *M. capsulatus* in our laboratory. Reliable protocols for the *M. capsulatus* fermentations were developed, and have since been improved by Thanos Salifoglou. The purification of the hydroxylase has led to the generation of large supplies of purified protein for spectroscopic, crystallographic, and mechanistic studies. The fact that the specific activity is consistently less than that reported for the *M. trichosporium* protein is most likely due to differences between the two proteins, not to purification and/or analysis problems. Since the X-ray structure has proven that the *M. capsulatus* hydroxylase contains two dinuclear iron centers (see Chapter 5), the most probable explanation for the measured value of 2 Fe atoms per protein molecule is that the hydroxylase as isolated is a mixture of 4 Fe and apo and/or iron-depleted protein.

Since only small amounts of the coupling protein can be purified from *M. capsulatus*, the expression of the coupling protein in *E. coli* and subsequent purification has provided large quantities of the coupling protein for use in spectroscopic, mechanistic, and future crystallographic studies. The expression of the α subunit in *E. coli* was attempted in order to obtain pure α subunit for crystallographic studies in the event that the holo $\alpha_2\beta_2\gamma_2$ hydroxylase did not crystallize or posed insurmountable crystallographic difficulties because of its large size. The crystallographic characterization of the holo hydroxylase proved successful, however, so the expression of the α subunit alone is no longer necessary. Instead, David Coufal is pursuing the expression of active holo hydroxylase in *E. coli* in order to prepare site-specific mutants.

References

- (1) Davies, S. L.; Whittenbury, R. *J. Gen. Microbiol.* **1970**, *61*, 227-232.
 - (2) Akent'eva, N. F.; Gvozdev, R. I. *Biokhimiya* **1988**, *53*, 91-96.
 - (3) Smith, D. D. S.; Dalton, H. *Eur. J. Biochem.* **1989**, *182*, 667-671.
 - (4) Fox, B. G.; Lipscomb, J. D. *Biochem. Biophys. Res. Comm.* **1988**, *154*, 165-170.
 - (5) Fox, B. G.; Froland, W. A.; Dege, J. E.; Lipscomb, J. D. *J. Biol. Chem.* **1989**, *264*, 10023-10033.
 - (6) Patel, R. N.; Savas, J. C. *J. Bacteriol.* **1987**, *169*, 2313-2317.
 - (7) Lund, J.; Dalton, H. *Eur. J. Biochem.* **1985**, *147*, 291-296.
 - (8) Green, J.; Dalton, H. *J. Biol. Chem.* **1985**, *260*, 15795-15801.
 - (9) Woodland, M. P.; Patil, D. S.; Cammack, R.; Dalton, H. *Biochim. Biophys. Acta* **1986**, *873*, 237-242.
 - (10) Whittenbury, R.; Phillips, K. C.; Wilkinson, J. F. *J. Gen. Microbiol.* **1970**, *61*, 205-218.
 - (11) Subramaniam, T. K.; Cangelosi, J. V. *Chemical Engineering* **1989**, *December*, 108-113.
 - (12) Wang, D. I. C.; Cooney, C. L.; Demain, A. L.; Dunnill, P.; Humphrey, A. E.; Lilly, M. D. *Fermentation and Enzyme Technology*; John Wiley and Sons: New York, 1979.
 - (13) Fox, B. G.; Froland, W. A.; Jollie, D. R.; Lipscomb, J. D. In *Methods In Enzymology* Academic Press: New York, 1990; Vol. 188; pp 191-202.
 - (14) Woodland, M. P.; Dalton, H. *J. Biol. Chem.* **1984**, *259*, 53-59.
 - (15) Pilkington, S. J.; Dalton, H. In *Methods In Enzymology* Academic Press: New York, 1990; Vol. 188; pp 181-190.
 - (16) Massey, V. *J. Biol. Chem.* **1957**, *229*, 763.
 - (17) Stookey, L. L. *Anal. Chem.* **1970**, *42*, 779-781.
 - (18) Bradford, M. M. *Anal. Biochem.* **1976**, *72*, 248.
-

- (19) Gill, S. G.; Hippel, P. H. v. *Anal. Biochem.* **1989**, *182*, 319.
 - (20) Turowski, P. N.; Armstrong, W. H.; Liu, S.; Brown, S. N.; Lippard, S. J. *J. Am. Chem. Soc.*, in press.
 - (21) Anthony, C. *The Biochemistry of Methylotrophs*; Academic Press: New York, 1982, p 296-379.
 - (22) Valentine, A. M.; Lippard, S. J., unpublished results.
 - (23) Wu, W. E., Lippard Laboratory Year End Report, 1990.
 - (24) Sambrook, J.; Fritsch, E. F.; Maniatis, T. *Molecular Cloning: A Laboratory Manual*; 2nd ed.; Cold Spring Harbor Laboratory Press: 1989.
 - (25) *Current Protocols in Molecular Biology*; Janssen, K., Ed.; Current Protocols: New York, 1993; Vol. 1.
 - (26) Sanger, F.; Nicklen, S.; Coulson, A. R. *Proc. Natl. Acad. Sci., U. S. A.* **1977**, *74*, 5463-5468.
 - (27) Brosius, J.; Holy, A. *Proc. Natl. Acad. Sci. USA* **1984**, *81*, 6929-6933.
 - (28) Broderick, J. B.; O'Halloran, T. V. *Biochemistry* **1991**, *30*, 7349-7358.
 - (29) Pilkington, S. J.; Salmond, G. P. C.; Murrell, J. C.; Dalton, H. *FEMS Microbiol. Lett.* **1990**, *72*, 345-348.
-

Figure 2.1 Flammability diagram for methane in an oxygen-nitrogen mixture at ambient temperature and pressure. The line ABCD represents the concentration of methane in air (79% N₂, 21% O₂). Point C shows the upper explosive limit for methane concentration in air, and point B shows the lower explosive limit for methane concentration in air. Points E and F show the upper and lower explosive limits if no nitrogen is present. Only a mixture that is bounded by points FBGCE can be ignited.

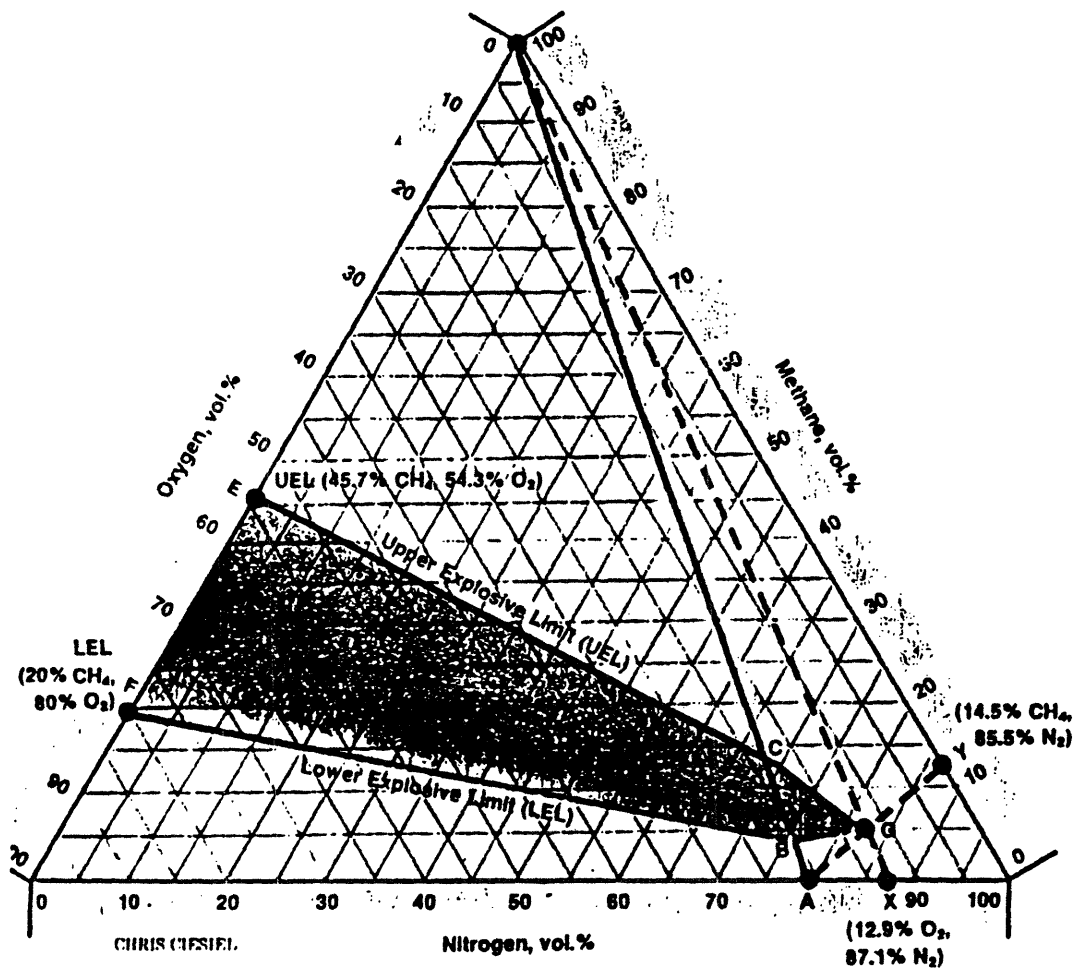
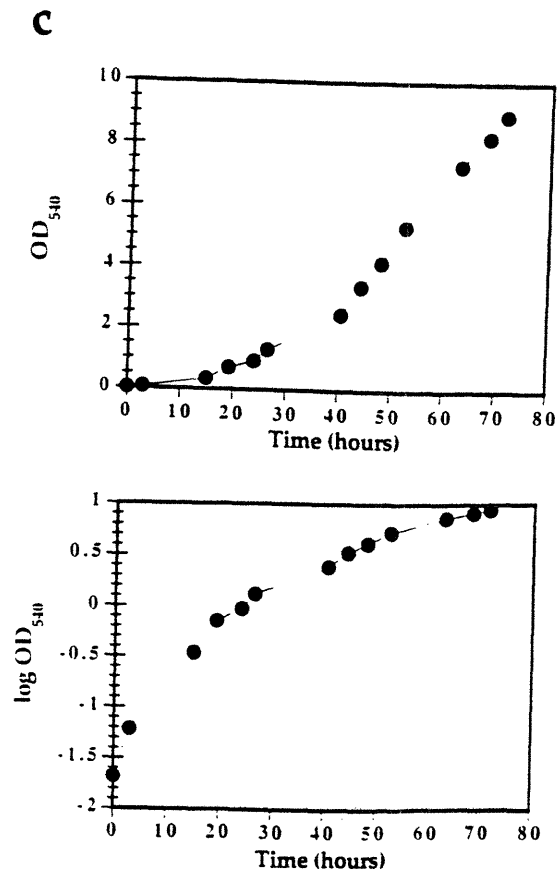
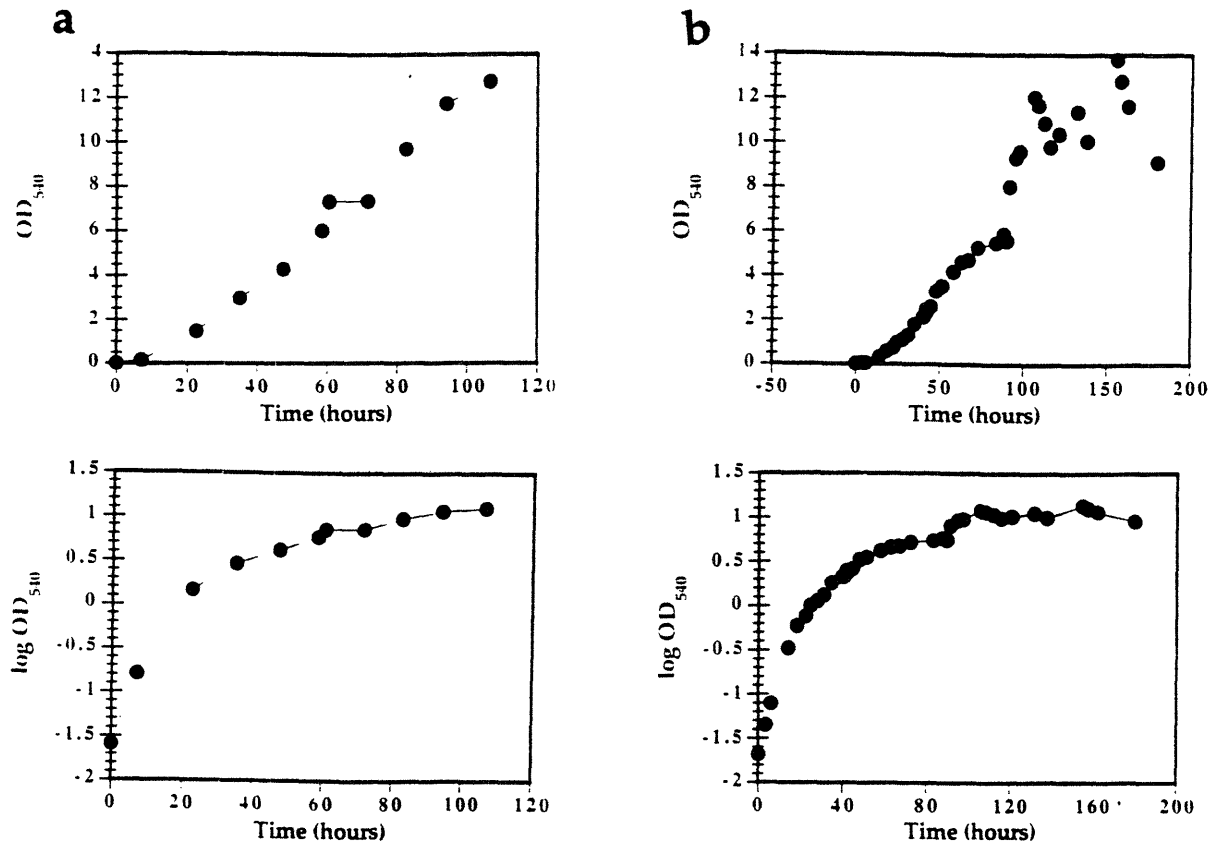
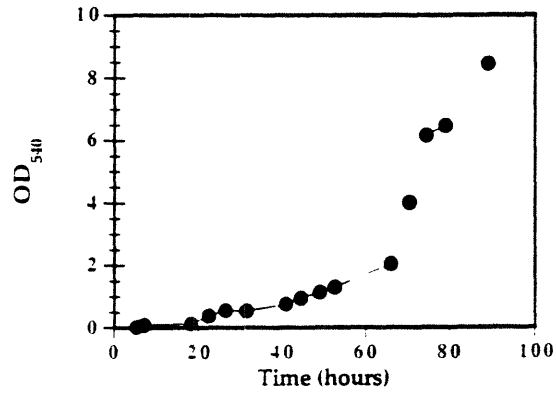


Figure 2.2 Fermentation kinetics for *M. capsulatus* growths. (a) growth I (batch), (b) growth II (continuous culture, (c) growth III (^{57}Fe), (d) growth IV (batch), (e) growth V (batch). For each fermentation, the top plot shows OD_{540} as a function of time, and the bottom plot shows $\log(\text{OD}_{540})$ as a function of time.



d



e

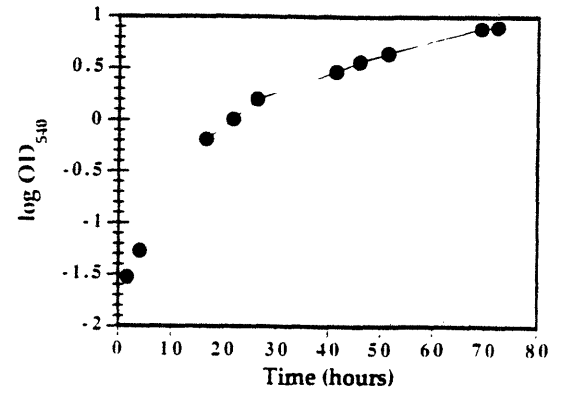
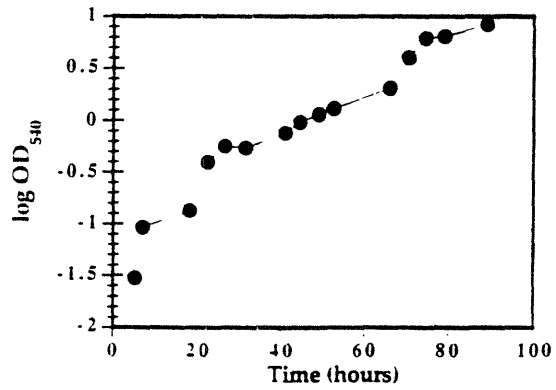
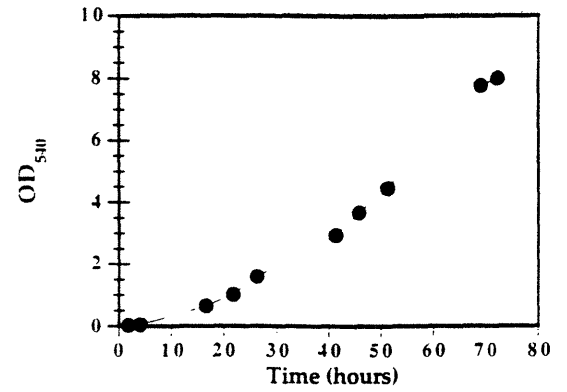


Figure 2.3 HPLC elution profile of the hydroxylase after separation from the reductase and the coupling protein on DEAE cellulose. A Pharmacia TSK G3000SWG gel filtration column (2.15 x 60 cm) equilibrated in 50 mM MOPS pH 7.0 containing 0.1 M NaCl was used at a flow rate of 3 ml/min.

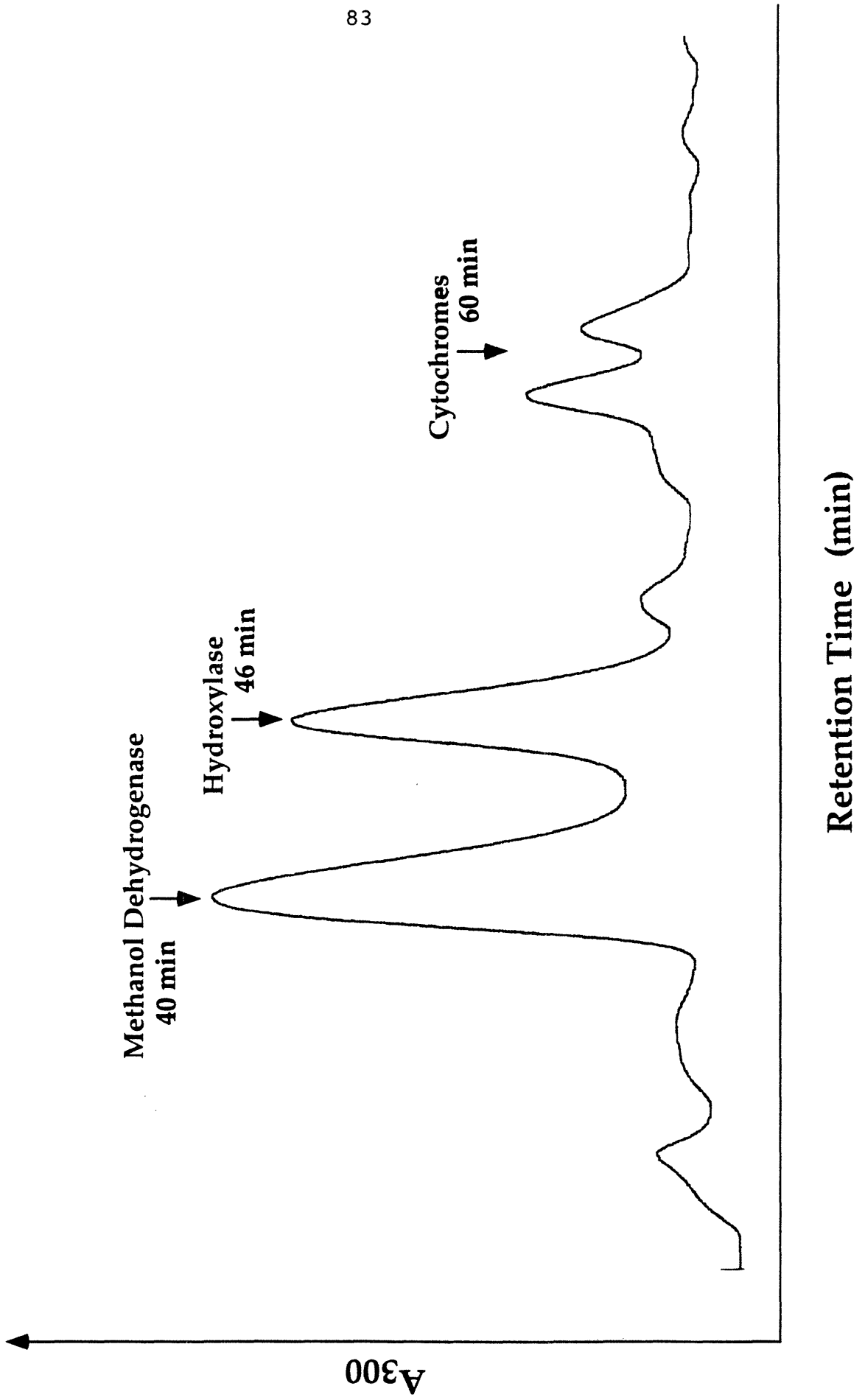


Figure 2.4 SDS PAGE of the purified hydroxylase. Lane 1, protein molecular weight standards (myosin, MW 200 kDa; phosphorylase B, MW 92.5 kDa; bovine serum albumin, MW 69 kDa; ovalbumin, MW 46 kDa; carbonic anhydrase, MW 30 kDa; trypsin inhibitor, MW 21.5 kDa; lysozyme, MW 14.3 kDa). Lanes 2 and 3, hydroxylase purified by anion exchange on DEAE cellulose and Q Sepharose (74 μ g, 185 μ g). Lanes 4-6, final purified hydroxylase after gel filtration on Sephacryl S-300 (30 μ g, 75 μ g, 150 μ g).

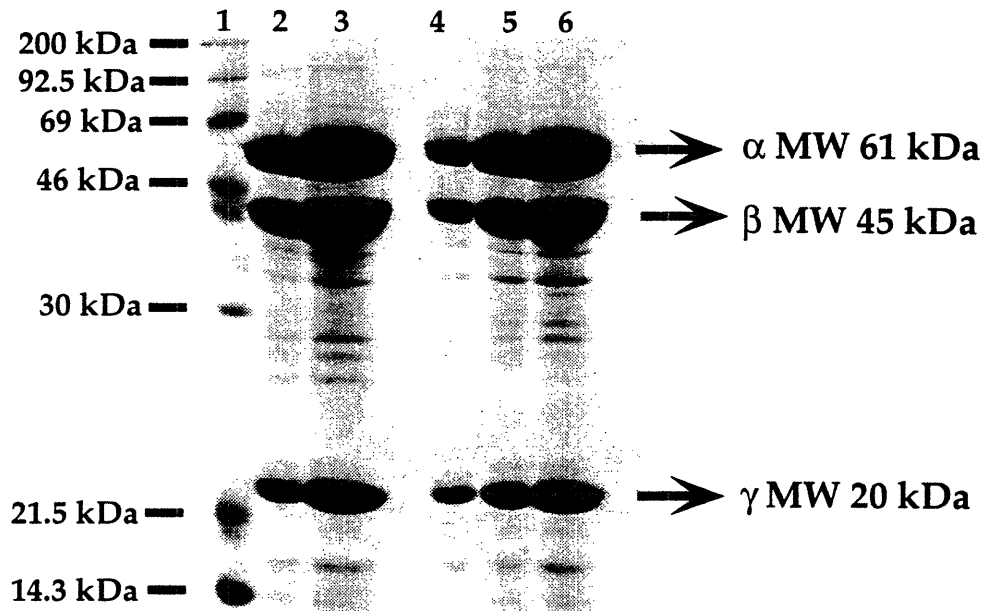


Figure 2.5 SDS PAGE of the highly purified hydroxylase. Lane 1, protein molecular weight standards (myosin, MW 200 kDa; phosphorylase B, MW 92.5 kDa; bovine serum albumin, MW 69 kDa; ovalbumin, MW 46 kDa; carbonic anhydrase, MW 30 kDa; trypsin inhibitor, MW 21.5 kDa; lysozyme, MW 14.3 kDa). Lane 2, crude hydroxylase purified by DEAE cellulose chromatography (84 μ g). Lane 3, hydroxylase purified by DEAE cellulose followed by FPLC on a Mono Q column (71 μ g). Lanes 4 and 5, hydroxylase from lane 3 further purified by HPLC on a TSK G3000SWG column (76 μ g, 29 μ g).

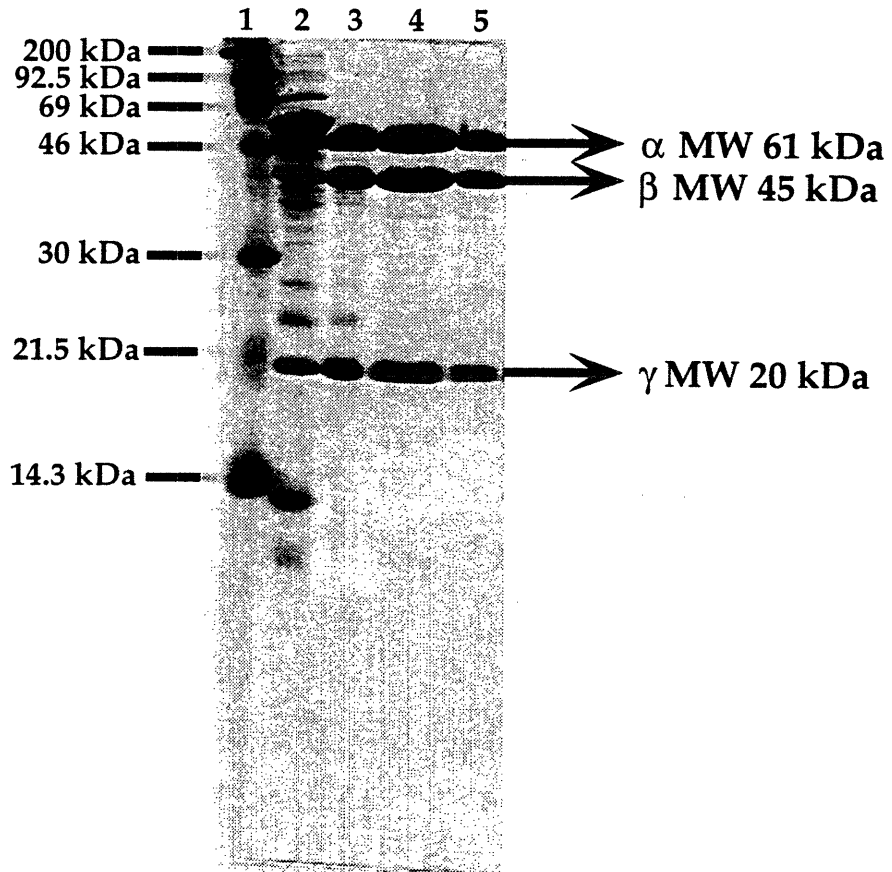


Figure 2.6 SDS PAGE of the purified *M. trichosporium* hydroxylase. Lane 1, protein molecular weight standards (myosin, MW 200 kDa; phosphorylase B, MW 92.5 kDa; bovine serum albumin, MW 69 kDa; ovalbumin, MW 46 kDa; carbonic anhydrase, MW 30 kDa; trypsin inhibitor, MW 21.5 kDa; lysozyme, MW 14.3 kDa). Lanes 2 and 3, DEAE cellulose fraction (600 µg, 240 µg). Lanes 4 and 5, DEAE Sepharose fraction (72 µg, 180 µg) Lanes 6 and 7, unidentified fractions from the DEAE Sepharose column. Lanes 8 and 9, final purified hydroxylase after gel filtration on Sephacryl S-300 (66 µg, 165 µg).

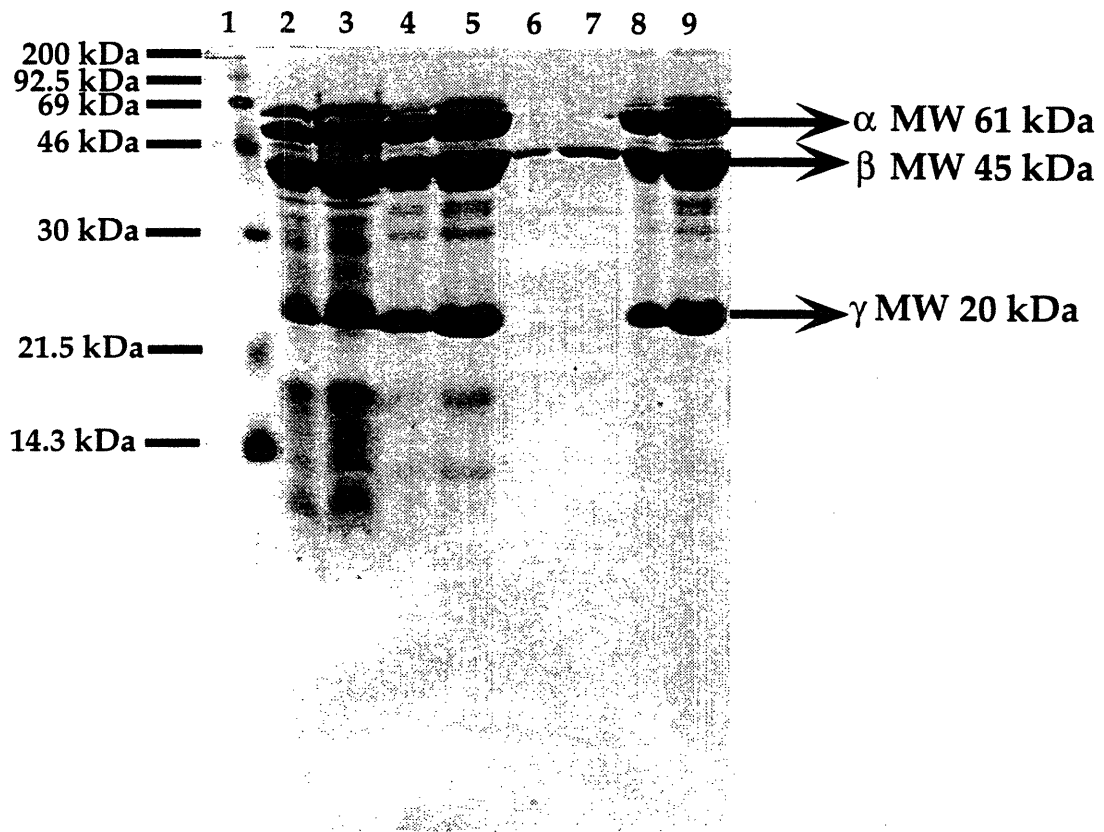


Figure 2.7 SDS PAGE of α subunit expression experiment. Lane 1, protein molecular weight standards (myosin, MW 200 kDa; phosphorylase B, MW 92.5 kDa; bovine serum albumin, MW 69 kDa; ovalbumin, MW 46 kDa; carbonic anhydrase, MW 30 kDa; trypsin inhibitor, MW 21.5 kDa; lysozyme, MW 14.3 kDa). Lane 2, purified hydroxylase (51 μ g) (the γ subunit has disappeared at the bottom of the gel). Lane 3, α 8-35 at t=0. Lane 4, α 8-35 at t=2. Lane 5, α 8-112 at t=0. Lane 6, α 8-112 at t=2. Lane 7, α 8-64 at t=0. Lane 8, α 8-64 at t=2. Lane 9, α 8-136 at t=0. Lane 10, α 8-136 at t=2. Lanes 3-8 were all loaded with 20 μ l of resuspended cell pellets.

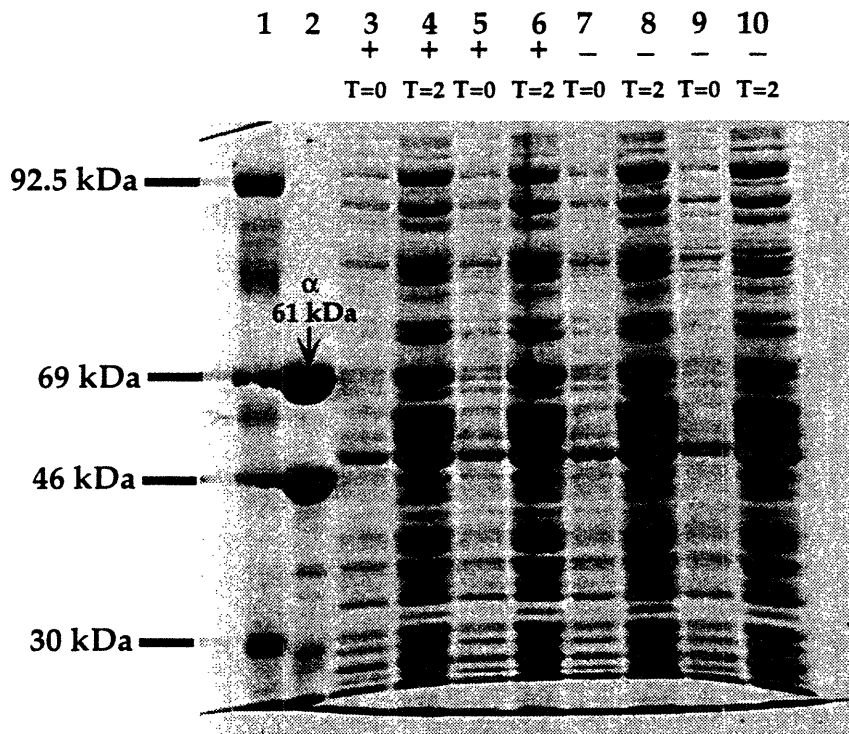
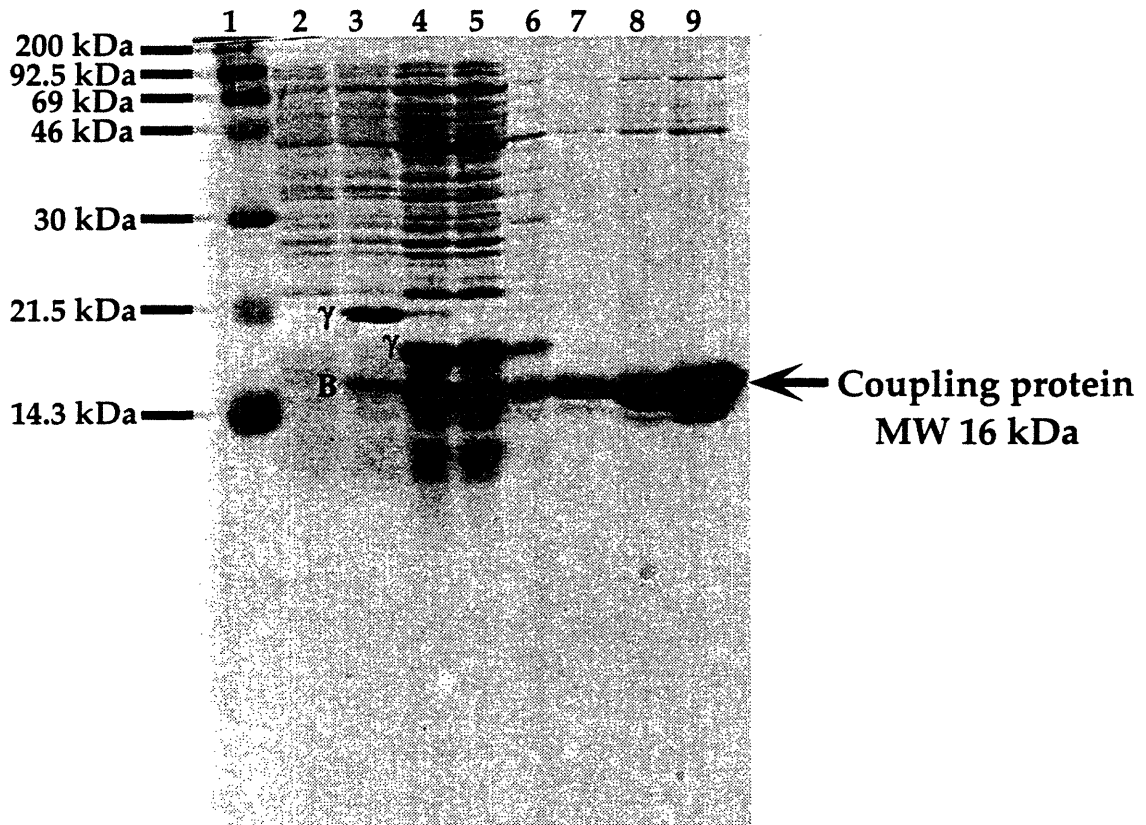


Figure 2.8 SDS PAGE of *E. coli* coupling protein purification. Lane 1, protein molecular weight standards (myosin, MW 200 kDa; phosphorylase B, MW 92.5 kDa; bovine serum albumin, MW 69 kDa; ovalbumin, MW 46 kDa; carbonic anhydrase, MW 30 kDa; trypsin inhibitor, MW 21.5 kDa; lysozyme, MW 14.3 kDa). Lane 2, cell pellet (20 μ l) from 1 ml cells lysed by boiling in SDS PAGE sample buffer immediately after induction with IPTG. Lane 3, cell pellet (20 μ l) treated as in lane 2, but 2 hours after IPTG induction. Lanes 4 and 5, crude extract (500 μ g, 500 μ g). Lane 6, Sephadex G50 fraction (68 μ g). Lanes 7-9, final purified coupling protein after anion exchange on DEAE Sepharose (24 μ g, 57 μ g, 170 μ g).



Chapter 3

Spectroscopic Studies of the Hydroxylase

I. Introduction

Electron paramagnetic resonance (EPR) spectroscopic studies of the *M. capsulatus* and *M. trichosporium* MMO hydroxylases have revealed the presence of a non-heme dinuclear iron center^{1,2} similar to those found in other iron oxo proteins such as hemerythrin and the R2 subunit of ribonucleotide reductase.^{3,4} In hemerythrin, the diiron center functions in dioxygen transport, and in the R2 protein, the diiron core reacts with dioxygen to form a tyrosyl radical which is involved in the reduction of ribonucleoside diphosphates to deoxyribonucleotide diphosphates for DNA synthesis. Both hemerythrin and the R2 protein have been structurally characterized by X-ray crystallography⁵⁻⁸ as well as by spectroscopic methods (Figure 3.1). In hemerythrin, the two Fe atoms are triply bridged by an oxo group and two carboxylates from glutamate and aspartate residues. The nonbridging ligands consist of 5 histidine nitrogen donors and one exogenous ligand in the metazido and deoxy forms. The R2 protein also contains an oxo bridge, but there is just one bridging carboxylate and only 2 histidine nitrogen donors are coordinated to the iron center. The remaining ligands are comprised of 3 carboxylates derived from 2 glutamate and 1 aspartate residue and 2 water molecules.

An initial X-ray absorption spectroscopic (XAS) investigation of the MMO hydroxylase, along with the lack of an optical spectrum beyond 300 nm,⁹ provided the first indication that the hydroxylase diiron center differs from those in hemerythrin and the R2 protein.¹⁰ In the XAS study, the oxidized Fe(III)Fe(III) protein sample photoreduced to the EPR detectable mixed valent Fe(II)Fe(III) form in the X-ray beam. In the data obtained for this photoreduced sample, no short Fe-O distance characteristic of the $[\text{Fe}_2\text{O}]^{4+}$ core in model compounds and other proteins¹¹ was detected. The extended X-ray absorption fine structure

(EXAFS) data were compared to data obtained for the oxo and hydroxo bridged model compounds $[\text{Fe}_2\text{O}(\text{OAc})_2(\text{HB}(\text{pz})_3)_2]$ ^{12,13} and $[\text{Fe}_2\text{OH}(\text{OAc})_2(\text{HB}(\text{pz})_3)_2](\text{ClO}_4)$ ¹⁴, where $\text{HB}(\text{pz})_3$ = hydrotris(pyrazolyl)borate. Since the EXAFS data resembled the data measured for the hydroxo bridged model compound, it was concluded that the hydroxylase diiron center contained a hydroxo rather than an oxo bridge. In order to characterize fully the diiron center and to establish a structural basis for the different reactivities of the diiron center in the hydroxylase and in the other iron oxo proteins, the hydroxylase diiron core has been studied extensively by optical spectroscopy, EPR spectroscopy, electron spin echo envelope modulation (ESEEM) spectroscopy, Mössbauer spectroscopy, and EXAFS spectroscopy.

I. Optical spectroscopy

Experimental

Optical spectra of the hydroxylase in the fully oxidized Fe(III)Fe(III) form were acquired by using a Perkin Elmer spectrophotometer. The interaction of the hydroxylase with N_3^- was examined in two different experiments. First, a sample of the hydroxylase (0.21 mM, 2.5 Fe/protein, 0.5 ml) was dialyzed for 20 hrs against 25 mM MOPS pH 7.0 containing 50 mM NaN_3 (2 x 500 ml). The NaN_3 was obtained from Fluka. The addition of N_3^- was carried out by dialysis because the addition of N_3^- directly to the protein had previously caused precipitation. In a second experiment, increasing amounts of N_3^- ranging from a 10-fold to a 2000-fold molar excess were added directly to a hydroxylase sample (0.21 mM, 2.3 Fe/protein, 0.5 ml) in a cuvet. No protein precipitation was observed.

Results and Discussion

Optical properties. The optical spectrum of the purified hydroxylase is shown in Figure 3.2. The protein exhibits an absorption maximum at 280 nm, and there are no significant features in the 300-700 nm range. The absence of optical features above 300 nm indicates that an oxo or phenoxo bridge is not present in the diiron center. For oxo bridged model compounds, optical features are observed at ~500 nm and between 600 and 700 nm.³ A broad feature at 375 nm is exhibited by the hydroxo bridged model compound $[\text{Fe}_2(\text{OH})(\text{OAc})_2(\text{HB}(\text{pz}_3)_2)]^+$ ¹⁴, but no such feature is observed for the hydroxylase. Another hydroxo bridged model complex, $[\text{Fe}_2(\text{OH})(\text{OAc})_2\{\text{CpCo}[\text{OP}(\text{OEt})_2]_3\}_2]^+$, exhibits no distinct optical features beyond 300 nm, except for a ligand band at 325 nm.¹⁵ Therefore, the presence of a hydroxo bridge in the hydroxylase diiron core could not be ruled out based on optical properties.

At high protein concentrations, a feature at 410 nm appears, accompanied by weaker features at 521 and 550 nm. Such a feature has been reported for the hydroxylase from *M. capsulatus*⁹ and for the hydroxylase from *Methylobacterium* CRL-26,¹⁶ and was attributed to the protein. Chemical reduction of the hydroxylase samples, however, increases these absorbances, and causes a shift of the 410 nm feature to 415 nm, indicating the presence of cytochrome impurity.¹⁷ The presence of this impurity is minimized by the use of gel filtration on a long Sephacryl S-300 column as the final purification step, but the impurity is usually still visible at high protein concentrations.

Azide binding. The effects of NaN_3 on the optical spectrum of the oxidized hydroxylase were investigated in an attempt to produce an optical feature which could then be utilized in resonance Raman spectroscopic studies. If the hydroxylase has one or two vacant coordination sites, it may be possible to bind

N_3^- and observe Fe- N_3^- interactions by both optical and resonance Raman spectroscopies. The optical spectrum for the N_3^- dialysis experiment exhibited a feature at 410 nm which can be attributed to the presence of ~3% cytochrome (calculated by using $\epsilon_{410} = 113,000 \text{ M}^{-1} \text{ cm}^{-1}$ for cytochrome c).¹⁸ Because of this impurity, it was difficult to detect any changes in the spectrum. A feature at ~460 nm seemed to grow in, and after the dialysis, the ratio A_{280}/A_{460} decreased significantly from 341 to 246. Further dialysis versus 25 mM MOPS pH 7.0 containing 0.1 M NaN_3 decreased this ratio to 146. The sample used for the second experiment, in which aliquots of concentrated NaN_3 solutions were added directly to the hydroxylase, also contained ~3% cytochrome. The results of this titration are shown in Figure 3.3. Upon addition of increasing amounts of N_3^- , the absorbance in the 420-500 nm range appears to increase, and the difference spectra reveal a broad band with $\lambda_{\text{max}} = 436 \text{ nm}$. The N_3^- anion is known to coordinate to hemerythrin, producing a charge transfer band at 445 nm (ϵ per 2 Fe = $3700 \text{ M}^{-1} \text{ cm}^{-1}$).¹⁹ Thus, it is reasonable that the band at 436 nm could indicate the formation of an azide adduct of the hydroxylase. Very high concentrations of N_3^- were required to produce this absorption feature, however, and the extinction coefficient at 436 nm calculated from this experiment is less than $1000 \text{ M}^{-1} \text{ cm}^{-1}$.

The formation of a weak hydroxylase - N_3^- adduct characterized by an absorption band at 425 nm ($\epsilon \sim 2400 \text{ M}^{-1} \text{ cm}^{-1}$) has been reported.²⁰ No optical spectra were included in this report, however. In addition, the interaction of fluoride ion, with the dimanganese form of the hydroxylase has been suggested by ^{19}F NMR,²¹ providing another possible example of exogenous ligand binding to the hydroxylase active center. In the same study, binding of F^- to the dimanganese form of the ribonucleotide reductase R2 protein was not observed, and it was argued that the two enzymes are different in terms of accessibility of

negatively charged species to the active center. The binding of N_3^- to the diferrous form of the R2 protein has since been reported,²² however, and the dimetal centers in the diferrous and dimanganese R2 proteins are somewhat similar.²³ A third example of exogenous ligand binding to the hydroxylase core involves phenol, which has been demonstrated to bind to the diiron center in the *M. trichosporium* hydroxylase by optical, CD, and resonance Raman spectroscopic studies.²⁴ Finally, the crystal structure of the oxidized hydroxylase reveals the presence of an exogenous acetate ligand bound to the diiron center, probably derived from the crystallization buffers (Chapter 5).

II. Electron paramagnetic resonance (EPR) spectroscopy

Experimental

Materials. Methyl viologen, proflavin, phenazine methosulfate, methylene blue, potassium indigo tetrasulfonate, dithionite, and Sephadex G-25 were obtained from Sigma. The brominated substrate 1-bromo-1-propene was purchased from Aldrich. For the copper perchlorate solution, CuSO_4 and NaClO_4 were obtained from Mallinckrodt, and HCl was purchased from Baker. Nitric oxide gas was obtained from Matheson.

Sample preparations and EPR spectroscopy. Hydroxylase for EPR samples was concentrated to 100-200 μM by using Centricon 30 ultrafiltration devices (Amicon). Samples to be reduced to the mixed valent Fe(II)Fe(III) and fully reduced Fe(II)Fe(II) forms were deoxygenated by slow, successive evacuation and back filling with argon on a vacuum line for several cycles. Samples were then transferred to an anaerobic wet box. Addition of reductants, incubation of samples, and transfer to EPR tubes were carried out in the box or on the vacuum line. Addition of coupling protein and the substrate 1-bromo-1-propene were carried out prior to reduction to the mixed valent form. After incubation times

ranging from 5 to 40 min, samples were removed from the box or vacuum line and immediately frozen in liquid nitrogen. EPR spectra were recorded at X-band at 9 K on a Bruker Model ESP 300 spectrometer with an Oxford Instruments EPR 900 liquid helium cryostat and a Bruker ER035M gaussmeter. Quantitation of the $g < 2$ mixed valent signal was performed under nonsaturating conditions by using a 1 mM solution of copper perchlorate (1 mM CuSO_4 , 2 M NaClO_4 , 0.01 M HCl). Transition probabilities were corrected for g -value anisotropy.²⁵

Results and Discussion

Three oxidation states. The EPR spectra of the hydroxylase in three oxidation states are shown in Figure 3.4. The oxidized sample exhibits signals at $g = 2$ and $g = 4.3$. Intensities of the $g = 2$ signal are variable and do not correlate with activity. The weak $g = 4.3$ signal is associated with mononuclear iron, and accounts for less than 5% of the Fe present in the sample. The weak rhombic signal at $g_{av} = 1.83$ (1.92, 1.86, 1.71) is characteristic of a Zeeman split $S = 1/2$ ground state of an antiferromagnetically coupled mixed valent Fe(II)Fe(III) center. Integration of the $g_{av} = 1.83$ signal reveals the presence of the mixed valent state in less than 2% abundance, based on dinuclear iron centers.

Chemical reduction of the oxidized hydroxylase with dithionite in the presence of phenazine methosulfate results in an increase in the $g_{av} = 1.83$ signal (Figure 3.4b), and integration of this signal indicates that ~17% of the iron in the sample was successfully converted to the mixed valent state. The intensity of the $g = 4.3$ signal does not change. Midpoint potentials for the appearance and disappearance of the EPR signature for the Fe(II)Fe(III) state during a redox titration of the hydroxylase were originally reported at 350 and -25 mV vs NHE.¹ Phenazine methosulfate, which has a redox potential of 80 mV, should therefore buffer the solution potential and optimize generation of the mixed valent state.

A redetermination of the midpoint potentials, however, yielded values of 48 and -135 mV, respectively, for the Fe(III)Fe(III)/Fe(II)Fe(III) and Fe(II)Fe(III)/Fe(II)Fe(II) redox couples.²⁶ These results indicate that phenazine methosulfate is not an optimal mediator for producing the mixed valent hydroxylase, affording a theoretical maximum yield of only 22% upon stoichiometric addition of dithionite. Based on these potentials, it was thought that the use of potassium indigo tetrasulfonate ($E^\circ = -46$ mV) and methylene blue ($E^\circ = 11$) in addition to phenazine methosulfate might buffer the potential more effectively. A ~30-40% yield was obtained by using these mediators. Since this yield proved adequate for generating samples for electron spin echo experiments, the mediator system was not further optimized.

The fully reduced Fe(II)Fe(II) form of the hydroxylase (Figure 3.4c) exhibits a signal at $g = 15$, which is the signature of a integer spin system. Addition of a 10-fold molar excess of dithionite in the presence of methyl viologen and proflavin reproducibly generated the fully reduced form in greater than 85% yield, as determined by Mössbauer spectroscopy. Low field EPR signals have also been observed for the azide complex of deoxyhemerythrin³ and for several diferrous model compounds.^{27,28} Quantitation of this signal for the *M. trichosporium* hydroxylase has revealed that this signal accounts for most of the iron present in the diferrous hydroxylase.²⁹

Effects of nitric oxide. The addition of nitric oxide gas to the fully reduced Fe(II)Fe(II) form was also investigated as an alternative route to the mixed valent state. Addition of NO to deoxyhemerythrin results in an EPR spectrum with g values of 2.76 and 1.84, which was interpreted as an Fe(II)Fe(III)NO⁻ species.³⁰ Addition of NO to the fully reduced hydroxylase generated by the addition of excess dithionite in the presence of methyl viologen and proflavin, which were removed by column chromatography on Sephadex G-25 prior to NO addition,

consistently resulted in an EPR spectrum with g values 4.1 and 2.0. The signal at $g = 2.0$ is due to excess NO, and the signal at $g = 4.1$ is most likely due to free Fe(II) complexed with NO. Proteins containing a mononuclear Fe(II) center typically exhibit an EPR signal at $g = 4.1$ upon complexation with NO.^{31,32} Since the signal observed for the hydroxylase only integrates to $< 5\%$ of the total Fe present, it is probably not generated by complexation of NO with the diiron center. A small amount of free Fe(II) in the sample, which persists after gel filtration on Sephadex G-25, probably reacts with NO to produce the observed $g = 4.1$ signal. There was no indication that NO facilitated formation of the Fe(II)Fe(III) form.

Effects of the coupling protein. The addition of coupling protein perturbs the EPR spectrum of the *M. trichosporium* Fe(II)Fe(III) hydroxylase, leading to the superimposition of two different spectra with $g_{av} = 1.85$ and $g_{av} = 1.75$, corresponding to mixed valent hydroxylase and mixed valent hydroxylase complexed with coupling protein, respectively.³³ For the *M. trichosporium* hydroxylase, the intensity of the $g_{av} = 1.75$ signal maximizes at approximately 2 moles of coupling protein per mole hydroxylase.³³ Therefore, hydroxylase was mixed with 2 molar equivalents of coupling protein, purified from the *E. coli* expression system (Chapter 2), and reduced to the mixed valent state as described above. The EPR spectrum of this sample (100 μ M, 1.5 Fe/protein) is shown in Figure 3.5. As expected, the spectrum of the hydroxylase complexed with coupling protein exhibits a mixture of two signals. At high microwave power (Figure 3.5b), only the signal with g values 1.87, 1.77, 1.62, $g_{av} = 1.75$ remains; the contribution of the signal with $g_{av} = 1.83$ attributable to uncomplexed hydroxylase disappears due to microwave power saturation. These EPR data further confirm what was shown by activity assays and SDS-PAGE (Chapter 2), that the coupling protein obtained from the expression system

is identical to the coupling protein isolated from *M. capsulatus*. Furthermore, this is the first EPR evidence of complex formation between the hydroxylase and coupling protein from *M. capsulatus*, and is similar to what has been observed in the *M. trichosporium* MMO system.

Effects of 1-bromo-1-propene. Finally, the mixed valent hydroxylase in the presence of several brominated substrates was investigated by EPR. The binding of a brominated substrate near the active site would allow an Fe-Br distance or Fe to substrate distance to be determined by EXAFS spectroscopy. The EPR spectrum of mixed valent hydroxylase in the presence of 500-fold excess 1-bromo-1-propene is compared to the normal EPR spectrum of the mixed valent hydroxylase in Figure 3.6. The difference in lineshape is consistently observed for all samples prepared in the presence of 1-bromo-1-propene, and suggests that 1-bromo-1-propene binds close to the diiron center.

III. Electron spin echo modulation (ESEEM) spectroscopy

Experimental

Materials. MOPS, dithionite, phenazine methosulfate, potassium indigo tetrasulfonate, and methylene blue were obtained from Sigma. Ethylene glycol was obtained from Baker.

Sample preparations. Five different samples were examined by ESEEM spectroscopy. Reduction to the mixed valent form was carried out in the same way as for the EPR samples by using a vacuum line and an anaerobic wet box. Sample ESE1 was concentrated to 1.4 mM (1.7 Fe per protein), reduced in the presence of dithionite and 1 mM phenazine methosulfate, and transferred to an EPR tube. All other samples were interrogated in a Mims transmission cavity. Samples ESE2 (1.7 mM, 1.9 Fe/protein) and ESE3 (2.0 mM, 2.3 Fe/protein) were prepared in 50 mM MOPS pH 7.0 containing 50% ethylene glycol, and reduced

by the addition of excess dithionite, 1.5 mM potassium indigo tetrasulfonate and 1.5 mM phenazine methosulfate. Samples ESE4 (1.3 mM, 1.3 Fe/protein) and ESE5 (1.3 mM, 1.3 Fe/protein) were prepared in an analogous fashion except that the dialysis into ethylene glycol containing buffer was eliminated and an additional mediator, methylene blue, was also used. Each sample was loaded directly into a teflon lined crevice in the Mims cavity while in the anaerobic wet box. The cavity was then removed from the box and immediately immersed in liquid nitrogen to freeze the sample.

ESEEM spectroscopy. The pulsed EPR spectrometer that was used in these experiments has been modified since it was last described.³⁴ The microwave pulses are formed on a two-channel bridge. Each channel is isolated (40 dB) and permits independent control of pulse duration, phase, and amplitude. The typical rise/fall time of the pulse is less than 5 ns, and the maximum pulse duration is 60 ns. The low power microwave pulses are amplified prior to the cavity, as in the past.³⁴ Modulation is recorded as an integrated echo amplitude taken as a 16 ns sample by using a homebuilt boxcar signal averager. The waveform consists of 1024 points (1000 steps of echo amplitude vs. time, plus 24 points of baseline). Transmission cavities resonant at 9 and 10 GHz were used. Their design has been described by Mims.³⁵ The tapered couplings to the WR-90 waveguide have been rendered asymmetric on the transmitter vs. receiving arm in order to minimize reflections of microwave pulse and echo. The cavity features a quality factor of 80, and the total instrument deadtime achieved during these experiments with the above spectrometer configuration was 100 ns.

Results and Discussion

Structural information can be obtained from a pulsed EPR experiment when the echo signal produced by the pulses is modulated by magnetic nuclei

coupled to the unpaired electron. In a 2-pulse experiment, the time τ between two microwave pulses is varied, and the echo intensity I is measured as a function of τ .^{36,37} When the time domain data is Fourier transformed, a spectrum of the nuclear precession frequencies is obtained. If a ^{14}N nucleus is weakly coupled by dipolar interactions, a single peak at or near the Larmor frequency of the ^{14}N nucleus (~ 1 MHz) will appear. As quadrupole and isotropic interactions contribute, peaks at higher frequencies will appear. In a 3-pulse experiment, the time τ between the first two pulses is held constant, and the time T between the second and third pulses is varied.^{36,37} The echo envelope intensity is measured as a function of T . Typically, 3-pulse ESE experiments are carried out on metalloproteins in order to detect the presence of nitrogen ligands to the metal center.

The experiment was originally attempted on sample ESE1, but the 3-pulse echo intensity was too weak to interpret. The echo intensity for samples ESE2-ESE5 was increased by the use of a Mims transmission cavity which improves the signal-to-noise ratio and maximizes the amount of sample in the resonant field. A representative 3-pulse echo modulation profile is shown in Figure 3.7. The shallow modulation depth is characteristic of many iron proteins, including cytochrome P450,³⁸ fumarate reductase,³⁹ and uteroferrin.⁴⁰ Fourier transform (FT) spectra at 3 distinct g -values are also shown in Figure 3.7. The most well resolved spectrum is obtained at $g = 1.92$. This spectrum exhibits 3 broad lines centered at 1.8, 3.6, and 7.3 MHz (indicated by $a-a''$ in Figure 3.7) and two sharp lines located at 1.8 and 3.1 MHz. (indicated by $b-b'$ in Figure 3.7). The spectrum could be simulated with two types of nitrogens, a ^{14}N nucleus characterized by a large contact hyperfine term (~ 5 MHz) (Figure 3.8, left) and a ^{14}N nucleus with a contact interaction of ~ 1 MHz (Figure 3.8, right), which is typical of an imino (non-coordinated) nitrogen of an imidazole ligand to a metal ion.⁴¹ Therefore,

two types of nitrogens are present in the hydroxylase diiron center. The 3 broad peaks in the spectrum were matched by using the theoretical model of an N nucleus with a relatively large contact hyperfine interaction, and the 2 sharp peaks were best simulated by using the imino nitrogen model. In both cases, simulation of a single nitrogen of each type gave the best fit; additional nuclei of either type yielded significant combination lines in regions that are unambiguously free of spectroscopic features in the experimental data (4.5 - 6.5 MHz).

The 2 sharp peaks at 1.8 and 3.2 MHz in the $g = 1.92$ FT spectrum were fit by using quadrupole parameters $e^2Qq = 1.8 \pm 0.1$ MHz and $\eta = 0.35 \pm 0.05$. The effective distance between the electron spin and the interacting nucleus was 3.2 ± 0.2 Å, and the contact hyperfine interaction was 0.8 ± 0.1 MHz. These parameters are consistent with those routinely observed for imino nitrogen of imidazole ligands to metals. In general, the imino nitrogen of imidazole ligands exhibits an e^2Qq less than 2.5 MHz and η greater than 0.4.⁴² This nitrogen therefore has been assigned as the non-coordinated nitrogen of the histidine coordinated to the effective Fe(III) in the diiron center. The optimum fit of the peaks for the second nitrogen was obtained by using quadrupole parameters $e^2Qq = 3.0 \pm 0.5$ MHz and $\eta = 0.3 \pm 0.1$. The contact hyperfine term was 5.0 ± 0.3 MHz and the effective interaction distance ranged between 2.2 and 3.1 Å. The quadrupole parameters seem too large to be attributable to an imino nitrogen, but are consistent with experimentally observed quadrupole parameters of peptide amino nitrogen, which are in the range $3.0 < e^2Qq < 3.4$ and $0.4 < \eta < 0.5$.⁴³ This type of coupled nitrogen is observed for Fe-S clusters, and has been attributed to a peptide nitrogen bridged via a hydrogen bond to a sulfur ligand on the cluster.^{39,44}

Originally, it was thought that this nitrogen could be a peptide nitrogen bridged via a hydrogen bond to an oxygen ligand on one of the Fe atoms. There

are no peptide nitrogens hydrogen bonded to iron ligands evident in the X-ray structure, however. Alternatively, the fact that the contact hyperfine term of 5.0 ± 0.3 MHz is considerably larger than the value determined for the peptide nitrogen in the Fe-S protein fumarate reductase, 1.1 MHz,³⁹ could be taken together with the shortest r_{eff} of 2.2 Å as evidence of a weakly coordinated nitrogen. The X-ray structure does reveal two histidine ligands, one coordinated to each Fe atom with its δ -N atom (Chapter 5). The non-coordinated nitrogen is the ϵ -N of one of these histidine ligands. The second nitrogen must be therefore assigned as the δ -N atom directly coordinated to the effective Fe(II) in the diiron center. This interpretation is consistent with the results of a recent ENDOR study of the *M. trichosporium* hydroxylase, in which two classes of ¹⁴N atoms associated with the diiron center were detected and assigned as one imidazole bound per Fe atom.⁴⁵ In the ENDOR study, however, the two nitrogens corresponded to the δ -N atoms of the coordinated histidines. By contrast, the ESEEM data reveal one non-coordinated ϵ -N atom and one directly coordinated δ -N atom.

IV. Mössbauer Spectroscopy

Experimental

Materials. An oxidized hydroxylase sample for Mössbauer experiments was prepared by using cells grown in an ⁵⁷Fe-containing medium (see Chapter 2). MOPS, DEAE cellulose, dithionite, methyl viologen, and proflavin were purchased from Sigma. Ethylene glycol was obtained from Baker.

Sample preparation. After purifying by DEAE cellulose chromatography and HPLC, the sample was concentrated to 0.5 ml (0.6 mM, 1.3 Fe/protein), dialyzed into 50 mM MOPS pH 7.0 containing 20% ethylene glycol, and frozen in a Mössbauer sample cell. A significant Fe loss was observed after concentration with an Amicon ultrafiltration device. After acquiring the Mössbauer spectrum,

the sample was thawed and reduced in an anaerobic dry box by adding a 10-fold excess of dithionite in the presence of methyl viologen and proflavin and incubating for 25 minutes.

Mössbauer spectroscopy. Zero-field Mössbauer spectra were recorded at 4.2 K and 80 K by using a conventional constant acceleration spectrometer equipped with a temperature controller maintaining temperatures within ± 0.1 K. The source was ^{57}Co in Rh. Isomer shifts are referred to Fe metal at room temperature. Data were collected for 96 hours at 80K - 100K counts per channel for protein samples containing approximately 40 mg of ^{57}Fe . Data were fitted with a sum of Lorentzian quadrupole doublets by using a least-squares routine.

Results and Discussion

The Mössbauer spectra of the oxidized and fully reduced forms of the hydroxylase are shown in Figure 3.9. The spectrum of the oxidized hydroxylase recorded at zero field was fit with one quadrupole doublet having $\Delta E_Q = 1.05$ mm/s and an isomer shift δ of 0.50 mm/s. The spectrum could also be fit with two doublets, for which $\Delta E_Q(1) = 0.95$ mm/s, $\Delta E_Q(2) = 1.47$ mm/s, $\delta(1) = 0.48$ mm/s, $\delta(2) = 0.55$ mm/s, without significant improvement of the fit. Similar observations were reported for the *M. trichosporium* hydroxylase.² No Fe^{2+} was evident in the sample, indicating that the hydroxylase, as isolated, is in the oxidized state. The isomer shift and quadrupole splitting are typical of Fe^{3+} . The quadrupole splitting is consistent with the presence of high spin Fe^{3+} , and lies between the values observed for oxo-bridged proteins and model complexes (1.5 - 1.8 mm/s) and for the hydroxo bridged model complex.⁴⁶ One possible explanation for the quadrupole splitting in the diferric hydroxylase is that the Fe atoms are hydroxo-bridged and pentacoordinate.

The 80 K Mössbauer spectrum of the reduced hydroxylase was fit with two quadrupole doublets, one associated with 15% unreacted oxidized protein and a second with parameters typical of high spin Fe^{2+} . This second doublet, which represents 85% of the total Fe in the sample, has $\Delta E_Q = 3.01$ mm/s and an isomer shift $\delta = 1.30$ mm/s, parameters consistent with high spin Fe^{2+} . No second heterogeneous component appeared in the Mössbauer of the fully reduced form, as was reported for the reduced hydroxylase from *M. trichosporium*.^{2,47} The higher quadrupole splitting reported for the *M. trichosporium* hydroxylase (3.14 mm/s at 4 K) is probably a temperature effect associated with the weakly coupled system. Such a temperature dependence has been reported for diferrous model compounds.²⁷

V. X-Ray Absorption Spectroscopy

Experimental

Materials. MOPS, dithionite, proflavin, and methyl viologen were purchased from Sigma, and ethylene glycol was obtained from Baker. The brominated substrate 1-bromo-1-propene was purchased from Aldrich. The EXAFS cells were obtained from Jane DeWitt at Stanford University.

Sample preparations Large quantities of hydroxylase and coupling protein were purified for EXAFS experiments. Since ~200 mg of purified hydroxylase were used for each EXAFS sample, each 25 g preparation of cell paste yielded just one EXAFS sample. Hydroxylase for EXAFS samples was concentrated to ~15 mg/ml by centrifugation in a Centriprep 30 concentrator (Amicon) and then dialyzed (MW cutoff 14,000) for 3 hours against 500 ml 50 mM MOPS pH 7.0 containing 5% ethylene glycol and then for 3 hours against 500 ml 50 mM MOPS pH 7.0 containing 50% ethylene glycol. EXAFS samples prepared in degassed 50% ethylene glycol buffers typically yield better data. Samples were further

concentrated by centrifugation in a Centricon 30 concentrator (Amicon) to a final volume of ~200 μ l, degassed, and transferred to an anaerobic wet box. Oxidized samples (EXAFS2, EXAFS4, EXAFS5, EXAFS7) were immediately loaded into capped lucite EXAFS cells (23 x 2 x 3 mm). Samples EXAFS2 - EXAFS4 were prepared by using purified hydroxylase obtained from Dalton. Chemical reduction to the diferrous form was carried out in the wet box by the addition of excess dithionite and the mediators proflavin and methyl viologen followed by a 25 min incubation (EXAFS3, EXAFS6). Upon removal from the box, the samples were immediately frozen in liquid nitrogen.

EXAFS samples containing oxidized hydroxylase and two molar equivalents of the coupling protein (EXAFS10, EXAFS12, EXAFS14 - EXAFS17) were prepared as follows. The two proteins were concentrated separately to ~15 mg/ml hydroxylase and ~10 mg/ml coupling protein. The two proteins were then combined and dialyzed (MW cutoff 3500) for 3 hours against 500 ml of 50 mM MOPS pH 7.0 containing 5% ethylene glycol and for 3 hours against the same buffer containing 50% ethylene glycol. For samples containing the substrate 1-bromo-1-propene (EXAFS11, EXAFS16 - EXAFS20), excess 1-bromo-1-propene was added to samples before the dialysis as well as to the dialysis buffers. The samples were then further concentrated in Centricon microconcentrator devices to a final volume of ~200 μ l, and excess 1-bromo-1-propene was again added to samples. The samples were degassed and transferred to the anaerobic wetbox. Samples EXAFS10-EXAFS14, EXAFS16, EXAFS18, and EXAFS20 were immediately loaded into capped lucite EXAFS cells (23 x 2 x 3 mm). Samples EXAFS15, EXAFS17, and EXAFS19 were reduced by the addition of excess dithionite and 4 mM each of the mediators proflavin and methyl viologen. After a 45 min incubation, these samples were loaded into

EXAFS cells, removed from the wet box, and frozen in liquid nitrogen. The EXAFS samples are summarized in Table 3.1.

EXAFS Data Collection, Reduction, and Analysis. Samples EXAFS2 - EXAFS4 were measured at SSRL on beamline 4-2 by using a Si(111) double-crystal monochromator and a detector that has been previously described.¹⁰ These samples were prepared and measured by others prior to this thesis, but are included in this discussion for comparison. Samples EXAFS5 and EXAFS6 were measured at NLS on beamline X19A (2.5 GeV, 90-200 mA) by using a Si(111) double-crystal monochromator detuned for harmonic rejection to 50% of the maximum at 7820 eV. The fluorescence signal was monitored by using a 13-element Ge solid-state array detector⁴⁸ windowed on the Fe K α signal. During the experiment, count rates of approximately 28,000 s⁻¹ (total per element) were measured at 7800 eV. The other samples were measured at SSRL on beamline 7-3 (3 GeV, 40 - 90 mA). A Si(220) double-crystal monochromator was used, detuned 45% at 7995 eV. For these experiments, count rates of 25,000 - 35,000 s⁻¹ (total per element) were maintained at 7997 eV. Energies were calibrated by using an internal iron foil standard,⁴⁹ assigning the first inflection point of the Fe absorption edge at 7111.2 eV. Calibrated scans were inspected individually and rejected if the signal-to-noise level was too high compared to the other scans as a result of beam instabilities, poor detector statistics, or loss of beam. The remaining scans were averaged and used for further analysis.

A pre-edge subtraction was performed by fitting the EXAFS region with a smooth polynomial which was extrapolated into the pre-edge region and subtracted. A three-segment spline was fit to the EXAFS region and subtracted and the data normalized to an edge jump of one. The spline was chosen so that it minimized residual low-frequency background, but did not reduce the EXAFS amplitude as checked by monitoring the Fourier transform of the EXAFS during

the background subtraction process. The normalized background-subtracted data were converted to k -space, where k is the photoelectron wavevector defined by $[2m_e(E - E_0)/h^2]^{1/2}$. In this expression, m_e is the electron mass, E is the photon energy, h is Planck's constant divided by 2π , and E_0 is the threshold energy, 7130 eV (where k is defined to be zero).

All curve-fitting was based on k^3 - weighted data. Analysis was performed with nonlinear least-squares curve-fitting techniques with empirical phase and amplitude parameters. The estimated errors are ± 0.03 Å for the distances and 25% for the coordination numbers. Empirical Fe-X backscattering parameters were obtained from the following model compounds: Fe-N from $[\text{Fe}(\text{1,10-phenanthroline})_3](\text{ClO}_4)_3$ ⁵⁰; Fe-O and Fe-C from $[\text{Fe}(\text{acetylacetonate})_3]$,^{51,52} and Fe-Fe from $[\text{Fe}_2(\text{OH})(\text{OAc})_2(\text{HB}(\text{pz})_3)_2](\text{ClO}_4)$.¹⁴ The EXAFS data from 3.5 to 12.5 Å⁻¹ were Fourier transformed to R (Å) space to isolate the first and second shell contributions to the data. The individual contributions of the first and second shells were then isolated, backtransformed to k space, and fit from 4.0 to 12.0 Å⁻¹. In addition, both shells were backtransformed together and fit between 4.0 and 12.0 Å⁻¹, as were the unfiltered data.

Results and Discussion

Photoreduction of the oxidized hydroxylase. The edge position of most of the oxidized samples (EXAFS2, EXAFS4, EXAFS7, EXAFS9-EXAFS14, EXAFS16, EXAFS18, EXAFS20) shifted approximately 1.5 eV to lower energy during the first four hours of exposure to the X-ray beam. This energy shift is due to photoreduction of the samples to the mixed valent state. For the same sample runs, the simultaneous Fe foil calibrations ensured that these shifts were well outside experimental error. In Figure 3.10 are presented edge data for a

nonphotoreduced, oxidized protein sample (EXAFS5), a dithionite reduced diferrous protein sample (EXAFS6), and a photoreduced sample (EXAFS2). The difference in sharpness of the edges arises from beamline-dependent resolution differences, and does not affect the observation that the edge shifts to lower energy by about 1.5 eV per added electron. All of the samples containing coupling protein and/or the substrate 1-bromo-1-propene photoreduced in the X-ray beam, and the rate of photoreduction was related to ring current. For example, after 21 hours in the beam between 58 and 30 mA, the edge of EXAFS14 only shifted 0.8 eV, but after injection to ~90 mA, an additional ~1 eV shift occurred in 11 hours. EPR measurements of sample EXAFS2 before and after X-ray exposure showed that the observed Fe K-edge shift (-1.4 to -1.7 eV) correlated with photoreduction of the sample as monitored by the efficient accumulation of signals arising from a free radical ($g = 2.0$) and an $S = 1/2$ mixed valent dinuclear iron center ($g < 2.0$). For the EXAFS2 sample, warmup to 298 K followed by recooling the EXAFS cell in the helium cryostat resulted in loss of the $g = 2.0$ signal without significant decline in the intensity of the Fe(II)Fe(III) signal ($g = 1.92, 1.86, 1.71$). Subsequent spin integration revealed $\sim 60 \pm 10\%$ conversion to the mixed valent state.

Uncomplexed oxidized, mixed valent, and reduced hydroxylase. The k^3 -weighted EXAFS of the protein samples EXAFS2-EXAFS6 are shown in Figure 3.11 and the Fourier transforms in Figure 3.12. The oxidized protein EXAFS (Figure 3.11c) and the EXAFS of $[\text{Fe}_2(\text{OH})(\text{OAc})_2(\text{HB}(\text{pz})_3)_2]\text{ClO}_4$ (Figure 3.11b) show strong similarity suggesting that the active site structure of the protein resembles that of the hydroxo-bridged model compound. The EXAFS of the semimet protein samples (Figure 3.11d-e) have peaks at ~ 7 and 11 \AA^{-1} that are only shoulders in the oxidized protein sample EXAFS. The overall features of the EXAFS of the semimet protein samples from the two bacterial species are similar,

despite the higher noise-level for the *M. trichosporium* OB3b sample (EXAFS4), as are the Fourier transforms indicating that the active sites of the hydroxylase from the two species are also comparable. The reduced protein EXAFS (Figure 3.11f-g) is shifted to lower k relative to the semimet and oxidized protein EXAFS and the first shell peak in the Fourier transform is shifted to higher R (Figure 3.12d-e) suggesting that the first shell coordination around the Fe is at a longer distance in the reduced form of the hydroxylase relative to the semimet and oxidized forms. Only one peak is seen in the Fourier transform of the reduced protein EXAFS; the peak attributed to Fe-Fe backscattering is absent, and the overall structure of the reduced protein EXAFS is less complicated than that of the semimet and oxidized protein EXAFS.

First shell fits. The results of first and second shell fits to the data have been described in detail elsewhere,^{17,53} and will be summarized only briefly here. For the oxidized hydroxylase sample (EXAFS5), an average first shell coordination of 5.8 N/O at 2.04 Å was found. Upon photoreduction to the semimet state, the first shell coordination distance increased to 5.6 N/O at 2.08 Å for EXAFS2 and to 5.8 N/O at 2.06 Å for EXAFS4. The average first shell coordination of the reduced protein samples (EXAFS3 and EXAFS6) was found to be 5.1 N/O at 2.15 Å). The presence of a short (~ 1.80 Å) Fe-O distance, indicative of an oxo bridged center, was also investigated. When a short Fe-O distance was included in the fits, either negative coordination numbers resulted, or the total oxygen contribution was split between two oxygen waves at distances on the order of 2.0 Å. Given the previously shown high sensitivity of EXAFS to the presence or absence of the short oxo bridge,¹¹ this result, together with the similarity of the oxidized and semimet hydroxylase EXAFS spectra to that of $[\text{Fe}_2(\text{OH})(\text{OAc})_2(\text{HB}(\text{pz})_3)_2](\text{ClO}_4)$ and the dissimilarity to that of $[\text{Fe}_2\text{O}(\text{OAc})_2(\text{HBpz}_3)_2]$ (Figure 3.11a-e), clearly indicates that the hydroxylase of

methane monooxygenase does not have an oxo bridge in its dinuclear iron center. The presence of a hydroxo bridge has since been established by proton ENDOR studies.⁵⁴

Second Shell Fits. The $[\text{Fe}_2(\text{OH})(\text{OAc})_2(\text{HB}(\text{pz})_3)_2](\text{ClO}_4)$ compound was chosen as a model compound for extracting parameters to determine the Fe...Fe interaction in MMO for two reasons: first, in this compound the distribution of atoms in the second coordination sphere is such that the Fe...Fe distance is more isolated from second shell Fe...low-Z scatterer distances than in the analogous oxo-bridged model $[\text{Fe}_2\text{O}(\text{OAc})_2(\text{HBpz}_3)_2]$ (the nearest C/N shell is about 0.25 Å away with only 2 O close to Fe in $[\text{Fe}_2(\text{OH})(\text{OAc})_2(\text{HB}(\text{pz})_3)_2](\text{ClO}_4)$ whereas there are 8 C/N within 0.02-0.15 Å in $[\text{Fe}_2\text{O}(\text{OAc})_2(\text{HBpz}_3)_2]$ ¹¹); second, since the first shell fits indicate that there is no oxo bridge in the iron protein center, a non-oxo bridged model should provide more suitable parameters to use in fits of the protein active site.⁵⁵ With the use of these empirical parameters in fits to the second shell data for hydroxylase samples EXAFS2, EXAFS4 and EXAFS5, two Fe...Fe minima were found, one at ~ 3.0 Å and one at ~ 3.4 Å, depending on the initial Fe...Fe distance used in the fit. From a detailed analysis of the fits, it was concluded that the 3.4 Å distance is the appropriate interpretation of the data and that the 3.0 Å distance results from correlation between Fe-Fe and Fe-C parameters. In addition, the longer distance is consistent with the location and large magnitude seen for both the protein samples and the dinuclear model complexes.¹¹ In analyzing the Fe...Fe distance, a model dependence of the fits was discovered. When cross fits were performed on the two model complexes $[\text{Fe}_2\text{O}(\text{OAc})_2(\text{HB}(\text{pz})_3)_2]$ and $[\text{Fe}_2(\text{OH})(\text{OAc})_2(\text{HB}(\text{pz})_3)_2]^+$, two Fe...Fe distances were found for each, the correct distance and a distance ~0.4 Å away. If the wrong model is used in the fit, for example the hydroxo model parameters to fit the oxo compound data, the result is then biased toward the wrong Fe...Fe

distance. This result is significant, and must be taken into account in future EXAFS studies of iron oxo proteins.

For the reduced samples EXAFS3 and EXAFS6, the Fourier transform shows very low intensity in the second shell region of the other samples (Figure 3.12d-e), and no Fe...Fe distance could be determined. The absence of a resolvable Fe-Fe interaction in diiron(II) and other reduced dinuclear metalloprotein cores and their model complexes is not unusual. In deoxyhemerythrin, the Fe...Fe second shell peak disappears upon warming the protein from 80 K to room temperature.⁵⁶ Also, no Cu(I)-Cu(I) peak is seen in the Fourier transform of deoxyhemocyanin data.⁵⁷ In addition, the Fe...Fe peak cannot be resolved in the semimet form (pink) of purple acid phosphatase.⁵⁸ This phenomenon might be caused by the loss of a bridging ligand upon reduction, resulting in uncorrelated vibrations of the metal atoms (increased Debye-Waller factor), or by destructive interference in the second shell EXAFS between the Fe...Fe wave and second shell Fe...N, Fe...C and/or Fe...O waves.

Complexes of mixed valent and reduced hydroxylase. The k^3 -weighted EXAFS of the mixed valent (photoreduced in the X-ray beam) samples in the presence of coupling protein and 1-bromo-1-propene are shown in Figure 3.13, and the Fourier transforms are shown in Figure 3.14. There are some differences in the EXAFS in the region between $k = 7$ and 9 \AA^{-1} . For the non-complexed hydroxylase (EXAFS2), the maximum at $k > 8 \text{ \AA}^{-1}$ is greater in amplitude than the maximum at $k < 8 \text{ \AA}^{-1}$ whereas in the samples with coupling protein (EXAFS10 and EXAFS14), the amplitude of the maximum at $k < 8 \text{ \AA}^{-1}$ is greater. In the sample with coupling protein and 1-bromo-1-propene (EXAFS16), these maxima are very close in amplitude. In addition, the minimum at $k = 9 \text{ \AA}^{-1}$ is deeper for the samples with coupling protein. In general, 1-bromo-1-propene causes little change in the EXAFS as compared to the non-complexed form.

There are also slight differences in the Fourier transforms. For example, the second shell peaks for the samples with coupling protein are less intense than for the other samples (EXAFS10 and EXAFS14). Whereas the positions of the first and second shell peaks in the complexed forms are within 0.05 Å of the noncomplexed form, the relative separation of the first and second shell peaks is slightly wider for EXAFS10 and slightly narrower for EXAFS16.

There are also differences in the complexed and uncomplexed forms of the reduced hydroxylase. The EXAFS of the reduced samples are shown in Figure 3.15, and the Fourier transforms are shown in Figure 3.16. The EXAFS of the hydroxylase in the presence of coupling protein are shifted to higher k , and the minimum at $k = \sim 8.5 \text{ \AA}^{-1}$ is more distinct in the complexed samples (EXAFS15, EXAFS19, EXAFS17). The sample with 1-bromo-1-propene is again more similar to the noncomplexed samples, but the $\sim 8.5 \text{ \AA}^{-1}$ minimum is shifted to lower k . In the Fourier transforms, the peak is located at 0.08-0.09 Å lower R for the complexed forms than for the noncomplexed forms. There is no second shell peak attributable to an Fe...Fe interaction in any of the samples.

The coupling protein has been shown to perturb the EPR spectrum of the mixed valent hydroxylases from both *M. capsulatus* (see above) and *M. trichosporium*,³³ and to change the redox potentials of the diiron center when the reductase is also present,²⁶ suggesting that the binding domain for the coupling protein is located near the active site. In addition, chemical cross-linking experiments on the *M. trichosporium* hydroxylase reveal that the α subunit, which houses the diiron center, cross-links to the coupling protein,³³ providing further evidence that the coupling protein binds close to the active site. The differences in the EXAFS of mixed valent samples complexed with the coupling protein are consistent with the coupling protein affecting the diiron site in some way. The average first shell coordination of the samples and the Fe...Fe distances are quite

similar for all the samples, however. Therefore, the EXAFS analysis cannot determine whether the differences in the presence of coupling protein result from actual changes in ligation or from distortion of the coordination environment.

The substrate 1-bromo-1-propene changes the EPR spectrum of the mixed valent hydroxylase (see above), suggesting that this substrate binds close to the diiron center. Since Br is a stronger backscatterer than Fe, an Fe-Br interaction could be detected by EXAFS if the Br were to bind within ~ 5 Å of an Fe atom. The EXAFS of the model compound $\text{Fe}(\text{3-Br-acac})_3$ exhibits a strong peak at a distance of ~ 5.2 Å,^{53,59} indicating that an Fe-Br interaction could be detectable for the protein complex. No interaction above 3.5 Å is observed for any of the samples, mixed valent or fully reduced, with 1-bromo-1propene (EXAFS11, EXAFS16, EXAFS18, EXAFS20 in Figure 3.14 and EXAFS17 and EXAFS19 in Figure 3.16). Therefore, the substrate must bind in an orientation such that the Br atom is > 5 Å from the Fe atoms. The X-ray structure reveals a hydrophobic pocket near the diiron center (Chapter 5). If 1-bromo-1-propene is oriented in this pocket with the methyl group close to the Fe atoms, the Br atom is 5-6 Å away, and therefore would not be detected by EXAFS.

First shell fits. Results of first and second shell fits to the data have been presented elsewhere,^{53,59} and will be summarized. For the mixed valent hydroxylase in the presence of coupling protein, average first shell coordinations of 6.4 N/O at 2.08 Å for EXAFS10 and 5.7 N/O at 2.08 Å for EXAFS14 were determined. In the presence of 1-bromo-1-propene, average coordinations of 5.6 N/O at 2.06 Å for EXAFS11 and 5.3 N/O at 2.07 Å for EXAFS18 and EXAFS20 were found. In the presence of both coupling protein and 1-bromo-1-propene (EXAFS16), the average coordination was 5.3 N/O at 2.07 Å. A short Fe-O distance, which would be consistent with the presence of an oxo bridged diiron center, was not present. For the reduced samples, the average coordination was

found to be 4.6 N/O at 2.11 Å in the presence of coupling protein (EXAFS15), 4.8 N/O at 2.14 Å in the presence of 1-bromo-1-propene (EXAFS19), and 4.4 N/O at 2.13 Å in the presence of both coupling protein and 1-bromo-1-propene.

Second shell fits. Since no oxo bridge is present in the hydroxylase, the hydroxo bridged model compound $[\text{Fe}_2(\text{OH})(\text{OAc})_2(\text{HB}(\text{pz})_3)_2](\text{ClO}_4)$ was used for extracting parameters to model the second shell Fe...Fe interaction. The Fe...Fe distance in the presence of coupling protein (EXAFS10 and EXAFS14) was found to be 3.39 Å. In the presence of 1-bromo-1-propene, Fe...Fe distances of 3.40 Å (EXAFS11) and 3.41 Å (EXAFS20) were determined. For the hydroxylase in the presence of both coupling protein and 1-bromo-1-propene, an Fe...Fe distance of 3.40 Å was found. Minima at ~3.0 Å were found for all the samples, and have been attributed to coincidence between the Fe-Fe and the Fe-C contributions.

Edge spectra. The edge spectra of the mixed valent samples are shown in Figure 3.17. There are three features, a low intensity feature at ~7114 eV (feature A), the main transition at ~7129 eV (feature B), and a broad maximum at ~7134 eV (feature C). In the presence of coupling protein (EXAFS10 and EXAFS16), the intensity of feature B increases, and a shoulder appears at ~7124 eV (feature A'). The intensity of the feature A increases in the presence of the coupling protein alone (EXAFS10). Upon reduction to the diferrous state (Figure 3.18), the main feature, feature B, shifts to lower energy (~7125 eV), and becomes more intense and more narrow in shape. The intensity of this peak decreases for the complexed samples, and a shoulder (feature C) at ~7131 eV appears in the presence of coupling protein. In addition, the shape of feature A changes in the presence of coupling protein (EXAFS15 and EXAFS17).

Feature A has been assigned as a formally dipole forbidden $1s \rightarrow 3d$ transition, which appears as a result of distortion from octahedral symmetry. As

seen in Figure 3.17, this feature increases in intensity for the hydroxylase - coupling protein complex (EXAFS10) as compared to the hydroxylase alone (EXAFS7), suggesting that the Fe site is more distorted in the presence of coupling protein. Feature A' is similar to features observed in Fe and Cu systems as a result of increased covalency of the metal site,^{60,61} and may imply an increased covalency in the presence of coupling protein and/or 1-bromo-1-propene. In the absence of substrate, the coupling protein and the reductase drastically change the redox potential of the diiron center, completely preventing reduction.²⁶ Since the coupling protein was added to samples before reduction, little or no conversion to the fully reduced form should be observed for these samples. The intensity difference for the main 1s→4p transition (feature B) for the mixed valent and fully reduced samples in the presence of coupling protein is indeed less than the intensity difference in the absence of coupling protein (Figure 3.19), suggesting less conversion to the reduced form. The shift of feature B to lower energy, however, clearly shows that reduction can occur in the presence of coupling protein.

As shown in Figure 3.18, the intensity of this transition is strongest for the non-complexed form (EXAFS6), followed by the 1-bromo-1-propene complex (EXAFS19), followed by the complex with both coupling protein and 1-bromo-1-propene (EXAFS17), followed by the complex with just coupling protein (EXAFS15). The redox potentials of the hydroxylase alone ($E_1^0 = 48$ mV, $E_2^0 = -135$ mV) as compared to the redox potentials in the presence of propylene ($E_1^0 = 30$ mV, $E_2^0 = -156$ mV) are consistent with slightly more difficult reduction in the presence of substrate. The fact that EXAFS15 exhibits the weakest main transition is also consistent with strong inhibition in the presence of coupling protein. According to the redox study, however, reduction is greatly facilitated

in the presence of both substrate and the coupling reductase proteins,²⁶ which would predict that the main transition should be more intense for EXAFS17.

VI. Conclusions

The results of the spectroscopic experiments can be interpreted in terms of the model shown in Figure 3.21. The lack of an optical spectrum above 300 nm together with the absence of a short Fe-O distance in the EXAFS spectrum, indicate that the two Fe atoms are neither bridged by an oxo exogenous ligand nor coordinated by a tyrosine phenolate. The spectroscopic data are more consistent with a hydroxo bridge connecting the two Fe atoms, which have an Fe...Fe distance of 3.4 Å in the oxidized and mixed valent forms. This Fe...Fe distance also implies the existence of at least one other bridging group, probably a carboxylate. No Fe...Fe backscattering was observed for the fully reduced form. The presence of a hydroxo bridge in the mixed valent form has recently been established by proton ENDOR studies.⁵⁴

The iron atoms are also coordinated by a mixture of nitrogen and oxygen donors with average Fe-O/N distances of 2.04 Å for the oxidized form, 2.06-2.08 Å for the mixed valent form, and 2.15 Å for the fully reduced form. The average first shell coordination of oxyhemerythrin, which contains 5 histidine ligands, consists of 5 N/O at 2.15 -2.16 Å whereas the ribonucleotide reductase R2 protein, which contains just 2 histidine ligands, has a first shell coordination of 5 N/O at 2.04-2.06 Å.³ The average distance in the oxidized hydroxylase of 2.04 Å suggests that, like the R2 protein, the diiron center in the hydroxylase contains more oxygen and fewer nitrogen donor atoms than oxyhemerythrin. The results of the ESEEM experiments further support the existence of two coordinated histidine residues. The ENDOR study revealed the presence of another exogenous ligand, a terminal water or hydroxo coordinated to one of the Fe

atoms.⁵⁴ Finally, the Mössbauer parameters are also consistent with the structure shown in Figure 3.21.

The effects of N_3^- , of the substrate 1-bromo-1-propene, and of the coupling protein on the spectroscopic properties of the diiron center were also investigated. The addition of N_3^- did produce an optical feature at ~ 436 nm, which is consistent with recent reports of F^- and N_3^- binding to the hydroxylase,^{20,21} and of N_3^- binding to the diferrous R2 protein.²² Whereas 1-bromo-1-propene affects the EPR spectrum of the mixed valent hydroxylase, no significant change in the coordination environment is seen by EXAFS. The absence of Fe-Br backscattering suggests that the 1-bromo-1-propenes binds with the Br atom > 5 Å from the diiron core. The coupling protein also perturbs the EPR spectrum of the mixed valent hydroxylase, and produces detectable changes in the EXAFS. The origin of these differences cannot be determined by EXAFS, but possibilities include distortion of the iron environment, changes in coordination of the Fe atoms, or a change in covalency of the diiron center, which is suggested by the presence of a shoulder in the edge data. Finally, the edge data show that reduction to the diferrous form does occur in the presence of the coupling protein, although it is likely that the potential is lowered since some inhibition is observed.

References

- (1) Woodland, M. P.; Patil, D. S.; Cammack, R.; Dalton, H. *Biochim. Biophys. Acta* **1986**, *873*, 237-242.
- (2) Fox, B. G.; Surerus, K. K.; Münck, E.; Lipscomb, J. D. *J. Biol. Chem.* **1988**, *263*, 10553-10556.
- (3) Que, L., Jr.; True, A. E. *Prog. Inorg. Chem.* **1990**, *38*, 97-200.
- (4) Vincent, J. B.; Olivier-Lilley, G. L.; Averill, B. A. *Chem. Rev.* **1990**, *90*, 1447-1467.
- (5) Stenkamp, R. E.; Sieker, L. C.; Jensen, L. H. *J. Am. Chem. Soc.* **1984**, *106*, 618-622.
- (6) Sheriff, S.; Hendrickson, W. A.; Smith, J. L. *J. Mol. Biol.* **1987**, *197*, 273-296.
- (7) Nordlund, P.; Sjöberg, B.-M.; Eklund, H. *Nature* **1990**, *345*, 593-598.
- (8) Nordlund, P.; Eklund, H. *J. Mol. Biol.* **1993**, *231*, 123-164.
- (9) Woodland, M. P.; Dalton, H. *J. Biol. Chem.* **1984**, *259*, 53-59.
- (10) Ericson, A.; Hedman, B.; Hodgson, K. O.; Green, J.; Dalton, H.; Bentsen, J. G.; Beer, R. H.; Lippard, S. J. *J. Am. Chem. Soc.* **1988**, *110*, 2330.
- (11) Hedman, B.; Co, M. S.; Armstrong, W. H.; Hodgson, K. O.; Lippard, S. J. *Inorg. Chem.* **1986**, *25*, 3708-3711.
- (12) Armstrong, W. H.; Lippard, S. J. *J. Am. Chem. Soc.* **1983**, *105*, 4837-4838.
- (13) Armstrong, W. A.; Spool, A.; Papaefthymiou, G. C.; Frankel, R. B.; Lippard, S. J. *J. Am. Chem. Soc.* **1984**, *106*, 3653-3667.
- (14) Armstrong, W. H.; Lippard, S. J. *J. Am. Chem. Soc.* **1984**, *106*, 4632-4633.
- (15) Feng, X.; Lippard, S. J., unpublished results.
- (16) Patel, R. N.; Savas, J. C. *J. Bacteriol.* **1987**, *169*, 2313-2317.
- (17) DeWitt, J. G.; Bentsen, J. G.; Rosenzweig, A. C.; Hedman, B.; Green, J.; Pilkington, S.; Papaefthymiou, G. C.; Dalton, H.; Hodgson, K. O.; Lippard, S. J. *J. Am. Chem. Soc.* **1991**, *113*, 9219-9235.

- (18) Stryer, L. In *Biochemistry* W. H. Freeman and Company: New York, 1988; pp 413.
- (19) Sanders-Loehr, J. In *Iron Carriers and Iron Proteins* VCH Publishers, Inc.: New York, 1989; pp 373-466.
- (20) Atta, M.; Fontecave, M.; Wilkins, P. C.; Dalton, H. *Eur. J. Biochem.* **1993**, *217*, 217-223.
- (21) Hamman, S.; Atta, M.; Ehrenberg, A.; Wilkins, P.; Dalton, H.; Beguin, C.; Fontecave, M. *Biochem. Biophys. Res. Commun.* **1993**, *195*, 594-599.
- (22) Elgren, T.; Hendrich, M.; L. Que, J. J. *Inorg. Biochem.* **1993**, *51*, 492.
- (23) Aberg, A. Ph. D. Thesis, Stockholm University, 1993.
- (24) Andersson, K. K.; Elgren, T. E.; L. Que, J.; Lipscomb, J. D. *J. Am. Chem. Soc.* **1992**, *114*, 8711-8713.
- (25) Aasa, R.; Vänngård, T. *J. Magn. Reson.* **1975**, *19*, 308-315.
- (26) Liu, K. E.; Lippard, S. J. *J. Biol. Chem.* **1991**, *266*, 12836-12839.
- (27) Borovik, A. S.; Hendrich, M. P.; Holman, T. R.; Münck, E.; Papaefthymiou, V.; L. Que, J. J. *Am. Chem. Soc.* **1990**, *112*, 6031-6038.
- (28) Tolman, W. B.; Liu, S.; Bentsen, J. G.; Lippard, S. J. *J. Amer. Chem. Soc.* **1991**, *113*, 152-164.
- (29) Hendrich, M. P.; Münck, E.; Fox, B. G.; Lipscomb, J. D. *J. Am. Chem. Soc.* **1990**, *112*, 5861-5865.
- (30) Nocek, J. M.; D. M. Kurtz, J.; Sage, J. T.; Debrunner, P. G.; Maroney, M. I.; L. Que, J. J. *Am. Chem. Soc.* **1985**, *107*, 3382.
- (31) Arciero, D. M.; Lipscomb, J. D.; Huynh, B. H.; Kent, T. A.; Münck, E. *J. Biol. Chem.* **1983**, *258*, 14981-14991.
- (32) Salerno, J. C.; Siedow, J. N. *Biochim. Biophys. Acta* **1979**, *579*, 246-251.
- (33) Fox, B. G.; Liu, Y.; Dege, J. E.; Lipscomb, J. D. *J. Biol. Chem.* **1991**, *266*, 540-550.

- (34) McCracken, J.; Peisach, J.; Dooley, D. M. *J. Am. Chem. Soc.* **1987**, *109*, 4064-4072.
- (35) Mims, W. B. *Rev. Sci. Instrum.* **1974**, *45*, 1583-1591.
- (36) Kevan, L. In *Time Domain Electron Spin Resonance*; L. Kevan and R. N. Schwartz, Ed.; John Wiley and Sons: New York, 1979.
- (37) Mims, W. B.; Peisach, J. In *Biological Magnetic Resonance*; L. J. Berliner and J. Reuben, Ed.; Plenum Press: New York, 1981.
- (38) Peisach, J.; Mims, W. B.; Davis, J. L. *J. Biol. Chem.* **1979**, *254*, 12379-12389.
- (39) Cammack, R.; Chapman, A.; McCracken, J.; Cornelius, J. B.; Peisach, J.; Weiner, J. H. *Biochim. Biophys. Acta* **1988**, *956*, 307-312.
- (40) Antanaitis, B. C.; Peisach, J.; Mims, W. B.; Aisen, P. *J. Biol. Chem.* **1985**, *260*, 4572-4574.
- (41) Mims, W. B.; Peisach, J. *J. Chem. Phys.* **1978**, *69*, 4921-4930.
- (42) Ashby, C. I. H.; Cheng, C. P.; Brown, T. L. *J. Am. Chem. Soc.* **1978**, *100*, 6057-6063.
- (43) Hunt, K. J.; Mackay, A. L. *J. Mag. Res.* **1976**, *22*, 295-301.
- (44) LoBrutto, R.; Haley, P. E.; Yu, C.; Ohnishi, T. In *Advances in Membrane Biochemistry and Bioenergetics*; C. H. Kim, H. Tedeschi, J. J. Diwan and J. C. Salerno, Ed.; Plenum Press: New York, 1987; pp 449-458.
- (45) Hendrich, M. P.; Fox, B. G.; Andersson, K. K.; Debrunner, P. G.; Lipscomb, J. D. *J. Biol. Chem.* **1992**, *267*, 261-269.
- (46) Kurtz, D. M. *Chem. Rev.* **1990**, *90*, 585-606.
- (47) Fox, B. G.; Hendrich, M. P.; Surerus, K. K.; Andersson, K. K.; Froland, W. A.; Lipscomb, J. D.; Münck, E. *J. Am. Chem. Soc.* **1993**, *115*, 3688-3701.
- (48) Cramer, S. P.; Tench, O.; Yocum, M.; George, G. N. *Nucl. Instrum. Methods Phy. Res.* **1988**, *A266*, 586-591.

- (49) Scott, R. A.; Hahn, J. E.; Doniach, S.; Freeman, H. C.; Hodgson, K. O. *J. Am. Chem. Soc.* **1982**, *104*, 5364-5369.
- (50) Johansson, L. *Chem. Scr.* **1976**, *9*, 30-35.
- (51) Iball, J.; Morgan, C. H. *Acta Cryst.* **1976**, *23*, 239-244.
- (52) Roof, R. B. *Acta Cryst.* **1956**, *9*, 781-786.
- (53) DeWitt, J. G. Ph. D. Thesis, Stanford University, 1992.
- (54) DeRose, V.; Liu, K. E.; Lippard, S. J.; Hoffman, B. J. *Am. Chem. Soc.* **1993**, *115*, 6440-6441.
- (55) Zhang, K.; Stern, E. A.; Ellis, F.; Sanders-Loehr, J.; Shiemke, A. K. *Biochemistry* **1988**, *27*, 7470-7479.
- (56) Elam, W. T.; Stern, E. A.; McCallum, J. D.; Sanders-Loehr, J. J. *Am. Chem. Soc.* **1983**, *105*, 1919-1923.
- (57) Co, M. S.; Hodgson, K. O. *J. Am. Chem. Soc.* **1981**, *103*, 3200-3201.
- (58) Kauzlarich, S. M.; Teo, B. K.; Zirino, T.; Burman, S.; Davis, J. C.; Averill, B. *A. Inorg. Chem.* **1986**, *25*, 2781-2785.
- (59) DeWitt, J. G.; Rosenzweig, A. C.; Hedman, B.; Lippard, S. J.; Hodgson, K. O., manuscript in preparation.
- (60) Shulman, R. G.; Yafet, Y.; Eisenberger, P.; Blumberg, W. E. *Proc. Natl. Acad. Sci. USA* **1976**, *73*, 1384-1388.
- (61) Kau, L.-S.; Spira-Solomon, D. J.; Penner-Hahn, J. E.; Hodgson, K. O.; Solomon, E. I. *J. Am. Chem. Soc.* **1987**, *109*, 6433-6442.

Table 3.1 EXAFS sample summary

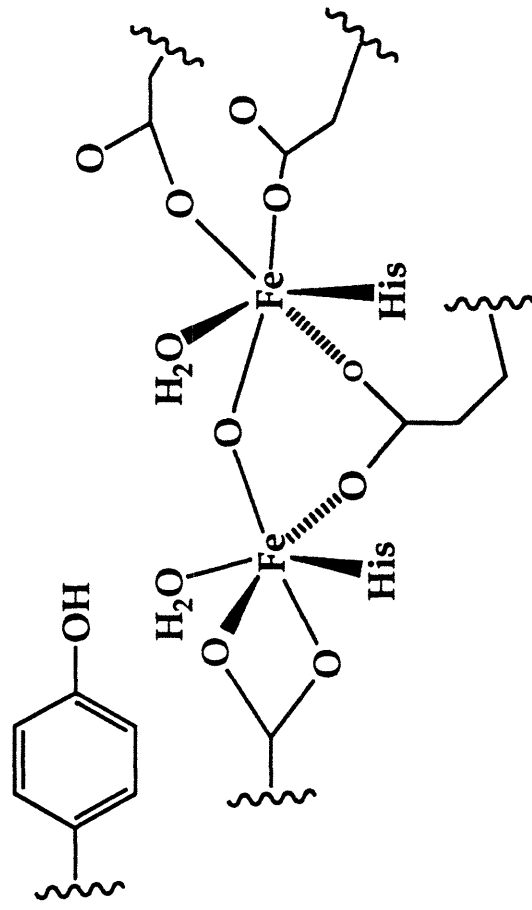
Sample	Description	[Protein] (mg/ml; mM hydroxylase)	[Fe] (mM)	Experiment; Result
EXAFS2 ^a	Oxidized hydroxylase			EXAFS and edge; sample photoreduced
EXAFS3 ^a	Fully reduced hydroxylase			EXAFS and edge
EXAFS4 ^a	Oxidized <i>M. trichosporium</i> hydroxylase			EXAFS and edge; sample photoreduced; similar to <i>M. capsulatus</i> data
EXAFS5 ^b	Oxidized hydroxylase			EXAFS and edge; sample did not photoreduce
EXAFS6 ^c	Fully reduced hydroxylase	710; 2.8	5.1	
EXAFS7 ^d	Oxidized hydroxylase	422; 1.7	3.4	EXAFS only; sample photoreduced
EXAFS8 ^d	Oxidized hydroxylase	415; 1.7	3.1	Sample not used due to low volume
EXAFS9 ^d	Oxidized hydroxylase	403; 1.6	1.9	Edge only; sample photoreduced
EXAFS10 ^d	Oxidized hydroxylase + 2 molar equivalents protein B	431	2.0	EXAFS and edge; sample photoreduced; EXAFS and FT different from that of semimet hydroxylase alone

EXAFS11 ^d	Oxidized hydroxylase + 1-bromo-1-propene	390; 1.6	3.2	EXAFS and edge; sample photoreduced; data identical to photoreduced hydroxylase with no substrate
EXAFS12 ^d	Oxidized hydroxylase + 2 molar equivalents protein B	364	1.5	Sample not used due to protein precipitation
EXAFS13 ^d	Oxidized hydroxylase + pentane	383; 1.5	2.8	Sample photoreduced; not enough data for a photoreduced data set
EXAFS14 ^e	Oxidized hydroxylase + 2 molar equivalents protein B	??	??	EXAFS and edge; sample photoreduced; EXAFS and FT similar to that of semiment hydroxylase alone; edge different
EXAFS15 ^e	Fully reduced hydroxylase + 2 molar equivalents protein B	343	0.9	EXAFS and edge; EXAFS, FT, and edge similar to that of reduced hydroxylase alone
EXAFS16 ^e	Oxidized hydroxylase + 2 molar equivalents protein B + 1-bromo-1-propene	290	1.2	EXAFS and edge; sample photoreduced; EXAFS and edge similar to that of reduced hydroxylase alone
EXAFS17 ^e	Fully reduced hydroxylase + 2 molar equivalent protein B + 1-bromo-1-propene	245	1.6	EXAFS and edge; EXAFS, FT, and edge similar to that of reduced hydroxylase alone

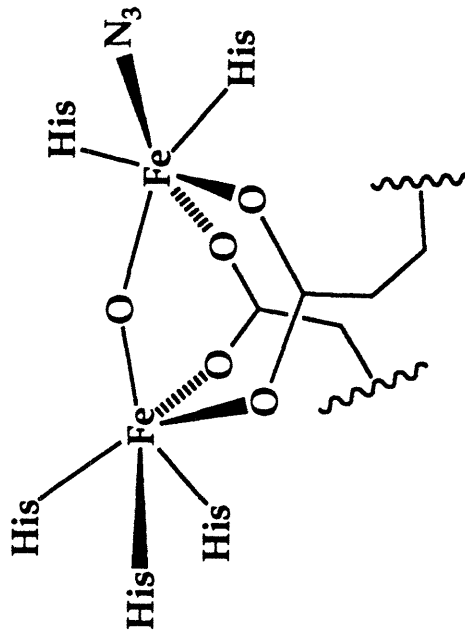
EXAFS18 ^e	Oxidized hydroxylase + 1-bromo-1-propene	338;1.3	1.8	EXAFS and edge; sample photoreduced; data identical to that of photoreduced hydroxylase with no substrate
EXAFS19 ^e	Fully reduced hydroxylase + 1-bromo-1-propene	294; 1.2	1.7	EXAFS and edge; EXAFS, edge, and FT similar to that of reduced hydroxylase alone
EXAFS20 ^e	Oxidized hydroxylase + 1-bromo-1-propene	1274; 5.0	1.9	EXAFS and edge; sample photoreduced; EXAFS, FT, and edge similar to that of photoreduced hydroxylase with no substrate

^aData collected Nov. 1987 at SSRL beamline 4-2. ^bData collected June 1989 at NSLS beamline X19A and Sept. 1989 at NSLS beamline X19A. ^cData collected Sept. 1989 at NSLS beamline X19A. ^dData collected Aug./Sept. 1991 at SSRL beamline 7-3. ^eData collected March 1992 at SSRL beamline 7-3.

Figure 3.1 Crystallographically characterized dinuclear iron proteins.



Ribonucleotide Reductase
R2 protein
Tyrosyl Radical Generation



Hemerythrin
O₂ Transport

Figure 3.2 Optical spectrum of the hydroxylase (1 mg/ml).

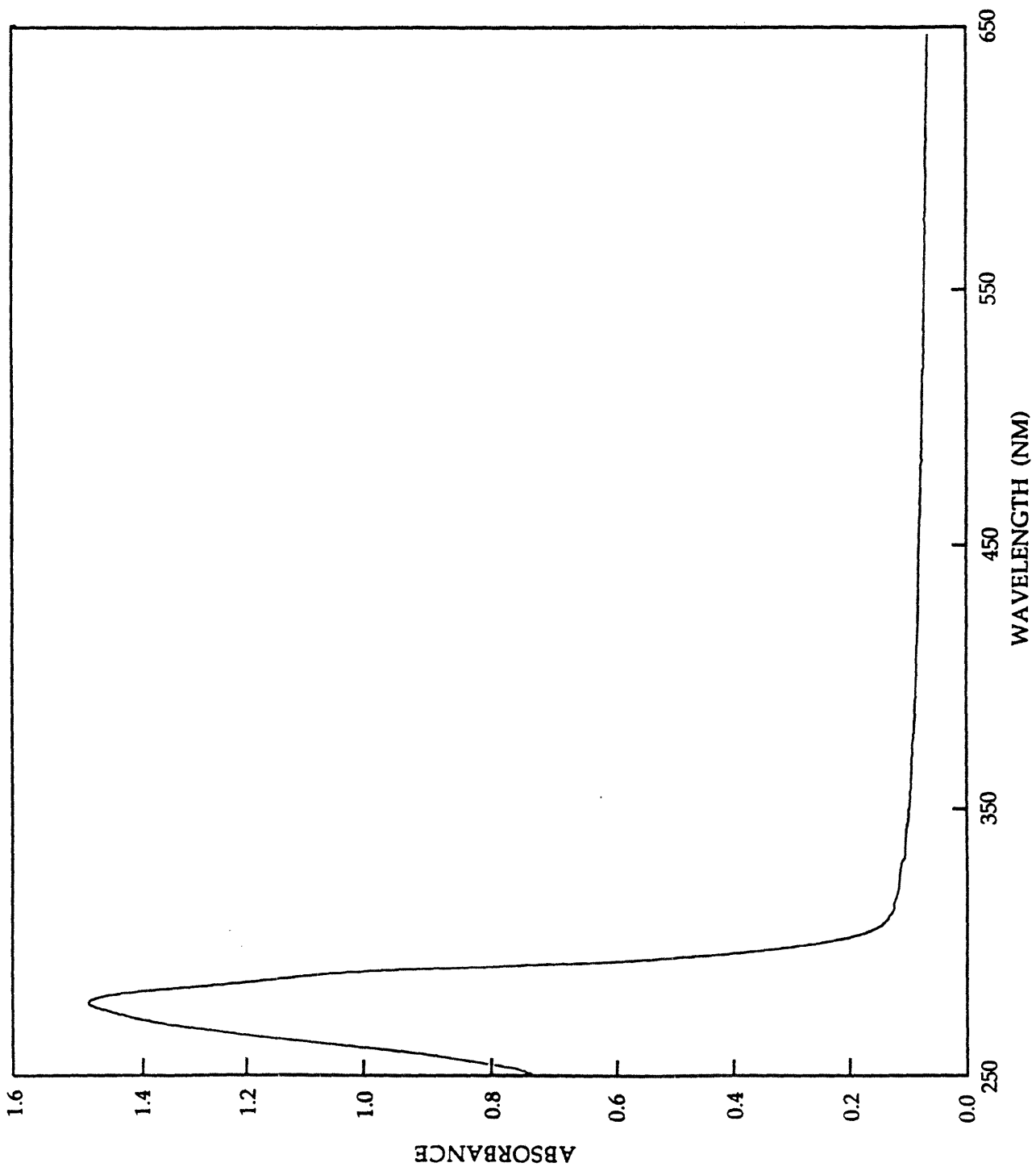


Figure 3.3 Top: effects of N_3^- on the optical spectrum of the oxidized hydroxylase. Bottom: difference absorption spectra. (a) $[\text{N}_3^-] = 0$, (b) $[\text{N}_3^-] = 2.1 \text{ mM}$, (c) $[\text{N}_3^-] = 10.5 \text{ mM}$, (d) $[\text{N}_3^-] = 21 \text{ mM}$, (e) $[\text{N}_3^-] = 52.5 \text{ mM}$, (f) $[\text{N}_3^-] = 105 \text{ mM}$, (g) $[\text{N}_3^-] = 210 \text{ mM}$, (h) $[\text{N}_3^-] = 420 \text{ mM}$.

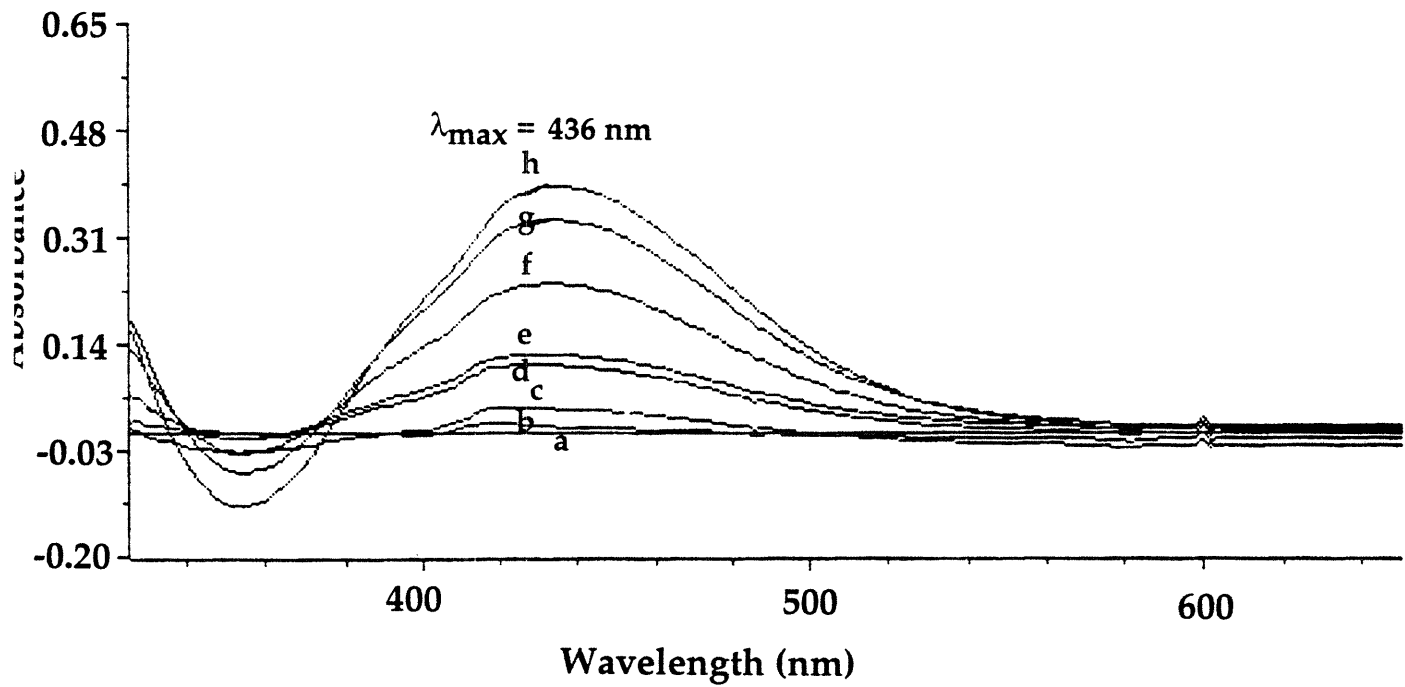
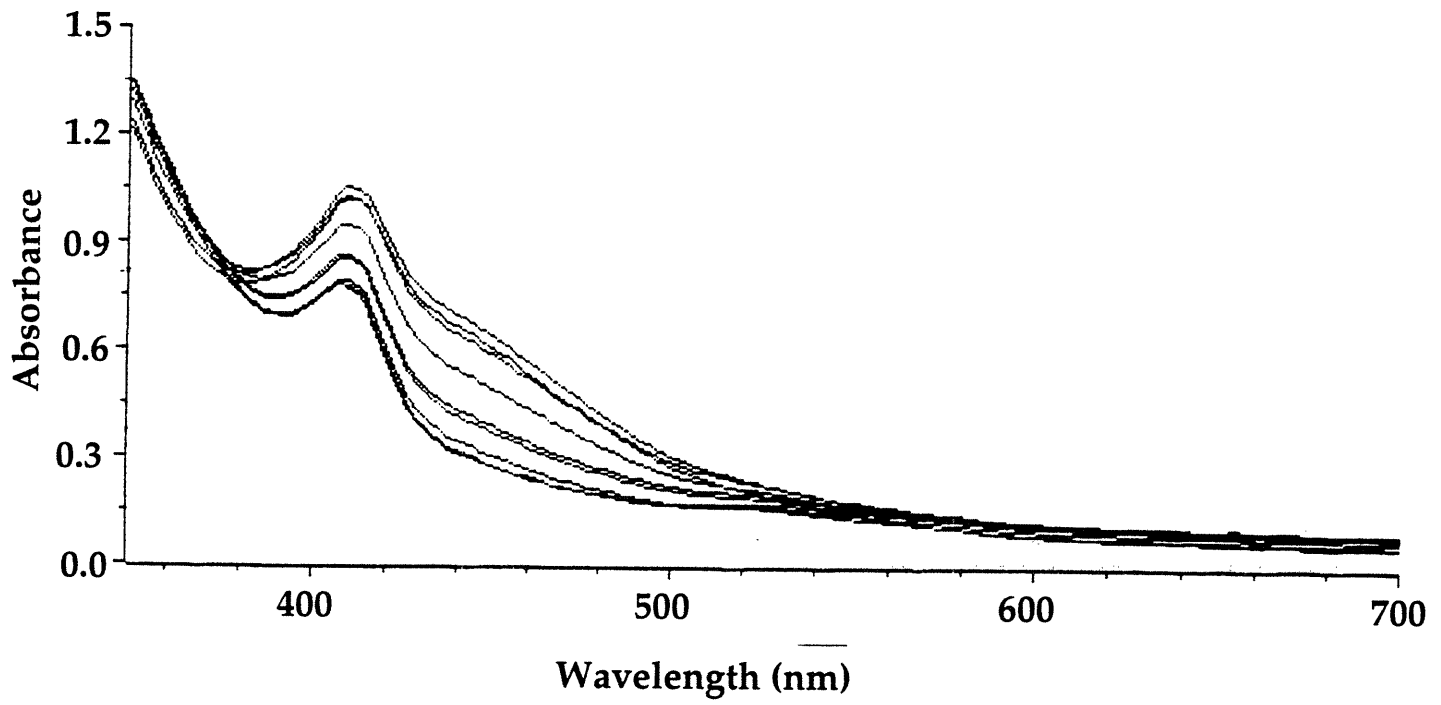


Figure 3.4 X-band EPR spectra of the hydroxylase (42 mg/ml, 166 μ M, 1.7 Fe/protein): (a) oxidized, 1 mW, (b) mixed valent, 1 mW, (c) fully reduced, 50 mW. Instrumental conditions were: scan range, 600 mT; field set, 305 mT; time constant, 83 ms; modulation amplitude, 8.0 mT; modulation frequency, 100 kHz; scan time, 3 min; microwave frequency, 9.44 GHz; T \approx 9 K.

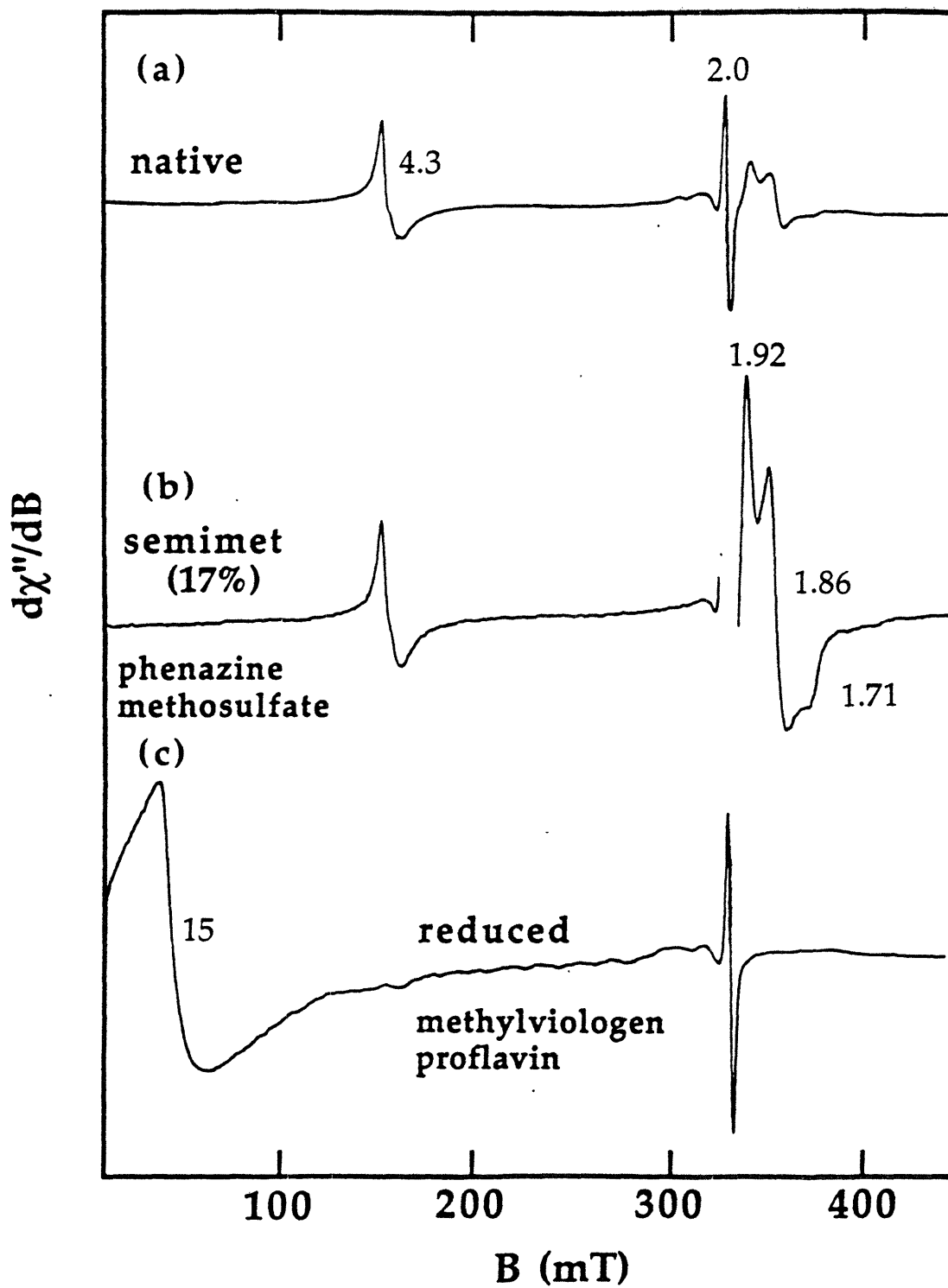


Figure 3.5 EPR spectrum of the mixed valent hydroxylase in the presence of a 2-fold molar excess of coupling protein. Instrumental conditions were: gain, 2×10^4 ; scan range, 200 mT; field set, 370 mT; time constant, 40.91 ms; modulation amplitude, 0.7 mT; modulation frequency, 100 kHz; scan time, 83.80 s; microwave frequency, 9.41 GHz; $T \approx 9.0$ K. (A) 10 mW, (B) 100 mW.

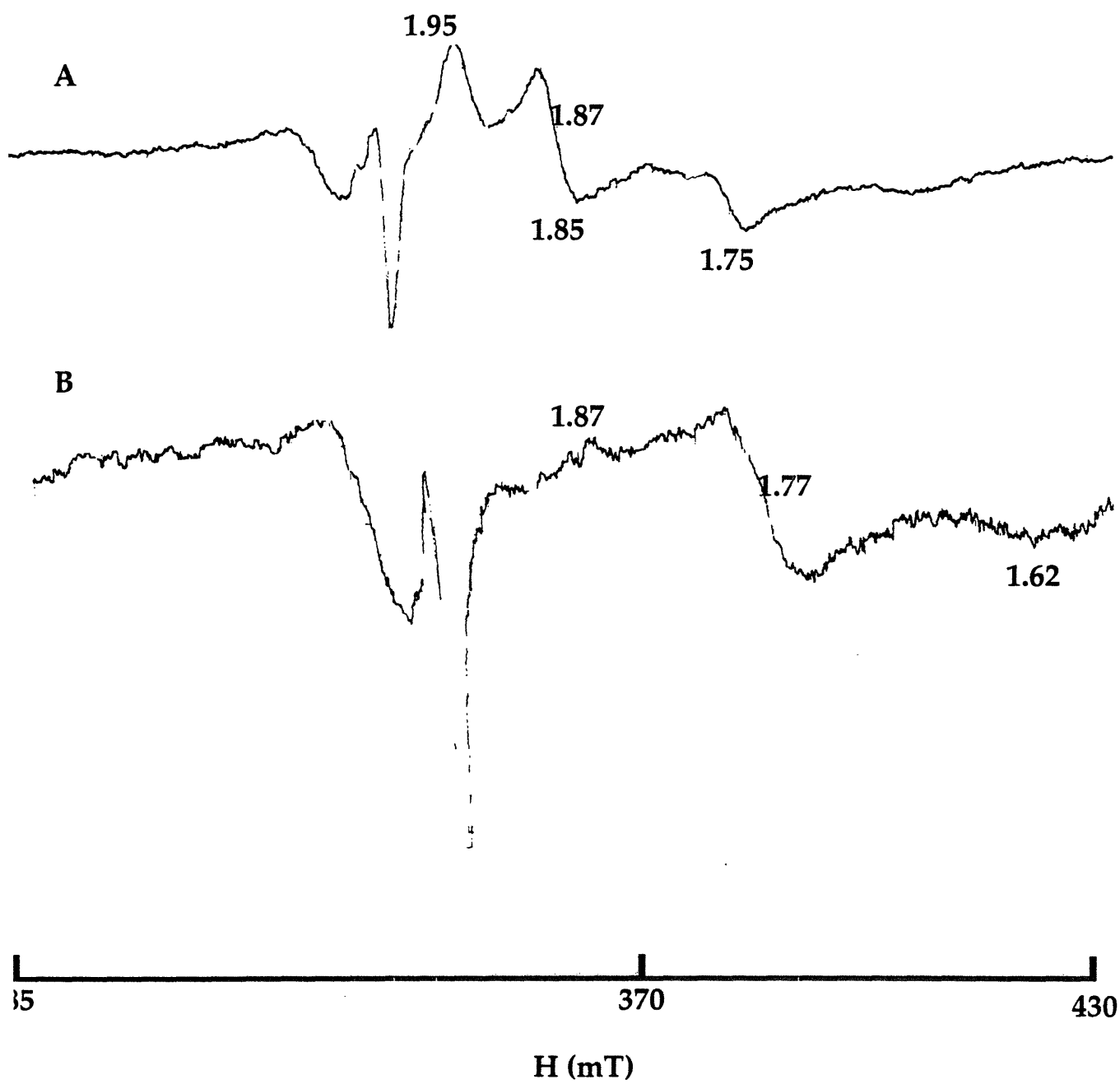


Figure 3.6 (A) EPR spectrum of the mixed valent hydroxylase. (B) EPR spectrum of the mixed valent hydroxylase in the presence of a 500-fold molar excess of 1-bromo-1-propene. Instrumental conditions were: gain, 2×10^4 ; scan range, 200 mT; field set, 370 mT; time constant, 40.91 ms; modulation amplitude, 0.7 mT; modulation frequency, 100 kHz; scan time, 83.89 s; microwave frequency, 9.41 GHz; $T \approx 9.0$ K; power, 100 μ W.

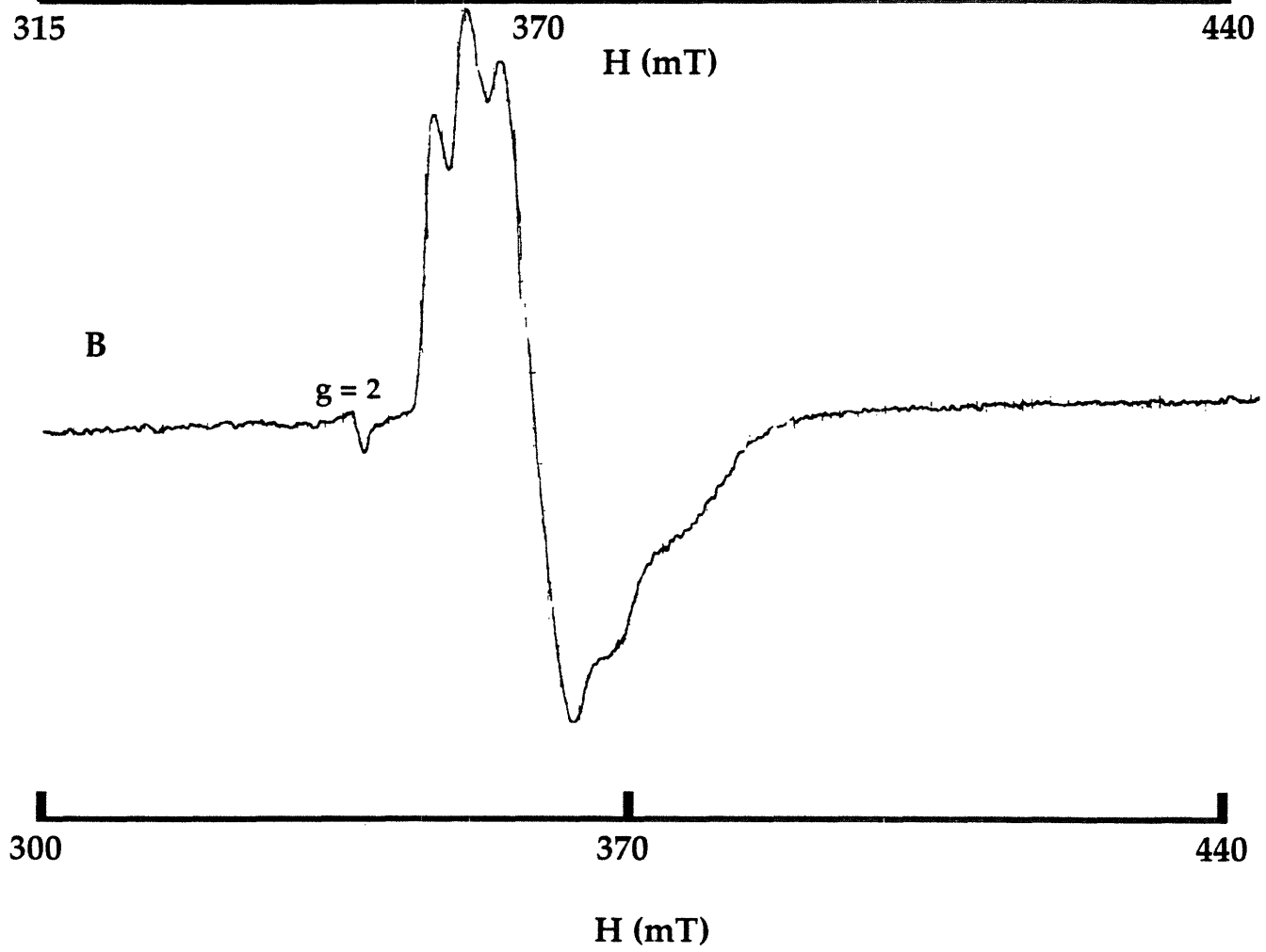
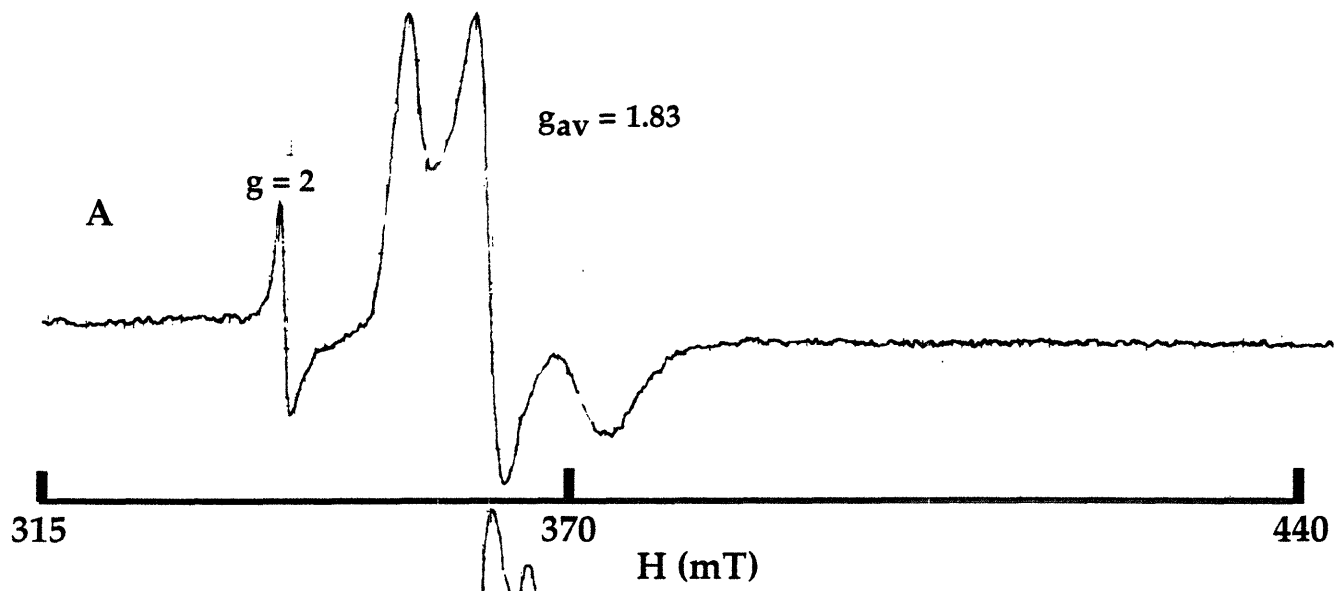


Figure 3.7 Three pulse ESE modulation (inset) and the cosine FT spectra of the hydroxylase at three g -values. Instrumental conditions: microwave frequency 8.9 GHz; $\tau = 135$ ns; $T \approx 10$ K.

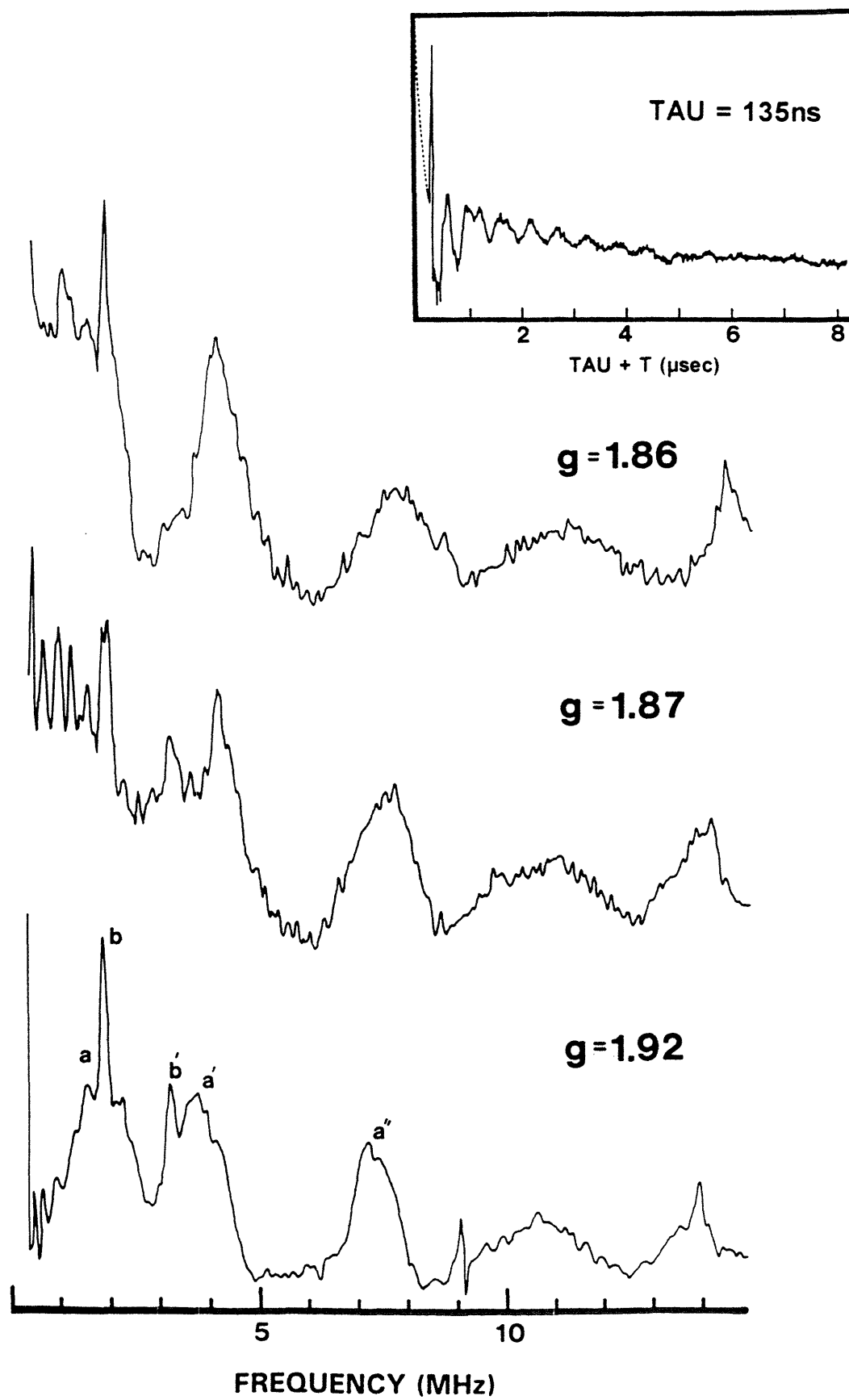
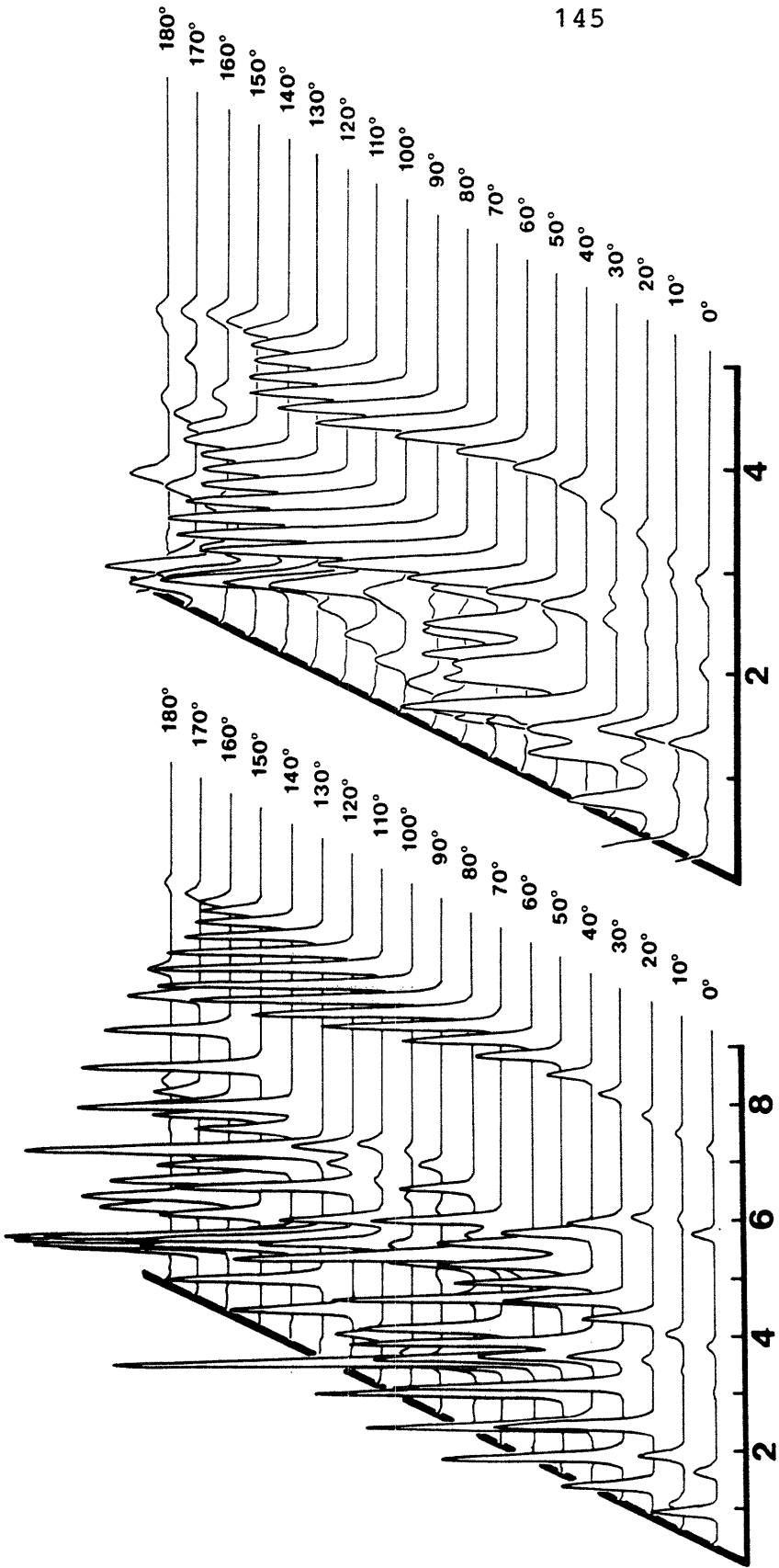


Figure 3.8 FT spectral simulations (at $g = 1.92$) of a single ^{14}N having a contact interaction of 5 MHz (left) and 0.8 MHz (right). Variation of the quadrupolar Euler angle ξ_2 (corresponding to the relative orientation of the y-axes) demonstrates that the experimentally observed simplified spectrum at $g = 1.92$ can be obtained only for a limited range of ξ_2 (40-80°).



FREQUENCY (MHZ)

FREQUENCY (MHZ)

Figure 3.9 Mössbauer spectra of the hydroxylase at 80 K and zero applied field (282 mg/ml, 0.6 mM, 1.3 Fe/protein): (a) oxidized, (b) fully reduced. Cells grown on ^{57}Fe enriched media.

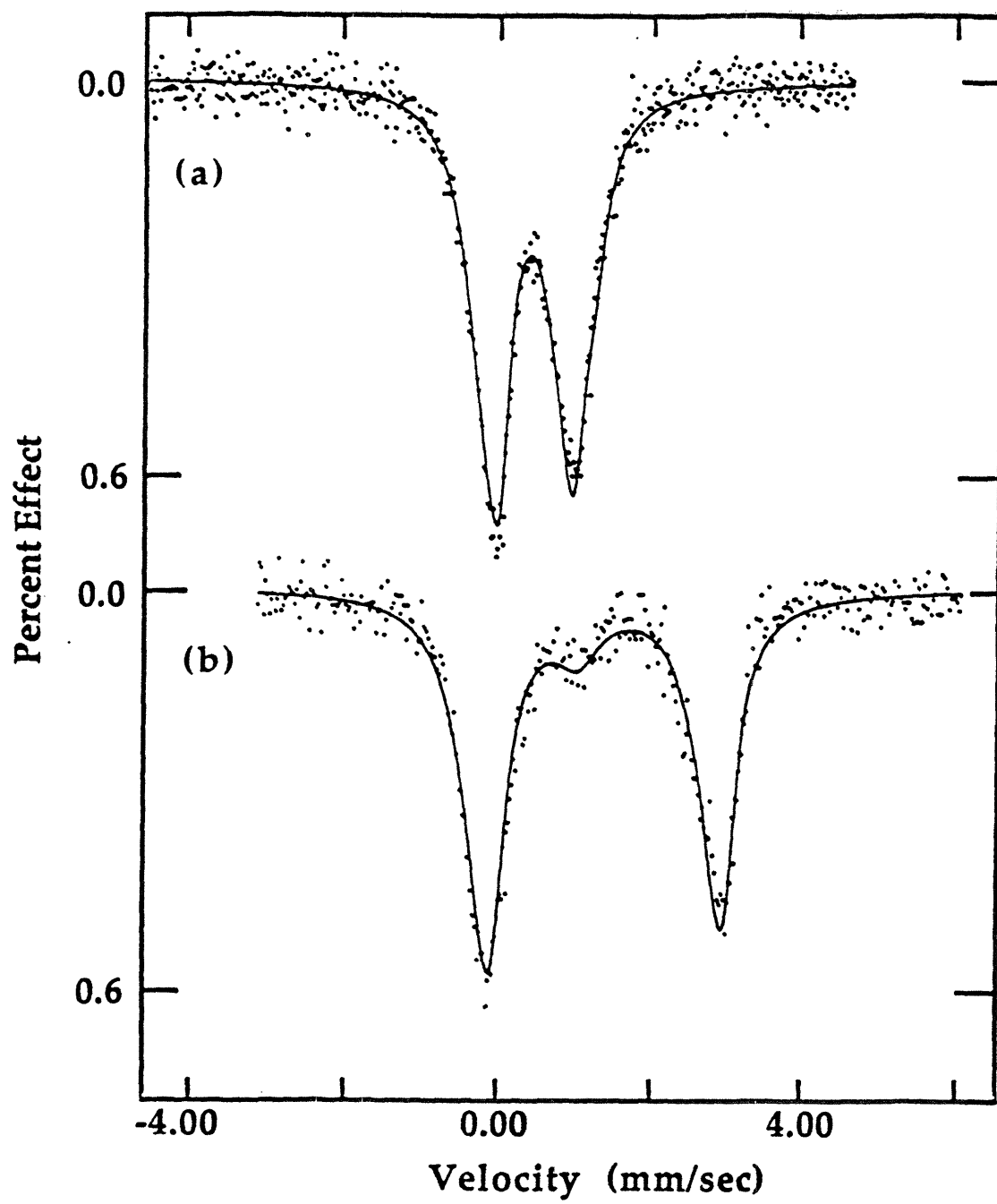


Figure 3.10 Fe K X-ray absorption edge position of the diferric (solid), photoreduced mixed valent (dash dot), and diferrous (dash) hydroxylase.

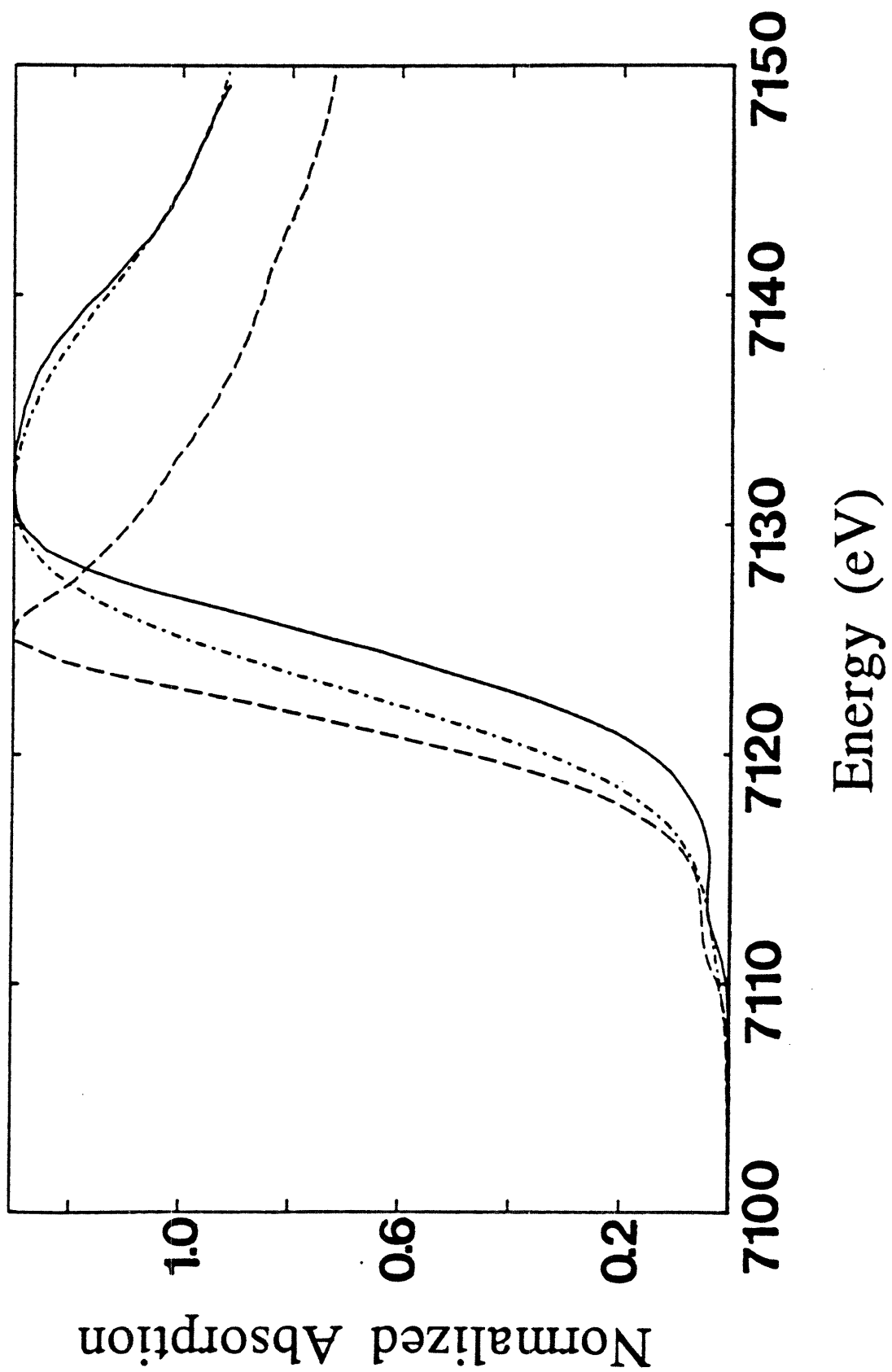


Figure 3.11 EXAFS data of the hydroxylase and dinuclear iron model compounds: (a) $[\text{Fe}_2\text{O}(\text{OAc})_2(\text{HBpz}_3)_2]$, (b) $[\text{Fe}_2\text{OH}(\text{OAc})_2(\text{HBpz}_3)_2]\text{ClO}_4$ (c) EXAFS5, (d) EXAFS2, (e) EXAFS4, (f) EXAFS3, (g) EXAFS6, (h) $\text{Fe}_2\text{O}(\text{O}_2\text{CH})_4(\text{BIPhMe})_2$.

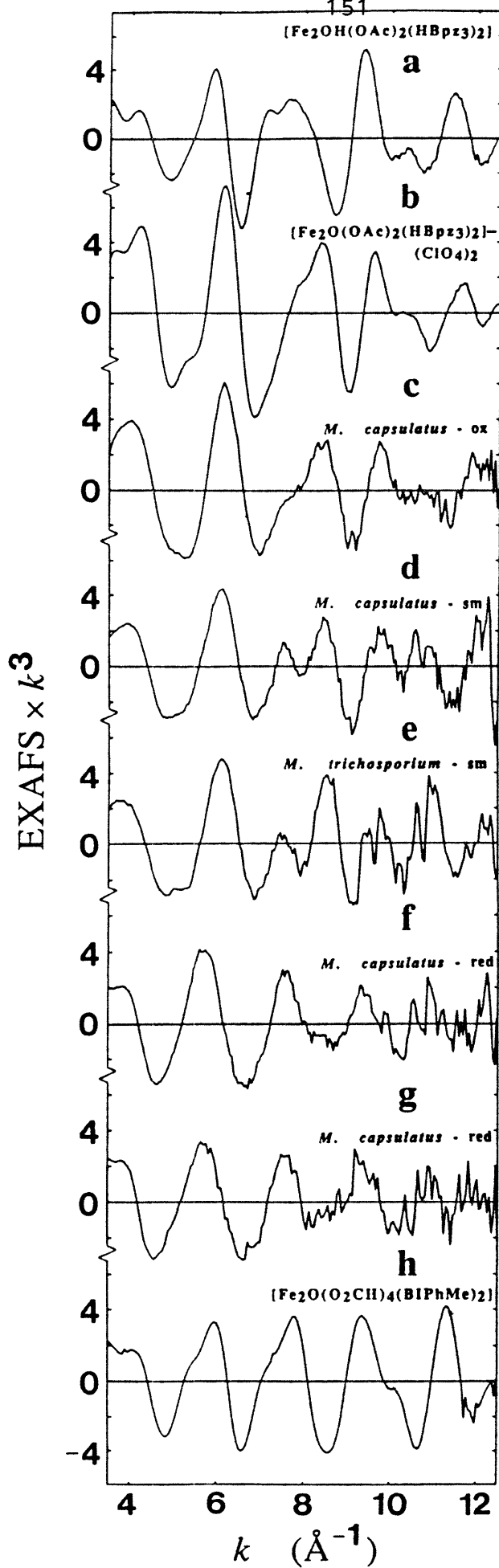


Figure 3.12 Fourier transforms of the EXAFS data shown in Figure 3.11 (c)-(h). (a) EXAFS5, (b) EXAFS2, (c) EXAFS4, (d) EXAFS3, (e) EXAFS6, (f) $\text{Fe}_2\text{O}(\text{O}_2\text{CH})_4(\text{BIPhMe})_2$. The bars on the figure represent the data backtransformed to R space for first (solid), second (dash), and wide shell (dot) fits.

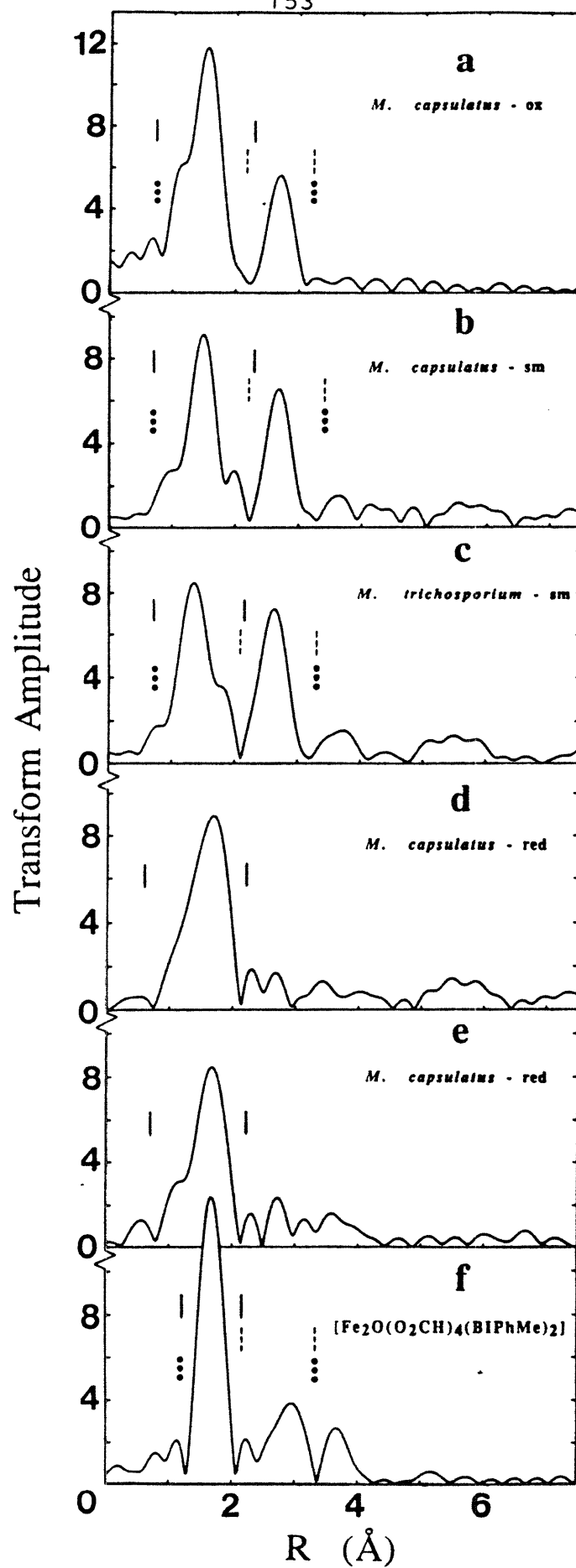


Figure 3.13 EXAFS data for the mixed valent (photoreduced) hydroxylase samples. (a) Mixed valent hydroxylase sample **EXAFS2**; in the presence of coupling protein: (b) **EXAFS10**, (c) **EXAFS14**; in the presence of 1-bromo-1-propene: (d) **EXAFS11**, (e) **EXAFS 18**, (f) **EXAFS20**; in the presence of both coupling protein and 1-bromo-1-propene: (g) **EXAFS16**.

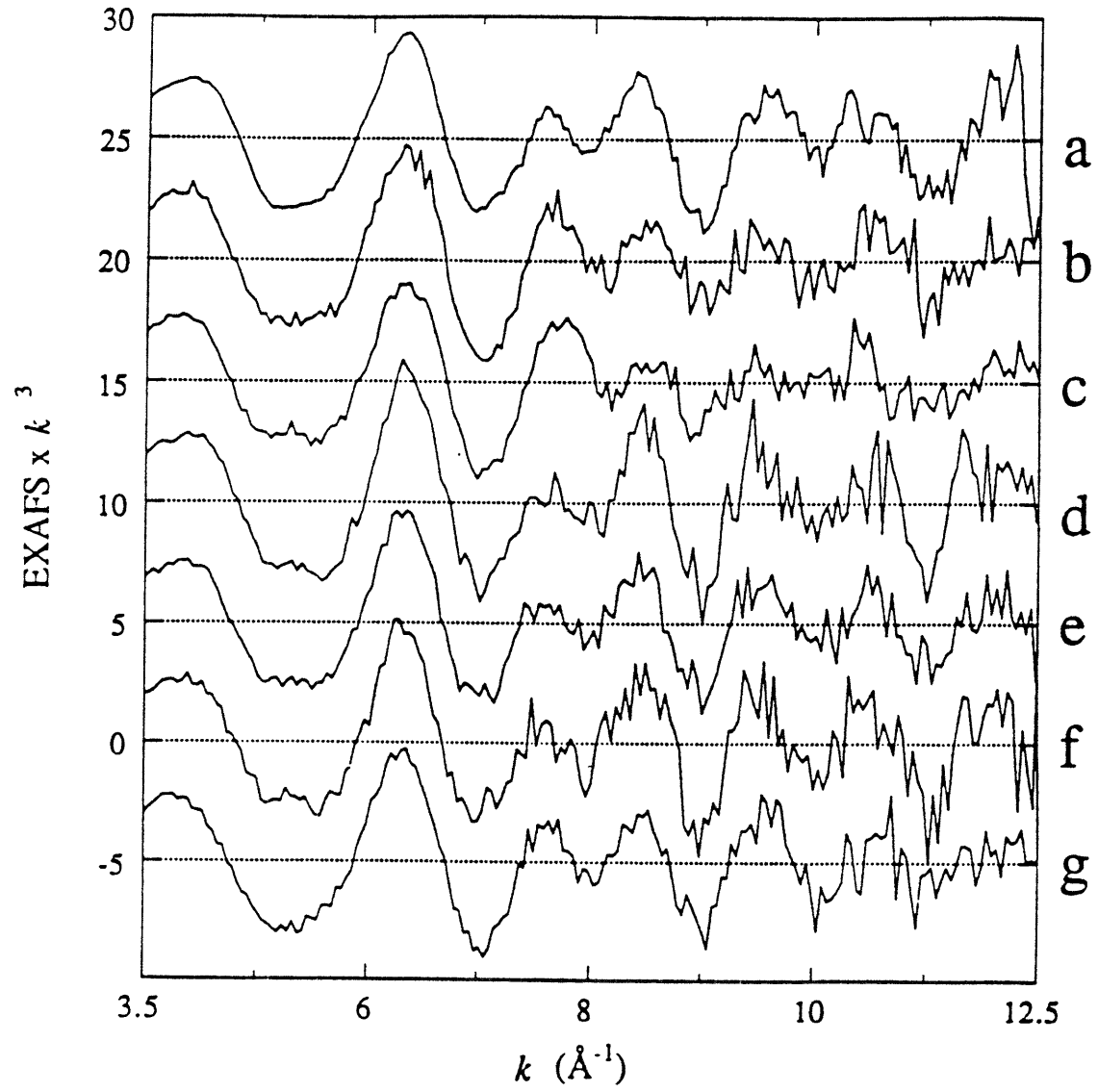


Figure 3.14 Fourier transforms of mixed valent hydroxylase EXAFS data shown in Figure 3.13. (a) Mixed valent hydroxylase sample EXAFS2; in the presence of coupling protein: (b) EXAFS10, (c) EXAFS14; in the presence of 1-bromo-1-propene: (d) EXAFS11, (e) EXAFS18, (f) EXAFS20; in the presence of coupling protein and 1-bromo-1-propene: (g) EXAFS16.

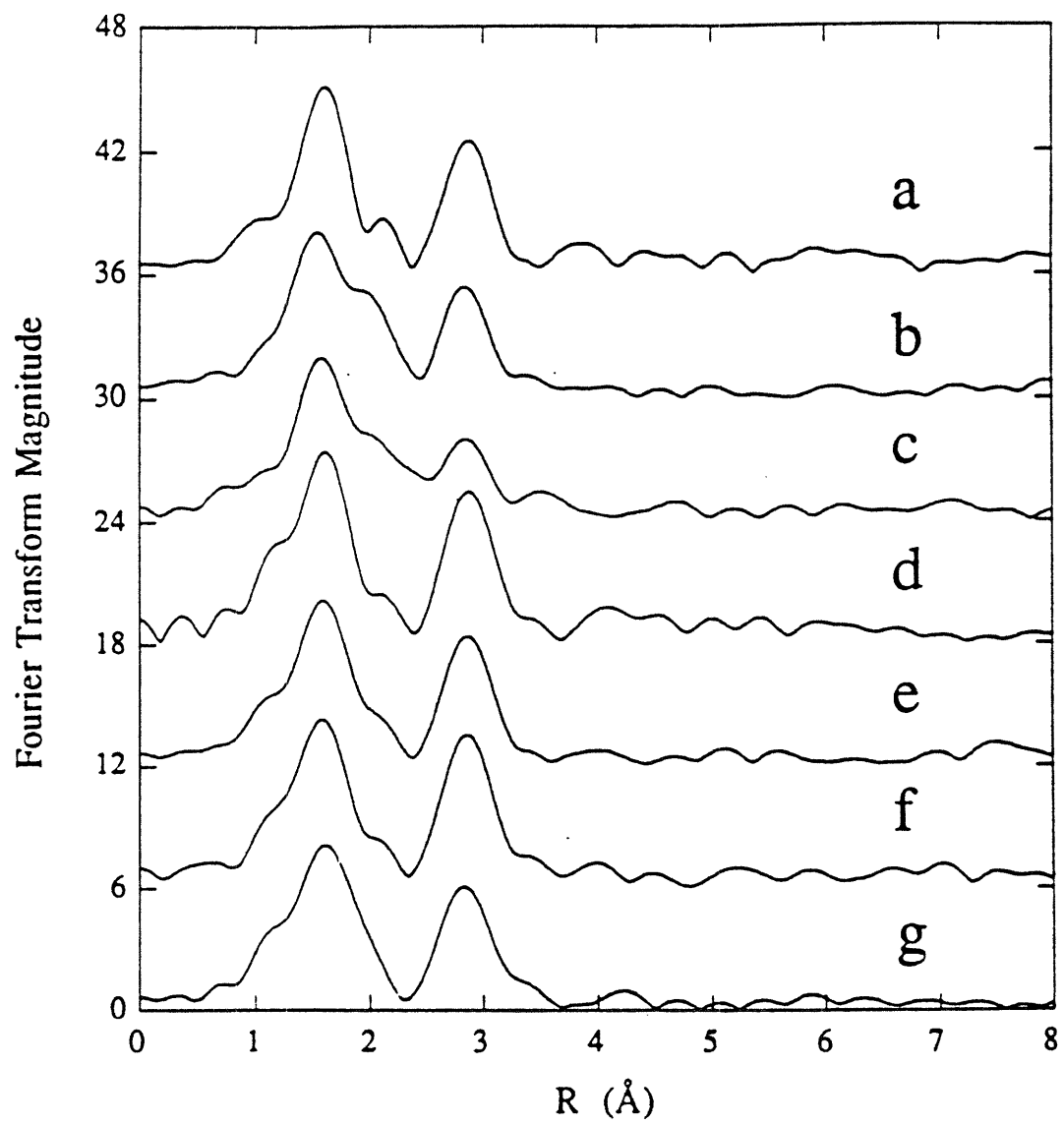


Figure 3.15 EXAFS data for the fully reduced hydroxylase samples. Reduced hydroxylase samples: (a) **EXAFS3**, (b) **EXAFS6**; in the presence of coupling protein: (c) **EXAFS15**; in the presence of 1-bromo-1-propene: (d) **EXAFS19**; in the presence of both coupling protein and 1-bromo-1-propene: (e) **EXAFS17**.

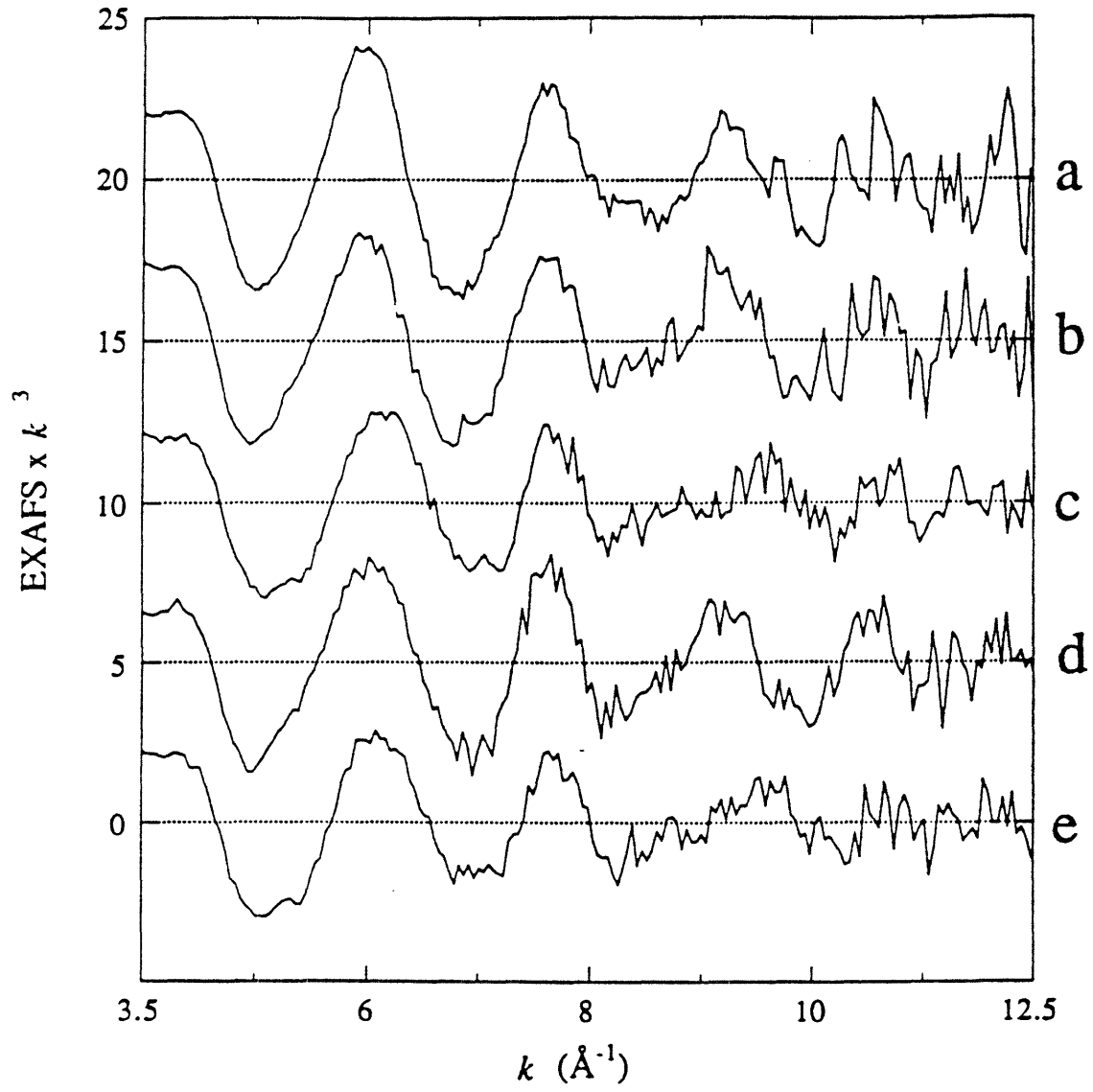


Figure 3.16 Fourier transforms of the fully reduced hydroxylase EXAFS data shown in Figure 3.15. Reduced hydroxylase samples: (a) **EXAFS3**, (b) **EXAFS6**; in the presence of coupling protein: (c) **EXAFS15**; in the presence of 1-bromo-1-propene: (d) **EXAFS19**; in the presence of both coupling protein and 1-bromo-1-propene: (e) **EXAFS17**.

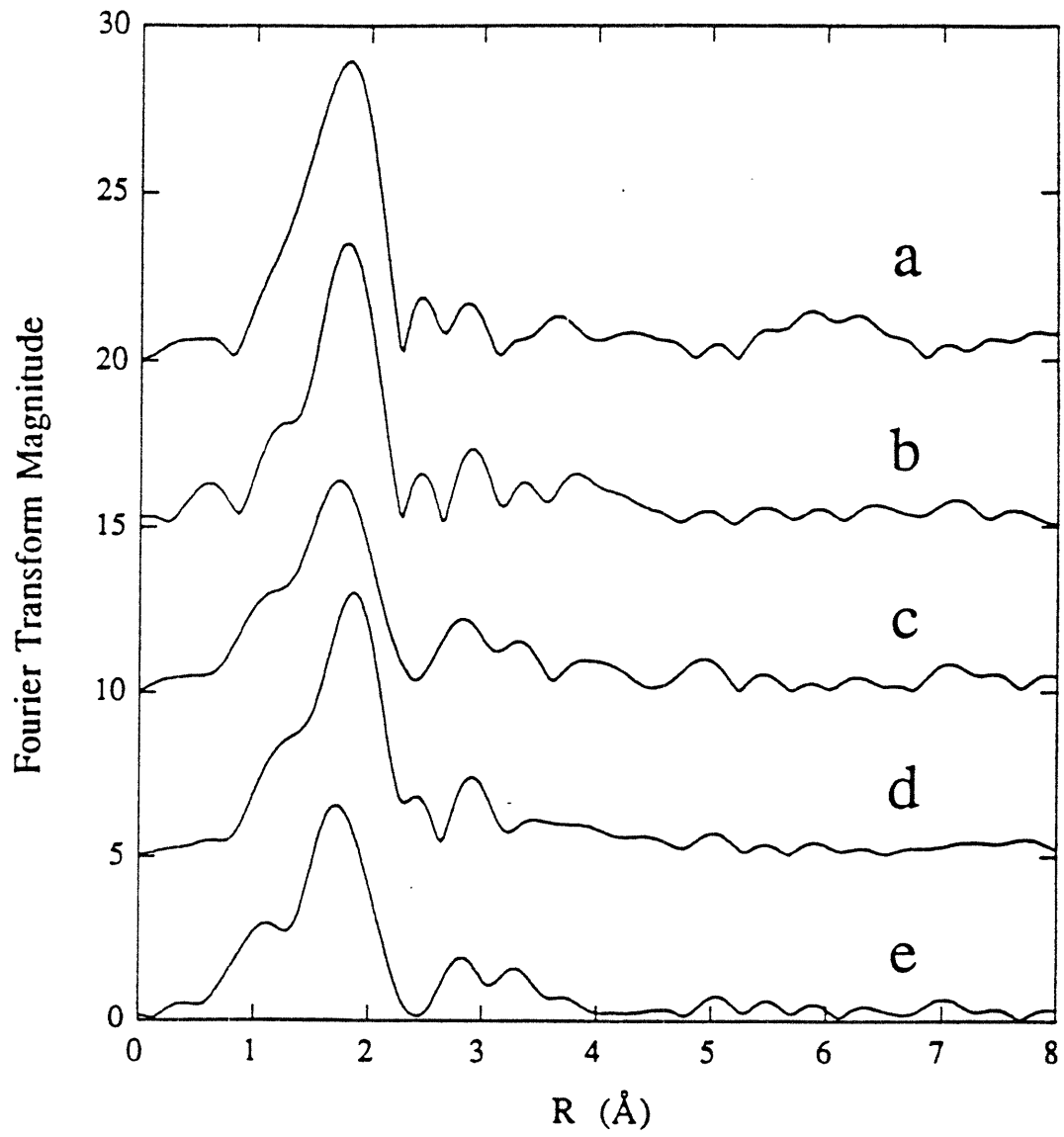


Figure 3.17 Edge spectra of the mixed valent (photoreduced) hydroxylase samples. Mixed valent sample, EXAFS7 (solid); in the presence of coupling protein, EXAFS10 (dash); in the presence of 1-bromo-1-propene, EXAFS18 (dot); in the presence of both coupling protein and 1-bromo-1-propene, EXAFS16 (dash dot).

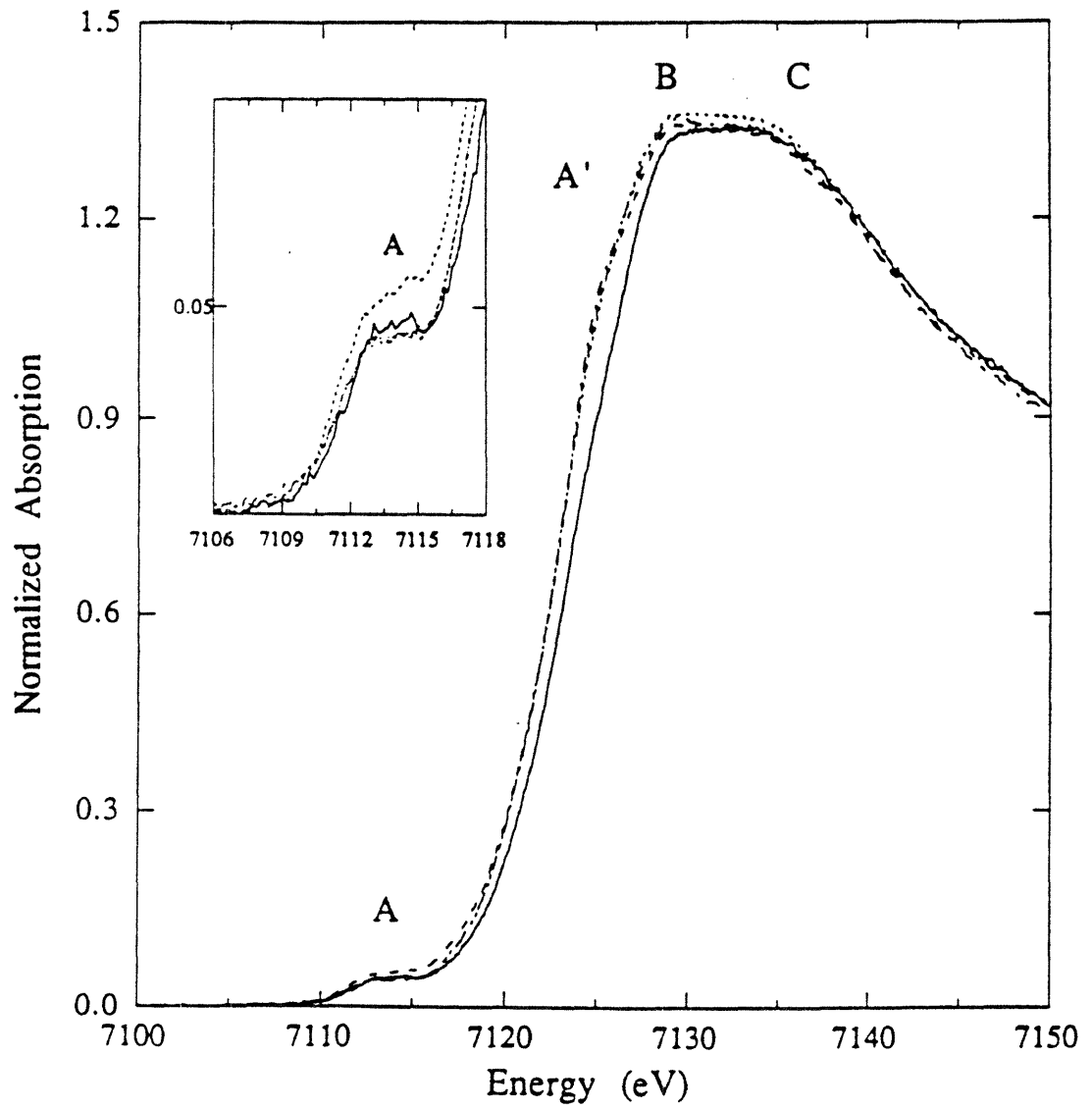


Figure 3.18 Edge spectra of the fully reduced hydroxylase samples. Reduced hydroxylase sample, **EXAFS6** (solid); in the presence of the coupling protein, **EXAFS15** (dash); in the presence of 1-bromo-1-propene, **EXAFS19** (dot); in the presence of both coupling protein and 1-bromo-1-propene, **EXAFS17** (dash dot).

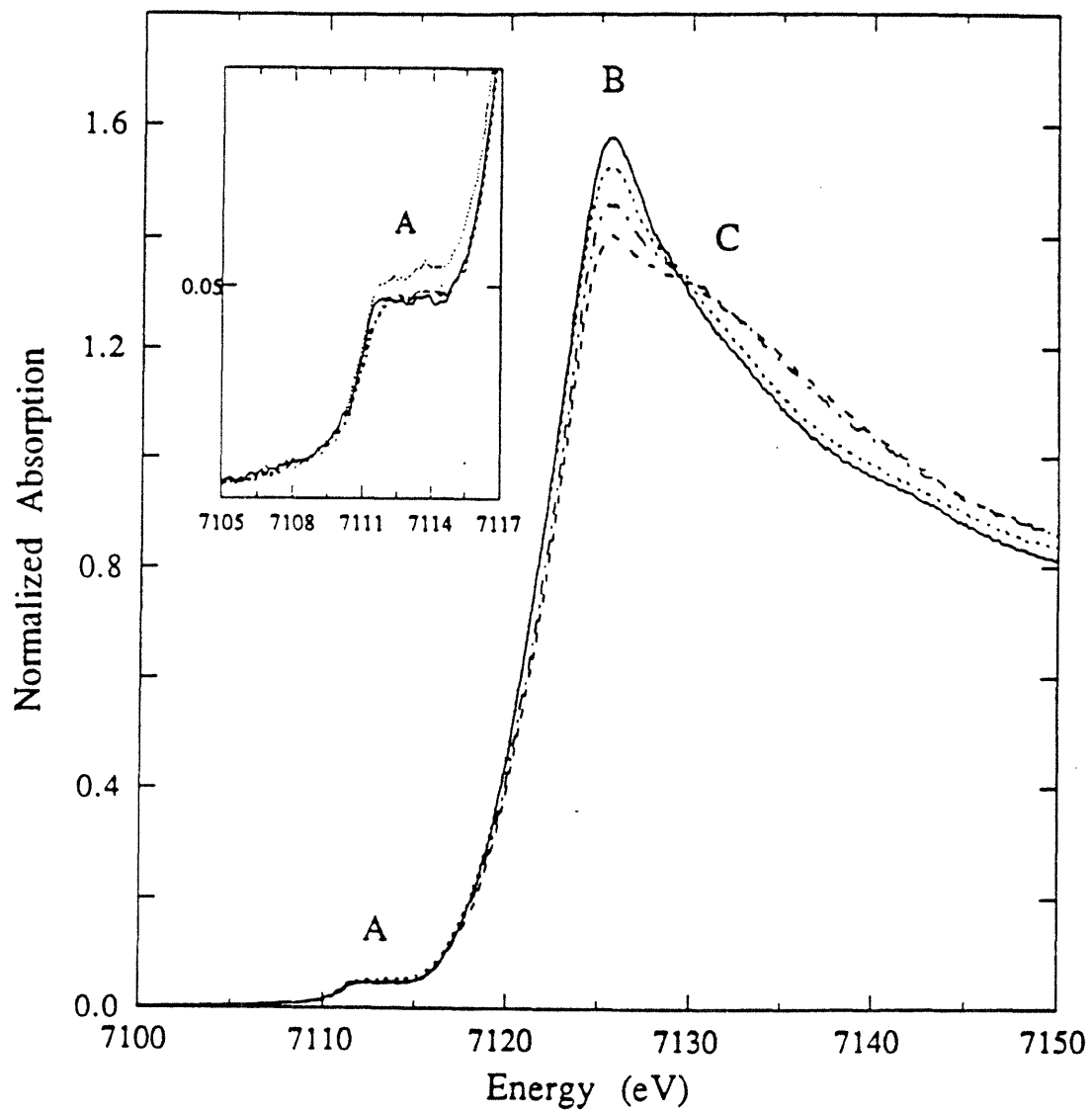


Figure 3.19 Edge spectra of the mixed valent (solid) and fully reduced hydroxylase samples (dash). (a) Fully reduced hydroxylase alone (EXAFS7 and EXAFS6), (b) In the presence of the coupling protein (EXAFS10 and EXAFS15).

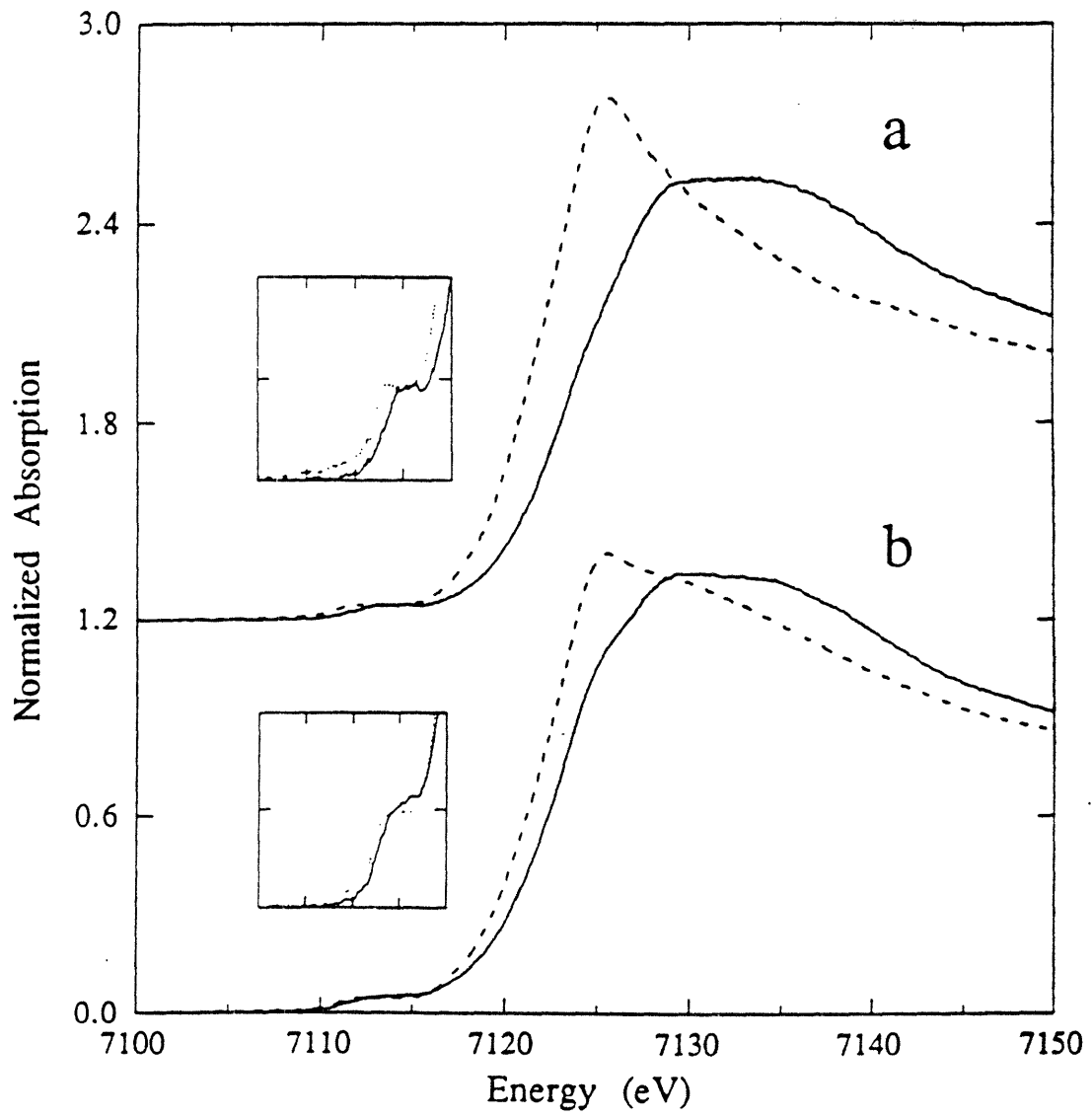
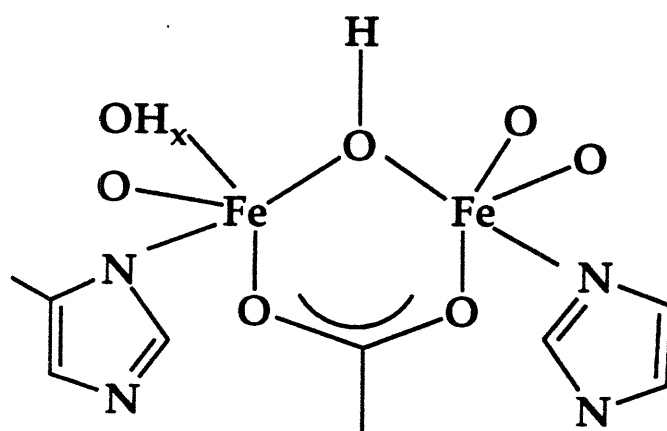


Figure 3.20 Model of the hydroxylase diiron center based on the results of optical, EPR, Mössbauer, ESEEM, EXAFS, and ENDOR spectroscopic studies.



Chapter 4

X-Ray Crystallography of the Hydroxylase

I. Introduction

According to the results of the spectroscopic studies, the dinuclear iron center in the MMO hydroxylase is significantly different from the iron cores found in hemerythrin and in the R2 protein of ribonucleotide reductase. Instead of an oxo bridge, the hydroxylase contains a hydroxo bridge¹ connecting two iron atoms with a 3.4 Å Fe...Fe distance,² along with one or two bidentate bridging carboxylates. In contrast to hemerythrin, which contains all histidine nonbridging ligands, the EXAFS data suggest that the hydroxylase may contain more oxygen than nitrogen nonbridging ligands.² The presence of at least one nitrogen ligand has been confirmed by the ESEEM studies. In addition, a terminal water or hydroxide ligand has been detected by ENDOR spectroscopy.¹ These studies provide some idea of the structure of the diiron core, but a detailed description of the active site, including the identities of specific amino acid residues coordinated to and close to the diiron center, requires additional structural information, such as can be provided by an X-ray analysis.

Several alignments of the amino acid sequence of the α subunit of the hydroxylase, which is believed to contain the diiron center,^{3,4} and the amino acid sequence of the R2 subunit of ribonucleotide reductase have been proposed.^{5,6} In the most detailed model,⁶ shown in Figure 4.1, the sequence of the α subunit is aligned with the iron-coordinating four helix bundle of the R2 protein. This alignment suggests that Glu 114, Glu 144, His 147, Glu 209, Glu 243, and His 246 are coordinated to the iron atoms, and that other specific residues, including Ile 239, Ile 217, and Thr 213, are present in the active site pocket. Notably, in the hydroxylase, a cysteine residue, Cys 151, is postulated to replace the functionally important tyrosyl radical site Tyr 122, found in the R2 protein.

The arrangement of the three hydroxylase subunits is also important. The hydroxylase consists of two copies each of three subunits, in an $\alpha_2\beta_2\gamma_2$ polypeptide chain arrangement. Chemical cross-linking experiments on the MMO proteins from *M. trichosporium* OB3b have provided some information about to the arrangement of the subunits,⁴ but the overall configuration is unknown. According to these chemical cross-linking studies, the α and β subunits are adjacent to one another. The chemical cross-linking studies also show that the coupling protein interacts with the α subunit. The coupling protein can then regulate the flow of electrons to the hydroxylase by changing the redox potentials of the diiron center.⁷ The specific binding region of the coupling protein has not been identified. In order to address these questions, which require detailed structural information, an X-ray crystallographic investigation of the holo hydroxylase was undertaken.

II. Crystallization

Experimental

Materials. Glass 9-well spot plates were obtained from Corning, and 24-well plastic crystallization plates were obtained from FLO Labs, Inc. Tissue culture plates (24-well) for hanging drops were purchased from Linbro. All buffers and salts for crystallization trials were obtained from Sigma, and glass capillary tubes were purchased from Charles Supper.

Crystallizations were carried out at 4 °C and 25 °C by the vapor diffusion method. Sitting drops or dips in silanized 9-well glass spot plates, in 24-well plastic crystallization plates, and hanging drops in 24-well tissue culture plates, were employed. Hydroxylase for crystallizations was concentrated by centrifugation in a Centricon 30 microconcentrator (Amicon). The hydroxylase was purified as described (Chapter 2), and protein from many different

purifications was used. Manipulations of crystals were performed by using glass capillary tubes of varying diameters (0.1 - 1.0 mm) attached to a 0.5 ml or a 1 ml syringe. The majority of crystallization trials were carried out in the 9-well Corning plates. The initial screening of crystallization conditions was approached in two ways. First, commonly used buffers, salts, and precipitating agents were employed. This screening was carried out in the 9-well plates. Second, a fast screening method, in which 29 stock solutions were prepared, and then combined to make 46 different screening solutions, was employed. For the fast screen, 2 μ l of hydroxylase (14 mg/ml) were combined with 2 μ l of each fast screen solution in the 24-well sitting drop crystallization plates. Each reservoir contained 0.7 ml of the fast screen solution. This fast screening method was subsequently expanded to include 70 different conditions.

Results and Discussion

Initial crystallization trials. Most of the initial crystallization trials resulted in precipitates. Only one of the fast screening conditions appeared promising. This crystallization trial, carried out at 4 °C, contained 0.1 M Li_2SO_4 , 50 mM Tris pH 8.5, and 15% PEG 4000 in the dip and 0.2 M Li_2SO_4 , 0.1 M Tris pH 8.5, and 30% PEG 4000 in the reservoir, and yielded oily circular drops overnight. It was thought that these oily drops may be precursors to crystalline material. In an attempt to convert the oily drops into crystals, the concentration of Li_2SO_4 was varied, the percentage of PEG 4000 was varied, and the pH was varied. The temperature was kept at 4 °C for all crystallizations and manipulations of crystals from this point onward. The same circular shapes always appeared. The addition of other salts in combination with the Li_2SO_4 either resulted in the same circular drops or in precipitate. The condition was then modified for use in the 9 well plates. The hydroxylase was exchanged directly into Tris buffer, and Li_2SO_4

and PEG 4000 were added directly to the protein in the dip. The reservoir consisted of only PEG 4000. The total volume in each well was 10 - 13 μ l. Clusters of tiny needles appeared in some of these dips after 7 - 20 days, depending on the condition.

In order to prove that the needles were protein crystals, control experiments were set up. Dips containing Li_2SO_4 , PEG 4000, and 50 mM Tris buffer at several different pHs were prepared and allowed to equilibrate extensively at 4 °C. These control dips remained clear, indicating that the needles were indeed protein. The effects of changing the original condition were then investigated. The pH of the 50 mM Tris buffer was varied in the 5.8 - 8.8 range by increments of 0.2, but needles appeared at pH values 6.0 - 7.4, indicating that needle formation was not highly dependent on pH. The protein concentration was lowered from the usual 14 - 18 mg/ml to ~6 - 7 mg/ml, resulting in less precipitate and cleaner needles. PEG 400, PEG 1500, and PEG 8000 were also tested as precipitants, but only resulted in precipitate. Decreasing the ionic strength of the buffer to 25 mM and adding less Li_2SO_4 yielded softer, more feathery needles.

Several approaches toward obtaining diffraction quality crystals from these needles were then pursued. First, additional purification steps were explored (see Chapter 2). The cleaner protein also crystallized as thin needles, but the presence of little or no precipitate in the dips clearly indicated that purer protein would improve crystal quality. In addition, the formation of very thin plates (0.005 x 0.05 x 0.5 mm) was observed. No crystals of any significant thickness could be obtained, however. Concurrent with the purification experiments, a variety of other conditions was tested in an effort to obtain larger and thicker crystals. Different buffers, salts, and additives such as glycerol and MPD were screened at various concentrations. In addition, the protein

concentration and concentration of PEG 4000 both in the dip and in the reservoir were varied. Those conditions which produced crystals are listed in Table 4.1. One condition, included in Table 4.1, produced thin plates rather than needles: 6 mg/ml protein in 25 mM MOPS pH 7.0 with 23 mM Li_2SO_4 , 23 mM NH_4OAc , and 9% PEG 4000 equilibrated versus a reservoir containing 20% PEG 4000. This condition served as a starting point for a long series of seeding experiments which led to the identification of an optimal condition for the formation of large single crystals.

Crystal seeding. Seeding of crystals is often used as a means of converting small crystals or even crystalline precipitate to large, die non-crystallographic. The method employed here for growing larger, thicker crystals is as follows. First, a small seed crystal, usually a very thin plate, was washed in solutions containing 50 mM Li_2SO_4 , 100 mM NH_4OAc , and first 20%, then 15% PEG 4000. The crystal was then deposited into a dip containing 15-35 mg/ml protein, 25 mM Li_2SO_4 , 50 mM NH_4OAc , and 5% PEG 4000, which had been equilibrated versus a reservoir of 20% PEG 4000 for several days. Large crystals usually appear within 2 weeks. The maximum dimensions ever obtained, not necessarily in the same crystal, are 0.05 mm in thickness, 0.25 mm in width, and 2.5 mm in length. A crystal obtained by this procedure is shown in Figure 4.2.

Whereas this procedure always results in crystal growth, the quality of crystals obtained varies. The crystals sometimes grow as large irregular conglomerates, or as many small plates rather than single large ones. In addition, the crystals are often stacks of very thin plates rather than a single thick plate. A number of factors probably contribute to these variations. First, it is impossible to manipulate each seed crystal in the same fashion. The amount of liquid transferred into the dip with the seed crystal varies, and the seed crystal may be bent or damaged slightly upon transfer. Second, the seed crystals used

are obtained from different dips, and some seeds may be of higher quality. Third, the protein preparation into which the seed is transferred influences the quality of crystal obtained. Although it seems that slightly purer preparations lead to better crystals, the differences among preparations were not necessarily obvious from comparison by comparison by SDS PAGE, and the tendency of a particular purification to crystallize was best tested empirically. Most if not all preparations do crystallize when the optimized seeding procedure was applied.

Because of these variations, some effort was directed toward developing a consistent seeding procedure. Instead of using small individual plates from different crystallizations for seeds, a seed stock was prepared by crushing high quality crystals and suspending them in a stabilizing solution of 25 mM MOPS pH 7.0, 25 mM Li_2SO_4 , 50 mM NH_4OAc , and 20% PEG 4000. Serial dilutions of this stock were made and added in small amounts to dips equilibrated under the same conditions used for the macroseeding procedure. The tube containing the seed stock was vortexed immediately before seeding to ensure an even distribution of seeds. The seed stock was added both in very small volumes and by using a whiskerstick fashioned from a cat whisker, which is purported to be an effective seeding tool.⁸ This procedure, which is referred to as microseeding, did not result in good quality crystals, however. Therefore, use of the variable macroseeding protocol was continued. In order to ensure an adequate supply of large, single crystals for derivative screening and for the trips to the synchrotron, large quantities of crystallization dips were set up and seeded periodically. Approximately 30% of the crystallizations usually resulted in usable crystals. A total of ~5000 crystallization drops were set up between the initiation of crystallization trials and the completion of the structure.

Crystal analysis. In order to confirm that the crystals were indeed the MMO hydroxylase, dissolved crystals were tested for activity and then analyzed

by SDS PAGE. Several large but twinned crystals of protein from two different preparations were harvested for activity assays. The crystals were washed carefully in stabilizing solution several times and then redissolved in 25 mM MOPS pH 7.0. After concentrating and rediluting several times in a Centricon microconcentrator in order to remove excess polyethylene glycol, activity assays were performed as described above (Chapter 2). Protein concentrations were determined by the Bradford microassay, and specific activities of 172 mU/mg and 336 mU/mg (1 U = 1 μ mole product/minute) were calculated for the two samples. Prior to crystallization, specific activities of 75 and 270 were measured for these two preparations. Because of variability in the quality of the mixture of coupling protein and reductase used for the assays, and because only one assay could be performed on the harvested crystals due to lack of material, comparisons of specific activity values are not valid. Redissolved crystals clearly exhibit activity, suggesting that the iron center remains intact in the crystals. The Fe concentration for the dissolved crystals could not be determined because there was not enough material for the ferrozine assay. An SDS gel of the crystals from one of the preparations used for the activity assays is shown in Figure 4.3. The α , β , and γ subunits are clearly evident, and the absence of bands in between the subunits indicates that a high degree of purity has been achieved by the crystallization process. Finally, the presence of Fe in the crystals was confirmed by a single crystal X-ray absorption experiment.¹⁰ In a preliminary experiment to assess the feasibility of single crystal EXAFS studies on the hydroxylase, the Fe K-edge absorption was observed, indicating that Fe is present in the crystalline hydroxylase.

Crystallization of the M. trichosporium hydroxylase. Crystallization of the hydroxylase from *M. trichosporium* OB3b was also achieved. The *M. trichosporium* protein crystallized readily under similar conditions as the *M. capsulatus* protein,

but only thin twinned crystalline plates were formed, and altering the conditions did not significantly improve the quality of these crystals. A factorial of 70 conditions was then used in order to search for conditions which might result in better crystals. The best crystals, very thin plates, were obtained from 50 mM sodium citrate pH 5.6, 100 mM Li_2SO_4 , and 10% PEG 8000, equilibrated versus a reservoir containing 20% PEG 8000. In an effort to improve the crystals obtained from this condition, the concentrations of sodium citrate, Li_2SO_4 , and PEG 8000 were varied, PEG 12,000 was tested, and several different seeding methods were attempted. Although the crystals improved somewhat, crystals suitable for an X-ray diffraction study were not obtained. A cluster of crystalline plates was mounted, however, and diffracted well to 3.5 Å resolution. Because the investigation of the *M. capsulatus* crystals was progressing quite well, the *M. trichosporium* crystals were abandoned at this point.

III. Preliminary X-Ray Analysis

Experimental

Crystals were mounted in glass capillary tubes which were sealed with dental wax and nail polish after the inclusion of a drop of mother liquor. The capillaries were then mounted on a standard goniometer by using either a brass pin and epoxy or by using clay. Precession photographs were taken with a Huber combination precession oscillation camera and nickel-filtered $\text{CuK}\alpha$ radiation generated from a Rigaku RU300 rotating anode source. Crystals for flash freezing experiments were transferred to the usual stabilizing solution containing 15% glycerol prior to freezing, and were frozen at $-120\text{ }^\circ\text{C}$ on a 19 mm diameter platinum loop. Native X-ray diffraction data were collected at $4\text{ }^\circ\text{C}$ by using a Marresearch imaging plate equipped with either a graphite monochromator or a Ni filter and the Rigaku rotating anode source operated at

50 kV and 100 mA. The temperature was maintained by using an FTS cooling system. Intensities of the diffraction spots were integrated by using the program MOSFLM, included in the CCP4 crystallographic program suite (Daresbury, U. K.). The data were then scaled and merged by using the programs ROTAVATA and AGROVATA, also in the CCP4 program package.

Results and Discussion

Unit cell. The initial diffraction pattern was obtained from a crystal of dimensions 0.01 x 0.1 x 0.3 mm. This crystal diffracted to 3.5 Å resolution. Subsequent crystals diffracted to better than 2.5 Å resolution, and were stable for approximately 30 hours at 4 °C in the X-ray beam. From a precession photograph of the h0l zone (Figure 4.4) and a still photograph with the c-axis parallel to the X-ray beam, approximate unit cell dimensions of 62 x 110 x 330 Å were determined. Assuming that there is one $\alpha_2\beta_2\gamma_2$ dimer of molecular weight 250 kDa in the asymmetric unit ($Z = 4$), the cell volume-to-mass ratio was 2.30 Å³/Da, which is a typical value for a protein crystal.¹¹ The lattice appeared to be orthorhombic, but the quality of the precession photograph precluded unambiguous determination of the crystal system and space group. Data collection was then attempted by using a Marresearch imaging plate. The size of the long cell dimension posed a resolution problem in data collection. In order to resolve the 330 Å spacing on the Marresearch imaging plate, which is 1200 pixels by 1200 pixels (1 pixel = 150 μm), the crystal to detector distance had to be increased, sacrificing resolution, or the spot size had to be decreased.

Space group determination and preliminary native data. All the native data sets collected are summarized in Table 4.2. Crystal mmo1 denotes crystal #1, i.e. the first crystal to be mounted and exposed to the X-ray beam. Typically, a crystal lasted for about 30 hours in the X-ray beam. Because of the 15-30 minute

exposure time required for each image, a full 90° of data could not be collected on a single crystal. All of the data sets except for mmo1 were collected in 0.5° rotation frames. If a 1° rotation per image was used, overlapping spots appeared. Because of the 0.5° rotation per image, large numbers of partial reflections were recorded in each data set. As shown for data set mmo24, the inclusion of partial reflections in the statistical analysis of the data increased the R_{sym} significantly. An examination of data set mmo24 confirmed that the lattice was most probably orthorhombic. Furthermore, an R_{sym} of 8.9% would not have been obtained from processing the data as orthorhombic if the crystal system were really monoclinic. Careful examination of the data revealed that the odd 0k0 and 00l reflections were systematically absent, indicating the presence of at least two twofold screw axes. Because a was the rotation axis during data collection, the h00 reflections were not present, and could not be examined for absences. In order to collect the h00 reflections, a partial data set was collected with the b -axis as the rotation axis (mmo35). From these data, it was determined that the odd h00 reflections were systematically absent, indicating the space group to be $P2_12_12_1$.

At a resolution of 4.6 Å (crystal-to-detector distance = 250 mm), the spots were clearly resolved with approximately 2 pixels of background intensity in between. At 3.7 Å resolution, this spacing also appeared resolved, but difficulty was encountered in processing data sets mmo3 and mmo18 with the MOSFLM program. It was eventually discovered that this program is not able to process data from a crystal with such a large cell dimension (vide infra). In addition to resolving the spots by increasing the crystal-to-detector distance, it is also possible to decrease the size of the spots by using Franks type optics, which involve the use of a double mirror arrangement to produce an intense, point-focused beam.¹² Data set mmo25 was collected by using this type of mirror

configuration. Although the spot size was appreciably smaller, the resolution was limited to 3.7 Å resolution. The diffraction pattern was clean and very intense (Figure 4.5), but the data were difficult to process, and the R_{sym} of 12.8% for mmo25 was clearly too high for diffraction data of that quality. Finally, freezing of the hydroxylase crystals was attempted several times at Harvard University in the Harrison laboratory by using a flash freezing apparatus. The frozen crystals diffracted well, indicating that flash freezing may be a valuable technique in the future. Frozen crystals can be stored in liquid nitrogen indefinitely, and will suffer much less, if any, radiation damage.

IV. Native Data Collection

Experimental

Native data sets were collected at the Dana Farber Cancer Institute, at Stanford Synchrotron Radiation Laboratory (SSRL) at Stanford University, and at the Photon Factory (Tsukuba, Japan). In the Dana Farber laboratory, data were collected by using the Marresearch imaging plate detector and $\text{CuK}\alpha$ radiation generated from a Rigaku rotating anode source. The detector setup was originally equipped with a monochromator, and then altered to include double focusing mirrors (Franks optics) and a Ni filter. A Marresearch imaging plate detector was also used at SSRL, and the synchrotron radiation wavelength was 1.08 Å. At the Photon Factory, a modified Weissenberg camera and Fuji imaging plates were employed. The wavelength at the Photon Factory was set to 0.9 Å. An FTS cooling system was used at Dana Farber and at Stanford to maintain a constant temperature at the crystal of 4 °C. The entire hutch at the Photon Factory was cooled to approximately 7 °C. Data collected on the Mar detector were collected as 0.5° oscillations, 180 images being required for a full 90° of data. The Weissenberg setup at the Photon Factory allowed the use of a much larger

oscillation range. The Mar data sets were integrated by using the program DENZO (written by Z. Otwinowski), and scaled and merged by using the programs ROTAVATA and AGROVATA in the CCP4 program package (Daresbury, U. K.). The Weissenberg data were integrated by using the program WEIS, followed by the standard CCP4 programs.

Crystals for travel to the synchrotron sources were prepared in several ways. Some crystals were premounted, some were placed in capillaries immersed in mother liquor, and some were placed in 3-500 μ l of stabilizing solution (25 mM MOPS pH 7.0, 25 mM Li_2SO_4 , 50 mM NH_4OAc , 20% PEG 4000) in 9 well plates and sealed with coverslips and clear tape. The crystals were carried in a small cooler, packed with prefrozen cooling blocks. This method proved reliable in maintaining a cool temperature (0 - 10 $^\circ\text{C}$) for up to 24 hours. All tools for mounting and soaking crystals were also carefully transported to the synchrotron sources.

Results and Discussion

As shown in Table 4.2, several high quality native data sets were obtained. The R_{sym} for data set mmo45 of 5.7% is much better than the values obtained during initial attempts at data collection (data sets mmo1 - mmo25). This improvement results from the use of the program DENZO rather than MOSFLM for integrating the images. The use of DENZO eliminated all the problems initially encountered in processing the data, and diffraction spots separated by just one pixel could easily be measured. The data sets collected at SSRL (mmo90 and mmo122) are of excellent quality, as are the data collected in the Dana Farber laboratory with the double focusing mirrors (mmo147). Because the X-ray beam at the synchrotron is so highly collimated, the number of partial reflections was greatly reduced, and data sets mmo90 and mmo122 are almost complete without

including partial reflections. With the mirrors at the Dana Farber laboratory, it was possible to obtain data to 3.5 Å resolution, and an increase in crystal lifetime was observed. Data sets mmo90, mmo122, and mmo147 were all collected on a single crystal by selecting a very long specimen and translating it periodically throughout the data collection, irradiating fresh parts of the crystal. This strategy has proved invaluable in data collection both at the Dana Farber laboratory and at the synchrotron sources.

The native data set collected at the Photon Factory (mmo142) is also of good quality, and is analyzed by resolution range in Table 4.3 and for completeness in Table 4.4. This crystal diffracted extremely well, with diffraction spots observable to 1.8 Å resolution. Because there are data to 1.8 Å resolution, the images were integrated to that resolution. The very high resolution data are weak, however, with an R_{sym} greater than 25% beyond 2.2 Å resolution. Therefore, the data were restricted to 2.2 Å resolution, which decreased the R_{sym} to 9.1% and increased the completeness to 88%. The native data sets from the Dana Farber and from SSRL all scale to one another quite well, with mean isomorphous differences of 6.0 - 8.0%, depending on the data sets combined. The mean isomorphous difference between the Photon Factory data and the SSRL data (mmo142 and mmo90) is 8.4%, which is quite a satisfactory value considering that very different detector set-ups were used to collect the two data sets.

IV. Heavy Atom Derivatives and Multiple Isomorphous Replacement (MIR)

Phasing

Experimental

Heavy atom compounds for derivatives were obtained from Aldrich, from the Lippard laboratory, and from the Harrison and Wiley laboratories at Harvard

University. Solutions of these compounds were prepared in a synthetic stabilizing mother liquor containing 25 mM MOPS pH 7.0, 50 mM Li_2SO_4 , 100 mM NH_4OAc , and 20% PEG 4000, all of which were obtained from Sigma. Crystals for soaking were first washed in this solution and then transferred to dips in 9-well glass Corning plates containing approximately 0.5 ml of the heavy atom solutions. The crystals were mixed into the solution with a Pasteur pipet and left to soak in the dark. A 1.0 mM heavy atom compound concentration was initially tested for each soak. Derivative data sets were integrated by using the program DENZO, and scaled and merged by using programs in the CCP4 program package. Later derivative data sets were scaled and merged by using SCALEPACK (written by Z. Otwinowski).

Results and Discussion

Initial soaks. An extensive search for isomorphous heavy atom derivatives of the hydroxylase crystals has been conducted. The derivative data are summarized in Table 4.5. Problems were encountered in obtaining full derivative data sets since soaking tended to decrease crystal lifetime significantly. In addition, the data were often less intense for the derivatized crystals, rendering the R_{sym} quite high. Nevertheless, it was apparent from the mean isomorphous differences that many if not all of the compounds initially tested were affording derivatized protein. The data sets up to mmo84Pt indicated that MeHgNO_3 , K_2PtCl_4 , TAMM, $\text{CH}_2(\text{HgI})_2$, and PIP were definitely binding. It was unclear whether $\text{Pb}(\text{CH}_3)_3\text{OOCCH}_3$ and $\text{K}_2\text{Pt}(\text{CN})_4$ were actually binding since the mean isomorphous differences were low. Difference Patterson maps for these derivatives could not be interpreted, probably due to the lack of complete data and to the mediocre quality of some of the data sets. It was not until the derivative data sets collected at SSRL (mmo109Hg, mmo112PIP,

mno126Pb) were analyzed that it was possible to determine the heavy atom positions in any of the derivatives.

Patterson analysis. The difference Patterson map for mno112PIP was interpretable with the help of the Patterson search program RSPS.¹³ Several strong sites were identified and refined with the programs HEAVY¹⁴ and MLPHARE.¹⁵ Difference Fourier techniques were then used to locate additional sites, and to determine the heavy atom structure of the SSRL TMM (mno109Hg) and Pb (mno126Pb) data sets as well as the MeHgNO₃ data (mno71Hg) and the TMM data (mno79Hg, mno80Hg, mno82Hg) collected in the Dana Farber laboratory. For each heavy atom site, the occupancy was refined first, with fixed B-values, and then the B-values was refined, with fixed occupancies. The heavy atom sites are listed in Table 4.6. Whereas the Dana Farber Pb(CH₃)₃OOCCH₃ (mno69Pb, mno78Pb) data indicated little or no binding, the SSRL mno126Pb data had an isomorphous difference of 0.186. This derivative contained all the PIP binding sites, however, and no other sites attributable to Pb. In addition, the mno109Hg derivative contained the TMM binding sites found for mno79Hg, mno80Hg, and mno82Hg, but also contained the PIP sites. It was concluded that the dips where these crystals were soaking somehow became contaminated with PIP. Despite the PIP contamination, these derivatives provided valuable phasing information.

Difference Fourier analysis. At this point, it became easier to screen for more derivatives since the heavy atom sites for each new derivative could be identified by using cross-phased difference Fourier maps. Due to the addition of double focusing mirrors, the data sets collected at the Dana Farber laboratory following the SSRL data sets (mno127EMTS - mno156Pt) were of much better quality than the early derivative data sets collected at the Dana Farber. The isomorphous difference between data sets (11 - 15 % for derivative versus native) is much less

for these later data sets, probably because the overall quality of the data was much improved. Of the compounds tested, five new derivatives, EMTS, $\text{Pt}(\text{NH}_3)_2\text{Cl}_2$, $\text{KAu}(\text{CN})_2$, $\text{UO}_2(\text{NO}_3)_2 \cdot 6\text{H}_2\text{O}$, and K_2PtCl_4 were identified. No binding was observed with $\text{Sm}(\text{NO}_3)_3$, $\text{Gd}(\text{NO}_3)_3$ or with the unknown TI compound. The sites for these derivatives are included in Table 4.6. Three derivative data sets were collected at the Photon Factory, EMTS (mmo143EMTS), $\text{KAu}(\text{CN})_2$ (mmo144Au), and TAMM (mmo145Hg). For unknown reasons, only part of the EMTS data could be processed with WEIS, and these data had a poor R_{sym} and contributed little phasing information. The $\text{KAu}(\text{CN})_2$ data were reasonable, but Au is not a particularly strong derivative. This data set was only collected because none of the Pt derivative crystals, including crystals soaked both at the Photon Factory and at the Dana Farber before the trip, diffracted well enough to collect a data set. The TAMM data were very weak and could not be processed.

Native maps and non-crystallographic symmetry. Initial 5 Å electron density maps calculated with multiple isomorphous replacement (MIR) phases and the mmo90 native data showed the molecule somewhat separated from solvent (Figure 4.6). The MIR phases were improved by solvent flattening.^{16,17} The heavy atom parameters were then re-refined with the program REFINE (CCP4) by using the solvent flattened phases as fixed protein phases,^{18,19} and new MIR phases were generated. Since the asymmetric unit consists of one $\alpha_2\beta_2\gamma_2$ dimer, the existence of a non-crystallographic twofold axis relating the two $\alpha\beta\gamma$ halves was investigated. The self rotation function of the native data was first searched for non-crystallographic symmetry elements by using the CCP4 program POLARRFN. The rotation function did show some peaks indicative of a twofold axis, but a transformation matrix could not be unambiguously assigned. Instead, the positions of the heavy atoms in the MeHgNO_3 and PIP derivatives were used

to locate the non-crystallographic twofold axis. Eight pairs of sites (Table 4.7) superimposed with a r.m.s. deviation of 0.59 Å, and were used to refine the symmetry. The initial symmetry rotation matrix and translation vector (NCS1) as calculated by the program O²⁰ are shown below. The twofold axis lies in the

[-1.00000	0.00050	0.00074]	82.88
[0.00050	-0.37480	0.92710]	27.56
[0.00074	0.92700	0.37480]	-18.63

yz plane. Interestingly, the UO₂(NO₃)₂·6H₂O sites were not related by the twofold axis, and instead were located between hydroxylase molecules in the unit cell, at the protein contacts.

At this point, a skeletonized electron density was generated from the map by using the program BONES.²¹ The molecular boundary was quite clear in this skeletonized density. A rough molecular envelope for non-crystallographic averaging was generated by placing two copies of the ribonucleotide reductase R2 protein "heart" in the hydroxylase skeleton. Twofold averaging was then performed by using the Bricogne programs.²² The averaged phases were combined with the MIR phases by using the program COMBINE (CCP4). The averaged map shown in Figure 4.7 is much more well defined than the nonaveraged map (Figure 4.6). The averaging and phase combination strategy is shown schematically in Figure 4.8. The molecular boundaries were clear, and some long helices were quite visible in 5 Å and 3.7 Å averaged maps. A new molecular envelope was then defined by using model coordinates determined from the skeletonized electron density of the averaged map instead of from the R2 model. The resulting averaged maps were not significantly improved, however.

Location of the diiron center. A hypothesis for the location of the diiron center was formulated at this stage. An anomalous map of the mmo142 native data from the Photon Factory was calculated, and exhibited many peaks, none of which were promising. When this map was rotated onto itself over the non-crystallographic twofold axis, however, only one of the peaks overlapped (was present in both subunits), suggesting that it might be the diiron center. In addition, two mercury binding sites were found close to this peak, and were postulated to be the cysteine residues near the diiron center (Cys151 and Cys211) predicted by the sequence alignment with the ribonucleotide reductase R2 protein.⁶ Enough helices were evident in the map to build the iron coordinating four helix bundle into the electron density, thus locating part of the α subunit. In addition, 7 other long helices were fitted as polyalanine peptides into the density. These additional helices were located in what appeared to be another subunit, and were tentatively assigned as part of the β subunit. In order to continue model building, however, higher resolution phases were necessary.

Higher resolution (3.0 Å) derivative data. Since none of the derivative data sets extended beyond 3.7 Å resolution, a second run at SSRL was carried out to collect derivative data to 3.0 Å resolution. Although the diffraction spots are extremely close together at this resolution, the successful processing of the mmo90 native data set indicated that 3.0 Å data could be obtained by using the Marresearch detector at SSRL. The crystals were extremely radiation sensitive during this run, more so than during the first SSRL run. During exposure to the X-ray beam, the crystals had to be translated frequently, and exhibited rapidly increasing mosaicity as evidenced by a larger spot size. Because of the high crystal mosaicity, many more partial reflections were measured and in some cases, comprised the entire data set. Since the program SCALEPACK includes an option to sum partial reflections, it was used instead of the CCP4 programs

ROTAVATA and AGROVATA to scale and merge these data sets. In addition, multiple data sets on different crystals were collected for each type of derivative. Because of these problems, the R_{sym} values are somewhat higher for these derivative data sets (mmo157 - mmo175) (Table 4.5). The coordinates of the heavy atom sites for these derivatives are listed in Table 4.6. The $\text{Pt}(\text{NH}_3)_2\text{Cl}_2$ data sets (mmo166Pt, mmo170Pt, mmo171Pt, mmo172Pt) exhibited very low mean isomorphous differences, indicating little or no binding of Pt. It is unclear why this problem occurred since derivatization with $\text{Pt}(\text{NH}_3)_2\text{Cl}_2$ initially yielded 9 sites (mmo141Pt, Table 4.6). The TAMM and EMTS derivatives contained all the sites previously observed plus several additional sites, and the $\text{UO}_2(\text{NO}_3)_2 \cdot 6\text{H}_2\text{O}$ derivatives contained the same sites as originally observed.

Fixed phase refinement and further averaging. Different combinations of the derivative data sets were refined together by using three different programs, HEAVY,¹⁴ MLPHARE,¹⁵ and REFINE (CCP4). The best phases as judged by the quality of the resulting MIR electron density map were obtained by using only SSRL derivative data. Three types of derivatives were included in the final phasing: PIP (mmo112, mmo126), TAMM (mmo157, mmo158, mmo177, mmo178), and EMTS (mmo162, mmo164, mmo165). The mean figure of merit as calculated by MLPHARE was 0.47 to 3.5 Å resolution. The anomalous data were not of sufficient quality to be used in the phasing. Although these data sets extended to 3.0 Å resolution, only data to 3.5 Å resolution were included in the phasing since phasing power dropped considerably below 1.0 beyond 3.5 Å resolution.

The twofold symmetry matrix was then re-refined by using four pairs of the EMTS heavy atom sites from data set mmo164 (Table 4.8), which superimposed with an r.m.s. deviation of 0.62 Å. The new rotation matrix

(NCS2), shown below, was very similar to the initial one. A set of programs

[-1.0000	0.00061	0.00090]	83.24
[0.00061	-0.37451	0.92722]	27.32
[0.00090	0.92722	0.37451]	-18.49

for molecular averaging, improvement of non-crystallographic symmetry, and molecular envelope definition written by T. A. Jones²³ was used for all averaging procedures from this point onward (Figure 4.8). New averaged maps to 3.5 Å resolution were generated by using the new symmetry matrix, and a new mask for averaging was generated from coordinates determined from the skeletonized electron density of this map. The envelope was generated by selecting grid points within 5.0 Å of the model coordinates. Several parameters in the mask generation program were varied, and the effects on the resulting averaged maps were compared. The twofold matrix was then further improved by using the program A_RT_IMPROVE,²³ which adds small rotations and translations to the current symmetry matrix to maximize the correlation coefficient between the electron density within the mask and the density within the mask after application of the non-crystallographic symmetry operator. The refined matrix (NCS3) is shown below. Averaging was performed again by using this new

[-0.99997	-0.00054	-0.00427]	84.24
[-0.00119	-0.36884	0.92948]	27.17
[0.00657	0.92947	0.36882]	-18.07

symmetry operator, and a new 3.5 Å averaged map was calculated.

The heavy atom sites for the derivatives used in the phasing were then re-refined once again by using the averaged phases as the fixed protein phases, and new MIR phases to be used in phase combination were calculated. An anisotropic B-value refinement was performed for the TAMM derivatives since the TAMM sites appeared as large anisotropic features in the difference Fourier maps. The final phasing statistics for the derivatives are summarized in Table 4.9. Averaging was performed again, and the averaged phases were combined with the new MIR phases to generate a new 3.5 Å combined map. The map inversion R-value after averaging was 21.5%, and the correlation coefficient was 0.86. In this map, more helices were located, and some long continuous pieces of density appeared. All of these continuous pieces of secondary structure were modeled as polyalanine segments.

V. Model Building, Phase Combination, and Refinement

Partial structural phase combination. Although the map had improved with averaging, it was not adequate to completely interpret the structure. Therefore, a strategy of partial structural phase combination was pursued. In this procedure, MIR phases are improved by the combination of phase information from a partial model. The refinement protocol used in the hydroxylase structure determination is shown schematically in Figure 4.8, and the results are summarized in Table 4.10. The initial partial model containing 462 amino acid residues was subjected to simulated annealing refinement by using the program X-PLOR.²⁴ The mmo142 native data from the Photon Factory were used in all X-PLOR refinements. The R-factor of this initial model was 52% for all reflections between 10.0 Å and 2.5 Å. After cooling the structure from 2000 K to 50 K in steps of 50 K with 50 dynamic steps of 0.5 fs at each temperature and 80 cycles of conjugate gradient positional refinement, the R-factor was 47.4% (Table 4.10,

Cycle 1). Non-crystallographic symmetry constraints were included in the refinement. This refined model was used to generate calculated phases which were combined with the MIR phases by using the program SIGMAA.²⁵ Model building was then continued at 3.5 Å resolution with the new combined electron density map. Five more refinements with X-PLOR were carried out (Cycles 2-6). Starting at Cycle 5, the structure was heated to 3000 K instead of 2000 K for the simulated annealing refinement. A restrained B-factor refinement was also performed starting with Cycle 7. After each of these refinements, a combined map was calculated, and model building was continued.

Molecular averaging. The combined maps showed small differences after these refinement cycles, but no great improvement was observed. After Cycle 7, the combined map was averaged. This averaged combined map appeared to be of slightly better overall quality than the combined map. Therefore, the next 13 cycles of model building, phase combination, and refinement were performed in the following way. After each X-PLOR refinement, the new model was used to calculate phases which were combined with the MIR phases. The resulting map was then averaged by using an averaging envelope generated from the coordinates of the refined model (rather than from a skeletonized electron density map). The averaged phases were then combined with the already combined calculated and MIR phases, and a new map was generated. The new map was used to rebuild the model, which was then subjected to the next cycle of X-PLOR refinement.

After Cycle 7, the maps used for model building were calculated at 3.0 Å resolution instead of 3.5 Å resolution. Combined averaged 3.0 Å maps were calculated with both the SSRL mmo90 native data and the Photon Factory mmo142 native data. The mmo142 data yielded a better map, and therefore were used for all further calculations. At Cycle 8, the non-crystallographic symmetry

constraints were removed, resulting in a drop in the R-factor from 44.1% to 36.9% and a more interpretable map. The refined model from Cycle 9 was used to generate a new non-crystallographic symmetry operator. Instead of using the heavy atom positions to refine the symmetry matrix, the coordinates of the C α atoms for 579 amino acid residues were superimposed with an r.m.s. deviation of 1.12 Å. The refined matrix (NCS4), which was used for further averaging cycles, is shown below. The 4 Fe atoms were included in the refinement beginning

[-0.99998	-0.00459	-0.00460]	84.22
[-0.00258	-0.37047	0.92884]	27.29
[-0.00596	0.92883	0.37045]	-18.18

with Cycle 10. In addition, native data between 10.0 Å and 2.35 Å, rather than 2.5 Å, were included in the refinement at Cycle 12. At Cycle 13, the low resolution cutoff was changed to 7.0 Å.

Although the non-crystallographic symmetry constraints were eliminated at Cycle 8, model building during most of the structure determination was carried out on only one half of the dimer, with the other half generated by rotation about the non-crystallographic twofold axis prior to each X-PLOR refinement. The two halves were then refined independently, but after refinement, only one half was adjusted again. Later in the structure determination (Cycle 18), the two halves of the dimer were modeled independently, so that each model adjustment then involved 2216 residues rather than just 2 x 1058 residues.

Sequence fitting. In Cycles 1-12, the only sequence that had been fitted was in the α subunit. The α sequence was gradually extended beginning with the

iron coordinating four helix bundle, which had been located by using two mercury binding sites which were assigned as the locations of the two cysteine residues near the diiron center (Cys151 and Cys211). Part of the electron density map in this region, which appeared to be a second domain of the α subunit, remained uninterpretable. In addition, no sequence could be fitted in the β subunit, and the location of the γ subunit was unclear. There was just one heavy atom binding site in the β subunit, a mercury binding site, and the β sequence fitting was initiated by assuming that this site was located at the second of two cysteine residues in the β sequence. It was then possible to fit approximately 250 residues of sequence in the β subunit between Cycles 12 and 14.

The location and sequence of the γ subunit were finally identified, also by using the heavy atom sites. There were two Pt binding sites on one helix that did not appear to be part of the α or the β subunit. The apparent ligands to these two sites were separated by 5 amino acid residues, and when the residues were fitted as two methionines near the beginning of the γ sequence, it was possible to fit the rest of the sequence. The fitting of the γ sequence was completed between Cycles 16 and 18. In addition, the second domain of the α subunit, which contains two beta hairpin motifs, was finally solved. At this point, only one piece remained that had not been fitted with sequence. This helix, which had originally been connected to the α subunit, turned out to be the N-terminus of the β subunit, which wraps around the top of the α subunit (see Chapter 5).

The averaging procedure was discontinued after Cycle 19, and $2F_o - F_c$ and $F_o - F_c$ maps were used to adjust the model. The combined averaged maps ceased to yield any useful information at Cycle 17 or 18. It was not until this point that the $2F_o - F_c$ and $F_o - F_c$ maps became useful, but after the R-factor decreased below 25%, valuable information began to appear in these maps. The native data included in the refinement were extended from 2.35 Å to 2.2 Å

starting with Cycle 20, and maps were calculated at 2.3 Å and 2.2 Å resolution. The low resolution cutoff was changed to 6.0 Å at Cycle 23. The sequence fitting was essentially complete after Cycle 19 with 1058 residues of 1084 residues present. The sequence fitting was only unsatisfactory in one region of the electron density map, the last 30 residues in the C-terminus of the β subunit. According to the published sequence,²⁶ residue 363 is a Gly, but the electron density clearly indicated the presence of a Trp at this position (Figure 4.9). Furthermore, the electron density following residue 363 did not fit the published sequence at all. The addition of either one thymidine or one cytidine base at position 4227 in the *mmo Y* gene sequence resulted in an appropriate frameshift, changing the GGA codon for Gly to TGG, which codes for Trp. The derived amino acid sequence was consistent with the electron density map, and includes two more residues at the C-terminus, so that the β subunit now contains 389 rather than 387 residues (Trp363-Ile-Glu-Asp-Tyr-Ala-Ser-Arg-Ile-Asp-Phe-Lys-Ala-Asp-Arg-Asp-Gln-Ile-Val-Lys-Ala-Val-Leu-Ala-Gly-Leu-Lys389). The presence of an additional cytidine base at position 4227 has been confirmed by sequencing of the *mmo Y* gene.²⁷ The new β sequence was included in the refinement at Cycle 22.

Water molecules and exogenous ligands. Well defined electron density corresponding to many water molecules appeared in the $F_o - F_c$ maps, and 411 water molecules were included in the refinement at Cycle 23. Two peaks also appeared at the diiron center, one between the two iron atoms, which has been interpreted as a hydroxo bridge, and the other bound to one iron atom, which has been interpreted as a terminal water ligand. In addition, another, larger region of electron density was visible in the $F_o - F_c$ map, located spanning the two iron atoms. This peak was interpreted as a bridging acetate, probably derived from the crystallization buffer. This ligand could also be bicarbonate ion,

but there are no hydrogen bonding interactions with this ligand. Radiolabeling experiments with ^{14}C -labeled acetate are currently in progress in order to determine whether the diiron center binds acetate ion. These three exogenous ligands were included in the refinement at Cycle 24. A bulk solvent correction was performed in Cycle 25, and all reflections between 40.0 and 2.0 Å were included in an attempt to clarify details of the diiron center. The data were restricted to reflections between 10.0 Å and 2.2 Å for Cycle 26, and then to the 5.0 Å - 2.2 Å range for Cycles 27 and 28. For Cycle 28, 444 additional water molecules were added.

Final refinement statistics. The current model includes 512 of the 527 residues in the α subunit, 384 of the 389 residues in the β subunit, and 162 of the 170 residues in the γ subunit. There is no density for the first 15 residues in the α subunit, the first 6 residues in the β subunit, and the first residue and last 7 residues in the γ subunit. It is probable that these parts of the structure are disordered. The present R-value is 17.0% to 2.2 Å resolution. The R-values for different resolution and F-amplitude ranges are shown in Table 4.11 along with root-mean-square deviations in bond lengths and bond angles. The r.m.s. deviations from ideal bond distances and angles are 0.013 Å and 2.9°, respectively. The root-mean-square deviation for dihedral angles is 22.5°. The Ramachandran plot²⁸ is shown in Figure 4.10. Most of the main chain torsion angles, which are defined in Figure 4.11, fall in allowed regions of the Ramachandran plot. There are a number of outliers, however, and each of these residues will be checked and adjusted after the completion of this thesis. The temperature factors are very similar in the two halves of the dimer, and are plotted as a function of residue number for each subunit in Figures 4.12 - 4.14. The three-dimensional structure of the hydroxylase is described in Chapter 5.

References

- (1) DeRose, V.; Liu, K. E.; Lippard, S. J.; Hoffman, B. J. *Am. Chem. Soc.* **1993**, *115*, 6440-6441.
- (2) DeWitt, J. G.; Bentsen, J. G.; Rosenzweig, A. C.; Hedman, B.; Green, J.; Pilkington, S.; Papaefthymiou, G. C.; Dalton, H.; Hodgson, K. O.; Lippard, S. J. *J. Am. Chem. Soc.* **1991**, *113*, 9219-9235.
- (3) Prior, S. D.; Dalton, H. *FEMS Microbiol. Lett.* **1985**, *29*, 105-109.
- (4) Fox, B. G.; Liu, Y.; Dege, J. E.; Lipscomb, J. D. *J. Biol. Chem.* **1991**, *266*, 540-550.
- (5) Stainthorpe, A. C.; Lees, V.; Salmond, G. P. C.; Dalton, H.; Murrell, J. C. *Gene* **1990**, *91*, 27-34.
- (6) Nordlund, P.; Dalton, H.; Eklund, H. *FEBS Lett.* **1992**, *307*, 257-262.
- (7) Liu, K. E.; Lippard, S. J. *J. Biol. Chem.* **1991**, *266*, 12836-12839.
- (8) Stura, E. A.; Wilson, I. A. *Methods* **1990**, *1*, 38-49.
- (9) Thaller, C.; Weaver, L. H.; Eichele, G.; Wilson, E.; Karlsson, R.; Jansonius, J. N. *J. Mol. Biol.* **1981**, *147*, 465-469.
- (10) Bufford, H.; Rosenzweig, A. C.; Hedman, B.; Lippard, S. J.; Hodgson, K. O., unpublished results.
- (11) Matthews, B. W. *J. Mol. Biol.* **1968**, *33*, 491-497.
- (12) Harrison, S. C.; Winkler, F. K.; Schutt, C. E.; Durbin, R. M. *Meth. Enz.* **1985**, *114*, 211-237.
- (13) Knight, S. Ph. D. Thesis, Swedish University of Agricultural Sciences, 1989.
- (14) Terwillinger, T. C.; Eisenberg, D. *Acta Cryst.* **1983**, *A39*, 813-817.
- (15) Otwinowski, Z. In *CCP4 Proc.* 80-88; Daresbury Lab., Warrington, U. K., 1991; pp .
- (16) Wang, B. C. *Meth. Enz.* **1985**, *115*, 90-112.

- (17) Leslie, A. *Acta Cryst.* **1987**, *A43*, 134-135.
 - (18) Nordlund, P. Ph. D. Thesis, Swedish University of Agricultural Sciences, 1990.
 - (19) Rould, M. A.; Perona, J. J.; Steitz, T. A. *Acta Cryst.* **1992**, *A48*, 751-756.
 - (20) Jones, T. A.; Bergdoll, M.; Kjeldgaard, M. In *Crystallographic Computing and Modeling Methods in Molecular Design*; C. Bugg and S. Ealick, Ed.; Springer-Verlag: New York, (1989).
 - (21) Jones, T. A.; Thirup, S. *EMBO J.* **1985**, *5*, 819-822.
 - (22) Bricogne, G. *Acta Cryst. Sect. A* **1976**, *32*, 832-847.
 - (23) Jones, T. A. In *Molecular Replacement*; E. J. Dodson, S. Glover and W. Wolf, Ed.; SERC Daresbury Laboratory: Warrington, U. K., 1992; pp 91-105.
 - (24) Brünger, T. A.; Kuriyan, J.; Karplus, M. *Science* **1987**, *235*, 458-460.
 - (25) Read, R. J. *Acta Cryst.* **1986**, *A42*, 140-149.
 - (26) Stainthorpe, A. C.; Murrell, J. C.; Salmond, G. P. C.; Dalton, H.; Lees, V. *Arch. Microbiol.* **1989**, *152*, 154-159.
 - (27) Coufal, D. E.; Lippard, S. J., unpublished results.
 - (28) Ramachandran, G. N.; Sassiexharan, V. *Adv. Prot. Chem.* **1968**, *28*, 283-437.
-

Table 4.1 Conditions which resulted in the formation of hydroxylase crystals*

[Protein] (mg/ml)	Buffer	[Li ₂ SO ₄] in dip (mM)	Additional salt in dip (mM)	% PEG 4000 in dip	% PEG 4000 in reservoir
11	50 mM Tris pH 7.0	91	2.3 mM MgCl ₂	9.1	15
11	50 mM Tris pH 7.0	91	2.3 mM Na ₃ C ₆ H ₅ O ₇ ·H ₂ O	9.1	15
11	50 mM Tris pH 7.0	91	2.3, 5.6, 9.6, 43 mM (NH ₄) ₂ HPO ₄	9.1	15
11	50 mM Tris pH 7.2	95		9.5	12.5, 21, 24, 27
18	50 mM Tris pH 7.4	95		9.5	21
10	50 mM Tris pH 6.0	95		9.5	14, 17, 21, 24, 27
8	50 mM Tris pH 6.4	95		9.5	14
14	50 mM Tris pH 6.2	95		9.5	17, 21
18	50 mM Tris pH 6.8	95		9.5	21, 27
12	50 mM Tris pH 7.2	95		9.5	21
10	50 mM Tris pH 6.6	95		9.5	27
11	50 mM Tris pH 7.0	95		9.5	27

7	50 mM Tris pH 7.2	95			21
9	25 mM Tris pH 7.2	24			20
6	25 mM MOPS pH 7.0	23	23 mM (NH ₄)OAc	9.1	20
4	25 mM Tris pH 7.2	23	23 mM HCOONa	9.1	20

*All of the crystallization trials listed were carried out at 4 °C.

Table 4.2 Data collection statistics for native data

Crystal id	Resolution (Å)	Total Observations	Unique Observations	R _{sym} ^g	Completeness (%)
mno1a	4.6	36131	7073	0.147	57
mno3a	3.7	64106	8826	0.111	37
mno18a	3.7	26981	4335	0.120	18
mno24a	4.6	83420	10033	0.087	80
mno24a,b	4.6	83420	12393	0.104	99
mno25c	3.7		12136	0.128	50
mno35a	4.6	34263	7421	0.136	64
mno45a	4.2	113245	12061	0.057	74
mno51a	4.2	78989	6887	0.091	42
mno90d	3.0	263429	39550	0.046	89
mno122d	3.7	138421	21641	0.045	91
mno142e	1.8	538762	162896	0.112	79
mno147f	3.5	173226	24167	0.049	86

^aMarresearch imaging plate detector at DFCI laboratory. ^bPartial reflections included. ^cMarresearch imaging plate at Children's

Hospital (Harrison-Wiley facility) equipped with double focusing mirrors. ^dMarresearch imaging plate detector at SSRL.

^eWeissenberg camera at the Photon Factory. ^fMarresearch imaging plate at DFCI equipped with double focusing mirrors. ^gR_{sym}

= $\sum I_{\text{obs}} - I_{\text{avg}} / \sum I_{\text{obs}}$, where the summation is over all reflections in a data set.

Table 4.3 R_{sym}^a for mmo142 native data set by resolution ranges

Resolution range (Å)	R_{sym}	Accumulated R_{sym}
8.03 - 100.0	0.055	0.055
5.68 - 8.03	0.062	0.058
4.64 - 5.68	0.055	0.057
4.02 - 4.64	0.055	0.056
3.60 - 4.02	0.060	0.057
3.29 - 3.60	0.076	0.061
3.04 - 3.29	0.095	0.065
2.85 - 3.04	0.118	0.069
2.68 - 2.85	0.142	0.074
2.55 - 2.68	0.169	0.078
2.43 - 2.55	0.194	0.083
2.32 - 2.43	0.220	0.088
2.23 - 2.32	0.246	0.092
2.15 - 2.23	0.246	0.097
2.08 - 2.15	0.315	0.101
2.01 - 2.08	0.350	0.105
1.95 - 2.01	0.376	0.108
1.90 - 1.95	0.401	0.110
1.85 - 1.90	0.421	0.111
1.80 - 1.85	0.446	0.112

$^aR_{\text{sym}} = \Sigma |I_{\text{obs}} - I_{\text{avg}}| / \Sigma I_{\text{obs}}$, where the summation is over all reflections in a data set.

Table 4.4 Completeness of mmo142 native data for different resolution ranges

Resolution range (Å)	% Complete	Accumulated %
		Complete
4.89 - 100.0	95.5	95.5
3.88 - 4.89	93.9	94.7
3.39 - 3.88	93.1	94.2
3.08 - 3.39	90.9	93.4
2.86 - 3.08	89.2	92.6
2.69 - 2.86	86.8	91.6
2.55 - 2.69	85.2	90.7
2.44 - 2.55	84.2	89.9
2.35 - 2.44	82.8	89.1
2.27 - 2.35	81.6	88.4
2.20 - 2.27	79.8	87.6
2.13 - 2.20	78.4	86.9
2.08 - 2.13	76.8	86.1
2.03 - 2.08	75.1	85.3
1.98 - 2.03	72.0	84.5
1.94 - 1.98	69.8	83.6
1.90 - 1.94	58.2	82.1
1.86 - 1.90	45.9	80.1
1.83 - 1.86	39.6	78.0
1.80 - 1.83	34.8	75.9

Table 4.5 Data collection statistics for derivative data

Crystal id	Compound	Conc. (mM)	Soak time	Resolution (Å)	# Unique reflections	% Complete	R _{sym}	Mean Iso. Diff.
mno50Hg ^a	MeHgNO ₃	0.36	o/n	4.2	7616	47	0.069	0.179
mno52Hg ^a	MeHgNO ₃	0.36	o/n	4.2	5967	37	0.081	0.195
mno53Hg ^a	MeHgNO ₃	0.36	3 days	4.2			0.117	0.191
mno57Pt ^a	K ₂ PtCl ₄	1.0	5 weeks	4.2	3190	20	0.119	0.275
mno63Hg ^a	MeHgNO ₃	0.38	17 hrs	4.2	7138	44	0.084	0.205
mno65Hg ^a	TAMMg	1.3	2 days	4.2	3702	23	0.107	0.223
mno67Hg ^a	CH ₂ (HgI) ₂	0.8	3 days	4.2	2860	18	0.104	0.200
mno68PIP ^a	PIP ^h	10	4 days	4.2	2812	17	0.134	0.280
mno69Pb ^a	Pb(CH ₃) ₃ OOCCH ₃	20	5 days	4.2	3459	21	0.116	0.156
mno70Pt ^a	K ₂ PtCl ₄	1.0	8 days	4.2	4271	26	0.114	0.239
mno71Hg ^a	MeHgNO ₃	0.36	o/n	4.2	10423	64	0.080	0.240
mno72Hg ^a	TAMM	1.3	3 days	4.2	2556	16	0.117	0.311
mno75PIP ^a	PIP	1.0	3 days	4.2	2168	13	0.122	0.266
mno76Hg ^{a,e}	TAMM	1.3	24 hrs	4.2				
mno77Hg ^{a,e}	TAMM	1.3	24 hrs	4.2				

mno78Pba	Pb(CH ₃) ₃ OOCCH ₃	40	10 days	4.2	2978	18	0.097	0.129
mno79Hg ^a	TAMM	0.2	20 hrs	4.2	6669	41	0.071	0.199
mno80Hg ^a	TAMM	0.2	20 hrs	4.2	4312	26	0.092	0.210
mno82Hg ^a	TAMM	0.2	20 hrs	4.2	3102	19	0.090	0.218
mno84Pt ^a	K ₂ Pt(CN) ₄	1.0	6 days	4.2	5256	32	0.073	0.136
mno109Hg ^b	TAMM	0.9	36 hrs	3.7	12876	54	0.058	0.241
mno112PIpb	PIP	0.1	44	3.7	12283	52	0.040	0.187
mno126Pbb	Pb(CH ₃) ₃ OOCCH ₃	75	3 days	3.7	7454	31	0.037	0.186
mno127Hg ^c	EMTS ⁱ	1.0	3 days	4.2	5839	36	0.107	0.136
mno128Sm ^c	Sm(NO ₃) ₃	1.0	5 days	4.2	5836	36	0.051	0.066
mno130Au ^c	KAu(CN) ₂	1.25	7 days	4.2	7724	47	0.060	0.091
mno135Gd ^c	Gd(NO ₃) ₃	1.0	3 days	4.2	6331	39	0.072	0.067
mno139Tl ^{c,f}	Tl ??	0.1	o/n	4.2	4165	26	0.050	0.081
mno140Hg ^c	EMTS	1.0	3 days	4.2	9669	59	0.061	0.157
mno141Pt ^c	Pt(NH ₃) ₂ Cl ₂	1.0	5 days	4.2	14278	87	0.060	0.115
mno143Hg ^d	EMTS	1.0	3 days	2.8	19573	36	0.120	0.193
mno144Au ^d	KAu(CN) ₂	2.0	4 days	2.8	27751	51	0.080	0.080
mno145Hg ^d	TAMM	1.0	20 hrs	2.8				

mno150U ^r c	UO ₂ (NO ₃) ₂ ·6H ₂ O	5.0	2 days	3.5	20186	72	0.069	0.132
mno156Pt	K ₂ PtCl ₄	4.0	o/n	3.5	27751	57	0.054	0.148
mno157Hg	TAMM	1.0	20 hrs	3.0	21535	49	0.073	0.192
mno158Hg	TAMM	1.0	20 hrs	3.0	17733	40	0.085	0.198
mno162Hg	EMTS	1.0	2 days	3.0	36302	82	0.093	0.148
mno164Hg	EMTS	1.0	2 days	3.0	30238	68	0.073	0.150
mno165Hg	EMTS	1.0	2 days	3.0	21216	48	0.064	0.150
mno166Pt	Pt(NH ₃) ₂ Cl ₂	1.0	3 days	3.0	14672	33	0.078	0.111
mno170Pt	Pt(NH ₃) ₂ Cl ₂	1.0	1 day	3.0	10617	24	0.062	0.080
mno171Pt	Pt(NH ₃) ₂ Cl ₂	1.0	1 day	3.0	18075	41	0.050	0.080
mno172Pt	Pt(NH ₃) ₂ Cl ₂	1.0	1 day	3.0	15094	34	0.050	0.080
mno174Ur	UO ₂ (NO ₃) ₂ ·6H ₂ O	2.5	20 hrs	3.0	36016	82	0.072	0.109
mno175Ur	UO ₂ (NO ₃) ₂ ·6H ₂ O	2.5	20 hrs	3.0	23982	54	0.074	0.120
mno177Hg	TAMM	1.0	12 hrs	3.0	20438	46	0.087	0.190
mno178Hg	TAMM	1.0	12 hrs	3.0	16793	38	0.073	0.191

^aMarresearch imaging plate detector at DFCI. ^bMarresearch imaging plate detector at SSRL. ^cMarresearch imaging plate detector at DFCI equipped with double focusing mirrors. ^dWeissenberg camera at the Photon Factory. ^eThe mosaicity of these crystals was so high that it precluded processing the data. ^fThe identity of this TI compound is unknown; it was a gift to Pär Nordlund from someone in England for whom it was useful. ^gTAMM = tetraakis(acetoxymercuri)methane. ^hIP = di-μ-iodobis-(ethylenediamine)diplatinum(II) nitrate. ⁱEMTS = sodium ethylmercurithiosalicylate. ^jThe mean isomorphous difference is equal to $\Sigma |I_{pH} - I_p| / \Sigma I_p$.

Table 4.6 Heavy atom sites

Crystal id	Compound	Number of sites	Fractional Coordinates			B (Å ²)	Occ./Sigma
			x	y	z		
mmo71Hg	MeHgNO ₃	11	0.6182	0.6340	0.1262	19.1	21
			0.0574	0.2717	0.1437	15.9	26
			0.7033	0.3717	0.1867	28.9	19
			0.7903	0.7651	0.1217	17.2	19
			0.2897	0.8686	0.1431	34.9	19
			0.2708	0.5522	0.0802	22.8	21
			0.0579	0.3241	0.2672	31.5	17
			0.3675	0.1600	0.0337	14.9	9
			0.4798	0.3859	0.3620	7.6	9
			0.5439	0.3060	0.2251	12.7	12
			0.1916	0.1881	0.1111	28.0	6
mmo79,80,82 Hg ^a	TAMM ^d	10	0.1300	0.2964	0.2013	53.8	9
			0.2901	0.4743	0.3506	67.0	
			1.0049	0.1188	0.3002	64.7	
			0.0806	0.3353	0.2745	53.9	
			0.7632	0.3225	0.2867	48.1	7
			0.7361	0.0450	0.4198	46.3	18
			0.0778	0.2702	0.1431	46.6	20
			0.7994	0.2015	0.3890	45.1	11
			0.7388	0.3903	0.3507	47.3	9
			0.4738	0.4344	0.3576	42.8	12
mmo109Hg ^b	TAMM, PIPe	18	0.2071	0.0546	0.2065	26.3	20
			0.9826	0.0042	0.2166	21.6	38
			0.8740	0.3054	0.4614	24.0	29
			0.6439	0.4651	0.4125	27.5	28
			0.0754	0.3344	0.2763	21.8	28
			0.0921	0.2739	0.1433	42.6	26
			0.6612	0.3620	0.4720	27.6	28
			0.7473	0.0469	0.4188	50.7	29
			0.9693	0.1387	0.2738	23.5	28
			0.4901	0.3561	0.1446	19.3	23
			0.1555	0.0198	0.3970	32.1	25
			0.4828	0.4324	0.3571	46.0	29
			0.8047	0.1990	0.3906	45.4	18
			0.7456	0.3955	0.3491	34.7	21
			0.1267	0.2993	0.2004	46.1	19
			0.7457	0.3640	0.3002	28.7	21
			0.7813	0.0588	0.4170	42.8	21
			0.8169	0.2998	0.2836	46.1	20

mmo112PIP	PIP	11	0.2051	0.0555	0.2062	21.1	66			
			0.3582	0.9648	0.0875	27.7	41			
			0.0728	0.3372	0.2766	21.3	41			
			0.3431	0.8597	0.0276	25.6	42			
			0.4929	0.3466	0.1437	23.0	33			
			0.1285	0.8041	0.0396	29.3	43			
			0.9713	0.1326	0.2745	23.6	38			
			0.9790	0.0018	0.2165	22.3	54			
			0.1477	0.0250	0.3973	20.3	31			
			0.2532	0.8970	0.1514	37.6	32			
			0.7438	0.3630	0.3002	21.9	27			
			mmo126Pb ^c	PIP	11	0.2051	0.0574	0.2065	25.3	58
						0.8748	0.3089	0.4604	34.9	31
						0.9776	0.0027	0.2169	26.1	44
						0.0776	0.3360	0.2765	30.2	28
0.6436	0.4661	0.4130				32.3	30			
0.9706	0.1313	0.2743				29.8	26			
0.6537	0.3581	0.4730				31.3	32			
0.4907	0.3434	0.1434				27.9	25			
0.1567	0.0209	0.3975				26.0	28			
0.7504	0.3956	0.3485				45.9	25			
mmo130Au	KAu(CN) ₂	2	0.7066	0.3650	0.3557	30.6	43			
			0.0551	0.3154	0.2703	30.9	15			
mmo140Hg	EMTS ^f	9	0.0668	0.2690	0.1444	32.3	34			
			0.7147	0.3674	0.1867	30.9	25			
			0.7043	0.3620	0.3577	35.1	22			
			0.7271	0.0501	0.4193	29.9	36			
			0.5473	0.3070	0.2246	30.1	17			
			0.0434	0.3233	0.2645	31.6	20			
			0.3798	0.1332	0.3737	32.5	26			
			0.4894	0.4230	0.3536	10.0	11			
mmo141Pt	Pt(NH ₃) ₂ Cl ₂	9	0.2039	0.0564	0.2062	21.1	31			
			0.8735	0.3022	0.4606	29.3	18			
			0.0710	0.3372	0.2765	21.3	14			
			0.6419	0.4648	0.4124	27.7	18			
			0.4924	0.3452	0.1434	22.9	14			
			0.6532	0.3625	0.4719	37.6	14			
			0.9715	0.1324	0.2744	23.7	29			
			0.9797	0.0020	0.2165	22.3	33			
			0.1486	0.0239	0.3975	20.3	16			
			mmo150Ur	UO ₂ (NO ₃) ₂	5	0.9442	0.0638	0.2687	30.5	24
0.6203	0.1274	0.2807				41.9	18			

			209	0.6874	0.4325	0.3292	32.5	15
				0.7981	0.4769	0.3028	35.7	11
				0.0224	0.3826	0.2959	33.8	13
mno156Pt	K ₂ PtCl ₄	13		.6644	0.3414	0.4771	42.5	33
				0.7909	0.4772	0.2789	41.9	18
				0.3974	0.0387	0.2676	30.2	26
				0.6233	0.4686	0.4125	48.7	22
				0.5043	0.3521	0.1506	55.5	27
				0.2095	0.0536	0.2083	54.9	33
				0.1579	0.0378	0.3918	47.9	27
				0.8590	0.3074	0.4619	67.9	27
				0.7115	0.3959	0.3477	35.2	22
				0.0729	0.3401	0.2758	54.9	22
				0.4403	0.3501	0.3044	37.7	22
				0.9675	0.1332	0.2765	37.2	16
				0.2572	0.2003	0.3028	41.2	16
mno157Hg	TAMM	11		0.0705	0.2677	0.1434	55.9	
				0.7278	0.0477	0.4200	34.0	
				0.4772	0.4340	0.3570	22.2	
				0.7581	0.3918	0.3477	67.5	
				0.1217	0.2970	0.2019	98.5	
				0.7930	0.2056	0.3909	112.8	
				1.0089	0.1235	0.3008	112.0	
				0.7871	0.3115	0.2799	32.7	
				0.7823	0.3466	0.2865	50.5	
				0.7786	0.0608	0.4168	62.8	
				0.0616	0.2961	0.2068	44.8	
mno158Hg	TAMM	9		0.0671	0.2672	0.1424	57.0	
				0.7294	0.0482	0.4197	35.0	
				0.4767	0.4357	0.3573	35.6	
				0.7554	0.3928	0.3483	61.2	
				0.1313	0.2949	0.1988	91.9	
				0.7926	0.1987	0.3869	92.7	
				1.0073	0.1162	0.2999	90.9	
				0.8125	0.3001	0.2853	25.9	
				0.7904	0.0411	0.4204	64.6	
mno162Hg	EMTS	9		0.0650	0.2698	0.1443	36.3	
				0.7266	0.0508	0.4193	34.7	
				0.7139	0.3760	0.1864	38.0	
				0.3760	0.1334	0.3736	43.0	
				0.0435	0.3239	0.2640	43.4	
				0.7064	0.3642	0.3579	43.0	
				0.2067	0.2625	0.3765	36.2	
				0.5468	0.3102	0.2250	35.8	
				0.4849	0.4266	0.3535	22.0	
mno164Hg	EMTS	9		0.0649	0.2693	0.1443	28.2	

			210	0.7270	0.0505	0.4193	22.8	
				0.7152	0.3665	0.1867	28.8	
				0.3756	0.1337	0.3736	32.2	
				0.0435	0.3242	0.2638	29.7	
				0.7069	0.3648	0.3579	35.8	
				0.2093	0.2623	0.3768	24.7	
				0.5471	0.3099	0.2250	22.2	
				0.4838	0.4240	0.3531	10.9	
mno165Hg	EMTS	9		0.0658	0.2698	0.1444	28.2	
				0.7265	0.0502	0.4193	26.0	
				0.7134	0.3650	0.1867	30.4	
				0.3758	0.1332	0.3733	32.3	
				0.0437	0.3243	0.2639	30.8	
				0.7062	0.3638	0.3578	34.6	
				0.2099	0.2631	0.3770	27.2	
				0.5495	0.3069	0.2248	27.2	
				0.4850	0.4238	0.3534	13.0	
mno174Ur	UO ₂ (NO ₃) ₂	5		0.9455	0.0619	0.2697	39.6	11
				0.6170	0.1242	0.2798	62.2	9
				0.6850	0.4316	0.3288	45.9	10
				0.8033	0.4722	0.3059	50.0	8
				0.0239	0.3818	0.2957	59.7	8
mno175Ur	UO ₂ (NO ₃) ₂	5		0.9443	0.0615	0.2693	30.5	11
				0.6169	0.1257	0.2790	41.9	8
				0.6807	0.4322	0.3303	32.5	11
				0.7962	0.4751	0.3054	35.7	8
				0.0260	0.3823	0.2945	33.8	7
mno177Hg	TAMM	11		0.0674	0.2678	0.1432	57.3	
				0.7270	0.0476	0.4200	37.4	
				0.4759	0.4330	0.3570	33.4	
				0.7573	0.3912	0.3472	61.2	
				0.1227	0.2999	0.2014	89.3	
				0.7975	0.2047	0.3909	96.7	
				1.0096	0.1207	0.3013	98.7	
				0.7887	0.3122	0.2802	33.3	
				0.7837	0.3441	0.2287	51.3	
				0.7740	0.0613	0.4165	51.0	
				0.0612	0.2993	0.2077	31.7	
mno178Hg	TAMM	11		0.0676	0.2682	0.1428	54.4	
				0.7269	0.0478	0.4199	35.4	
				0.4760	0.4348	0.3572	33.4	
				0.7549	0.3905	0.3481	60.5	
				0.1292	0.2948	0.1994	101.0	
				0.7920	0.1991	0.3880	100.9	
				1.0068	0.1168	0.3006	121.7	
				0.7953	0.3140	0.2805	39.3	

211	0.7824	0.3420	0.2871	30.8
	0.7752	0.0573	0.4154	58.0
	0.0527	0.2967	0.2086	26.0

^aThe three TAMM data sets were combined. ^bDue to PIP contamination, the 11 PIP sites are present in addition to the 7 TAMM sites. ^cThe binding sites present for mmo126Pb are identical to those listed for mmo112PIP. ^dTAMM = tetrakis(acetoxymmercuri)methane. ^ePIP = di- μ -iodobis(ethylenediamine)diplatinum(II). ^fEMTS = sodium ethylmercurithiosalicylate.

Table 4.7 Heavy atom sites used for determination of noncrystallographic symmetry operator NCS1

Crystal id	Compound	Site ^a	Fractional Coordinates		
			x	y	z
mmo71Hg	MeHgNO ₃	M11	0.2708	0.5522	0.0802
		M12	0.0574	0.2717	0.1437
		M21	0.7033	0.3717	0.1867
		M22	0.6182	0.6340	0.1262
		M31	0.7903	0.7651	0.1217
		M32	0.5439	0.3060	0.2251
		M41	0.2897	0.8686	0.1431
		M42	0.0579	0.3241	0.2672
mmo112PIP	PIP ^b	P11	0.2051	0.0555	0.2062
		P12	0.1285	0.8041	0.0396
		P21	0.0728	0.3372	0.2766
		P22	0.2532	0.8970	0.1514
		P31	0.3582	0.9648	0.0875
		P32	0.9713	0.1326	0.2745
		P41	0.3431	0.8597	0.0276
		P42	0.9790	0.0018	0.2165

^aPairs of sites related by noncrystallographic symmetry appear consecutively in the table, and are labeled as M11 and M12, M21 and M22, etc. ^bPIP = di- μ -iodobis(ethylenediamine)diplatinum(II).

Table 4.8 Heavy atom sites used for determination of noncrystallographic symmetry operator NCS2

Crystal id	Compound	Site ^a	Fractional Coordinates		
			x	y	z
mmo164Hg	EMTS ^b	M11	0.0649	0.2693	0.1443
		M12	0.7270	0.0505	0.4193
		M21	0.7152	0.3665	0.1867
		M22	0.3756	0.1337	0.3736
		M31	0.0435	0.3242	0.2638
		M32	0.7069	0.3648	0.3579
		M41	0.2093	0.2623	0.3768
		M42	0.5471	0.3099	0.2250

^aPairs of sites related by noncrystallographic symmetry appear consecutively in the table, and are labeled as M11 and M12, M21 and M22 etc. ^bEMTS = sodium ethylmercurithiosalicylate.

Table 4.9 Final phasing statistics

Compound	Resolution (Å)	Unique reflections	Completeness (%)	R_{merge} (%)†	Isomorphous difference (%)	Number of sites	Phasing power§ (Resolution)
Native	2.2	103,751	92	9.4			
PIP1* (<i>mm</i> o112PIP)	3.7	12,283	52	4.0	18.7	9	1.83 (4.3 Å)
PIP2 (<i>mm</i> o126Pb)	3.7	7,454	31	3.7	18.6	9	1.77 (3.8 Å)
TAMM1 (<i>mm</i> o157Hg)	3.0	18,147	41	7.0	19.2	11	1.17 (3.5 Å)
TAMM2 (<i>mm</i> o158Hg)	3.0	18,279	41	7.9	19.8	9	1.32 (3.8 Å)
TAMM3 (<i>mm</i> o177Hg)	3.0	18,597	42	6.4	19.0	11	1.23 (3.5 Å)
TAMM4 (<i>mm</i> o178Hg)	3.0	15,215	34	6.7	19.1	11	1.32 (3.5 Å)

EMTS1	3.0	18,012	40	7.5	14.8	9	1.55 (3.5 Å)
(mno162Hg)							
EMTS2	3.0	27,471	62	6.3	15.0	9	1.78 (3.5 Å)
(mno164Hg)							
EMTS3	3.0	18,634	42	5.1	15.0	9	1.53 (3.5 Å)
(mno165Hg)							

*PIP, di- μ -iodobis(ethylenediamine)diplatinum(II) nitrate; TAMM, tetrakis(acetoxymethyl)mercuriethane; EMTS, sodium ethylmercurithiosalicylate. $\dagger R_{\text{merge}} = \frac{\sum |I_{\text{obs}} - I_{\text{avg}}|}{\sum I_{\text{obs}}}$ where the summation is over all reflections. \ddagger Phasing power = $\frac{\text{rms}(|F_H|_{\text{calc}})/\text{rms}(\epsilon)}{\text{rms}(|F_H|_{\text{calc}})}$ where $\text{rms}(|F_H|_{\text{calc}})$ is the root mean square calculated heavy atom structure factor and $\text{rms}(\epsilon)$ is the root mean square lack of closure error calculated by the program PHASE (CCP4 program package, SERC, Daresbury, U. K.).

Table 4.10 Refinement of the hydroxylase structure

Cycle	R-factor after refinement (%) ^a	Number of amino acid residues	Number of atoms	Averaging envelope	R-value	
					after averaging (%) ^a	after averaging (%) ^a
					Correlation Coefficient ^b	Figure of merit
1	47.4 ^c	462	3215			
2	47.3	638	4307			
3	45.1	792	5276			
4	43.1	792	5276			
5	45.3	791	6064			
6	45.7	791	6061			
7	44.1	847	5709	e5	22.7	0.866
8 ^d	36.9	847	11,810	e5	31.6	0.774
9	36.9	885	12,452	e6	21.6	0.873
10	35.9	835	12,716	e7	21.2	0.877
11	34.5	866	14,022	e8	20.8	0.882
12	34.9 ^e	907	14,962	e9	20.1	0.891

13	33.5 ^f	907	16,626	e10	19.3	0.898	0.82
14	32.3	929	17,224	e11	18.8	0.904	0.84
15	29.2	956	17,812	e12	18.4	0.909	0.86
16	28.9	978	14,878	e13	18.2	0.911	0.87
17	26.2	1012	16,198	e14	15.6	0.937	0.89
18	24.4	1038	16,904	e15	14.9	0.942	0.90
19	22.6	1058	17,254	e16	16.1	0.945	0.84
20	22.48	1058	21,308				
21	21.4	1058	18,881				
22	20.8	1058	21,302				
23	19.2 ^h	1058	22,549				
24	19.6	1058	22,561				
25	21.9	1058	22,527				
26	20.2	1058	22,527				

27	18.2	1058	22,527
28	17.0	1058	23,859

^aThe R-value is the crystallographic R-factor, $R = \frac{\sum | | F_{obs}(hkl) | - | F_{calc}(hkl) | |}{\sum | F_{obs}(hkl) |}$, where the summation is over all reflections. The R-value after averaging is the map inversion R-value after symmetry averaging. ^bThe correlation coefficient reflects the agreement between the observed structure factor amplitudes and those calculated from the averaged electron density map by Fourier inversion. ^cNative data in the 2.5 - 10.0 Å range were used in the refinement. ^dAt Cycle 8, the noncrystallographic symmetry constraints were removed. ^eThe high resolution cutoff was changed to 2.35 Å at Cycle 12. ^fThe low resolution cutoff was changed to 7.0 Å at Cycle 13. ^gThe high resolution cutoff was changed to 2.2 Å at Cycle 20. ^hThe low resolution cutoff was changed to 6.0 Å at Cycle 23.

Table 4.11 Refinement statistics

	<u>r.m.s deviation from ideal geometry</u>	
Distances (Å)	0.013	
Bond Angles (degrees)	2.9	
Dihedral Angles (degrees)	22.5	
Resolution (Å)	R-factor*	# Reflections
4.33 - 5.00	0.129	5187
3.92 - 4.33	0.123	5081
3.63 - 3.92	0.126	5053
3.41 - 3.63	0.146	5046
3.24 - 3.41	0.156	4985
3.09 - 3.24	0.162	4885
2.97 - 3.09	0.184	4821
2.87 - 2.97	0.240	4769
2.78 - 2.87	0.238	4704
2.70 - 2.78	0.239	4647
2.63 - 2.70	0.247	4604
2.56 - 2.63	0.256	4534
2.50 - 2.56	0.258	4577
2.45 - 2.50	0.258	4449
2.35 - 2.40	0.251	4498
2.31 - 2.35	0.264	4361
2.27 - 2.31	0.268	4415
2.23 - 2.27	0.272	4314
2.20 - 2.23	0.286	4269

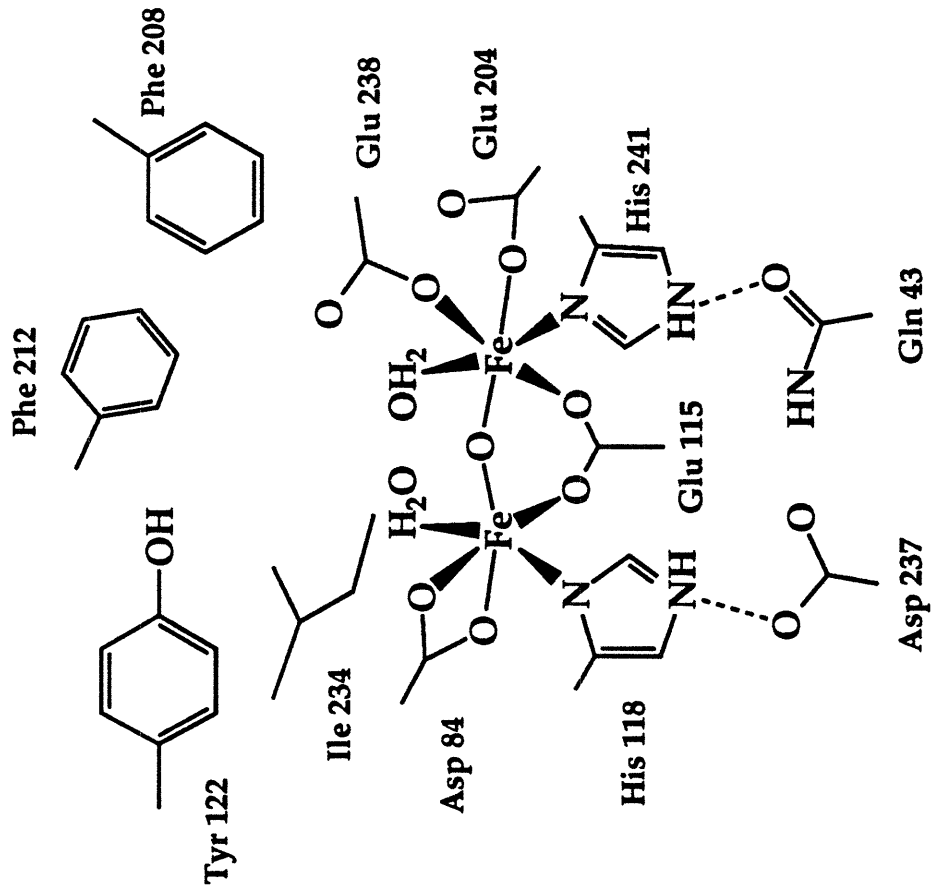
F-amplitude Range	R-factor*	# Reflections
1615 - 1699	0.053	40
1531 - 1615	0.060	66
1447 - 1531	0.064	127
1364 - 1447	0.068	176
1280 - 1364	0.072	258
1196 - 1280	0.084	380
1112 - 1196	0.080	555
1028 - 1112	0.084	830
944 - 1028	0.092	1154
861 - 944	0.103	1636
777 - 861	0.106	2217
693 - 771	0.121	3056
609 - 693	0.130	4221
525 - 609	0.147	5800
441 - 525	0.167	8384
357 - 441	0.196	12227
274 - 357	0.239	17098
190 - 274	0.308	19396
106 - 190	0.433	12754
22 - 106	1.028	3078

*The R- factor is the crystallographic R-factor, $R = \sum | |F_{\text{obs}}(\text{hkl})| - |F_{\text{calc}}(\text{hkl})| / \sum |F_{\text{obs}}(\text{hkl})|$,

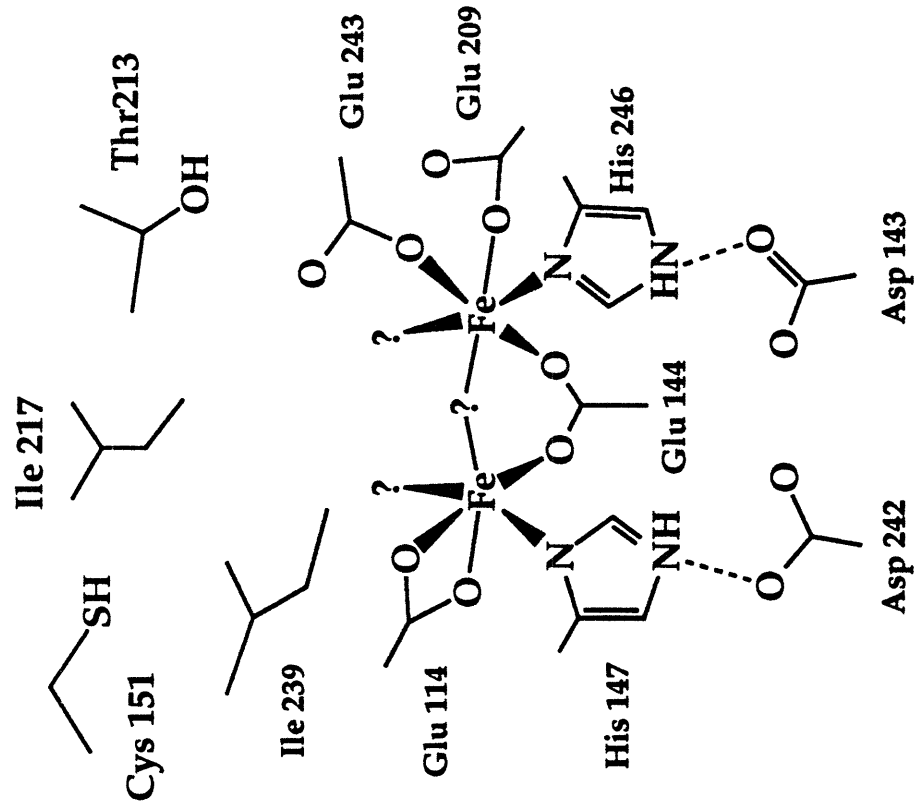
where the summation is over all reflections.

Figure 4.1 The diiron cores in the active site model of the hydroxylase and in the R2 protein of ribonucleotide reductase. This model of the hydroxylase active site is based on an alignment of the amino acid sequences of the α subunit and of the R2 protein.

R2



MMO



Nordlund et al., (1992) FEBS Lett. 307, 257.

Figure 4.2 A crystal of the hydroxylase. The longest dimension is 0.6 mm.



Figure 4.3 SDS PAGE of redissolved crystals used for activity assays. Lane 1, protein molecular weight standards (myosin, MW 200 kDa; phosphorylase B, MW 97.4 kDa; bovine serum albumin, MW 68 kDa; ovalbumin, MW 43 kDa; carbonic anhydrase, MW 29 kDa; β -lactoglobulin, MW 18.4 kDa; lysozyme, MW 14.3 kDa). Lane 2, redissolved crystals (13 μ g).

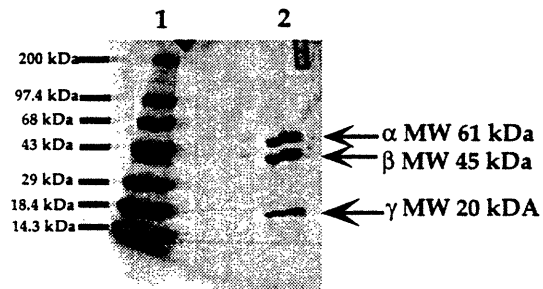


Figure 4.4 Precession photograph of the $h0l$ zone ($\mu=12^\circ$, $T=4^\circ\text{C}$, 15 hour exposure, crystal-to-film distance = 100 mm).

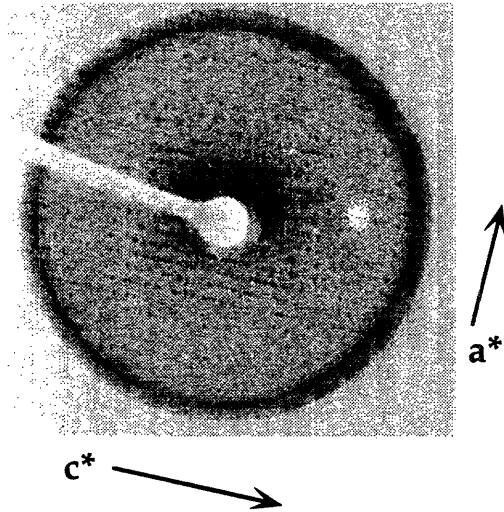


Figure 4.5 Diffraction pattern to 3.7 Å resolution. The picture shows a 0.5° rotation with the *a*-axis along the spindle (horizontal) and the *b*-axis parallel to the X-ray beam (shooting into the edge of the crystal).

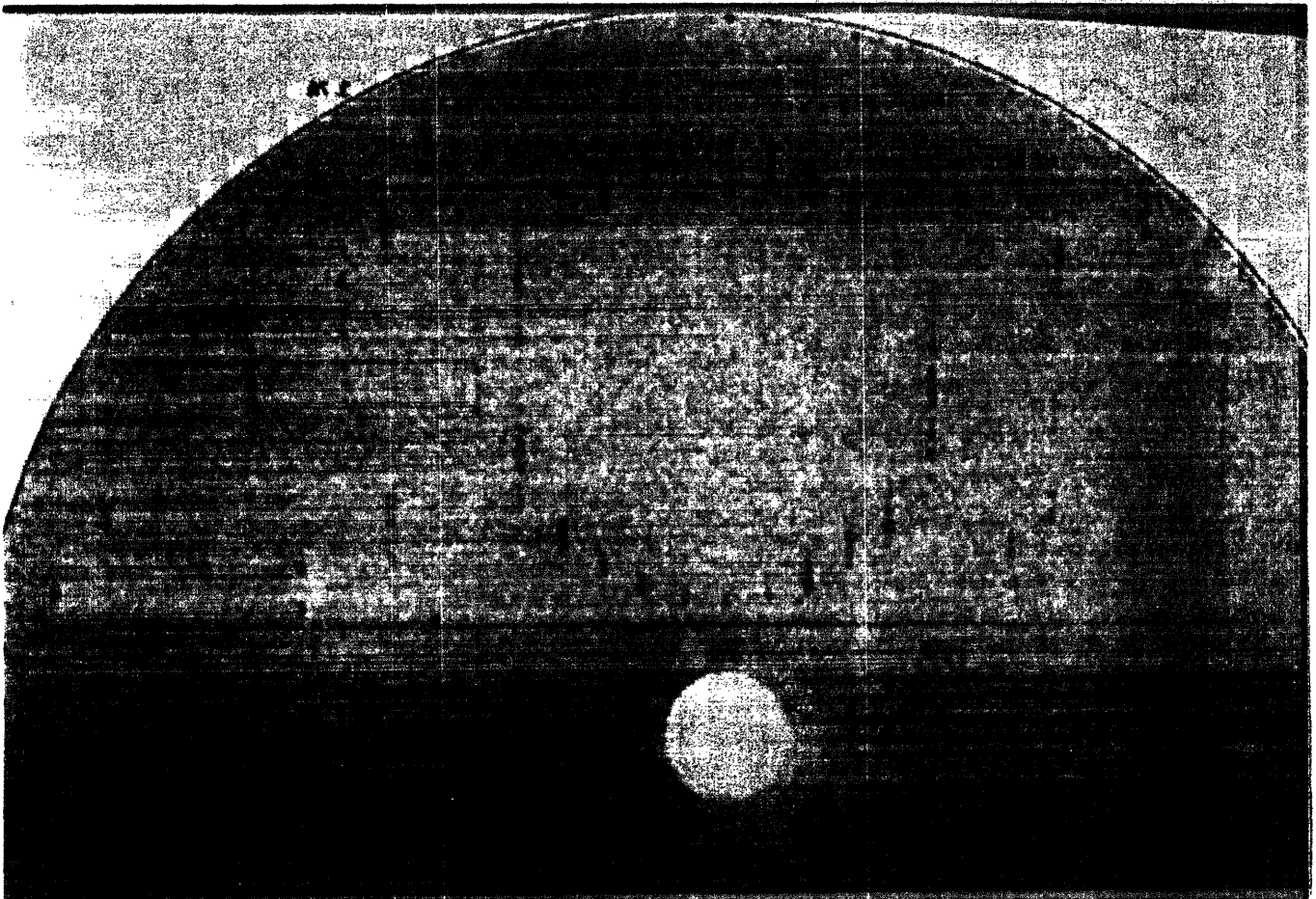


Figure 4.6 Native MIR electron density map at 5 Å resolution. The map shows 40 1-Å sections of density along the *c*-axis. Each division corresponds to 10 Å.

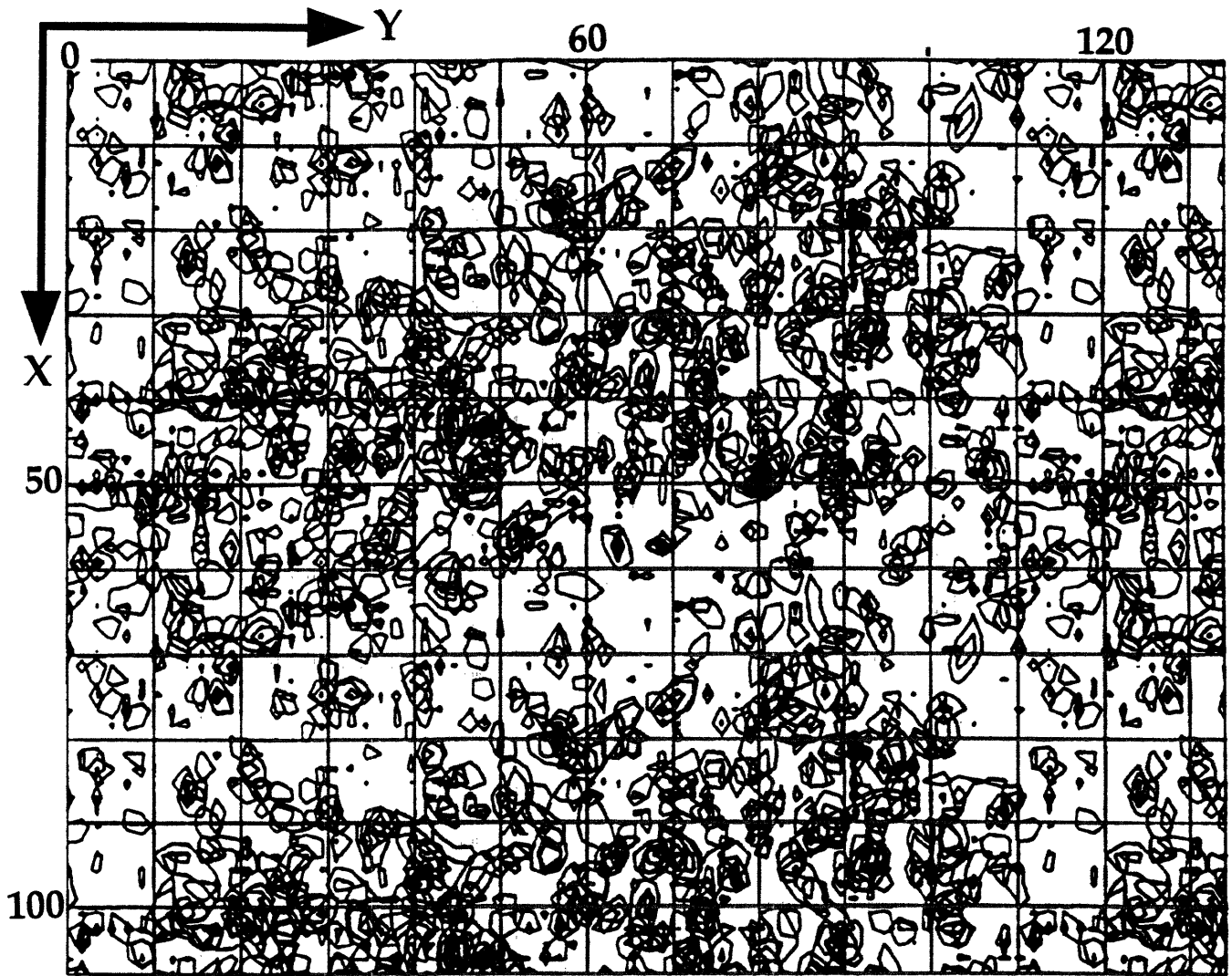


Figure 4.7 Native averaged map at 5 Å resolution. The map shows 40 1 Å sections of density along the *c*-axis. Each division corresponds to 10 Å.

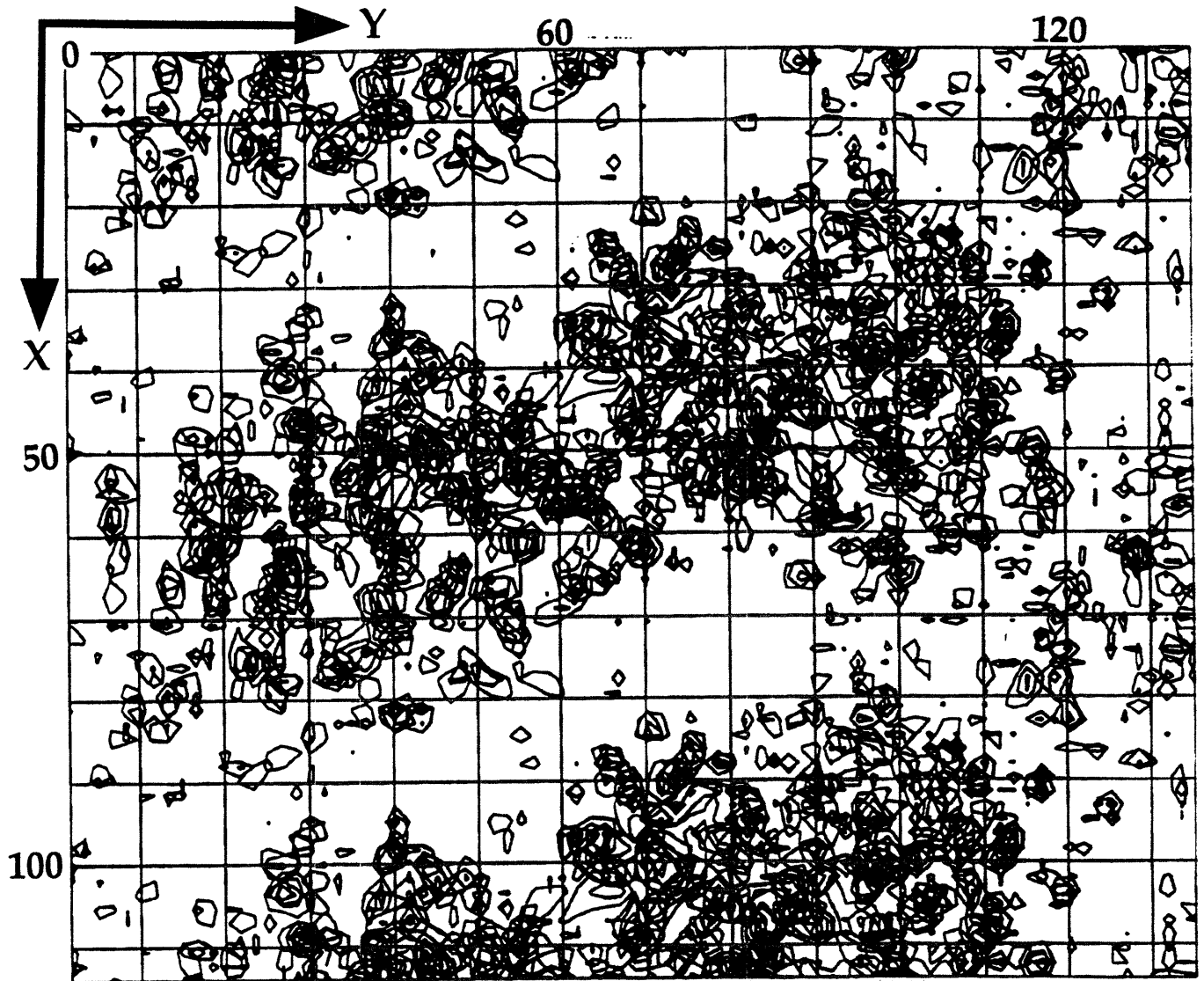


Figure 4.8 Structure solution and refinement protocol.

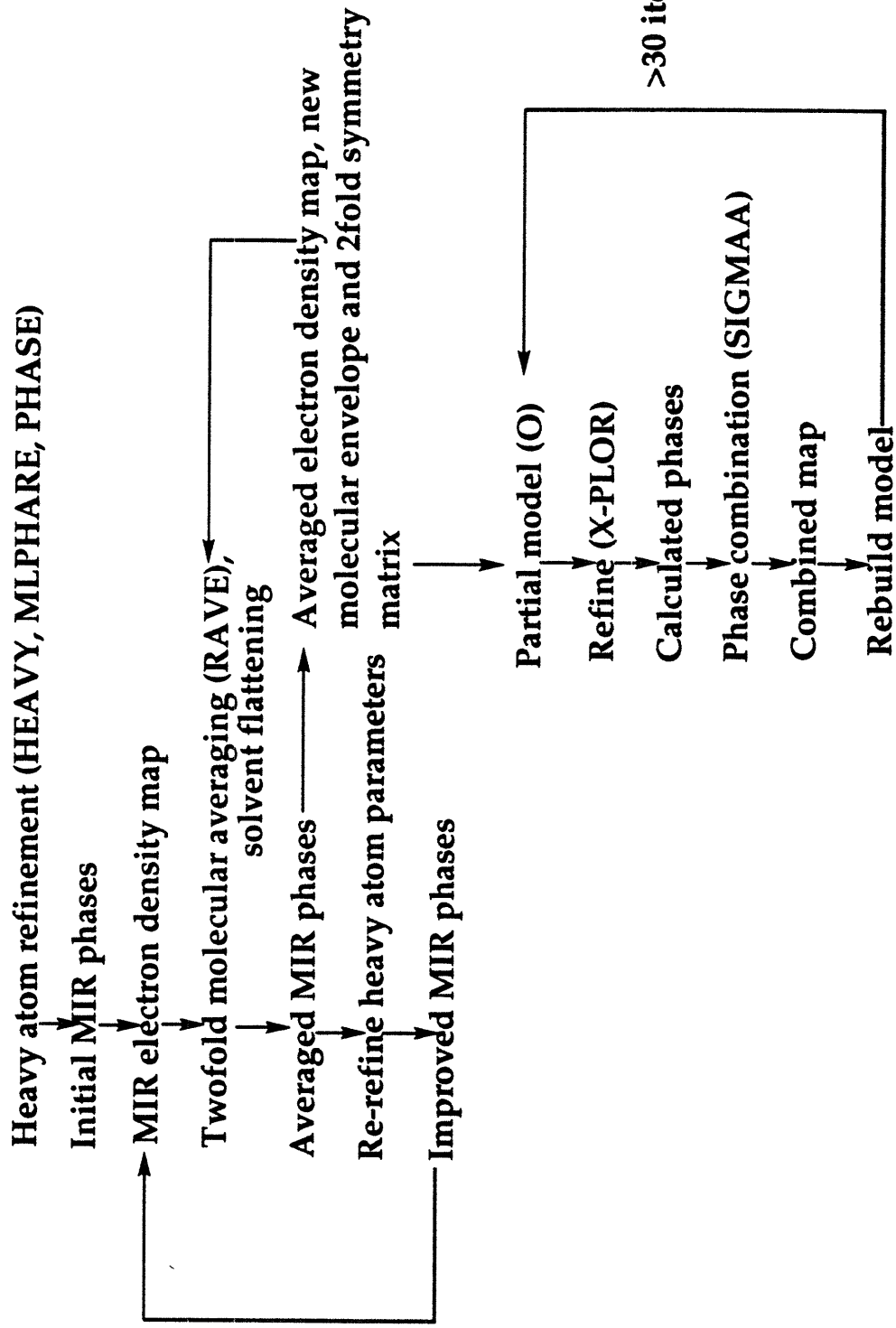


Figure 4.9 Electron density map at 2.2 Å resolution of residue 363 in the β subunit. The top picture shows the density fitted with a glycine residue, according to the published sequence. The bottom picture shows the density correctly fitted with a tryptophan residue.

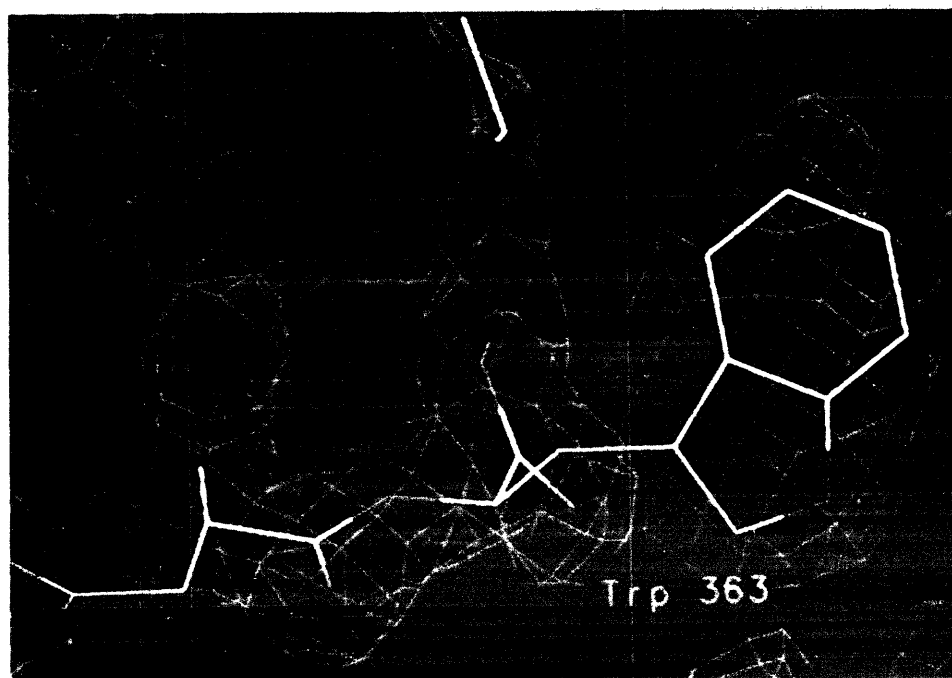
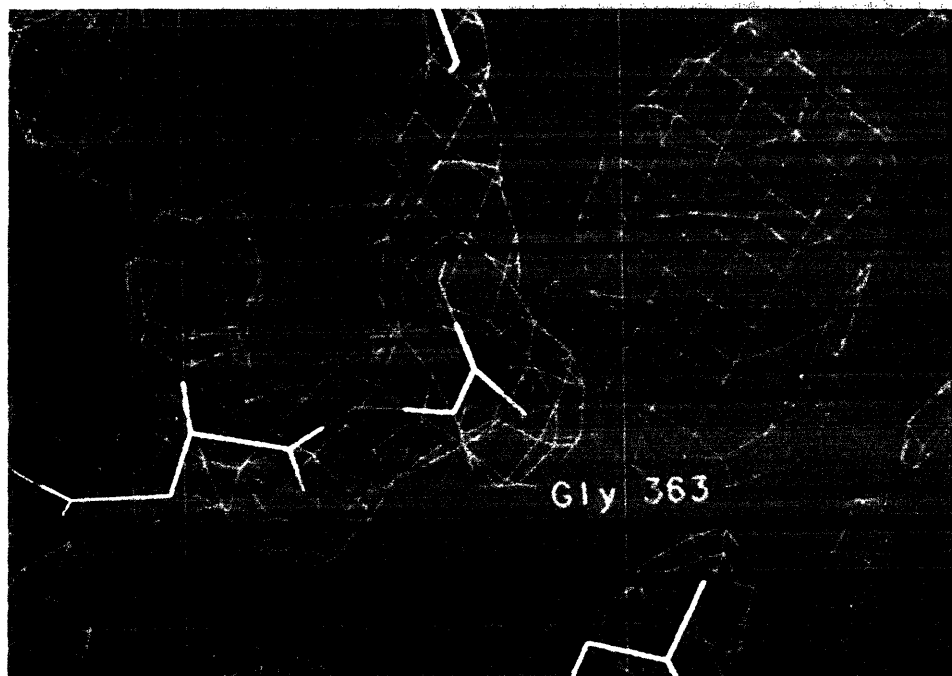


Figure 4.10 Ramachandran plot for all residues in both halves of the $\alpha_2\beta_2\gamma_2$ dimer. The square symbol indicates glycine residues.

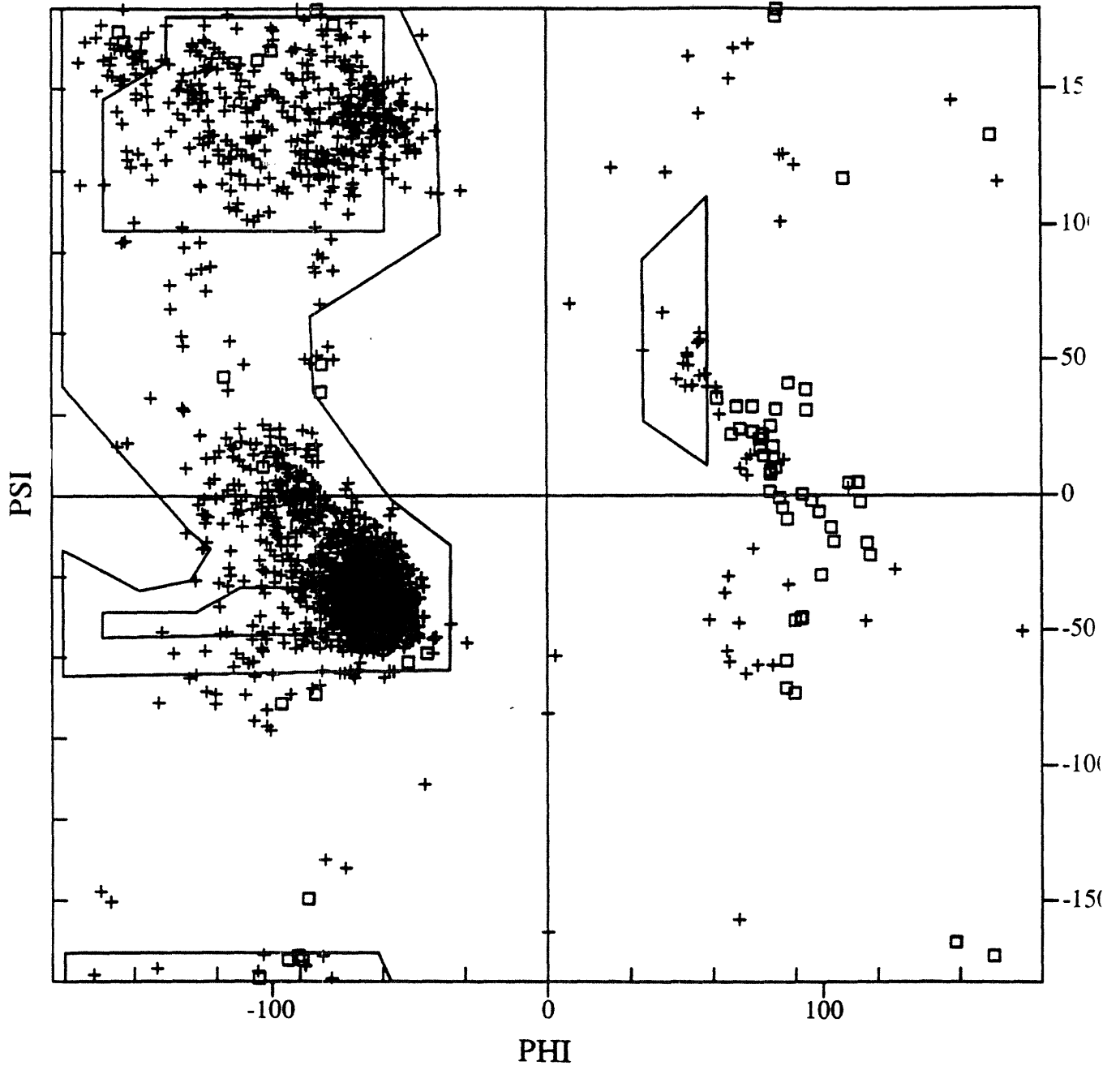


Figure 4.11 Diagram showing the Ramachandran angles phi (ϕ) and psi (ψ) (from Branden, C.; Tooze, J. *Introduction to Protein Structure*; Garland Publishing, Inc.: New York, 1991, p. 8). The angle of rotation around the N-C $_{\alpha}$ bond is called ϕ and the angle of rotation around the C $_{\alpha}$ -C' bond is called ψ .

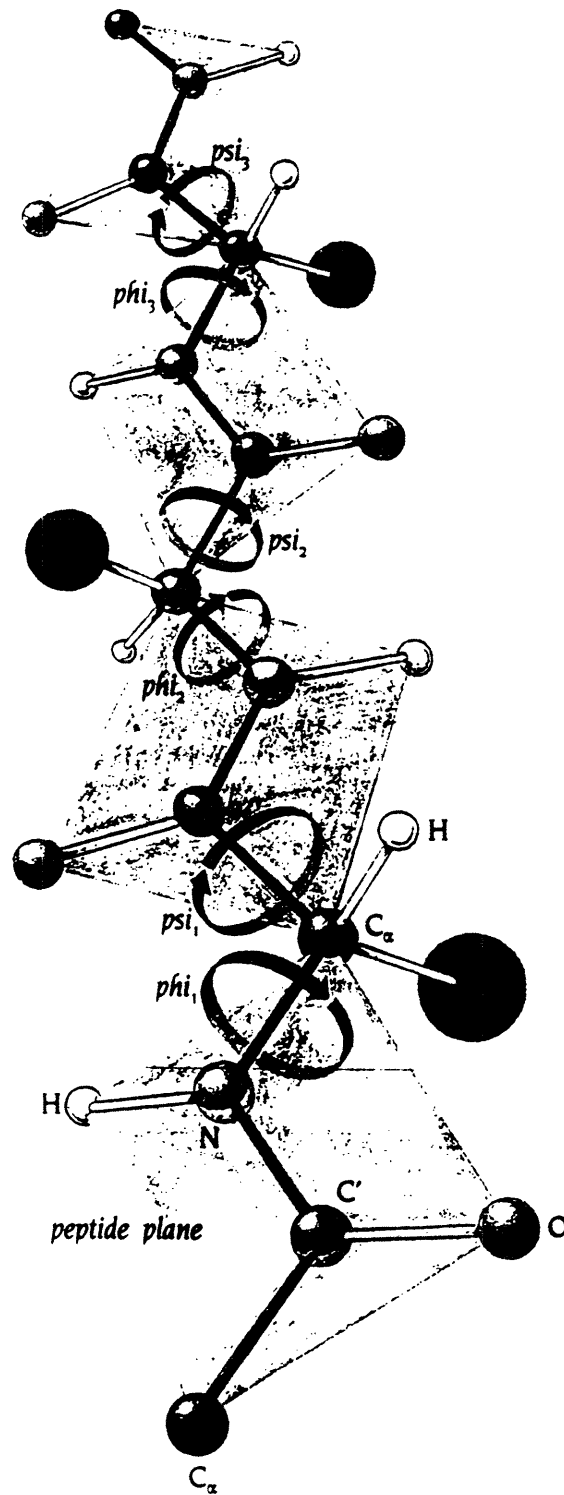


Figure 4.12 Main chain temperature factors for the α subunit. The top plot corresponds to the A protomer and the bottom plot corresponds to the B protomer.

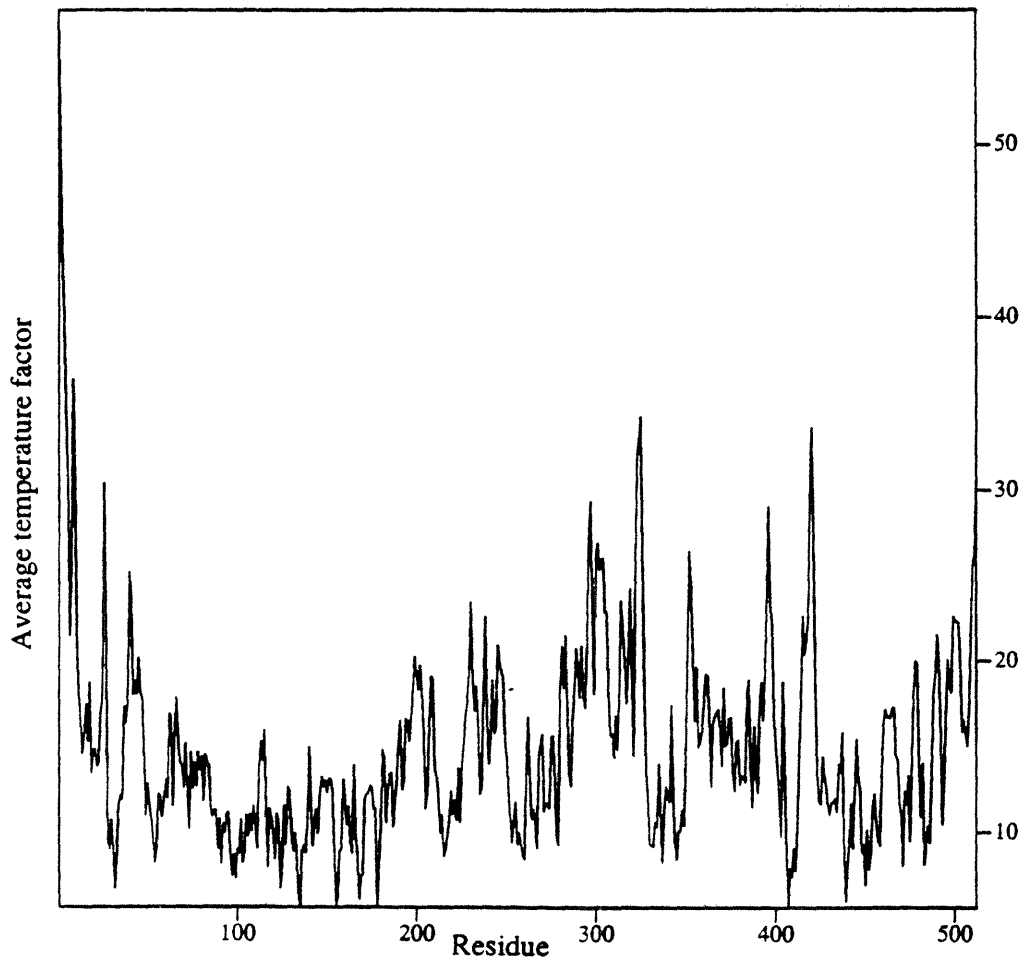
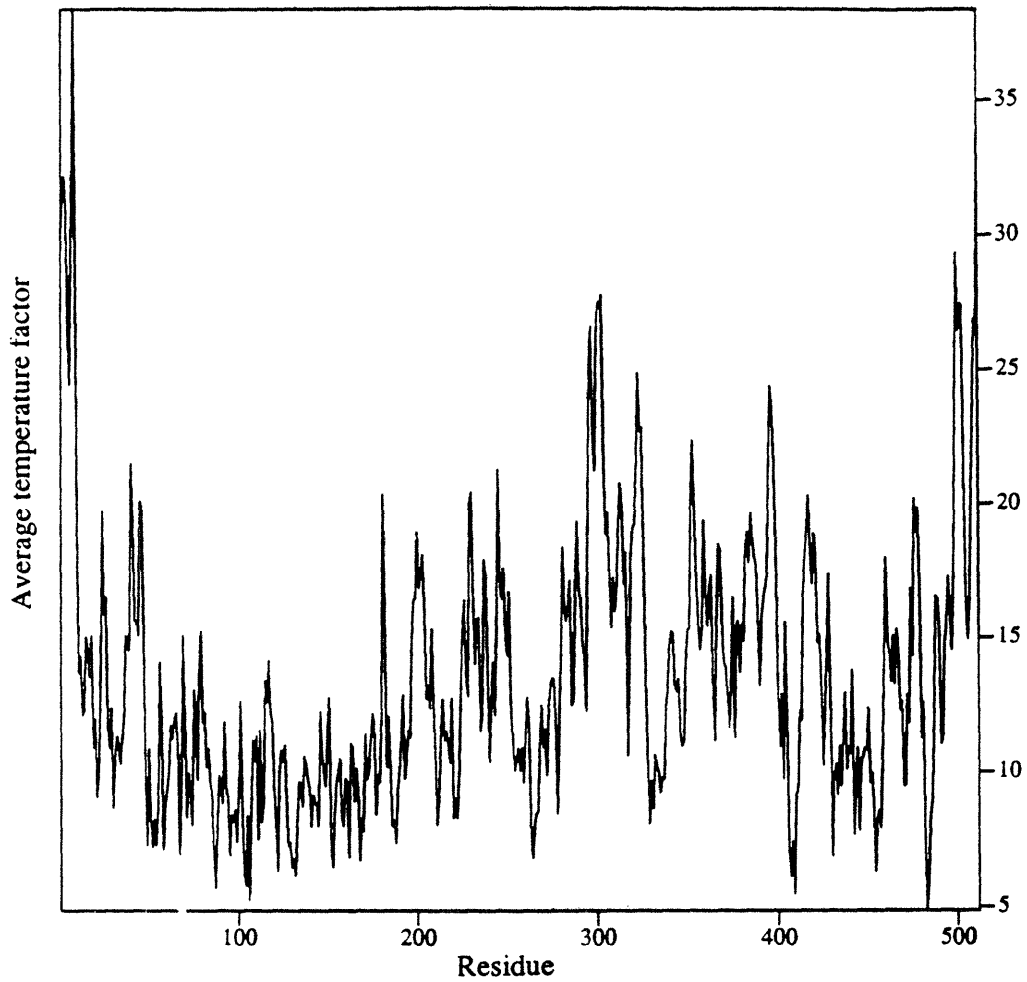


Figure 4.13 Main chain temperature factors for the β subunit. The top plot corresponds to the A protomer and the bottom plot corresponds to the B protomer.

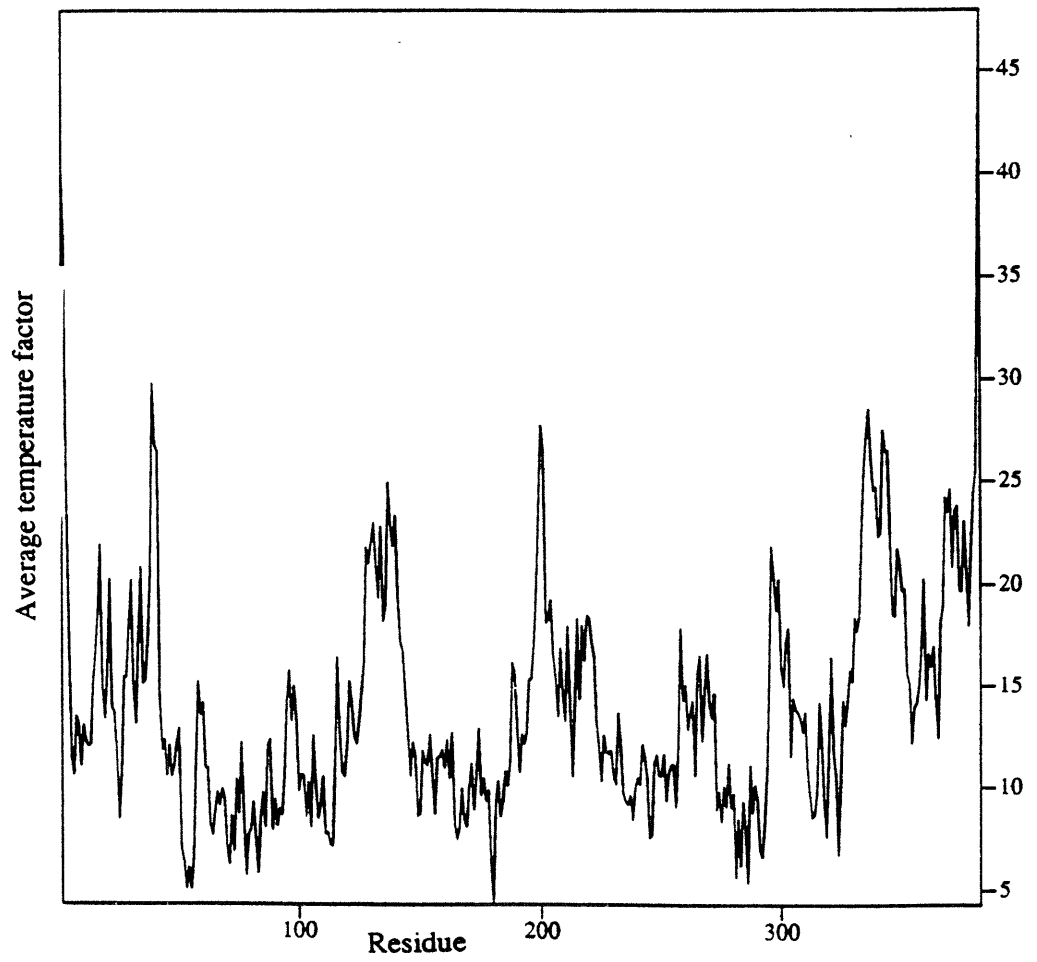
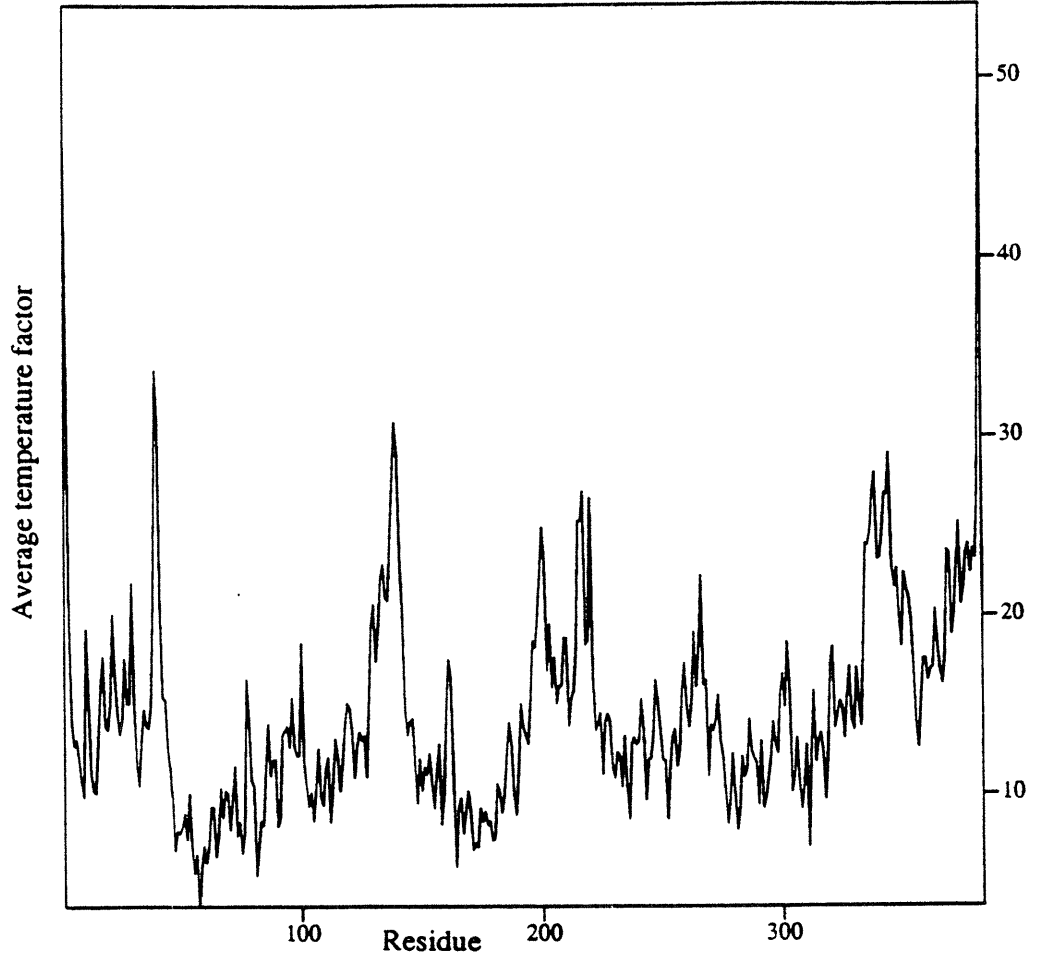
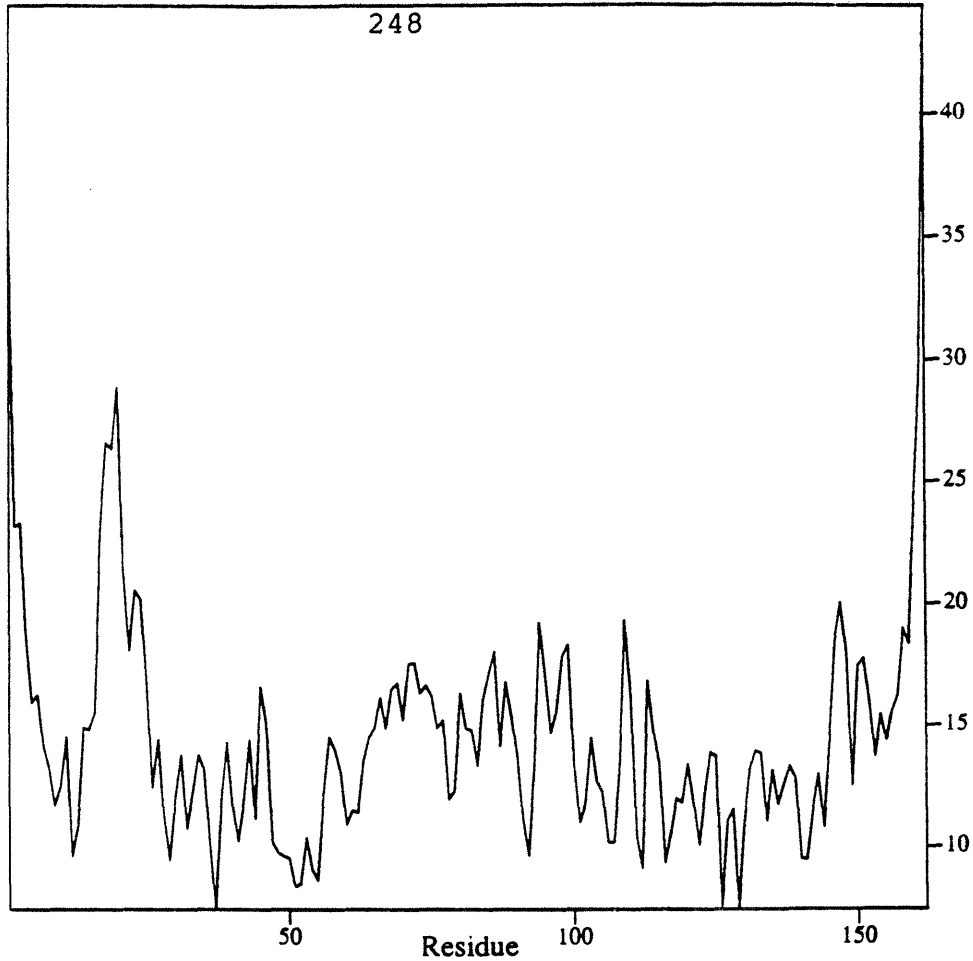


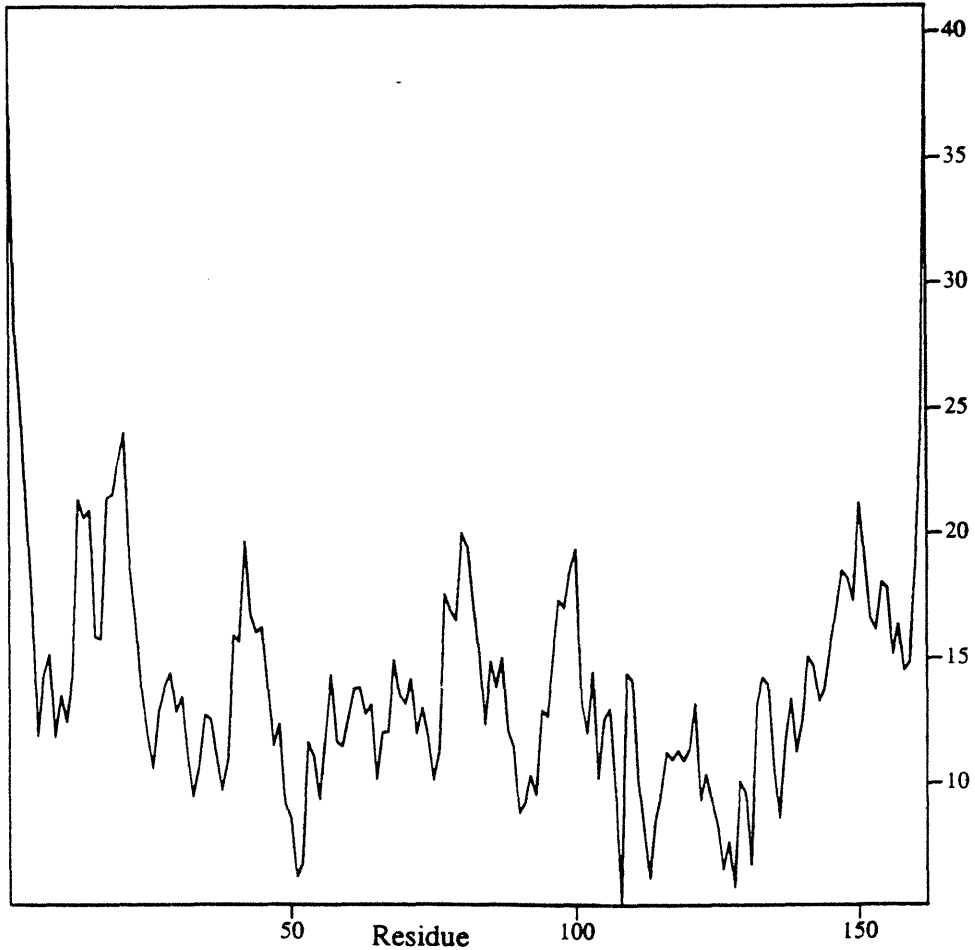
Figure 4.14 Main chain temperature factors for the γ subunit. The top plot corresponds to the A protomer and the bottom plot corresponds to the B protomer.

248

Average temperature factor



Average temperature factor



Chapter 5

The Three-Dimensional Structure of the Hydroxylase

I. Introduction

The 2.2 Å crystal structure of the *M. capsulatus* hydroxylase is presented in this chapter. The three-dimensional structure of the hydroxylase provides several important insights about biological methane oxidation, including how this inert gas might diffuse to and bind near the active site, the identification of protein residues that could participate in the catalytic mechanism, possible domains of interaction with the coupling protein and reductase, and the architecture of the dinuclear iron core.

II. The overall structure

The holo hydroxylase is a relatively flat molecule with approximate dimensions 60 x 100 x 120 Å. The arrangement of the subunits, two $\alpha\beta\gamma$ protomers related by a non-crystallographic twofold symmetry axis, is shown in Figure 5.1. There is a wide canyon running along the dimer interface with an opening in the center of the molecule. The interaction between the two protomers involves helices from the α and β subunits with no participation of the two γ components. Most of the dimer contacts involve the β subunits. Interactions between α and β subunits within the protomers resemble those in the ribonucleotide reductase R2 protein dimer interaction, which has the shape of a heart.^{1,2} The hydroxylase dimer can therefore be viewed as the juxtaposition of two heart-shaped protomers to form a molecule more than twice the size and oriented approximately perpendicular to the two components (Figure 5.1). The secondary structure of the three subunits is primarily helical, with one small region of beta structure in the α subunit.

Secondary structure of the α subunit. The α subunit is shown in Figure 5.2. The dinuclear iron centers are positioned entirely within the α subunits, which is

consistent with chemical labelling experiments.³ The α subunit contains two domains, one of which is comprised of 6 very long helices (A-C and E-G) and 6 smaller ones. This N-terminal domain is arranged in three layers, the first containing helices A-D and 1-2, the second composed of helices E-G and 3, and the third containing helices H and 4. The second domain, at the C-terminus, consists of 8 smaller helices and two beta hairpin motifs. Six of the helices in the first domain are very long (A-C and E-G), with more than 25 residues. The ribonucleotide reductase R2 protein also contains 6 very long helices, and the fold of the α subunit is very similar to that of the R2 protein.^{1,2} The principal helices in the α subunit have therefore been labeled A-H in accord with the nomenclature used for the R2 protein. The iron-coordinating helices of the α subunit and of the R2 protein are superimposed in Figure 5.3. As predicted by a model based on comparisons of the amino acid sequences of the α subunit and the R2 protein (Figure 4.1),⁴ the hydroxylase iron ligands are derived from helices α B, α C, α E, and α F, which form a four helix bundle.

Secondary structure elements of the α subunit are summarized in Table 5.1. There is one 3_{10} helix (Figure 5.4), helix α 8 (residues 403-412), which contains 4 consecutive 1-4 type hydrogen bonds. In addition, 1-4 type hydrogen bonds are observed at the beginning of helix α 1, in the middle of helix α B, at the end of helix α D, at the beginning of helix α E, in the middle of helix α F, at the end of helix α H, and at the ends of helices α 5, α 11, and α 12. This type of 3_{10} hydrogen bonding is commonly observed at the C termini of α helices.⁵ Bifurcated hydrogen bonds, in which a main chain amino group is hydrogen bonded to both the $n-3$ and $n-4$ carbonyl groups,⁶ are present in helices α A, α B, α C, α D, α E, α F, and α H. Main chain N to carbonyl O distances are long for hydrogen bonding in some distorted regions of the helices. Helix α 1 is slightly distorted, and helix α A is distorted at its C-terminus. There are distortions in

helices α B and α F near the diiron center, and helix α D is bent. Helix α 7 is distorted at its N-terminus. Helix α E contains an extra residue in the middle (a π turn), which causes a distortion near the diiron center. As a result, regular 1-5 type hydrogen bonding is disrupted, and some 1-6 type hydrogen bonds are observed. Helix α H, which also contains a π turn, exhibits a similar hydrogen bonding pattern. There are 4 beta strands, labeled β 1- β 4, which form 2 beta hairpin motifs.

A variety of tight turns (Figure 5.4) is found in the α subunit and detailed in Table 5.2. Type III turns, which are characterized by 3_{10} hydrogen bonding, are located at residues 339-342 (B protomer only), at residues 378-381, and at residues 521-524, which are at the C-terminus. The Type III turn at residues 339-342 in the B protomer is replaced by a Type I turn in the A protomer. The α subunit also contains 13 Type I turns, which are present in both protomers and 3 Type II turns, also present in both protomers. Residues 39-42 and 53-56 form Type I turns in the A protomer and Type II turns in the B protomer. Residues 489-492 form a Type II turn in the A protomer and a Type I turn in the B protomer. Both protomers contain one Type I' turn connecting beta strands β 3 and β 4 in the second beta hairpin motif. For both Type II and Type I' turns, Gly is typically found in the third position,^{5,7} and glycine residues occupy the third position in the 3 Type II turns present in both protomers as well as in the Type I' turn.

Secondary structure of the β subunit. The β subunit is shown in Figure 5.5. This subunit, which is completely helical, contains 12 helices, 6 of which are 22 residues or longer. A remarkable feature of the hydroxylase structure is that ten helices of the α and β subunits possess virtually identical folds. The two subunits have completely different primary sequences, however, with no detectable homology. The β subunit therefore also exhibits a fold similar to that seen in the

ribonucleotide reductase R2 protein.^{1,2}, and superimposes quite well with the R2 protein (Figure 5.3). The N-terminal helix of the β subunit lies near the non-crystallographic twofold axis and is connected to the rest of the β subunit by a long connecting loop which wraps around the α subunit.

The secondary structure elements present in the β subunit (Figure 5.5) are listed in Table 5.3. The β subunit contains fewer 1-4 type hydrogen bonds than the α subunit (Table 5.1), with 1-4 hydrogen bonding observed at the C-terminus of helix α G. Bifurcated hydrogen bonds are observed in helices α 1, α A, α C, α 3, α F, α G, and α H. Helices α B and α G are bent at the beginning, resulting in several main chain N to carbonyl O distances too long for regular hydrogen bonding. Helix α E is also bent, and helix α F exhibits a distortion at the C-terminus. The tight turns present in the β subunit are included in Table 5.2. There are 6 Type III turns. Two of these turns are located consecutively in between helices α B and α C. There are two more consecutive Type III turns at the beginning of helix α F. The other Type III turns are found at the end of helix α 1 and at the beginning of helix α E. The β subunit also contains 12 Type I turns, present in both A and B protomers. Residues 100-103 form a Type II turn in the A protomer and a Type I turn in the B protomer. Finally, 4 Type II turns, all of which contain a glycine residue in the third position, are present in the β subunit.

Secondary structure of the gamma subunit. The γ subunit, shown in Figure 5.6, consists of 8 helices, the longest of which, helix α 3, contains 22 residues. These helices are described in Table 5.4. Bifurcated hydrogen bonds are present in helices α 1, α 2, α 6, and α 7. Several main chain N-to-carbonyl-O distances are too long for hydrogen bonding, including 74 O - 78 N in helix α 4, 109 O - 113 N and 112 O - 116 N in helix α 6, and 126 O - 130 N and 134 O - 138 N in helix α 7. There is one Type III turn in the γ subunit, located at the N-terminus of helix α 6. In addition, there are 2 Type I turns, one between helices α 2 and α 3 and one

between helices $\alpha 4$ and $\alpha 5$. Residues 144-147 form a Type II turn with an asparagine residue in the third position, located at the end of helix $\alpha 7$. In protomer A, residues 5-8 form a Type II' turn, and in protomer B, these residues form a Type I turn. Finally, there is a Type VIa cis-proline turn formed by residues 119-122, in between helices $\alpha 6$ and $\alpha 7$.

The dimer. The two copies of each subunit are related to one another by the non-crystallographic twofold symmetry axis with only slight deviations from twofold symmetry. The r.m.s. deviations for the C_{α} carbons are 0.49 Å for the α subunit, 0.31 Å for the β subunit, and 0.45 Å for the γ subunit. Figure 5.7 shows a stereo view of the superpositions of the three subunits from the two halves of the dimer. In addition, the differences between the two halves of the dimer are plotted as a function of residue number for each subunit in Figure 5.8. For the α subunit, the largest deviation is observed for residues 431-438, with the most variation in residues 433 and 434, which lie at the beginning of beta strand $\beta 3$. There are additional deviations at the N terminus (residues 15-30), at residues 51-59, a region near the surface containing many charged residues and the site of a Type I turn in the A protomer and a Type II turn in the B protomer (residues 53-56), and near residue 195, which is at the beginning of helix αE . Residues 336-341, which include a Type I turn in the A protomer and a Type III turn in the B protomer (residues 339-342) and residues 489-494, which are the site of a Type II turn in the A protomer and a Type I turn in the B protomer (residues 489-492) also differ between the two halves of the dimer. The largest differences in the β subunit are found at residues 20-25, which are at the end of helix $\alpha 1$, at residues 39-48, which are at the beginning of helix $\alpha 2$, at residues 101-105, which lie near the opening in the center of the dimer and include a Type II turn in the A protomer and a type I turn in the B protomer (residues 100-103), at residues 306-313, which are at the beginning of helix αG , and at residues 347-351, which are at

the beginning of helix α H. The largest differences for the γ subunit are found at the N-terminus, at residues 16-25, a loop region connecting helices α 1 and α 2, at residues 90-97, which represent most of helix α 5, and at residues 100-102, which connect helices α 5 and α 6. All of these regions of deviation must be carefully examined for possible errors in interpretation of the electron density map.

Heavy atom binding sites. The heavy atom binding sites for the PIP, TAMM, and EMTS derivatives are shown in Table 5.5 and the structure of these three compounds are shown in Figure 5.9. There are 11 PIP binding sites, 10 of which are related by non-crystallographic symmetry. PIP can interact with proteins either covalently, forming a bond with an amino acid side chain, or ionically, through electrostatic, ion pair, van der Waals' or hydrogen bonding interactions.⁸ In the hydroxylase, PIP binds primarily to methionine residues with just one cysteine binding site, Cys517, and one histidine binding site, His382, both in the α subunit. The site at γ Met31 is the strongest with consistently high occupancies. Thiolate anion, the methionine S-CH₃ group, and the unprotonated imidazole are all good nucleophiles, suggesting that the PIP is bound covalently in these sites. Possible covalent binding modes for PIP⁸ are shown in Figure 5.9. A comparison of the B-values for the PIP sites and those for the TAMM, K₂PtCl₄ and Pt(NH₃)₂Cl₂ derivatives (Table 4.6) suggests that binding modes b or c, those involving just 1-2 heavy atoms, are probable. Six of the methionine sites are located quite near the surface of the molecule, 4 in the γ subunit and 2 in the α subunit. The α Met70 site is found in the canyon near the opening in the center of the dimer. The Cys517 site, which is also found in the TAMM and EMTS derivatives, is at the C-terminus of the α subunit. Finally, the His382 site is located near the surface in the α subunit, and is not found in the B protomer, perhaps due to differences in the crystal lattice contacts for the two protomers in this region.

In contrast to PIP, which appears to bind with just 1 or 2 heavy atoms, the TAMM derivatives probably contain all 4 Hg atoms. The B-values for the TAMM sites are quite high as compared to those for the other derivatives (Table 4.4). Six of the TAMM binding sites occur at cysteine residues, 3 at one of the 2 cysteine residues in the β subunit, Cys302. This cysteine residue is located in the canyon at the dimer interface. The two sites identified at this location in the B protomer, T2 and T10, may actually represent the same site. There is one cysteine TAMM site in the α subunit, Cys426, which is in the β hairpin region, close to the surface. This site is also an EMTS binding site. Another site, at α_A His382 is close to the Cys426 site, but as in the PIP derivative, is only present in the A protomer. TAMM only binds to the α Cys517 site, which is present in all three derivatives, in the B protomer. There are also TAMM binding sites at the $\alpha\beta$ interface, involving residues γ His7 and α His486. Two sites are located in this region in the A protomer (T5 and T11), but only one site is found here in the B protomer. Finally, it is unclear which residue is involved in site T7, which lies near a crystal lattice contact and may involve a disordered part of the β subunit N-terminus.

The EMTS binding sites are located exclusively at cysteine residues (Table 5.5), which suggests that EMTS is particularly selective for this amino acid. Like TAMM, EMTS binds at β Cys302 in both protomers. In addition, EMTS binds to 2 cysteine residues in the α subunit near the diiron center, Cys151 and Cys211. The position of Cys151 corresponds to the position of the functionally important tyrosyl radical Tyr122 in the ribonucleotide reductase R2 protein, an observation which was first predicted by sequence homology between the α subunit and the R2 protein.⁴ When the α subunit and the R2 protein are superimposed (Figure 5.3), Cys151 is located 2.3 Å from the Tyr122 OH, in the direction away from the iron atoms. Cys211 is located near the active site and near the canyon at the dimer interface. The EMTS binding site at α Cys517 is also a binding site for PIP

and for TAMM, indicating that this site is particularly accessible. Finally, there is an EMTS binding site at α Cys426 in the B protomer, also seen in the TAMM derivative. It is not clear why EMTS does not bind at this site in the A protomer.

Charged residues and subunit-subunit interactions. Charged residues buried in the three subunits of the hydroxylase are listed in Tables 5.6 - 5.8. The α subunit contains ~50 buried charged residues, the greatest number of which are glutamic acid residues (Table 5.6). Most of these charged residues are located at subunit-subunit interfaces, and are often involved in hydrogen bonding with residues from other subunits. There are also a large number of water molecules at the subunit-subunit interfaces. There are a number of salt bridges linking the subunits within each protomer, including α Glu230- β Arg9, α Glu454- γ Arg156, α Glu462- γ Arg143, α Glu465- γ Arg44, α Glu465- β Lys75, and α Lys185- β Asp68. Two such interactions, α Glu465- β Lys75 and α Lys185- β Asp68, are shown in Figure 5.10 Several charged residues, including α Asp164, α Asp170, α Glu101 and α Lys104 are located near the loop region of the β subunit which connects helix α 1 of the β subunit to the rest of the β subunit. In addition to the subunit-subunit interfaces within each protomer of the dimer, there are charged residues buried at the dimer interface, some of which participate in the dimer interaction. For example, α Arg94 is linked by a hydrogen bond to the carbonyl group of Thr12 on the β_B subunit.

The opening in the center of the molecule at the dimer interface contains many charged residues, including α Lys65 and α Lys74. This region of charged residues extends in the direction of the active site, with significant stretches of charged residues in both helices α A (residues 66-77) and α F (residues 240-245). The other internal charged residues in the α subunit are associated with the diiron center. Four glutamate residues, Glu114, Glu144, Glu209, and Glu 243, are coordinated to the iron atoms. In addition, Asp143 and Asp242 are hydrogen

bonded to the ϵ -N atoms of two coordinated histidine residues, Asp143 to His246 and Asp242 to His147. These hydrogen bonds link helices α C and α F.

The β subunit also contains close to 50 internal charged residues, with a large number of aspartic acid residues (Table 5.7). Most of these residues are located at subunit-subunit interfaces. In addition to the $\alpha\beta$ salt linkages described above, there are several interactions between the β and γ subunits, including β Asp61- γ Arg12, β Arg91- γ Glu61, and β Glu86- γ Arg115. Since most of the dimer interaction involves the two β subunits, there are extensive hydrogen bonding interactions between the β_A and β_B subunits, mostly occurring near the opening in the center of the dimer. Residue β_A Arg122 is linked to β_B Glu115 and β_B Glu116 while β_A Glu115 is hydrogen bonded to β_B Arg118 and β_B Arg122 and β_A Glu116 is linked to β_B Arg122. There are a few internal charged residues in the γ subunit as well (Table 5.8), located mainly at subunit-subunit interfaces and involved in the interactions with the α and β subunits mentioned above. The importance of the specific residues in the 3 subunits involved in inter-subunit linkages is underscored by the fact that every one of these residues is conserved between the *M. capsulatus* and *M. trichosporium* gene sequences,^{9,10} which exhibit overall sequence identities of 85% for the α subunit, 59% for the β subunit, and 49% for the γ subunit. Finally, charged residues cover the surface of the hydroxylase with the exception of one small region near the second domain of the α subunit, encompassing residues 412-416, 425-428, and 433-435.

The only information about the arrangement of the three subunits prior to the X-ray structure was derived from chemical cross-linking experiments with the *M. trichosporium* hydroxylase.¹¹ Reaction of the holo hydroxylase with the covalent zero length cross-linking reagent 1-ethyl-3-(3-dimethylaminopropyl)-carbodiimide (EDC) resulted in several products, two of which were identified as an attachment of the α and β subunits and a dimer of β subunits. Since EDC is a

zero-length cross-linking reagent, the sites of attachment probably correspond to salt bridges. As described above and listed in Tables 5.6 - 5.8, there are a number of α - β subunit salt linkages, some of which are good candidates for cross-linking sites, including α Glu465- β Lys75, α Lys185- β Asp68, and α Lys65- β Asp188. In addition, there are significant interactions between the two β subunits in the dimer. No cross-linking of the γ subunit was observed, even in the presence of a cross-linking catalyst.¹¹ Although the γ subunit is located on the sides of the dimer and does not participate in the dimer interaction, there are interactions between the γ subunit and the other two subunits. All the inter-subunit salt bridges with the γ subunit involve arginine residues, which have a high pK_a , and are less likely to form a stable amide bond than lysine residues. The interactions between the two β subunits also involve only arginine residues, which suggests that no $\beta\beta$ cross-linking should occur. A low yield $\beta\beta$ cross-linked product was observed, however.¹¹ The cross-linking experiments were carried out on the *M. trichosporium* hydroxylase, which could account for discrepancies between the cross-linking data and the X-ray structure if the two structures were different. Since every residue involved in inter-subunit interactions in the *M. capsulatus* hydroxylase is conserved in the *M. trichosporium* sequence, however, it is highly unlikely that the two structures have different subunit interactions.

Water molecules. The hydroxylase contains a large number of internal water molecules, many of which are located at the subunit-subunit and dimer interfaces. Most of these water molecules are hydrogen bonded to at least one protein atom. Typically, the best ordered water molecules are involved in multiple hydrogen bonding interactions and have lower temperature factors than the less ordered water molecules.⁶ In the hydroxylase structure, the buried water molecules have B-values of 10-25 Å² whereas the surface accessible water molecules have higher B-values, usually > 25 Å².

Crystal packing interactions. The hydroxylase molecules are stacked along the thin dimension (Figure 5.11). The molecules are tightly packed, consistent with the solvent content of 44%, which is slightly low value for a protein crystal.¹² The tight packing may account for the excellent diffraction by these crystals. Most of the interactions between molecules in the crystal occur at the top surface of the large heart formed by the two $\alpha\beta\gamma$ protomers and on the sides of the molecule, near the γ subunit. There is a large space between molecules in the region of the canyon formed at the dimer interface. The major contacts involve the α and γ subunits. Specifically, residues α_A 385-392 interact with residues γ_A 27-37, residues α_A 499-505 interact with residues γ_A 43-46, and residues α_A 258-259 and α_A 319-325 interact with residues γ_A 13-21. This last interaction is also present for the α and γ subunits in the B protomer. In addition, residues α_B 373-374 and 381 interact with residues γ_A 96 and 99 in a contact between the two different protomers. The remainder of interactions include two contacts between the α and β subunits, involving residues α_A 377-381 with residues α_B 392-393 and residues α_A 427-435 with residues α_B 504-505. Finally, there is one region of contact between the β and γ subunits, where residues β_A 220-222 interact with residues γ_B 153-165.

III. The iron center and the active site

Location of the diiron center. The dinuclear iron centers reside completely within the α subunits, one on each α subunit in the dimer. Therefore, the *M. capsulatus* hydroxylase can accommodate 4 Fe atoms, although the purified enzyme typically contains closer to 2 Fe per protein molecule.¹³ It may be that 4 Fe hydroxylase was selectively crystallized from a mixture containing some apo (iron-free) and/or iron-depleted protein. Preliminary data have indicated that apo hydroxylase can be precipitated by centrifugation, resulting in a 4 Fe

preparation.¹⁴ The presence of two diiron centers is consistent with quantitative work on the *M. trichosporium* hydroxylase.¹⁵ In a recent study of the *M. capsulatus* hydroxylase, however, reconstitution of the apo hydroxylase with Mn(II) ions was quantitated by EPR spectroscopy and yielded a value of 2 Mn(II) ions per hydroxylase dimer, thus suggesting that the hydroxylase only contains a single diiron site.¹⁶ The two diiron centers are 45 Å apart, each housed in a four helix bundle comprised of helices α B, α C, α E, and α F, which contribute the coordinating ligands. Helices α E and α F, which form part of the canyon, separate the iron atoms from the solvent.

Coordination of the iron atoms. The $2F_o-F_c$ and F_o-F_c electron density maps of the diiron center in the B protomer are shown in Figure 5.12, and a schematic representation of the iron core is shown in Figure 5.13. The iron-to-ligand bond distances and angles are listed in Tables 5.9 and 5.10. The two iron atoms are 3.4 Å apart in both protomers (Table 5.9), a distance consistent with EXAFS studies of the *M. capsulatus* and *M. trichosporium* hydroxylases.¹³ By contrast, an Fe...Fe distance of 3.0 Å has been reported for the hydroxylase from *Methylobacterium* CRL-26.¹⁷ The iron atoms are doubly bridged by two exogenous ligands. These two non-protein ligands, which appeared in F_o-F_c maps during the late stages of the refinement, have been assigned as a bridging hydroxide and a bridging acetate. The Fe1- μ OH distance is 1.7 Å in both protomers and the Fe2- μ OH distance is 2.0 Å in both protomers, suggesting that the hydroxide bridge may be asymmetrical. At 2.2 Å resolution, however, the r.m.s. deviation of these distances could be as much as ± 0.3 Å.¹⁸ The lack of a short Fe-O distance in the EXAFS data for the hydroxylase¹³ and the absence of Raman and optical spectroscopic features typical of a μ -oxo bridge are consistent with the presence of a hydroxo bridge in the diferric Fe(III)Fe(III) hydroxylase. Furthermore, the presence of a hydroxo bridge in the mixed valent Fe(II)Fe(III) form has been

revealed by proton ENDOR studies.^{19,20}

The second exogenous ligand has been modeled as acetate because the crystallization buffer contained 50 mM ammonium acetate. Another possibility for this ligand is bicarbonate ion, but there are no hydrogen bonding interactions with this ligand. If this ligand is present in the resting enzyme in cells, it would be lost upon reduction of the diiron center during the catalytic cycle. During turnover, the oxidized substrate, methoxide ion, could occupy the space occupied by the acetate ligand prior to protonation and release from the active site. Other ions such as azide,¹⁶ fluoride,²¹ and phenoxide²² have been reported to bind to the diiron center. Crystalline needles of the hydroxylase can be obtained in the absence of acetate (Table 4.1), and if larger crystals can be obtained, collection of data on this material may clarify the nature of this ligand. The acetate ligand has not refined well, with discrepancies between the two halves of the dimer and better overall results for the B protomer. The Fe1-Ac O1 distance is 3.2 Å in both protomers, but the Fe1-Ac O2 distance is 2.8 Å in the A protomer and 2.0 Å in the B protomer. The Fe2-Ac O1 distance is 2.2 Å in the A protomer and 2.0 Å in the B protomer, whereas the Fe2-Ac O2 distance is 3.9 Å in the A protomer and 3.4 Å in the B protomer.

In addition to the two bridging exogenous ligands, there is a semi-bridging carboxylate ligand, Glu144. The Fe1-O distances for Glu144 are 2.1 and 2.2 Å, which are normal coordinating distances, but the Fe2-O distances of 2.5 and 2.7 Å are high for coordinating distances. Glu144 has therefore been characterized as a semi-bridging ligand. In the absence of the acetate ligand, Glu144 might become a normal bidentate bridging ligand. In addition, there is a hydrogen bond between Glu144 and Gln140, which may affect the bond between Glu144 and Fe2. This type of variation in binding modes of carboxylate ligands to dinuclear metal centers, called the carboxylate shift,²³ has been observed in

many small molecules, and is observed in the ribonucleotide reductase R2 protein upon reduction to the diferrous form.²⁴

Fe1 is also ligated by a monodentate carboxylate, Glu114, a histidine δ -nitrogen atom, His147, and a water molecule, resulting in pseudooctahedral coordination. There is a hydrogen bond between Glu114 and the water molecule. The bond angles for the B protomer (Table 5.10) are all within 10° of perfect octahedral geometry, but the A protomer exhibits more variation, due to the long Fe1-Ac O2 bond distance. The Fe1-O distance for Glu114 is 1.9 Å in both protomers. The Fe1-N distance for His147 is 2.4 Å in the A protomer and 2.2 Å in the B protomer. The water molecule, which was detected in F_o-F_c difference Fourier maps, has Fe1-O bond distances of 2.2 Å and 2.4 Å. The presence of a terminal OH^- or H_2O ligand in the mixed valent Fe(II)Fe(III) hydroxylase has been previously detected by proton ENDOR spectroscopy.¹⁹ If this ligand is assigned as water and the monodentate bridging ligand is assigned as hydroxide ion, the overall charge of the active site is neutral.

The second Fe atom, Fe2, is also coordinated by a histidine ligand, His246, with an Fe2-N distance of 2.2 Å. Like the R2 protein,² the Fe atoms in the hydroxylase are coordinated by the δ -nitrogen atoms of the histidine ligands. By contrast, in hemerythrin, which also contains a diiron center, the histidine ϵ -nitrogen atoms are coordinated to the iron atoms.²⁵ Two monodentate carboxylate ligands, Glu209 and Glu243 complete the coordination of Fe2, with Fe2-O distances of 2.3 Å and 1.9 Å for Glu209 and 1.8 Å and 1.9 Å for Glu243. There is a hydrogen bond between Glu243 and the water molecule coordinated to Fe1. The bond angles for Fe2 deviate more from octahedral coordination values in both protomers than those for Fe1. All of the iron-coordinating residues are conserved in the sequences of the *M. capsulatus*⁹ and *M. trichosporium*¹⁰ proteins, with the exception of Glu209, which is an aspartic acid

in the *M. trichosporium* hydroxylase. This difference may account for some subtle variations in reactivity observed for the two enzymes.^{26,27} The overall coordination of the diiron center accounts well for the spectroscopic properties of both enzymes,^{13,28} including the asymmetry of the diiron center described for the *M. trichosporium* hydroxylase.²⁸ Therefore, it is likely that the two active sites are quite similar.

The two histidine ligands are involved in hydrogen bonding interactions (Figure 5.14), which may explain why the hydroxylase contains a hydroxo bridge rather than an oxo bridge, as found in the R2 protein.² Each histidine ϵ -nitrogen atom is hydrogen bonded to an aspartic acid residue, His147 to Asp242 and His246 to Asp143. These interactions link helices α C and α F. In addition, Asp143 hydrogen bonds to Arg245 and His67, and Asp242 hydrogen bonds to Arg146 and Arg245. These negatively charged aspartic acid residues, along with the bridging acetate anion, will raise the pK_a value of the bridging hydroxo ligand. In the R2 protein, only one of the histidine residues, His118, is hydrogen bonded to an aspartic acid residue, Asp237. This residue is in turn hydrogen bonded to Trp48, which is proposed to be involved in electron transfer.² There is no analogous residue present in the hydroxylase. The other histidine ligand in the R2 protein, His241, is hydrogen bonded to a glutamine residue, Gln43.

Access to and composition of the active site. The diiron center and surrounding residues, shown in Figure 5.15, form a cavity, which is shown in Figure 5.16 as Cavity I. The two iron atoms and the coordinating residues are located on one surface of this cavity. The rest of the cavity, with the exception of Thr213, is lined with hydrophobic side chains, including Ile217, Ile239, Phe236, Leu110, Phe188, Ala117, Phe192, Leu204, and Gly208. This type of environment, consisting of a metal binding site with a shell of hydrophilic coordinating residues surrounded by a second shell of hydrophobic residues, has been

observed in a variety of metalloproteins.²⁹ The diiron center in the R2 protein is also located in a hydrophobic cavity,² which is smaller by at least 2 Å in some directions than that found in the hydroxylase. The hydroxylase cavity must accommodate a wide range of substrates, including small molecules like methane as well as larger compounds like 2,2-diphenyl-methylcyclopropane, whereas the R2 protein does not bind exogenous substrates. Instead, the diiron center in the R2 protein catalyzes the oxidation of Tyr122 to a tyrosyl radical, which is involved in ribonucleotide reduction. In the hydroxylase, Cys151 is located in the position that Tyr122 occupies in the R2 protein. This cysteine residue is in the back of the active site cavity, and its accessibility is demonstrated by the fact that it binds to a mercury atom in the EMTS derivative (Figure 5.17). The Fe-Cys S distances are 10.3 and 10.4 Å for the two protomers (Table 5.9).

The α subunit contains a number of additional hydrophobic cavities (Figure 5.16), most of which are located between the active site and the second domain. Although there is no direct pathway to the active site from the surface of the protein, these cavities may demarcate a route for substrate to access the active site. The pocket closest to the diiron center (Cavity II) is completely hydrophobic, lined with residues Val105, Val106, Phe109, Leu110, Met184, Phe188, Leu216, Phe282, Val285, Leu286, and Leu289; it does not contain a single water molecule. Conformational changes in the side chains of either Phe188 or Thr213 could result in direct linkage of this cavity to the active site cavity. Two more large cavities (Cavities III and IV, Figure 5.16) lie just beyond Cavity II, and almost reach the surface. These two cavities are also lined with primarily hydrophobic side chains (Cavity III: Lys98, Glu101, Thr102, Val105, Leu180, Met288, Leu289, Val292, Gly293, Tyr347, Ala350, Phe359, Arg360, Leu361, Ala362, Val501; Cavity IV: Phe109, Arg175, Gly178, Pro179, Leu180, Trp181, Leu346, Leu349, Ala350, Leu353, Trp354, Thr356, Gly357, Phe359, Leu361,

Pro424). It is conceivable that substrate could approach the active site through these pockets, that product could leave by this pathway, or that both substrate and product could access the active site via these pockets. Alternatively, the active site could be accessed by a much shorter route, between helices E and F. The distance from the diiron center to the surface in this region is only $\sim 10\text{-}12$ Å. Finally, there is another extremely large cavity, with approximate dimensions $5 \times 6 \times 11$ Å, evident in Figure 5.16 (Cavity V). This cavity, which is lined with all types of side chains and contains a number of water molecules, seems less likely to be linkable either to the active site or to the surface.

The catalytic mechanism. The mechanism by which oxygen is activated for incorporation into methane is the focus of current research efforts utilizing both the *M. capsulatus* and the *M. trichosporium* proteins. The hydroxylase mechanism has often been proposed to resemble the cytochrome P450 mechanism,³⁰⁻³² which involves a high valent ferryl intermediate and a substrate radical. Like MMO, cytochromes P450 also activate oxygen for incorporation into a wide variety of substrates.³⁰ An intermediate detected for the *M. trichosporium* hydroxylase has been assigned as a diferryl species based on freeze quench Mössbauer studies.³³ In addition, evidence for substrate radical intermediates has been reported for the *M. trichosporium* enzyme.^{26,34} The use of radical clock substrates revealed no evidence for radical intermediates for the *M. capsulatus* enzyme, however,²⁷ and several mechanisms which do not involve substrate radicals have been proposed for the *M. capsulatus* hydroxylase.^{27,35}

One of these mechanisms, shown in Figure 5.18, is directly related to the structure in that Cys151, which occupies the same position as Tyr122 in the R2 protein, is involved. This mechanism would account for the results of the radical clock experiments. The sulfur atom of Cys151 is 7.1 Å from Fe1 in the A protomer and 7.2 Å from Fe1 in the B protomer. In the R2 protein, the oxygen

atom of Tyr122 is located 5.3 Å from the closest iron atom. Since Cys151 binds to a mercury atom in the EMTS derivative, inactivation of the enzyme by EMTS or by similar compounds would provide some evidence that this cysteine residue is mechanistically important. These experiments are now in progress. Additional information could be gained from site-directed mutagenesis experiments.

The coordination of the diiron center and the surrounding environment also provides some clues about what might occur during the catalytic cycle. The bridging acetate ligand and the terminal water ligand indicate possible binding sites for dioxygen to the reduced hydroxylase, for peroxy and oxo ligands in intermediates and for methoxide ion and other oxidation products. The hydrophobic residues present in the active site pocket may be involved in positioning substrate near the diiron center during catalysis. Finally, Thr213, which is the only protonated side chain in the active site cavity besides Cys151, might supply protons during catalysis, as has been proposed for Thr252 in cytochrome P450.^{36,37}

Comparison to cytochromes P450. As mentioned above, the hydroxylase has often been compared to cytochromes P450 based on its similar reactivity. In cytochrome P450_{CAM}, there is a hydrophobic pocket near the oxygen activation site on the heme.^{36,37} This cavity contains two residues, Gly249 and Thr252, conserved in all cytochromes P450, which have very divergent sequences.³⁸ These residues are located in the I helix, which is 34 residues long, and sit at the position of a distortion in the helix which results from the presence of an extra residue (a π turn). When Thr252 is changed to an alanine, the resulting mutant P450 is less efficient at oxidation, and an uncoupling of the hydroxylation reaction is observed, resulting in the production of hydrogen peroxide and water rather than hydroxylated product. The X-ray structure of this mutant protein shows that helix I is even more distorted and that solvent molecules have greater

access to the substrate binding cavity.³⁷ In the hydroxylase, Thr213 is located at a similar distortion in helix α E. The presence of a threonine residue at a helical distortion may very well be an important feature conserved in dioxygen activation centers in enzymes, the function of which could either be structural, stabilizing the helical distortion through hydrogen bonding, and/or catalytic, controlling the delivery of protons.

IV. Component Interactions

The methane monooxygenase system involves two proteins in addition to the hydroxylase, both of which are essential for activity. The reductase (MW 38.6 kDa) transfers electrons from NADH to the hydroxylase and contains two cofactors, a 2Fe-2S cluster and an FAD molecule.³⁹ The coupling protein (MW 15.5 kDa) has been implicated in several regulatory roles. No crystallographic data are currently available for these two proteins. Since the coupling protein perturbs the EPR spectrum of the hydroxylase and changes the redox potential of the diiron center,^{11,40} it is expected to bind to the hydroxylase close to the active site. In addition, cross-linking of the coupling protein and the α subunit has been observed.¹¹ Although oxidation can occur in the absence of coupling protein if hydrogen peroxide is added to the diferric hydroxylase or if dioxygen is added to the diferrous hydroxylase (single turnover),^{41,42} the binding of coupling protein dramatically affects both the rate and regioselectivity of substrate oxidation.^{41,42} For example, the addition of coupling protein has been reported to induce at least a 30-fold increase in the rate constant for the formation of 4-nitrophenol from nitrobenzene.⁴²

These experiments strongly suggest that the coupling protein causes a conformational change in the active site. The binding of coupling protein could affect one or more of the iron-coordinating helices, thus changing the active site

cavity and even the coordination of the diiron center, probably in the form of carboxylate shifts. The canyon formed between the two $\alpha\beta$ pairs of the hydroxylase dimer provides a good candidate for the coupling protein binding site. The coupling protein could bind in this canyon near the iron-coordinating helices E and F, which are exposed in the canyon, and affect the diiron center through these helices, specifically through the carboxylate ligands Glu209 and Glu243. Since the hydroxylase dimer binds 2 moles of coupling protein for optimal activity,¹¹ another molecule of coupling protein could bind in the other canyon related by the non-crystallographic twofold symmetry.

The reductase does not affect the spectroscopic properties of the diiron center and does not affect product distributions, but has been shown to interact with the hydroxylase. Cross-linking of the reductase to the β subunit has been observed.¹¹ If the reductase binds closer to the β subunit than to the α subunit, it is reasonable that perturbations of the diiron center are not observed. In addition, binding of the reductase has been shown to quench the tryptophan fluorescence of the hydroxylase by 86%.¹¹ The reductase may bind in the canyon also, but closer to the β subunit. Because the α and β subunits are both large proteins, the exposed surface areas in the canyon provide enough space for both the reductase, which is a bit smaller than the β subunit and the coupling protein, which is smaller than the γ subunit, to bind. If the reductase quenches tryptophan fluorescence of the hydroxylase, it is likely that it binds near exposed tryptophan residues. There are approximately 15 tryptophan residues in the canyon. Of these residues, two, Trp31 on the α subunit and Trp43 on the β subunit, are the most probable candidates for quenching by binding of the reductase. The other tryptophan residues are either already quite buried or are too close to the active site and the proposed coupling protein binding site. The reductase, which is approximately the size of the β subunit, could interact with

both of these tryptophan residues.

V. Comparison to other diiron proteins

The alignment of the α subunit sequence with that of the R2 protein of ribonucleotide reductase resulted in a model of the iron center in the hydroxylase that was quite accurate.⁴ In Figure 5.19 (adapted from ref. 45), the sequences of the α subunit and of the R2 protein are compared to the sequences of several other proteins involved in reactions with dioxygen. Although there is no strong overall homology among any of these proteins, sequences analogous to those containing the iron-coordinating ligands in the α subunit and in the R2 protein are present in each of these proteins. Phenol hydroxylase, which catalyzes the oxidation of phenol to catechol,⁴³ and toluene-4-monooxygenase, which converts toluene to *p*-cresol,⁴⁴ both contain two Asp-Glu-X-Arg-His sequences, similar to the iron-coordinating sequences in the hydroxylase. These proteins may contain a dinuclear center like those found in the hydroxylase and the R2 protein. A dinuclear iron center has recently been discovered in stearoyl acyl carrier protein Δ -9 desaturase, and also contains two Glu-X-Arg-His segments in its proposed iron-coordinating sequence.⁴⁵ Finally, rubrerythrin, for which no reaction with dioxygen has yet been reported, also contains two Glu-X-X-His sequences, which are postulated to ligate the iron atoms in a non-heme iron center.⁴⁶ These sequence comparisons may prove very useful in determining the three-dimensional structures of the other non-heme iron proteins, which will ultimately lead to an understanding of the factors that govern the differential reactivities of the diiron centers.

VI. Conclusions

The three-dimensional structure of the hydroxylase is an important step

toward a complete understanding of the biological oxidation of methane. The hydrophobic pocket near the diiron center provides insight as to how methane might bind at the active site, and the other cavities suggest possible routes for the entry of substrate and the departure of product. Specific amino acid residues such as Cys151 and Thr213 are obvious targets for site-directed mutagenesis experiments aimed at unraveling the catalytic mechanism. In addition, the identification of all the amino acid residues in the first and second coordination spheres of the two iron atoms will facilitate interpretation of kinetic and time-resolved spectroscopic studies. The structure also reveals possible binding sites for the coupling protein and the reductase. Confirmation of these binding sites requires X-ray structure determinations of the hydroxylase in the presence of the other proteins, if co-crystals can be obtained. In addition, site-directed mutagenesis experiments can identify specific residues essential for complex formation. The combination of X-ray crystallographic investigations with site-directed mutagenesis experiments and ongoing kinetic and spectroscopic studies will undoubtedly provide much more information about this remarkable enzyme system in the future.

References

- (1) Nordlund, P.; Sjöberg, B.-M.; Eklund, H. *Nature* **1990**, *345*, 593-598.
- (2) Nordlund, P.; Eklund, H. *J. Mol. Biol.* **1993**, *231*, 123-164.
- (3) Prior, S. D.; Dalton, H. *FEMS Microbiol. Lett.* **1985**, *29*, 105-109.
- (4) Nordlund, P.; Dalton, H.; Eklund, H. *FEBS Lett.* **1992**, *307*, 257-262.
- (5) Richardson, J. S. *Advan. Prot. Chem.* **1981**, *34*, 167-338.
- (6) Baker, E. N.; Hubbard, R. E. *Prog. Biophys. Mol. Biol.* **1984**, *44*, 97-179.
- (7) Sibanda, B. L.; Thornton, J. M. *Nature* **1985**, *316*, 170-174.
- (8) O'Halloran, T. V.; Lippard, S. J.; Richmond, T. J.; Klug, A. *J. Mol. Biol.* **1987**, *194*, 705-712.
- (9) Stainthorpe, A. C.; Murrell, J. C.; Salmond, G. P. C.; Dalton, H.; Lees, V. *Arch. Microbiol.* **1989**, *152*, 154-159.
- (10) Cardy, D. L. N.; Salmond, G. P. C.; Murrell, J. C. *Mol. Microbiol.* **1991**, *5*, 335-342.
- (11) Fox, B. G.; Liu, Y.; Dege, J. E.; Lipscomb, J. D. *J. Biol. Chem.* **1991**, *266*, 540-550.
- (12) Matthews, B. W. *J. Mol. Biol.* **1968**, *33*, 491-497.
- (13) DeWitt, J. G.; Bentsen, J. G.; Rosenzweig, A. C.; Hedman, B.; Green, J.; Pilkington, S.; Papaefthymiou, G. C.; Dalton, H.; Hodgson, K. O.; Lippard, S. J. *J. Am. Chem. Soc.* **1991**, *113*, 9219-9235.
- (14) Valentine, A. M.; Lippard, S. J., unpublished results.
- (15) Fox, B. G.; Froland, W. A.; Dege, J. E.; Lipscomb, J. D. *J. Biol. Chem.* **1989**, *264*, 10023-10033.
- (16) Atta, M.; Fontecave, M.; Wilkins, P. C.; Dalton, H. *Eur. J. Biochem.* **1993**, *217*, 217-223.
- (17) Prince, R. C.; George, G. N.; Savas, J. C.; Cramer, S. P.; Patel, R. N. *Biochim. Biophys. Acta* **1988**, *952*, 220-229.

- (18) Petsko, G., personal communication.
- (19) DeRose, V.; Liu, K. E.; Lippard, S. J.; Hoffman, B. J. *Am. Chem. Soc.* **1993**, *115*, 6440-6441.
- (20) Thomann, H.; Bernardo, M.; McCormick, J. M.; Pulver, S.; Andersson, K. K.; Lipscomb, J. D.; Solomon, E. I. *J. Am. Chem. Soc.* **1993**, *115*, 8881-8882.
- (21) Hamman, S.; Atta, M.; Ehrenberg, A.; Wilkins, P.; Dalton, H.; Beguin, C.; Fontecave, M. *Biochem. Biophys. Res. Commun.* **1993**, *195*, 594-599.
- (22) Andersson, K. K.; Elgren, T. E.; L. Que, J.; Lipscomb, J. D. *J. Am. Chem. Soc.* **1992**, *114*, 8711-8713.
- (23) Rardin, R. L.; Tolman, W. B.; Lippard, S. J. *New J. Chem.* **1991**, *15*, 417-430.
- (24) Aberg, A. Ph. D. Thesis, Stockholm University, 1993.
- (25) Sheriff, S.; Hendrickson, W. A.; Smith, J. L. *J. Mol. Biol.* **1987**, *197*, 273-296.
- (26) Priestley, N. D.; Floss, H. G.; Froland, W. A.; Lipscomb, J. D.; Williams, P. G.; Morimoto, H. *J. Am. Chem. Soc.* **1992**, *114*, 7561-7562.
- (27) Liu, K. E.; Johnson, C. C.; Newcomb, M.; Lippard, S. J. *J. Amer. Chem. Soc.* **1993**, *115*, 939-947.
- (28) Fox, B. G.; Hendrich, M. P.; Surerus, K. K.; Andersson, K. K.; Froland, W. A.; Lipscomb, J. D.; Münck, E. *J. Am. Chem. Soc.* **1993**, *115*, 3688-3701.
- (29) Yamashita, M. M.; Wesson, L.; Eisenman, G.; Eisenberg, D. *Proc. Natl. Acad. Sci. U.S.A.* **1990**, *87*, 5648-5652.
- (30) *Cytochrome P-450: Structure, Mechanism, and Biochemistry*; Ortiz de Montellano, P. R., Ed.; Plenum Press: New York, 1986.
- (31) Andersson, K. K.; Froland, W. A.; Lee, S.-K.; Lipscomb, J. D. *New J. Chem.* **1991**, *15*, 411-415.
- (32) Wilkins, P.; Dalton, H.; Podmore, I. D.; Deighton, N.; Symons, M. C. R. *Eur. J. Biochem.* **1992**, *210*, 67-72.
- (33) Lee, S.-K.; Fox, B. G.; Froland, W. A.; Lipscomb, J. D.; Münck, E. *J. Am.*

Chem. Soc. **1993**, *115*, 6450-6451.

- (34) Ruzicka, F.; Huang, D.-S.; Donnelly, M. I.; Frey, P. A. *Biochemistry* **1990**, *29*, 1696-1700.
- (35) Feig, A. L.; Lippard, S. J. *in press* **1994**,
- (36) Poulos, T. L.; Finzel, B. C.; Howard, A. J. *J. Mol. Biol.* **1987**, *195*, 687-700.
- (37) Raag, R.; Martinis, S. A.; Sligar, S. G.; Poulos, T. L. *Biochemistry* **1991**, *30*, 11420-11429.
- (38) Poulos, T. L.; Finzel, B. C.; Gunsalus, I. C.; Wagner, G. C.; Kraut, J. *J. Biol. Chem.* **1985**, *260*, 16122-16130.
- (39) Lund, J.; Dalton, H. *Eur. J. Biochem.* **1985**, *147*, 291-296.
- (40) Liu, K. E.; Lippard, S. J. *J. Biol. Chem.* **1991**, *266*, 12836-12839.
- (41) Froland, W. A.; Andersson, K. K.; Lee, S.-K.; Lie, Y.; Lipscomb, J. D. *J. Biol. Chem.* **1992**, *267*, 17588-17597.
- (42) Liu, K. E.; Feig, A. L.; Goldberg, D. P.; Watton, S. P.; Lippard, S. J. In *The Activation of Dioxygen and Homogeneous Catalytic Oxidation*; D. H. R. Barton, A. E. Martell and D. Sawyer, Ed.; Plenum Press: New York, 1993.
- (43) Nordlund, I.; Powlowski, J.; Shingler, V. *J. Bacteriol.* **1990**, *172*, 6826-6833.
- (44) Yen, K. M.; Karl, M. R.; Blatt, L. M.; Simon, M. J.; Winter, R. B.; Fausset, P. R.; Lu, H. S.; Harcourt, A. A.; Chen, K. K. *J. Bacteriol.* **1991**, *173*, 5315-5327.
- (45) Fox, B. G.; Shanklin, J.; Somerville, C.; Münck, E. *Proc. Natl. Acad. Sci. USA* **1993**, *90*, 2486-2490.
- (46) Kurtz, D. M., Jr.; Pickril, B. C. *Biochem. Biophys. Res. Comm.* **1991**, *181*, 337-341.

Table 5.1 Secondary structure elements in the alpha subunit*

Name	Residues	Length	Comment
$\alpha 1$	24-34	11	24 O - 27 N, 1-4 H bond 27 O - 31 N too long for H bond, 4.5 Å 28 O - 32 N too long for H bond, 3.6 Å 29 O - 33 N too long for H bond, 4.5 Å 30 O - 34 N too long for H bond, 5.9 Å 31 O - 34 N, 1-4 H bond
αA	63-89	27	70 N - 66 O, 67 O, bifurcated H bonds 70 O - 74 N, too long for H bond, 4.0 Å 73 O - 77 N, too long for H bond, 3.5 Å 76 O - 80 N, too long for H bond, 4.3 Å 81 O - 85 N, too long for H bond, 3.5 Å 82 O - 86 N, too long for H bond, 4.4 Å 83 O - 87 N, too long for H bond, 4.8 Å
αB	96-127	32	96 O - 99 N, 1-4 H bond 100 O - 104 N, too long for H bond, 3.6 Å 101 O - 105 N, too long for H bond, 3.8 Å 101 O - 104 N, 1-4 H bond 104 O - 108 N, too long for H bond, 3.4 Å 108 O - 112 N, too long for H bond, 3.4 Å 109 O - 113 N, too long for H bond, 3.6 Å 110 O - 113 N, 1-4 H bond 114 N - 110 O, 111 O, bifurcated H bonds 115 O - 119 N, too long for H bond, 3.8 Å 122 N - 118 O, 119 O, bifurcated H bonds 127 N - 123 O, 124 O, bifurcated H bonds
αC	130-160	31	130 O - 133 N, 1-4 H bond 141 N - 137 O, 138 O, bifurcated H bonds 148 N - 144 O, 145 O, bifurcated H bonds 153 N - 149 O, 150 O, bifurcated H bonds 156 N - 152 O, 153 O, bifurcated H bonds
$\alpha 2$	171-177	7	172 O - 176 N, too long for H bond, 5.7 Å 173 O - 176 N, 1-4 H bond
αD	180-193	14	186 N - 182 O, 183 O, bifurcated H bond 186 O - 190 N, too long for H bond, 4.1 Å 187 O - 191 N, too long for H bond, 4.4 Å 188 O - 192 N, too long for H bond, 5.5 Å 189 O - 192 N, 1-4 H bond

α E	196-227	32	196 O - 199 N, 1-4 H bond 203 N - 199 O, 200 O, bifurcated H bond 202 O - 206 N, too long for H bond, 3.5 Å 202 O - 207 N, H bond 203 O - 207 N, too long for H bond, 4.3 Å 203 O - 208 N, H bond 204 O - 208 N, too long for H bond, 3.4 Å 204 O - 209 N, H bond 205 O - 209 N, too long for H bond, 3.8 Å 205 O - 210 N, H bond 206 O - 210 N, too long for H bond, 4.5 Å 206 O - 313Trp NE1, H bond 209 O - 213 N, too long for H bond, 3.6 Å 209 O - 214 N, H bond 210 O - 214 N, too long for H bond, 5.7 Å 211 O - 215 O, too long for H bond, 4.9 Å, 215 is a Pro 214 O - 218 N, too long for H bond, 3.9 Å 216 N - 212 O, 213 O, bifurcated H bonds 217 O - 221 N, too long for H bond, 3.4 Å 222 N - 218 O, 219 O, bifurcated H bonds
α F	231-256	26	234 O - 238 N, too long for H bond, 3.8 Å 237 O - 241 N, too long for H bond, 3.6 Å 238 O - 242 N, too long for H bond, 4.1 Å 239 O - 243 N, too long for H bond, 3.8 Å 240 O - 243 N, 1-4 H bond 241 O - 245 N, too long for H bond, 5.5 Å 242 O - 246 N, too long for H bond, 3.7 Å 247 N - 243 O, 244 O, bifurcated H bonds
α 3	261-266	5	261 O - 265 N, too long for H bond, 3.8 Å
α G	267-292	26	277 O - 281 N, too long for H bond, 3.8 Å 280 O - 284 N, too long for H bond, 4.7 Å, 284 is a Pro 283 O - 287 N, too long for H bond, 3.8 Å
α H	301-320	20	307 O - 311 N, 312 N, bifurcated H bonds 308 O - 312 N, too long for H bond, 3.8 Å 308 O - 313 N, H bond 309 O - 313 N, too long for H bond, 4.0 Å 309 O - 314 N, H bond 310 O - 314 N, too long for H bond, 3.7 Å 310 O - 315 N, H bond 314 O - 318 N, too long for H bond, 4.6 Å 317 O - 320 N, 1-4 H bond 313 O - 318 N, H bond 318 O - 321 N, 1-4 H bond
α 4	331-339	9	

$\alpha 5$	341-353	13	344 O - 348 N, too long for H bond, 3.4 Å 345 O - 349 N, too long for H bond, 4.0 Å 351 O - 354 N, 1-4 H bond
$\alpha 6$	365-375	11	
$\alpha 7$	379-393	15	380 O - 385 N, H bond 381 O - 385 N, too long for H bond, 5.0 Å 382 O - 386 N, too long for H bond, 3.4 Å
$\alpha 8$	403-412	10	3_{10} helix 403 O - 406 N, 1-4 H bond 404 O - 407 N, 1-4 H bond 405 O - 408 N, 1-4 H bond 406 O - 409 N, 1-4 H bond
$\beta 1$	413-419	7	
$\beta 2$	420-428	9	
$\beta 3$	435-442	8	
$\beta 4$	443-449	7	
$\alpha 9$	451-460	10	
$\alpha 10$	468-474	7	
$\alpha 11$	478-486	9	483 O - 486 N, 1-4 H bond
$\alpha 12$	509-515	7	511 O - 515 N, too long for H bond, 4.2 Å 513 O - 516 N, 1-4 H bond

*The secondary structure elements are labeled according to Figure 5.2, with alpha helices denoted by α and beta strands denoted by β .

Table 5.2 Tight turns*
A. The alpha subunit

Residues	Sequence	Type	Protomer	Ramachandran angles (deg.)			
				ϕ_2	ψ_2	ϕ_3	ψ_3
39-42	FKNN	I	A	-40	-53	-85	23
		II	B	-79	118	109	3
53-56	ANET	I	A	-85	-1	-106	20
		II	B	-71	131	73	8
87-90	TRLN	I	A	-70	-29	-81	0
		I	B	-83	0	-64	-35
159-162	AKNG	I	A	-63	-39	-120	-1
		I	B	-64	-44	-121	6
165-168	NAGH	II	A	-60	130	90	-47
		II	B	-59	129	92	-45
255-258	VSIA	I	A	-69	-21	-113	-3
		I	B	-70	-25	-107	-5
257-260	IAND	I	A	-66	-26	-92	2
		I	B	-61	-34	-85	13
319-322	GRLG	I	A	-63	-29	-98	12
		I	B	-64	-17	-104	-4
329-332	PRSL	I	A	-60	-21	-90	7
		I	B	-62	-20	-88	8
339-342	AYWA	I	A	-41	-53	-101	-4
		III	B	-54	-47	-63	-45
354-357	WPTG	I	A	-62	-11	-88	-7
		I	B	-58	-19	-97	5
376-379	YPGW	II	A	-60	125	116	-18
		II	B	-51	114	114	-2

378-381	GWYD	III	A	-58	-51	-63	-46
		III	B	-56	-47	-64	-44
391-394	RARG	I	A	-56	-32	-80	-4
		I	B	-64	-37	-69	-14
394-397	GCED	I	A	-56	-29	-91	-3
		I	B	-56	-25	-84	-15
397-400	DPSS	I	A	-59	-27	-77	-5
		I	B	-56	-25	-84	-15
419-422	RVSQ	I	A	-83	-70	-73	-18
		I	B	-85	-72	-76	-19
427-430	PSLA	I	A	-71	-16	-110	-32
		I	B	-71	-20	-104	-34
441-444	YNGE	I'	A	50	40	82	14
		I'	B	50	49	78	23
460-463	EPER	I	A	-59	-38	-72	-13
		I	B	-64	-24	-86	0
473-476	YEGR	II	A	-48	128	81	2
		II	B	-50	129	81	8
489-492	RSDG	II	A	-66	138	126	-28
		I	B	-69	-2	125	-29
521-524	NPVK	III	A	-55	-30	-66	-22
		III	B	-67	-17	-78	-17

B. The beta subunit

Residues	Sequence	Type	Protomer	Ramachandran angles (deg.)			
				ϕ_2	ψ_2	ϕ_3	ψ_3
20-23	ILKA	III	A	-62	-35	-73	-24
		III	B	-60	-39	-59	-28
41-44	PRWK	I	A	-72	-39	-113	58

		I	B	-76	-31	-116	39
63-66	GAGG	II	A	-33	110	102	-14
		II	B	-31	113	104	-17
76-79	FHGG	II	A	-55	120	114	-21
		II	B	-63	135	100	-30
94-97	DWFK	I	A	-74	-9	-99	8
		I	B	-74	-14	-95	18
100-103	DPLR	II	A	-51	149	81	-21
		I	B	-52	-35	-85	5
131-134	GQIR	I	A	-65	-13	-63	-27
		I	B	-74	-9	-66	-20
133-136	IRAM	I	A	-51	-29	-91	-3
		I	B	-55	-22	-102	2
166-169	GAKE	III	A	-63	-35	-84	-39
		III	B	-58	-32	-58	-45
172-175	SDVT	III	A	-55	-54	-63	-33
		III	B	-66	-49	-62	-44
201-204	AKIV	I	A	-82	-38	-91	-22
		I	B	-85	-33	-94	-22
204-207	VPGF	II	A	-46	126	88	-7
		II	B	-55	124	88	-7
222-225	EVYK	I	A	-70	-42	-97	6
		I	B	-63	-34	-103	5
234-237	LWQE	I	A	-67	-67	-100	-8
		I	B	-74	-86	-92	-2
240-243	DWNE	III	A	-67	-27	-83	-32
		III	B	-58	-32	-78	-31
266-269	QRLA	I	A	-76	-44	-95	-24
		I	B	-80	-35	-102	-28
270-273	PRFG	I	A	-66	-12	-115	23

		I	B	-65	-24	-98	18
276-279	LTPF	III	A	-56	-43	-53	-31
		III	B	-65	-46	-50	-37
277-280	TPFF	III	A	-53	-31	-64	-43
		III	B	-50	-37	-65	-45
306-309	DPEF	I	A	-64	-25	-108	-35
		I	B	-58	-33	-99	-32
343-346	PAGT	II	A	-53	143	91	-5
		II	B	-64	140	83	11
369-372	SAID	I	A	-61	-29	-118	18
		I	B	-60	-29	-112	13
385-388	LAGL	I	-60	-16	-102	-8	
		I	-52	-23	-103	11	

C. The gamma subunit

Residues	Sequence	Type	Protomer	Ramachandran angles (deg.)			
				ϕ_2	ψ_2	ϕ_3	ψ_3
5-8	GIHS	II'	A	71	-74	-124	-3
		I	B	-60	-36	-127	8
41-44	TPFR	I	A	-66	-8	-99	15
		I	B	-56	-20	-90	6
81-85	TAFG	I	A	-55	-16	-98	12
		I	B	-60	-16	-87	0
103-106	DKWE	III	A	-60	-23	-74	-43
		III	B	-63	-24	-78	-38
119-122	KPcis-PI	VIa	A	-48	139	-86	17
		VIa	B	-43	143	-84	19
144-147	NLNY	II	A	-77	124	55	44
		II	B	-80	123	51	52

*The tight turns are defined as in Ref. 5. For Type I turns, the Ramachandran angles (shown in Figure 4.11) are approximately $\phi_2 = -60^\circ$, $\psi_2 = -30^\circ$, $\phi_3 = -90^\circ$, $\psi_3 = 0^\circ$. Type II turns have approximately $\phi_2 = -60^\circ$, $\psi_2 = 120^\circ$, $\phi_3 = 90^\circ$, $\psi_3 = 0^\circ$. Type I' and Type II' turns have the mirror image backbone conformation as Types I and II, and have the inverse ϕ and ψ values. Type III turns, which are indistinguishable from a 3_{10} helix, have $\phi_2, \phi_3 = -60^\circ$ and $\psi_2, \psi_3 = -30^\circ$.

Table 5.3 Secondary structure elements in the beta subunit*

Name	Residues	Length	Comment
$\alpha 1$	13-20	8	19 N - 15 O, 16 O, bifurcated H bonds
$\alpha 2$	47-54	8	
αA	105-128	24	115 N - 111 O, 112 O, bifurcated H bonds 117 N - 113 O, 114 O, bifurcated H bonds 122 N - 118 O, 119 O, bifurcated H bonds 126 N - 122 O, 123 O, bifurcated H bonds
αB	137-166	30	141 O - 145 N, too long for H bond, 3.6 Å 142 O - 146 N, too long for H bond, 4.6 Å 145 O - 149 N, too long for H bond, 3.5 Å 146 O - 150 N, too long for H bond, 3.8 Å 148 O - 152 N, too long for H bond, 3.4 Å
αC	175-201	27	181 N - 177 O, 178 O, bifurcated H bonds 182 O - 186 N, too long for H bond, 3.6 Å 188 N - 184 O, 185 O, bifurcated H bonds 190 O - 194 N, too long for H bond, 3.4 Å 191 N - 187 O, 188 O, bifurcated H bonds 192 N - 188 O, 189 O, bifurcated H bonds 198 N - 194 O, 195 O, bifurcated H bonds 198 O - 202 N, too long for H bond, 3.5 Å
$\alpha 3$	210-219	10	216 N - 212 O, 213 O, bifurcated H bonds
αD	226-234	9	
αE	243-266	24	249 O - 253 N, too long for H bond, 5.3 Å 250 O - 254 N, too long for H bond, 5.5 Å 253 O - 257 N, too long for H bond, 3.5 Å 254 O - 258 N, too long for H bond, 4.5 Å 260 O - 264 N, too long for H bond, 3.4 Å 261 O - 265 N, too long for H bond, 3.9 Å 262 O - 266 N, too long for H bond 3.9 Å
αF	280-301	22	289 O - 293 N, too long for H bond, 3.7 Å 290 N - 286 O, 287 O, bifurcated H bonds 298 O - 302 N, too long for H bond, 3.6 Å 299 O - 303 N, too long for H bond, 3.8 Å

α G	309-336	28	322 O - 326 N, too long for H bond, 3.7 Å 323 O - 327 N, too long for H bond, 4.7 Å, 327 is a Pro 331 N - 327 O, 328 O, bifurcated H bonds 333 O - 337 N, too long for H bond, 4.2 Å 334 O - 337 N, 1-4 H bond 335 N - 331 O, 332 O, bifurcated H bonds 335 O - 338 N, 1-4 H bond
α H	348-364	17	355 N - 351 O, 352 O, bifurcated H bonds 358 N - 354 O, 355 O, bifurcated H bonds 359 N - 355 O, 356 O, bifurcated H bonds 365 N - 361 O, 362 O, bifurcated H bonds
α 4	377-384	8	383 O - 387 N, too long for H bond, 4.6 Å

*The secondary structure elements are labeled according to Figure 5.4, with alpha helices denoted by α .

Table 5.4 Secondary structure elements in the gamma subunit*

Name	Residues	Length	Comment
$\alpha 1$	9-18	10	18 N - 14 O, 15 O, bifurcated H bonds
$\alpha 2$	25-38	14	28 N - 24 O, 25 O, bifurcated H bonds 36 N - 32 O, 33 O, bifurcated H bonds
$\alpha 3$	49-70	22	
$\alpha 4$	73-80	8	74 O - 78 N, too long for H bond, 3.4 Å
$\alpha 5$	86-98	13	
$\alpha 6$	106-116	11	109 O - 113 N, too long for H bond, 4.7 Å 110 N - 106 O, 107 O, bifurcated H bonds 112 O - 116 N, too long for H bond, 5.4 Å
$\alpha 7$	124-143	20	126 O - 130 N, too long for H bond, 3.6 Å 131 N - 127 O, 128 O, bifurcated H bonds 134 O - 138 N, too long for H bond, 3.5 Å 141 N - 137 O, 138 O, bifurcated H bonds
$\alpha 8$	151-158	8	

*The secondary structure elements are labeled according to Figure 5.5, with alpha helices denoted by α .

Table 5.5 Heavy atom binding sites in the PIP, TAMM, and EMTS derivatives
A. PIP^a binding sites

Site	Specific residue(s)	Comment
P1	γ A Met31	Near the surface
P2	α B Met445	Near the surface
P3	α A Cys517	Near the surface, at the C-terminus
P4	γ B Met37	Near the surface
P5	α A Met70	In the canyon, near the central opening
P6	γ B Met31	Near the surface
P7	α A Met445	Near the surface
P8	γ A Met37	Near the surface
P9	α B Met70	In the canyon, near the central opening
P10	α B Cys517	Near the surface, at the C-terminus
P11	α A His382	Near the surface, not present in the B protomer

^aPIP = di- μ -iodobis(ethylenediamine)diplatinum(II)

B. TAMM^b binding sites

Site	Specific residue(s)	Comment
T1	β A Cys302	In canyon, the only mercury binding site in the β subunit
T2	β B Cys302	In canyon, the only mercury binding site in the β subunit
T3	α B Cys426	In the β hairpin region of the second domain, near the surface
T4	α B Cys517	Near the surface, not present in the A protomer
T5	γ A His7, α A His486	At the $\alpha\beta\gamma$ interface, very close to T11
T6	γ B His7, α B His486	At the $\alpha\beta\gamma$ interface, two sites are located here in the A protomer, but not in the B protomer

T7		Near a crystal contact, may be bound to the N-terminus of β_B , for which there is no electron density
T8	α_A Cys426	In the β hairpin region, near the surface
T9	α_A His382	In the β hairpin region, near the surface, not present in the B protomer
T10	β_B Cys302	In canyon, may be the same as site T2
T11	γ_A His7, α_A His486	At the $\alpha\beta\gamma$ interface, very close to T5

^bTAMM = tetrakis(acetoxymmercuri)methane

C. EMTS^c binding sites

Site	Specific residue(s)	Comment
E1	β_A Cys302	In canyon, the only mercury binding site in the β subunit
E2	β_A Cys302	In canyon, the only mercury binding site in the β subunit
E3	α_A Cys151	Near the diiron center
E4	α_B Cys151	Near the diiron center
E5	α_A Cys517	Near the surface, at the C-terminus
E6	α_B Cys 517	Near the surface, at the C-terminus
E7	α_B Cys211	Near the active site and canyon
E8	α_A Cys211	Near the active site and canyon
E9	α_B Cys426	In the β hairpin region of the second domain, near the surface, not present in the A protomer

^cEMTS = sodium ethylmercurithiosalicylate

Table 5.6 Buried charged residues in the alpha subunit

Residue	Accessible surface area (Å ²)		Comment
	Protomer A	Protomer B	
Asp75	1	1	At $\alpha\beta$ interface, H bonds to Arg146
Asp126	0	0	At $\alpha\beta$ interface, H bonds to β Ser164,Thr44, N 45
Asp143	0	0	Near active site, H bonds to Arg245, His67, His246, His246 is a metal ligand
Asp164	0	0	Near loop after first helix in β subunit, H bonds to Arg489, Lys104, Arg380
Asp170	0	0	At $\alpha\beta$ interface, near loop after first helix in β subunit, H bonds to Thr174, Trp37, N 67
Asp190	0	0	At $\alpha\beta$ interface, H bonds to β Ser82, β N 73
Asp196	0	0	At $\alpha\beta\gamma$ interface, H bonds to Lys49, Thr48, N 49
Asp229	0	0	At $\alpha\beta$ interface, H bonds to Thr232, Trp99
Asp242	0	0	Near active site, H bonds to Arg146, Arg245, His147, His147 is a metal ligand
Asp270	0	0	At $\alpha\gamma$ interface, H bonds to Lys49, Tyr50
Asp418	0	0	At $\alpha\beta$ interface, H bonds to Ser421
Asp450	0	0	H bonds to Lys280, N 453

Arg94	0	9	At AB dimer interface, near N-terminal helix of β subunit, H bonds to β_B O 12
Arg146	0	0	At $\alpha\beta$ interface, H bonds to Asp242, Asp75
Arg172	0	0	At $\alpha\beta$ interface, H bonds to β O 51, β O 52, β O 54, Glu111
Arg175	0	0	At $\alpha\beta$ interface, H bonds to N 108
Arg186	0	0	At $\alpha\beta$ interface, H bonds to β Gln74, Tyr464
Arg245	1	1	At $\alpha\beta$ interface, near active site, H bonds to Asp242, Asp143
Arg360	0	0	At $\alpha\beta$ interface, H bonds to Glu101, O 501
Arg419	0	0	At $\alpha\beta\gamma$ interface, H bonds to Glu471, O 445, O 466
Arg455	6	5	At $\alpha\gamma$ interface, H bonds to γ Tyr147, γ O 150
Arg463	0	0	At $\alpha\beta$ interface, H bonds to Glu199, O 194
Arg489	2	1	At $\alpha\beta$ interface, H bonds to β O 29, O 496
Glu58	0	0	H bonds to N 135, His29
Glu71	0	0	Near active site, H bonds to Lys74, Arg146
Glu101	0	0	Near loop after first helix in β subunit, H bonds to Arg360, Lys104
Glu111	0	0	At $\alpha\beta$ interface, H bonds to Arg172

Glu114	0	0	Metal ligand
Glu132	1	2	H bonds to N 58
Glu144	0	0	Metal ligand
Glu199	0	0	At $\alpha\beta$ interface, H bonds to Arg463
Glu209	0	0	Metal ligand
Glu230	0	0	At $\alpha\beta$ interface, H bonds to β Arg9
Glu243	0	0	Metal ligand
Glu291	0	0	H bonds to N 301, Tyr376, His343
Glu368	0	1	H bonds to Lys297
Glu454	0	0	At $\alpha\gamma$ interface, H bonds to γ Arg156, Arg437, His439
Glu460	0	0	At $\alpha\gamma$ interface, H bonds to γ Tyr147
Glu462	0	0	At $\alpha\beta\gamma$ interface, H bonds to γ Arg143, β N 78
Glu465	0	0	At $\alpha\beta\gamma$ interface, H bonds to β Lys75, γ Arg44
Glu471	0	2	At $\alpha\gamma$ interface H bonds to Arg419, N 468
Lys45	0	0	At $\alpha\beta$ interface, H bonds to β Gln165
Lys49	0	0	At $\alpha\gamma$ interface, H bonds to Asp196, Asp270
Lys65	0	0	At $\alpha\beta$ interface, near opening in center of molecule, H bonds to β Gln283, β Tyr287, β Asp188

Lys74	7	16	Near opening in center of molecule, H bonds to Glu71, Asp242, Thr241
Lys98	0	1	H bonds to O 292, O 294
Lys104	0	0	Near loop after first helix in β subunit, H bonds to Glu101, Asp164, O 166
Lys134	0	0	At $\alpha\beta$ interface, H bonds to O 125, O 128
Lys182	0	0	At $\alpha\beta$ interface
Lys185	0	0	At $\alpha\beta$ interface, H bonds to β Asp68
Lys280	0	0	H bonds to Ser449, Asp450

Table 5.7 Buried charged residues in the beta subunit

Residue	Accessible surface area (Å ²)		Comment
	Protomer A	Protomer B	
Asp13	7	4	H bonds to Arg8
Asp30	0	1	In loop that wraps around α subunit, H bonds to α Ser490
Asp61	2	7	At $\beta\gamma$ interface, H bonds to γ Arg12
Asp68	0	0	At $\alpha\beta\gamma$ interface, H bonds to α Lys185
Asp71	0	0	At $\alpha\beta\gamma$ interface, H bonds to Lys7 5,N 72
Asp100	0	0	H bonds to Arg104
Asp112	2	7	Near opening in center of molecule, H bonds to Arg118
Asp130	0	0	H bonds to Gln285, Arg262, Gln132
Asp173	0	0	At $\alpha\beta$ interface, H bonds to N 55, N 56, N 174
Asp185	0	0	At $\alpha\beta$ interface, H bonds to Lys113
Asp188	0	0	At $\alpha\beta$ interface, H bonds to α Lys65, Lys113
Asp240	0	0	At $\beta\gamma$ interface, H bonds to Thr88, N 89, N 242
Asp253	0	0	H bonds to Arg261, Lys186
Asp274	0	0	H bonds to Thr277, Trp140, N 276
Asp297	6	2	H bonds to Arg42, N 99

Asp306	0	0	At $\beta\gamma$ interface, H bonds to Lys287, Thr92, N308, N 309
Asp362	1	1	Near N terminus of α subunit, H bonds to Arg134, Arg262
Asp366	2	5	Near N terminus of α subunit, H bonds to Lys292
Arg9	1	3	At $\alpha\beta$ interface, H bonds to α Glu230
Arg80	0	0	At $\alpha\beta$ interface, H bonds to Glu169
Arg91	0	0	At $\beta\gamma$ interface, H bonds to γ Glu61
Arg99	0	0	Near opening in center of molecule, H bonds to Glu50, O 96
Arg104	0	1	Near opening in center of molecule, H bonds to Asp100
Arg122	9	1	Near opening in center of molecule and AB dimer interface, H bonds to β_B Glu115, β_B Glu116, β_B O 112
Arg168	0	0	At $\alpha\beta$ interface, H bonds to Trp83, α Tyr115
Arg176	0	0	H bonds to Gln57, Tyr115, O 168
Arg197	0	0	At $\alpha\beta$ interface, H bonds to Gln194, O 208, O 209, O 210, Asn146
Arg228	12	14	At $\alpha\beta$ interface, H bonds to O 219
Arg261	0	0	H bonds to Asp253, Glu156, Gln258
Arg262	1	1	H bonds to Asp362, O 130
Arg267	3	2	H bonds to Thr347, Glu351
Glu50	0	0	H bonds to Thr47, Arg99, N 42

Glu86	0	0	At $\beta\gamma$ interface, H bonds to γ Arg115
Glu89	0	0	At $\beta\gamma$ interface, H bonds to γ Asn125
Glu115	2	3	Near opening in center of molecule and AB dimer interface, H bonds to β_B Arg122, β_B Arg118
Glu116	0	0	Near opening in center of molecule and AB dimer interface, H bonds to Tyr287, β_B Arg122
Glu156	0	0	H bonds to Lys186, Arg261
Glu169	0	0	At the $\alpha\beta\gamma$ interface, H bonds to Arg80, α Tyr46
Glu196	0	0	H bonds to Thr277, Lys323, Trp324
Glu243	0	0	H bonds to γ N 126
Glu263	0	0	Near N terminus of a subunit, H bonds to Arg262, Arg358
Lys75	0	0	At $\alpha\beta\gamma$ interface, H bonds to α Glu465, Asp71
Lys113	0	0	Near opening in center of molecule, at $\alpha\beta$ interface, H bonds to Asp185, Asp188
Lys186	0	0	H bonds to Asp253, Glu156
Lys292	3	8	At N terminus of α subunit, H bonds to Asp366, Gln289

Table 5.8 Buried charged residues in the gamma subunit

Residue	Accessible surface area (Å ²)		Comment
	Protomer A	Protomer B	
Asp50	4	0	At $\alpha\gamma$ interface, H bonds to Arg44
Asp52	2	2	At $\alpha\gamma$ interface, H bonds to Asn9
Arg12	2	1	At $\beta\gamma$ interface, H bonds to β Asp61
Arg36	0	0	At $\beta\gamma$ interface, H bonds to Glu61, O 119, O 120
Arg44	0	0	At $\alpha\gamma$ interface, H bonds to α Glu465, Asp50
Arg115	0	0	At $\beta\gamma$ interface, H bonds to β Glu86, Glu132
Arg143	0	0	At $\alpha\beta\gamma$ interface, H bonds to α Glu462, Glu108, β His77
Arg156	11	15	At $\alpha\gamma$ interface, H bonds to α Glu454
Arg159	1	1	At $\alpha\gamma$ interface, H bonds to α O 458, Glu108
Glu57	0	0	H bonds to Arg36, Lys119
Glu61	0	0	At $\beta\gamma$ interface, H bonds to Arg36, β Arg91
Glu62	5	3	At $\beta\gamma$ interface, H bonds to Lys59
Glu108	2	0	H bonds to Arg108, Arg143, Arg159
Glu132	0	0	At $\alpha\beta\gamma$ interface, H bonds to Arg115
Lys68	0	0	At $\beta\gamma$ interface, H bonds to O 80
Lys119	0	0	At $\beta\gamma$ interface, H bonds to Glu57

Table 5.9 Diiron center distances

Atom	Atom	Distance (Å)	
Fe1 _A	Fe1 _B	42.8	
Fe2 _A	Fe2 _B	46.8	
Fe1 _A	Fe2 _B	44.7	
Fe2 _A	Fe1 _B	44.8	
		Protomer A	Protomer B
Fe1	Fe2	3.4	3.4
Fe1	Glu114 OE1	1.9	1.9
Fe1	His147 ND1	2.4	2.2
Fe1	Glu144 OE2	2.1	2.2
Fe1	μOH	1.7	1.7
Fe1	OH2	2.2	2.4
Fe1	Ac O1	3.2	3.2
Fe1	Ac O2	2.8	2.0
Fe1	Cys151 SG	7.1	7.2
Fe2	Glu209 OE2	2.3	1.9
Fe2	His246 ND1	2.2	2.2
Fe2	Glu243 OE2	1.8	1.9
Fe2	Glu144 OE1	2.5	2.7
Fe2	μOH	2.0	2.0
Fe2	Ac O1	2.2	2.0
Fe2	Ac O2	3.9	3.4
Fe2	Cys151 SG	10.3	10.4

Table 5.10 Iron to ligand angles

Atom	Atom	Atom	Bond angle (degrees)	
			Protomer A	Protomer B
Fe1	μ OH	Fe2	133	131
Glu144 OE2	Fe1	His147 ND1	93	96
Glu144 OE2	Fe1	Glu114 OE1	94	91
Glu144 OE2	Fe1	OH2	170	171
Glu144 OE2	Fe1	μ OH	87	90
Glu144 OE2	Fe1	Ac O2	100	86
His147 ND1	Fe1	Glu114 OE1	106	94
His147 ND1	Fe1	OH2	94	93
His147 ND1	Fe1	μ OH	86	84
His147 ND1	Fe1	Ac O2	166	175
Glu114 OE1	Fe1	μ OH	168	178
Glu114 OE1	Fe1	OH2	90	87
Glu114 OE1	Fe1	Ac O2	68	82
OH2	Fe1	μ OH	87	93
OH2	Fe1	Ac O2	73	100
Glu144 OE1	Fe2	His246 ND1	87	81
Glu144 OE1	Fe2	Glu243 OE1	174	167
Glu144 OE1	Fe2	Glu209 OE2	82	89
Glu144 OE1	Fe2	μ OH	81	72
Glu144 OE1	Fe2	Ac O1	78	87
His246 ND1	Fe2	Glu243 OE1	87	87
His246 ND1	Fe2	Glu209 OE2	103	94
His246 ND1	Fe2	μ OH	91	89

His246 ND1	Fe2	Ac O1	165	168
Glu209 OE2	Fe2	Glu243 OE1	101	96
Glu209 OE2	Fe2	μ OH	157	160
Glu209 OE2	Fe2	Ac O1	77	86
Glu243 OE2	Fe2	μ OH	97	103
Glu243 OE2	Fe2	Ac O1	107	105

Figure 5.1 Structure of the hydroxylase. a, Viewed down the molecular twofold symmetry axis. The α subunits are shown in red, the β subunits in blue, and the γ subunits in yellow. b, Viewed with the twofold axis running vertically. c, Alternative view with the twofold axis running vertically. d, The ribonucleotide reductase R2 dimer viewed with the twofold axis running horizontally.

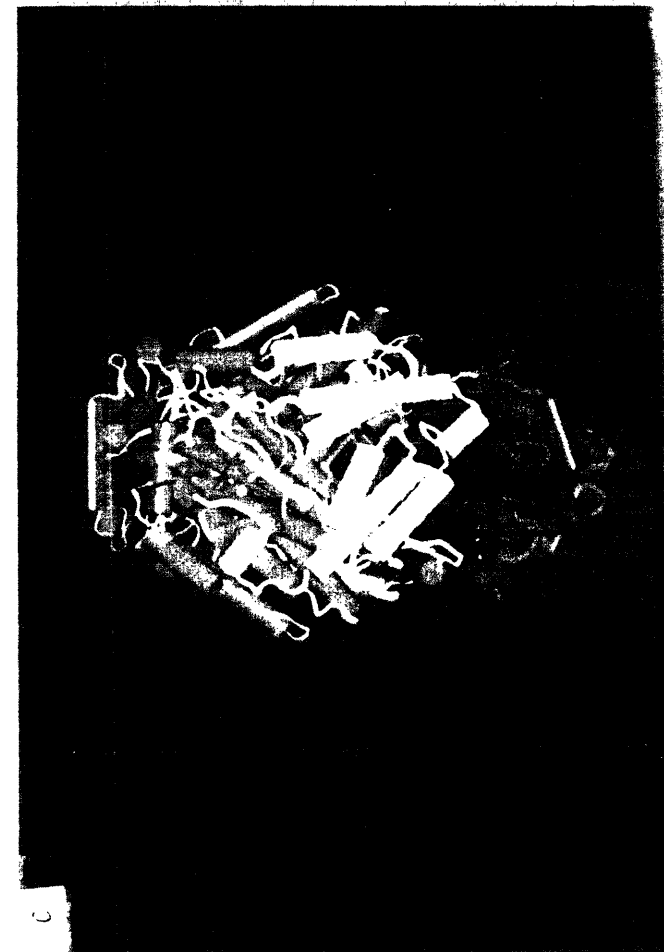
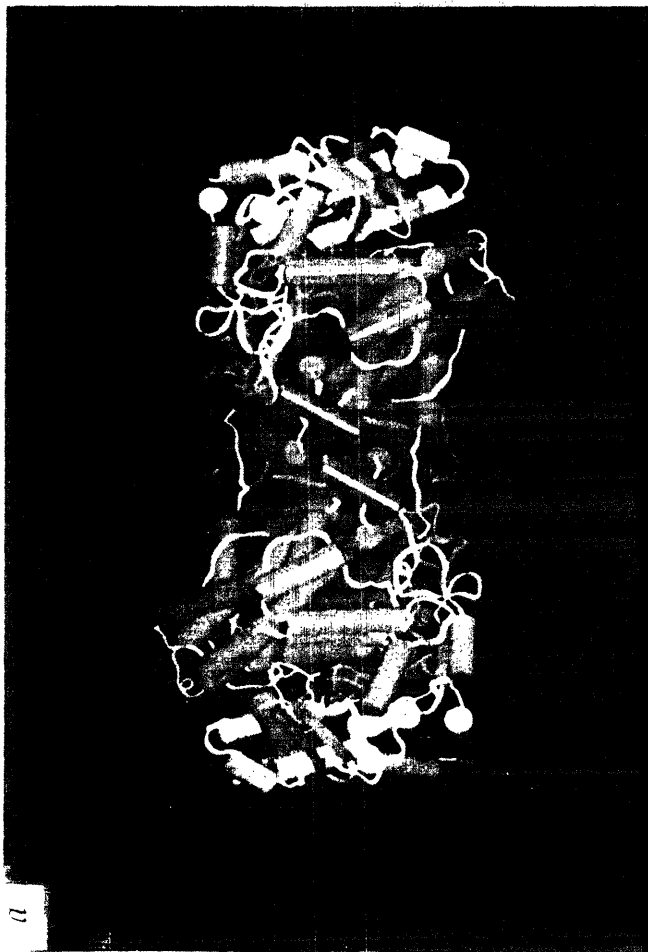
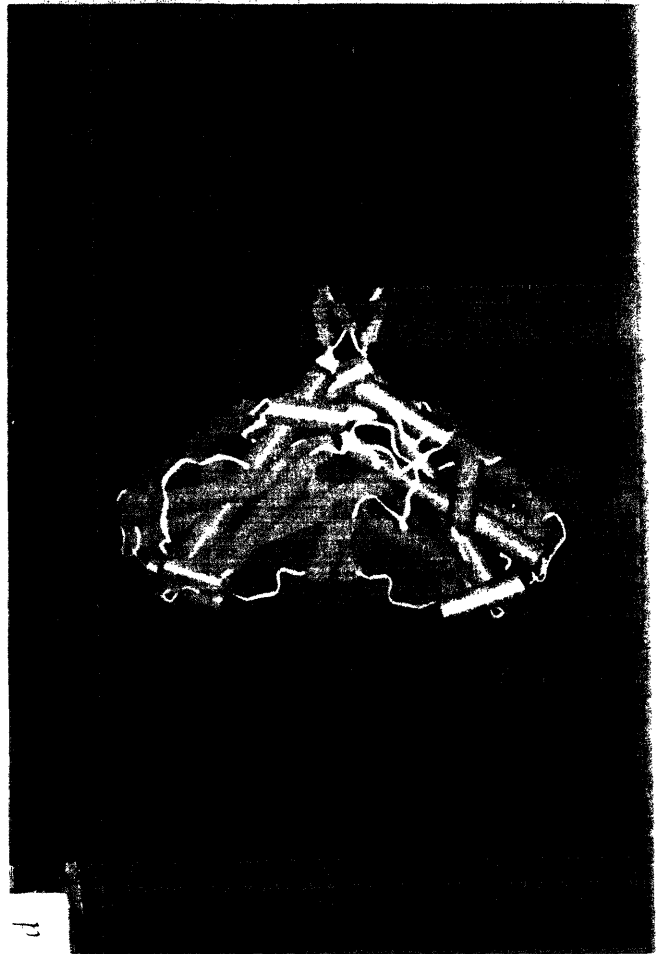


Figure 5.2 Secondary structure of the α subunit. a, The first domain of the α subunit is all helical. The principal helices are labeled A-H in accord with the naming scheme used for the R2 protein. The iron-coordinating ligands are derived from helices B, C, E, and F. The principal helices extend between the following residues: α A 63-89; α B 97-127; α C 131-161; α D 180-193; α E 197-226; α F 231-257; α G 267-294; α H 301-321. b, The second domain of the α subunit. The two beta hairpin structures lie close to the surface.

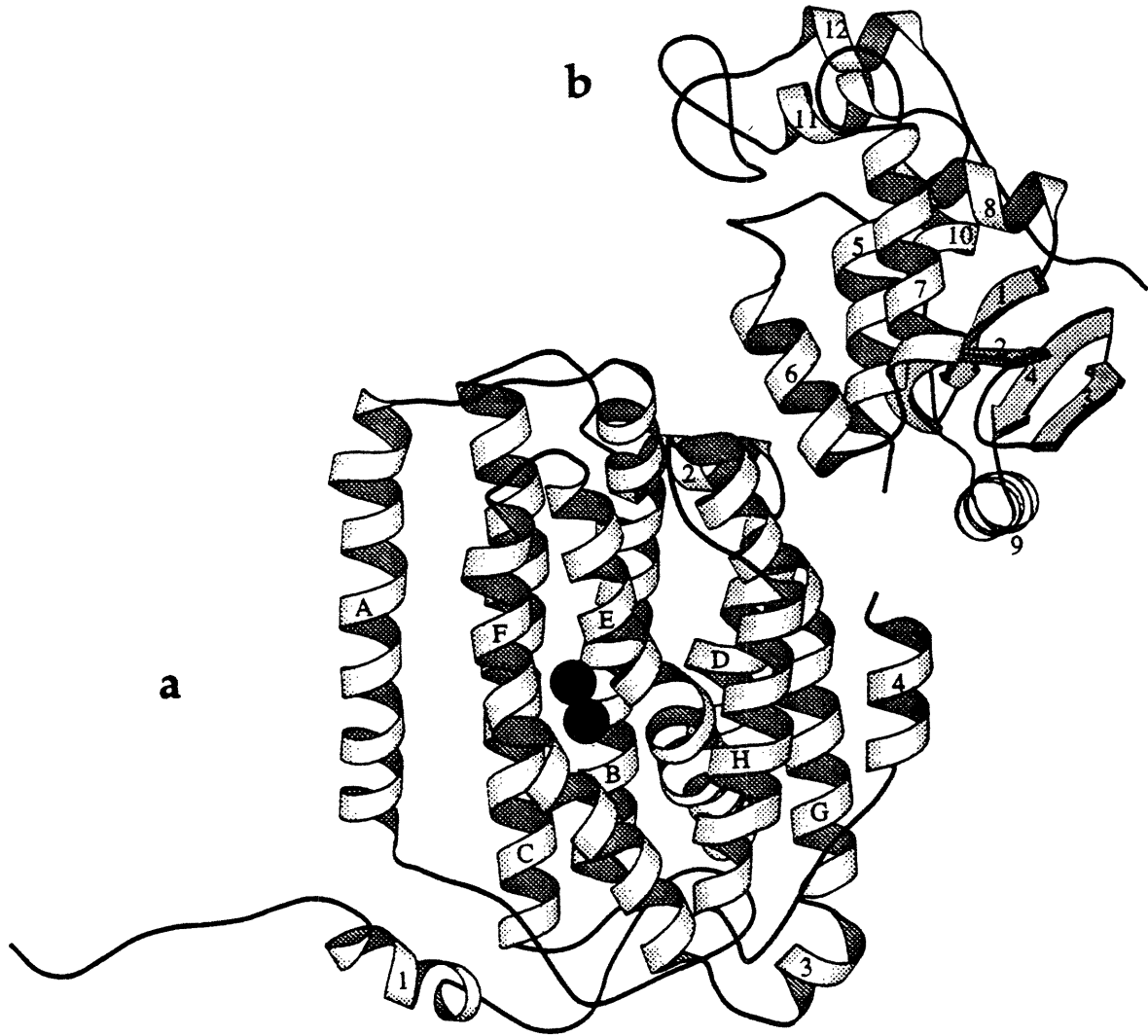


Figure 5.3 Superposition of the α and β subunits and the R2 protein. The α subunit is shown in red, the β subunit in magenta and the R2 protein in blue. The iron atoms in the α subunit are represented as yellow spheres. Top: Viewed down the iron coordinating four helix bundle. Bottom: Viewed with the R2 protein 90° from the view shown in Figure 5.1d. The similarity between the R2 "heart" and the heart formed by the first domain of the α subunit and the β subunit is striking.

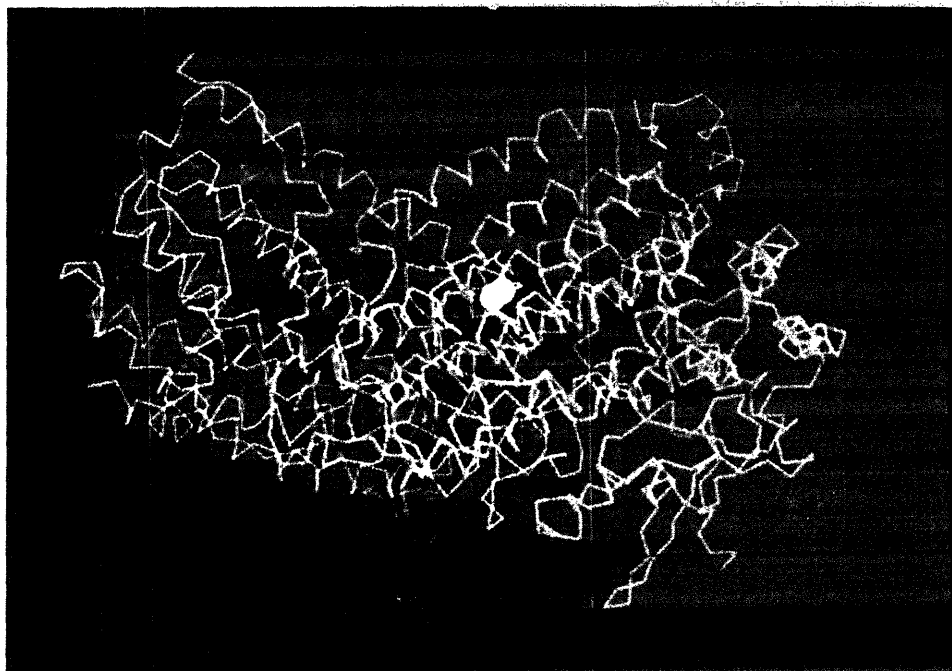
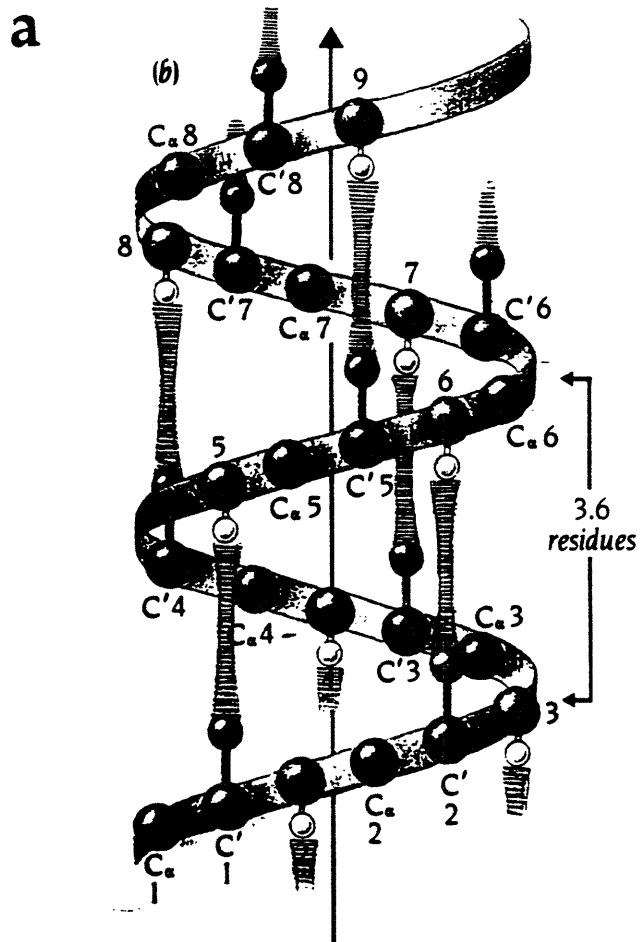
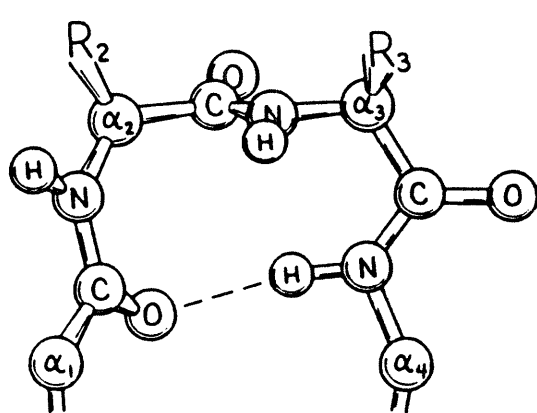


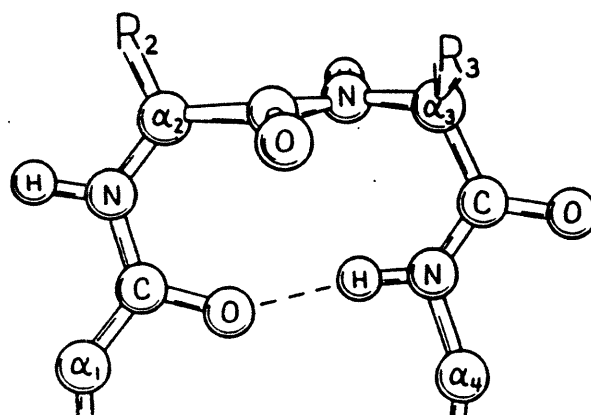
Figure 5.4 a, Schematic diagram of an α helix (from Branden, C.; Tooze, J. *Introduction to Protein Structure*; Garland Publishing, Inc.: New York, 1991, p. 8). There are 3.6 residues per turn with a hydrogen bond between the CO of residue n and the NH of residue $n + 4$ (1-5 hydrogen bonding). In a 3_{10} helix, there are 3 residues per turn with a hydrogen bond between the CO of residue n and the NH of residue $n + 3$ (1-4 hydrogen bonding). b, Type I and Type II tight turns (from Ref. 5). In the Type II turn, R_3 is typically glycine.



b



a: Type I



b: Type II

Figure 5.5 Secondary structure of the β subunit. The helices in the bundle are again labeled A-H, to emphasize the similarity to the α subunit. The principal helices extend between the following residues: α A 101-125; α B 132-164; α C 167-199; α D 219-233; α E 236-267; α F 271-301; α G 305-337; α H 344-363.

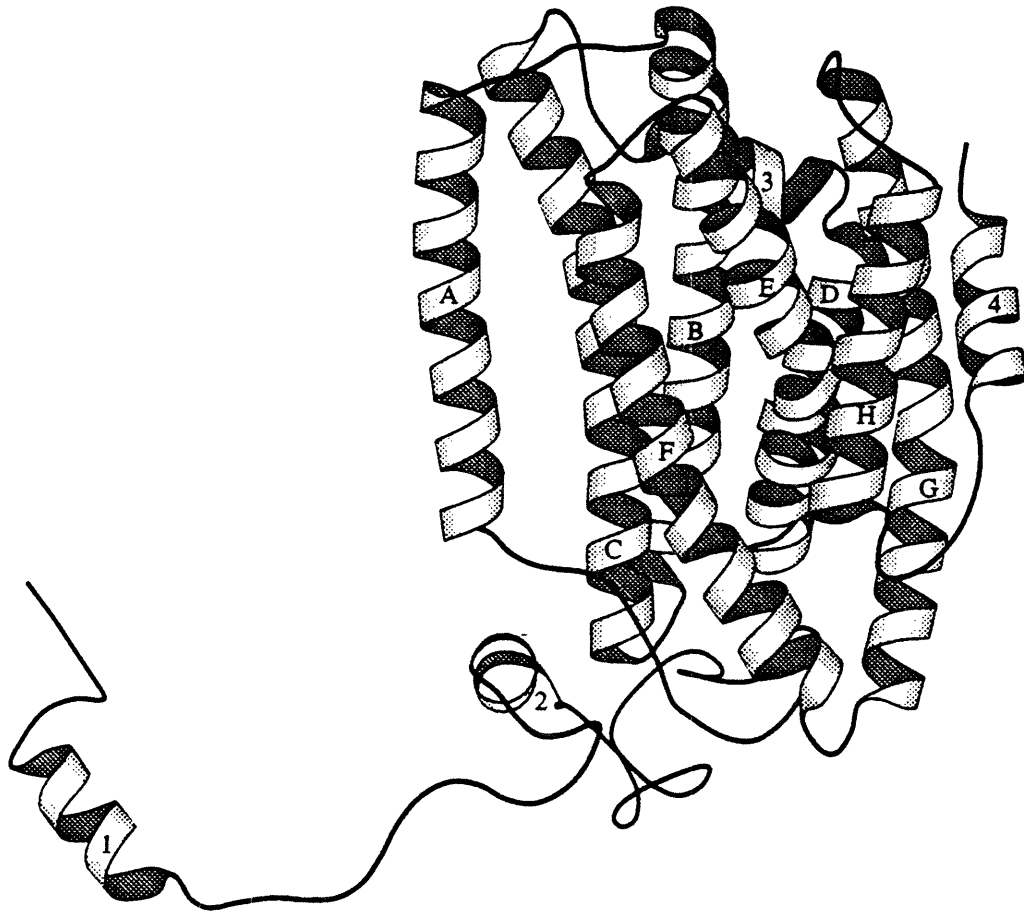


Figure 5.6 Secondary structure of the γ subunit. The arrangement of the first four helices resembles the arrangement of the last four helices, resulting in pseudo twofold symmetry.



Figure 5.7 Stereo views of the superposition of the C α atom backbones of the three subunits from the two halves of the $\alpha_2\beta_2\gamma_2$ dimer. a, The two α subunits. b, The two β subunits. c, The two γ subunits.

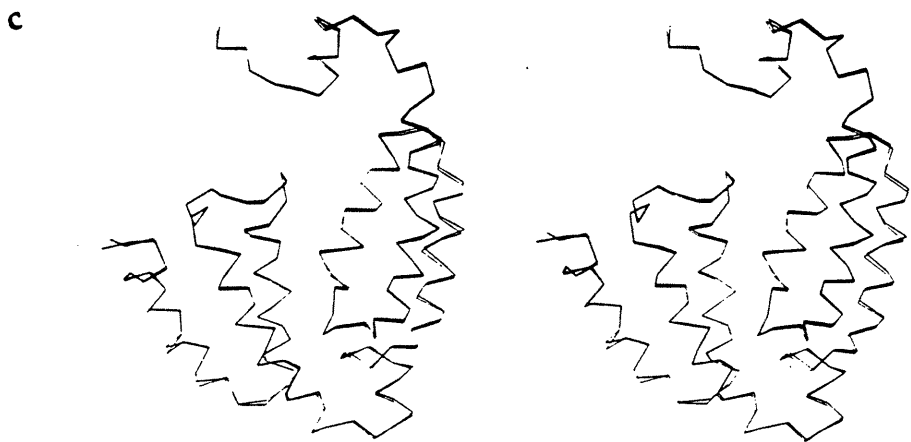
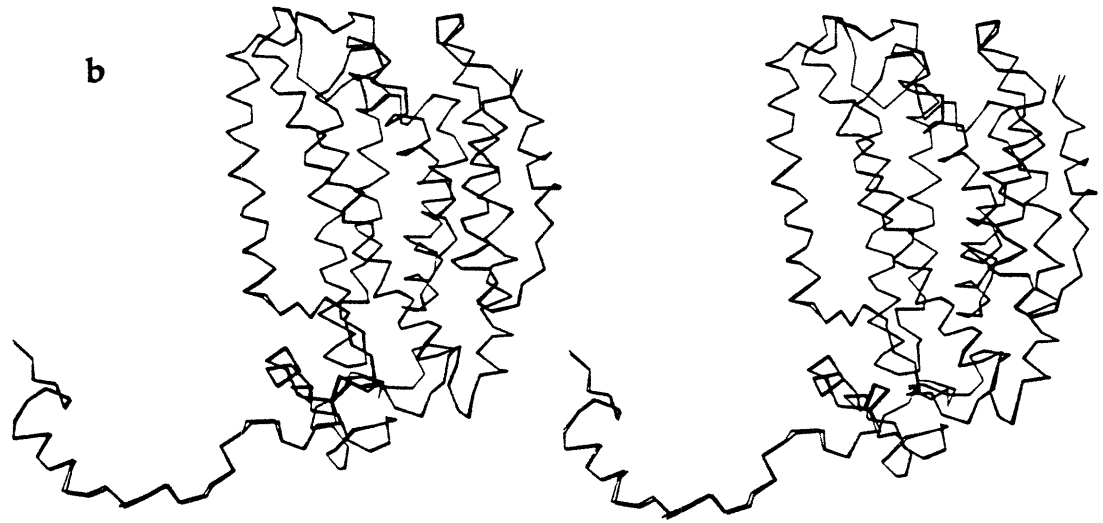
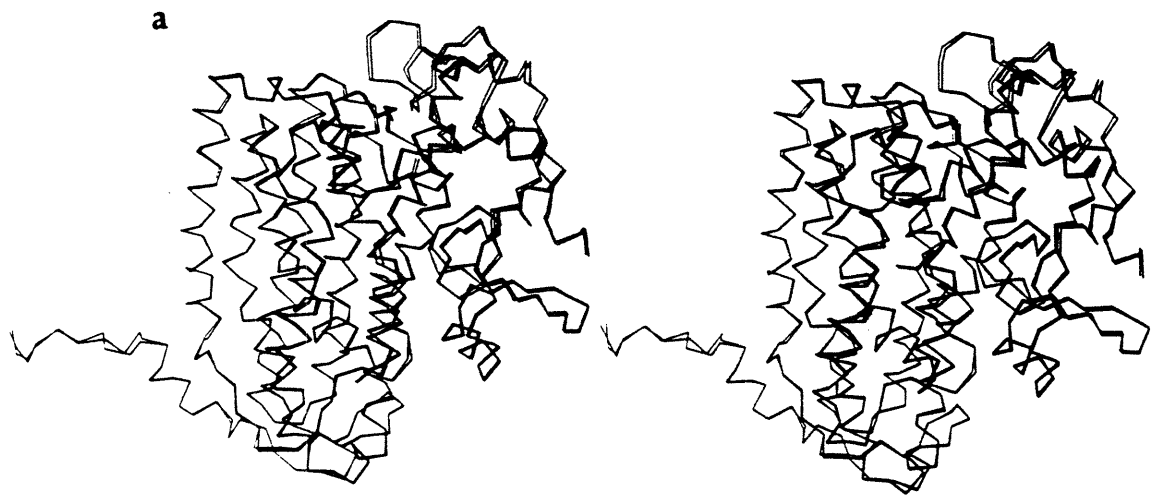
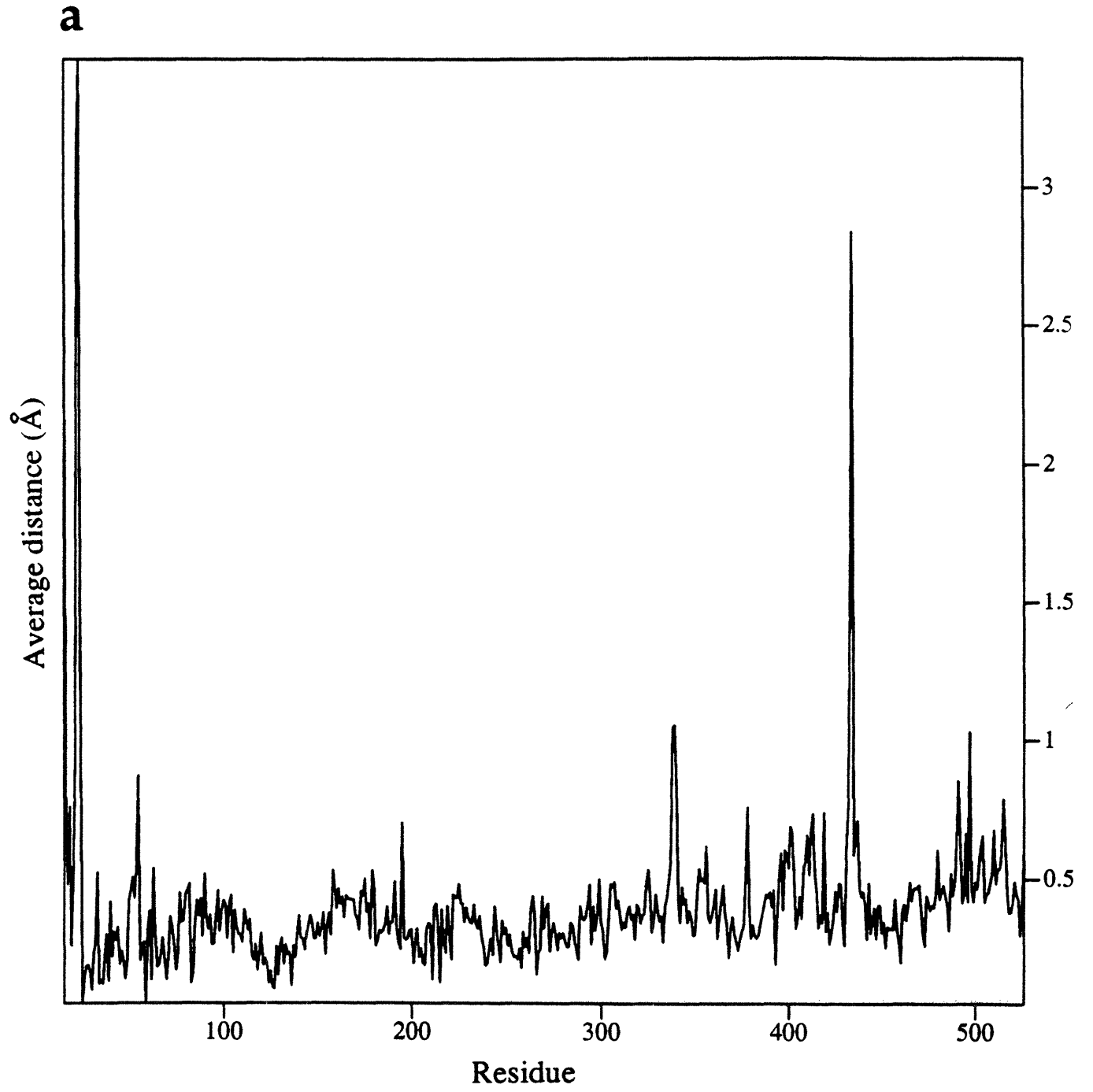
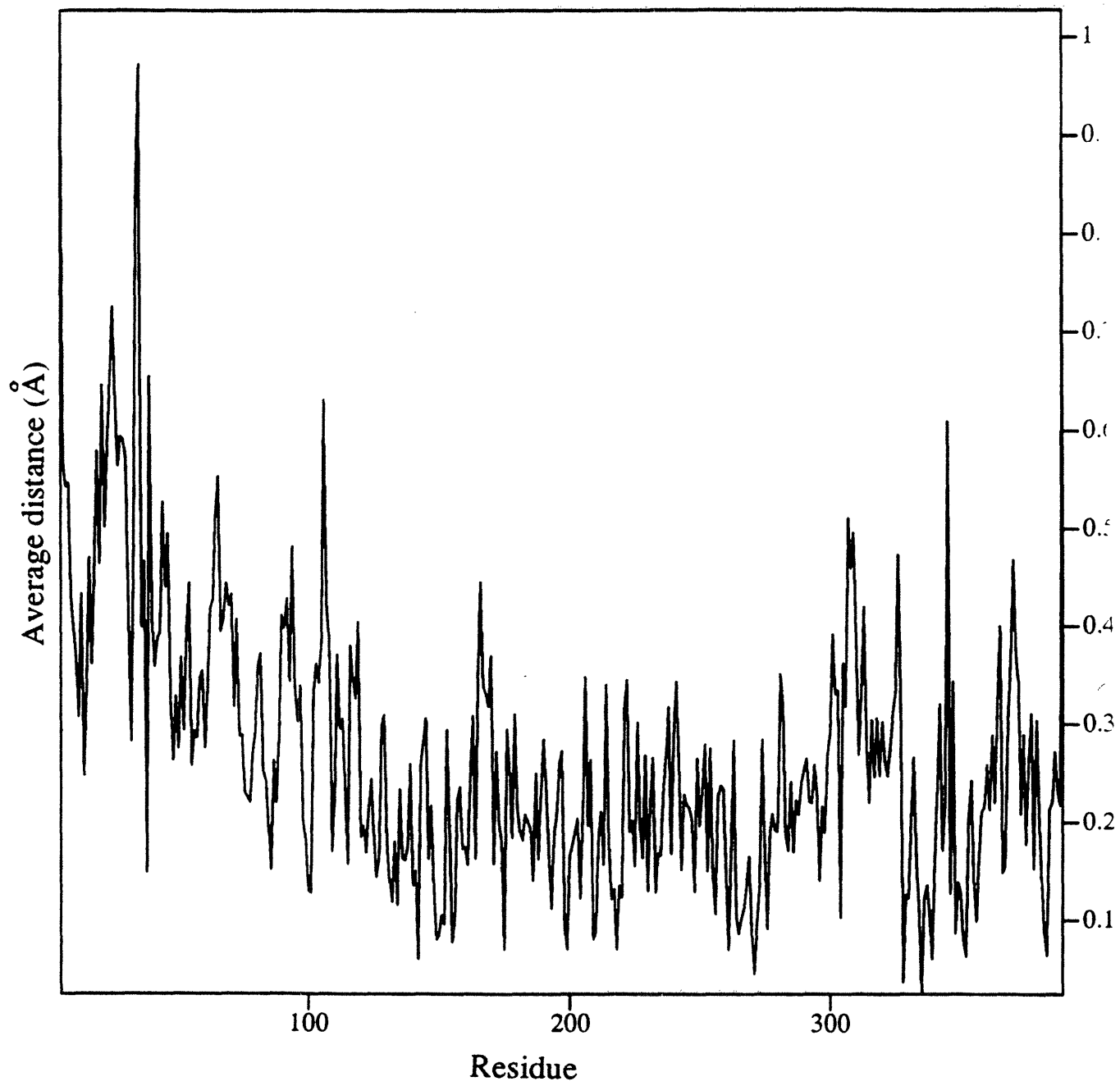


Figure 5.8 The differences in the two halves of the $\alpha_2\beta_2\gamma_2$ dimer as a function of residue number. a, The α subunit. b, The β subunit, c, The γ subunit.



b

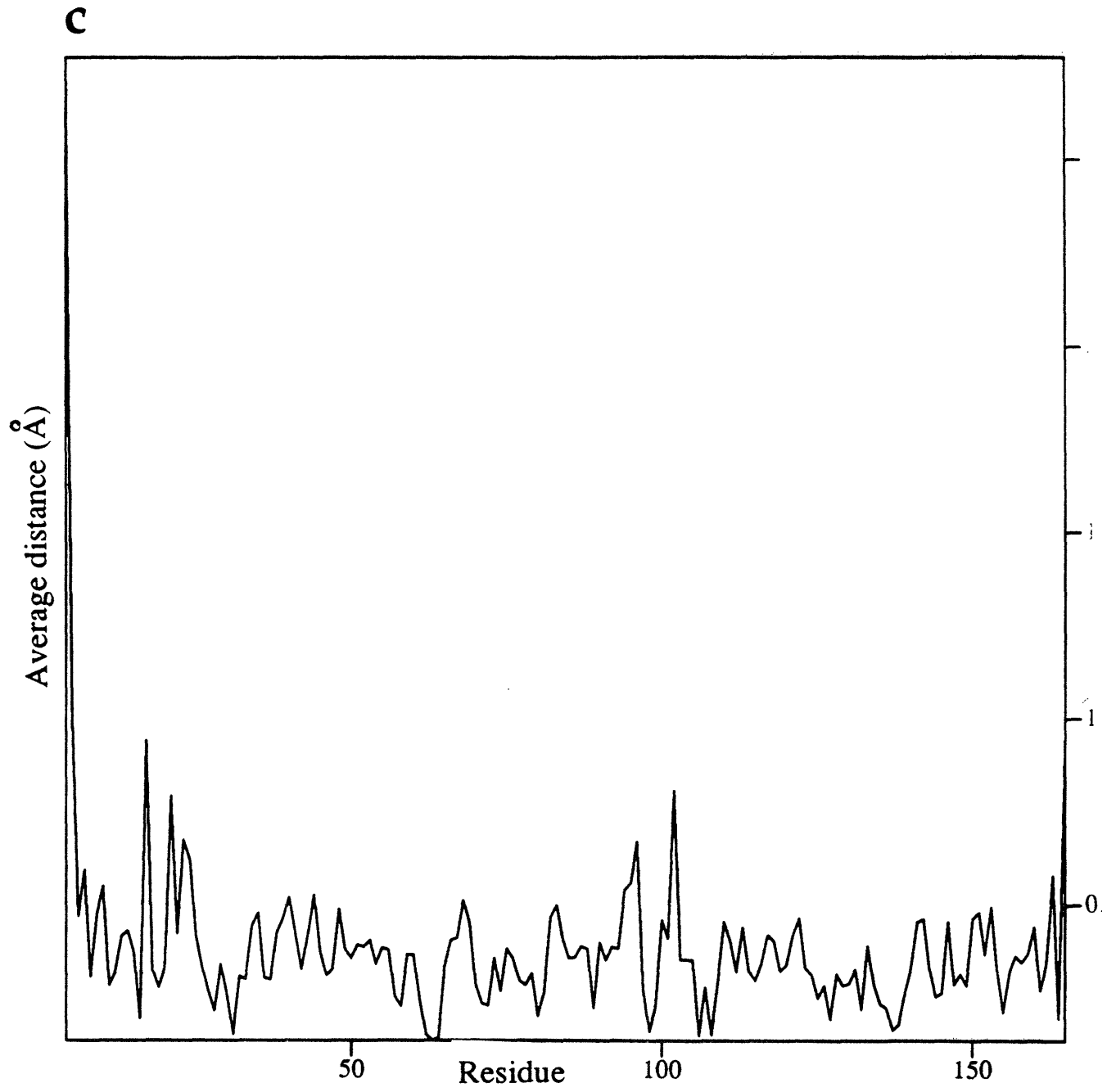


Figure 5.9 a, Structure of di- μ -iodobis(ethylenediamine)diplatinum(II) (PIP). b, Structure of tetrakis(acetoxymercuri)methane (TAMM). c, Structure of sodium ethylmercurithiosalicylate (EMTS). d, Possible types of interactions between PIP and a protein.

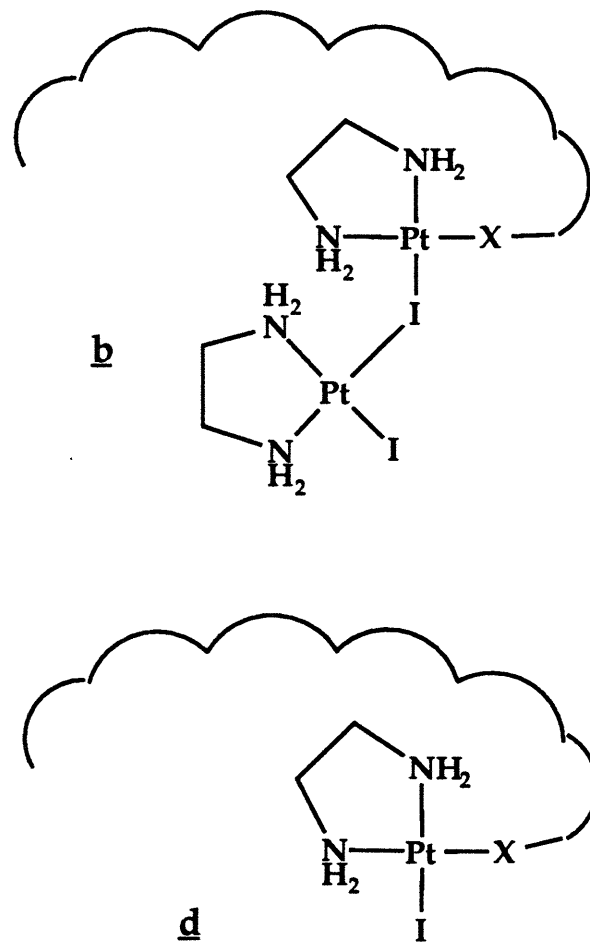
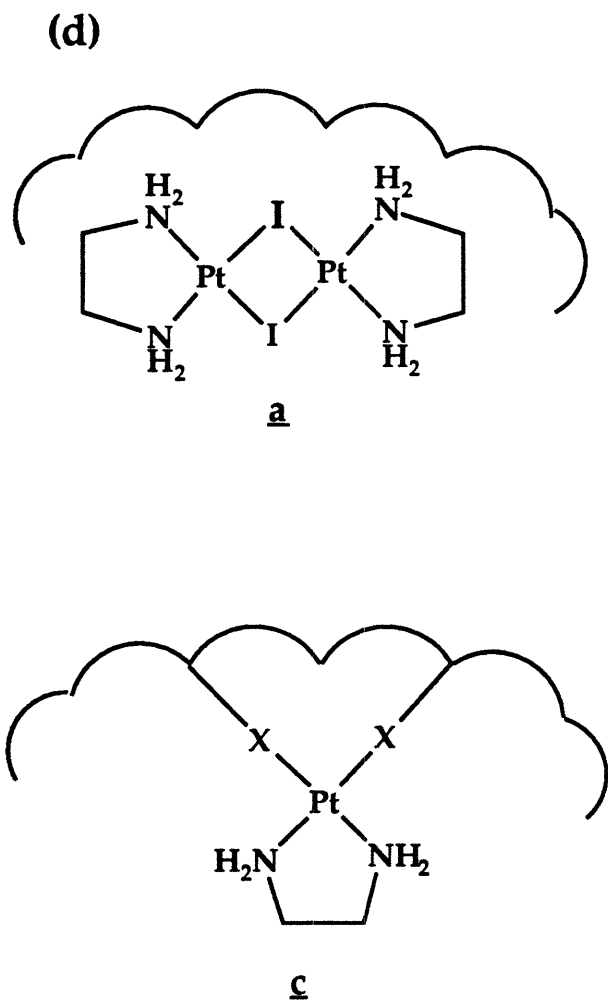
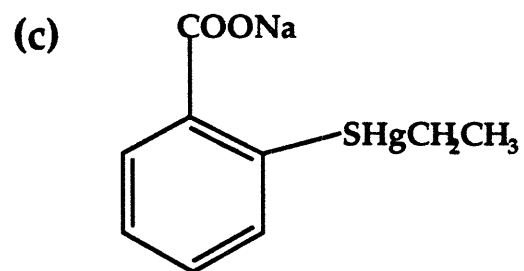
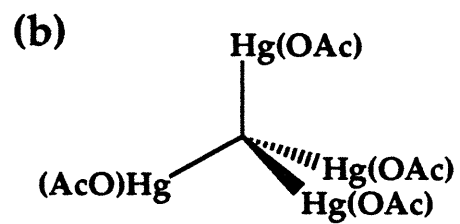
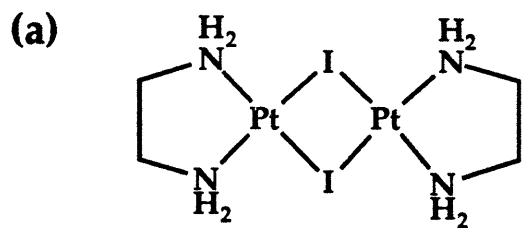


Figure 5.10 A region of the $\alpha\beta$ subunit-subunit interface. The α subunit is shown in red, and the β subunit is shown in blue. The yellow dashed lines represent the hydrogen bonding interactions between α Glu465 and β Lys75, and between α Lys185 and β Asp68.



Figure 5.11 Crystal lattice packing of the hydroxylase molecules. Top: Viewed down the molecular twofold symmetry axis with the thin dimension of the molecule running vertically. Middle: Viewed with the twofold axis running vertically. Bottom: Alternative view with the twofold axis running vertically.

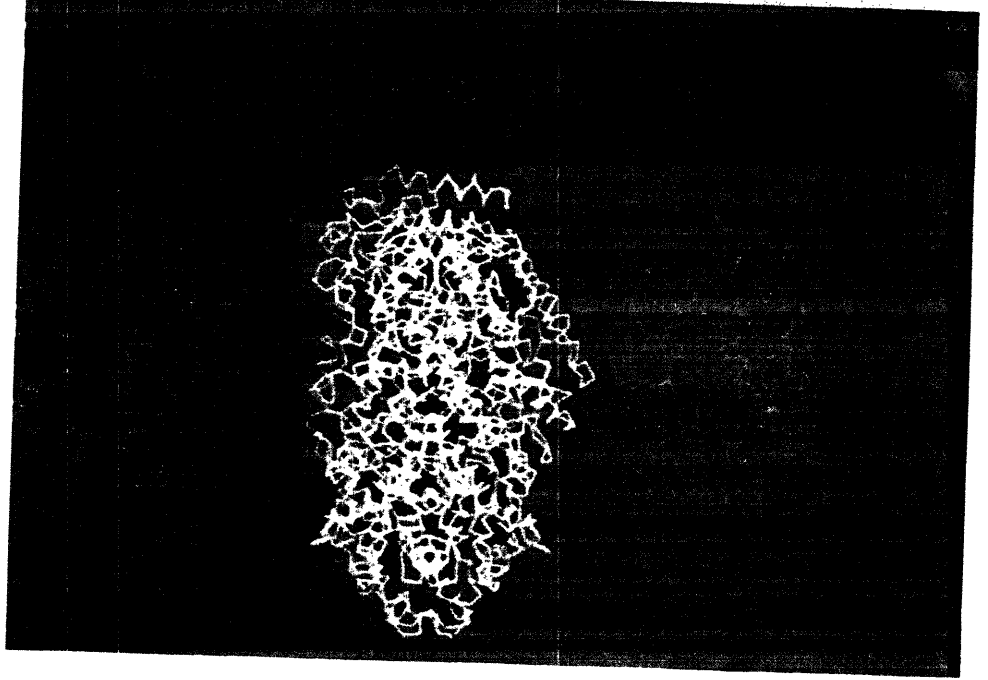
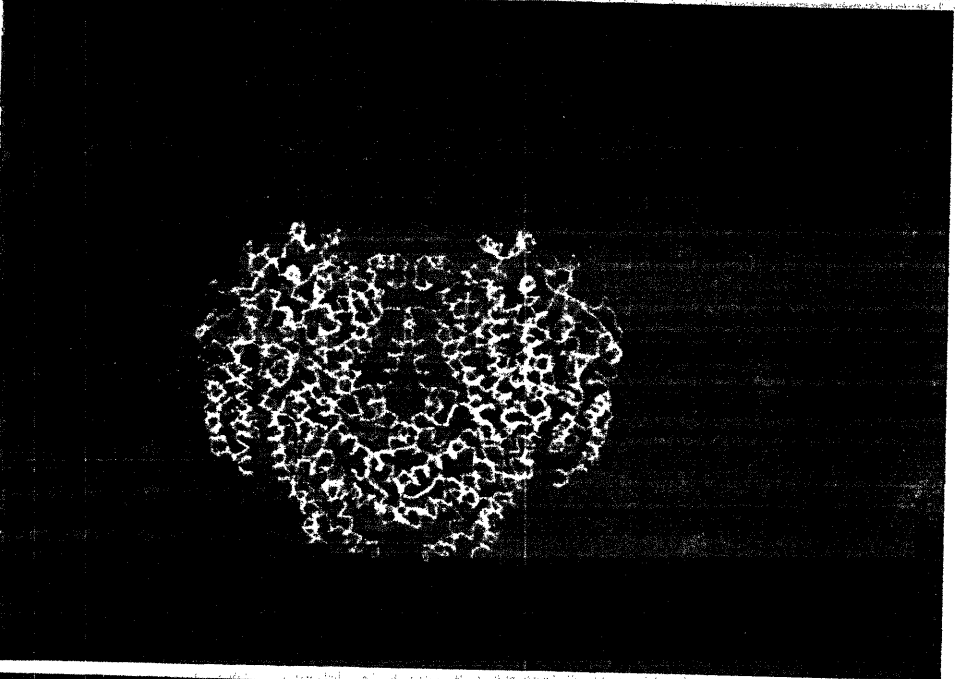
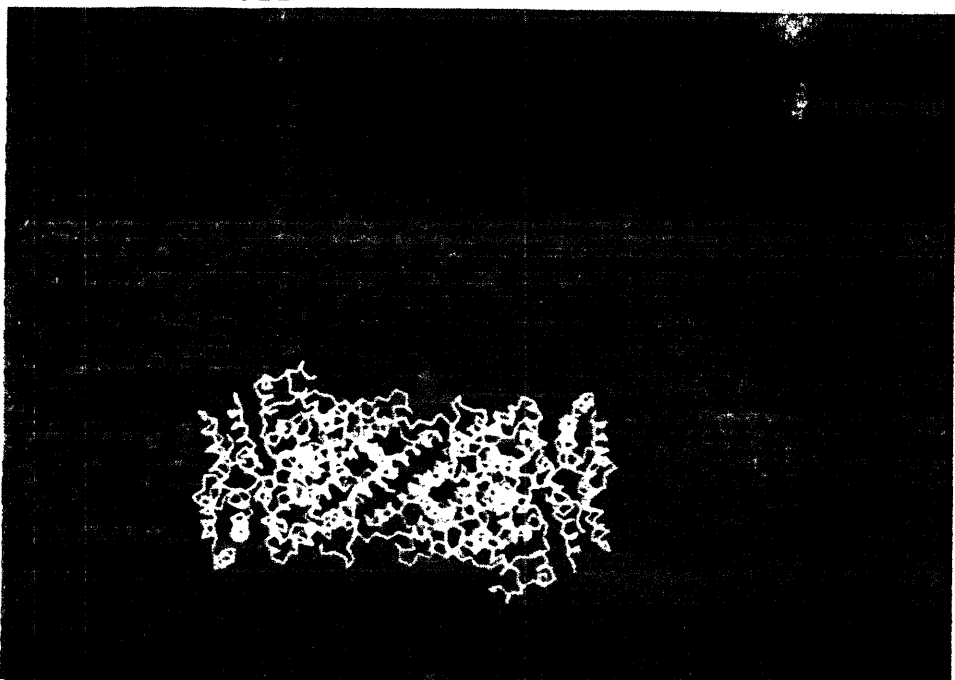


Figure 5.12 Final $2F_o - F_c$ electron density map of the diiron center at 2.2 Å resolution shown in blue. The $F_o - F_c$ difference maps for the hydroxo bridge and the water molecule coordinated to Fe1 are superimposed in green. For this map, F_c was calculated from a model refined without the hydroxo bridge and water molecule. The green contours are 3 times the standard deviation of the map.

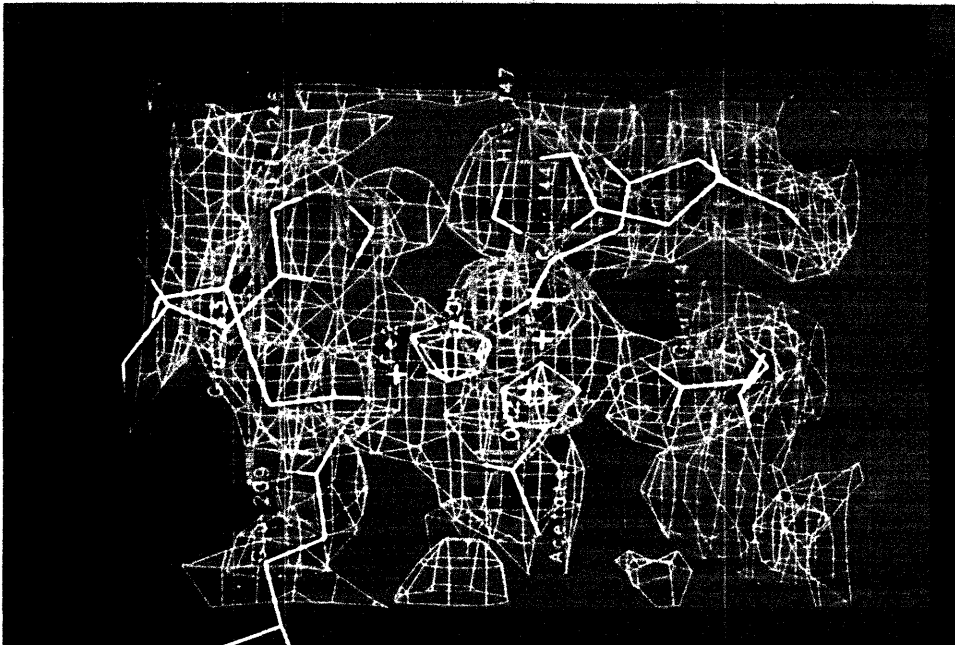
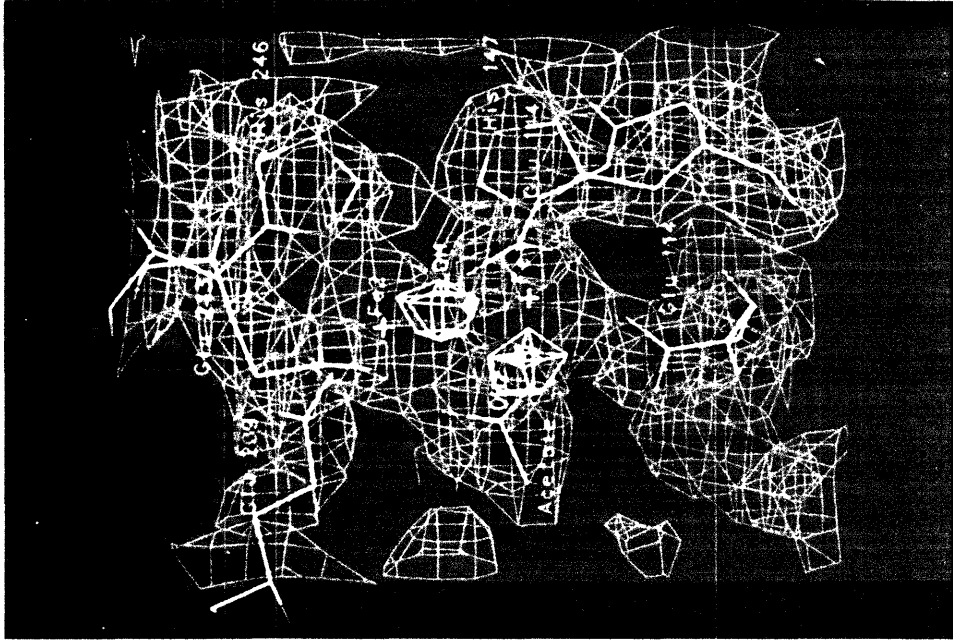


Figure 5.13 Schematic representation of the dinuclear iron center.

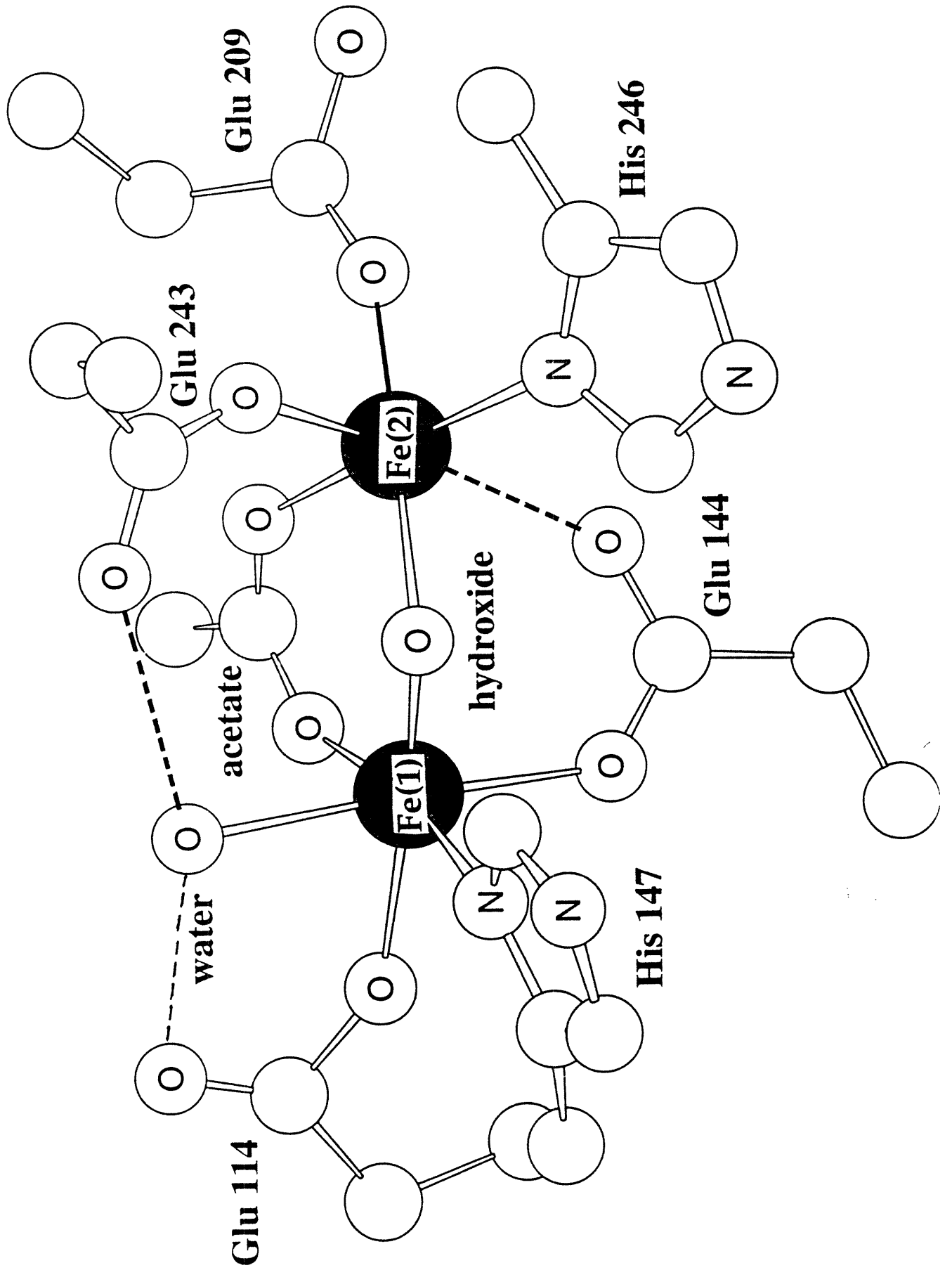


Figure 5.14 Hydrogen bonding interactions of the coordinated histidine ligands. The iron atoms are shown as white spheres and the bridging hydroxo is shown as a red sphere. His147 (left) is hydrogen bonded to Asp 242, and His246 (right) is hydrogen bonded to Asp143, thereby linking helices α C and α F.

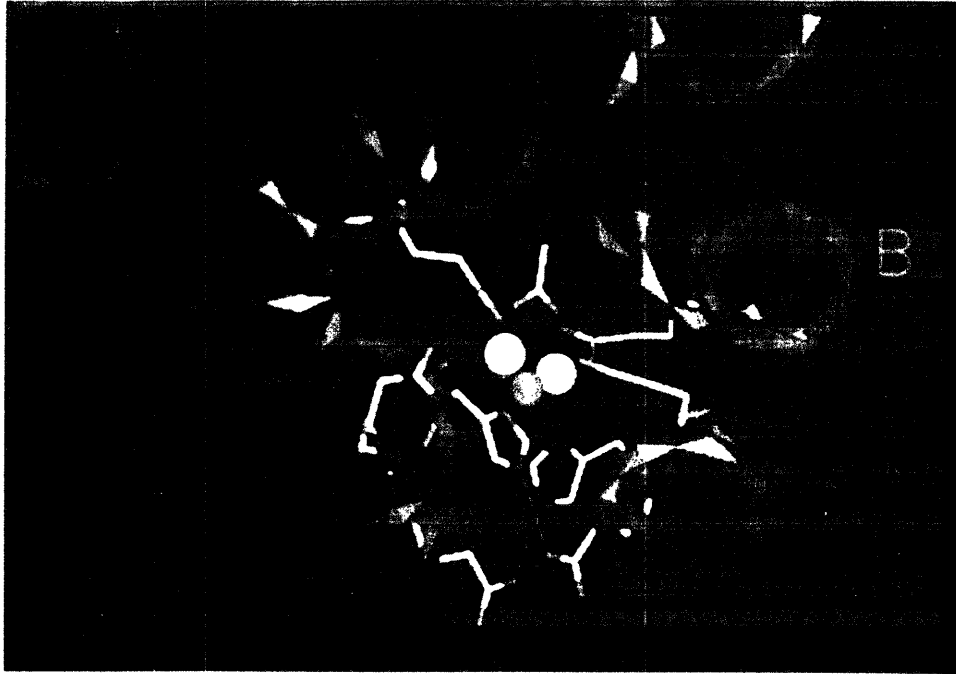


Figure 5.15 The active site. The top picture shows a stereo view. The diiron center is located in cavity composed of hydrophobic residues (Ile 217, Ile 239, Phe 236, Leu 110, Phe 188, Ala 117, Phe 192, Leu 204, Gly 208). Each coordinated histidine is hydrogen bonded to an aspartic acid, His 147 to Asp 242 and His 246 to Asp 143. There is a cysteine, Cys 151, in the back of the cavity, in the same position as Tyr 122 in the R2 protein. In the bottom picture, Cys151 is in the upper left corner with the sulfur atom in green. Thr213 is directly in front of the iron atoms, which are shown as white spheres.

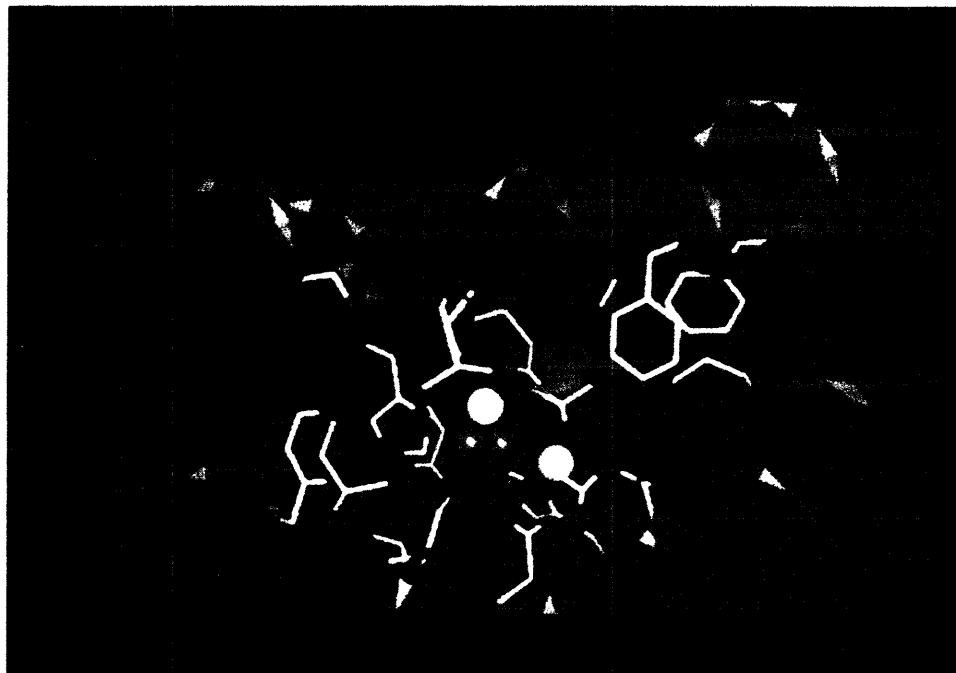
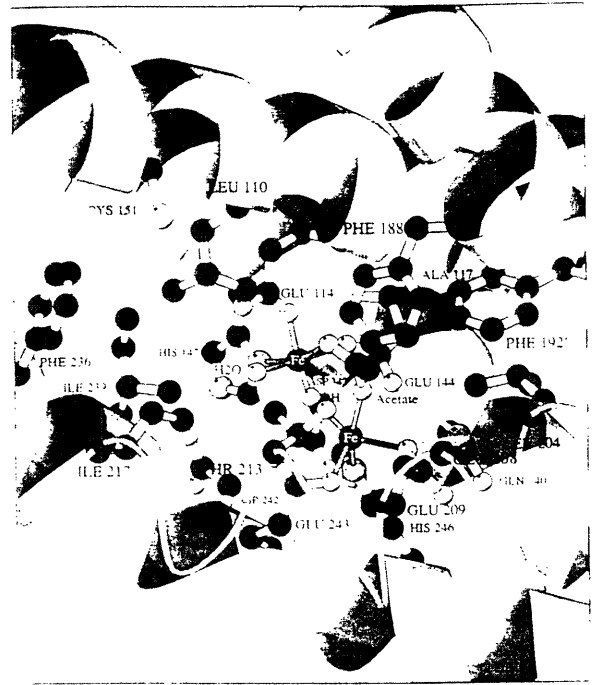


Figure 5.16 Cavities present in the α subunit. The C_{α} backbone of the α subunit is shown with the iron atoms as yellow spheres and the ligands to the iron center in yellow. Cavity I, the active site cavity, is shown in red. The cavity closest to the active site, Cavity II, is also shown in red. Cavities III and IV lie just beyond Cavity II, and are shown in blue. Cavity V, the largest pocket, is shown in green.

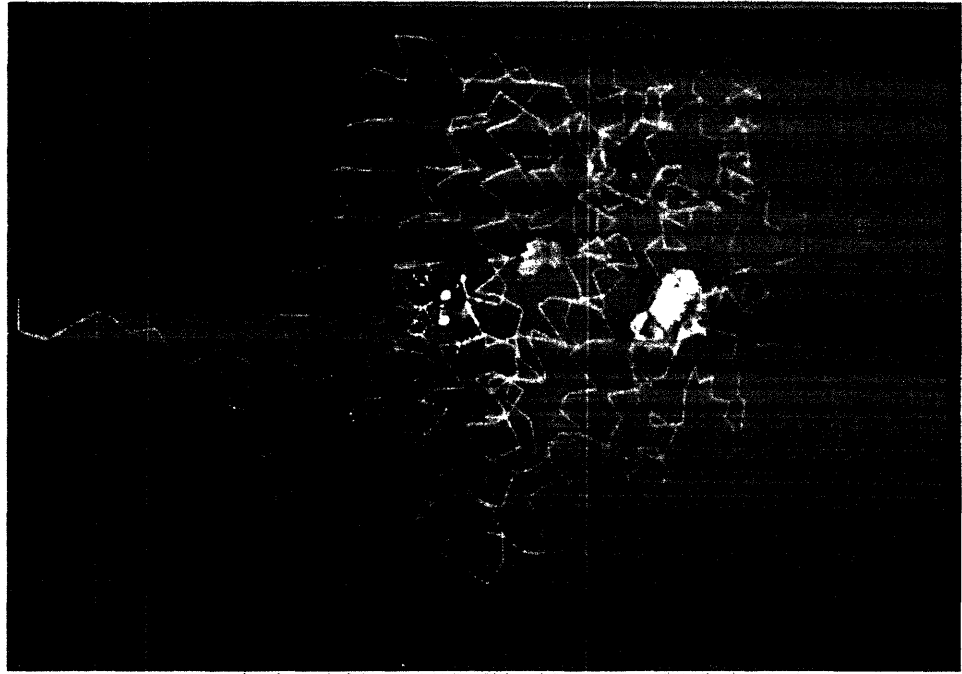


Figure 5.17 The difference Fourier electron density map for the EMTS derivative at Cys151.

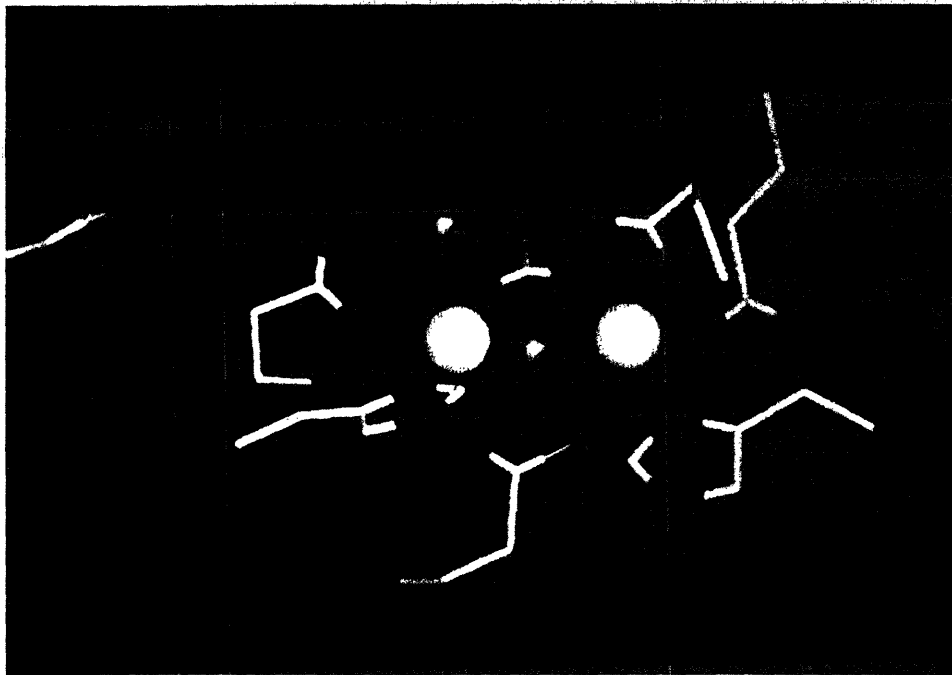


Figure 5.18 Mechanism for methane hydroxylation involving Cys151.

There is no evidence to either support or refute this mechanism.

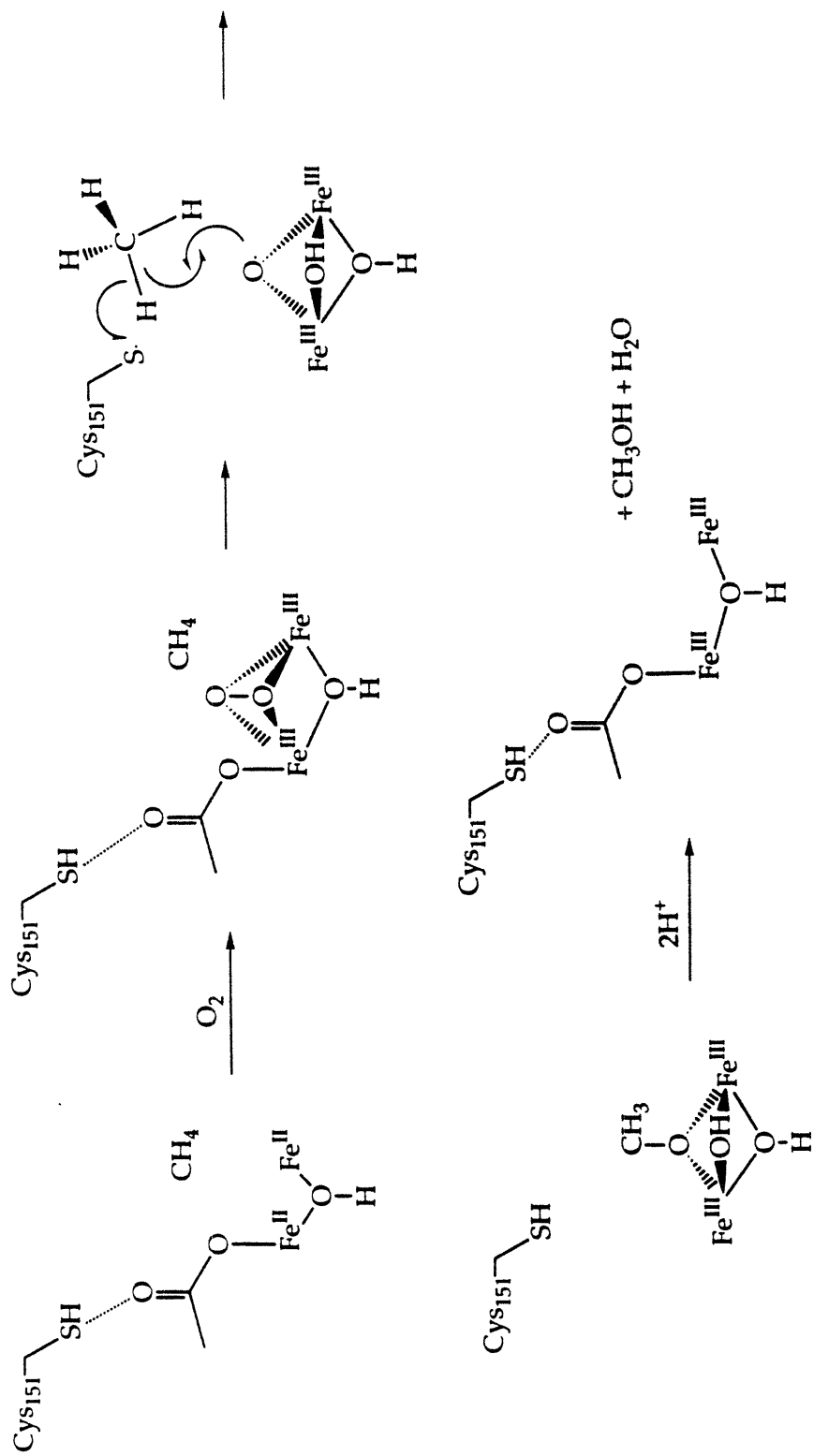


Figure 5.19 Comparison of the amino acid sequence of the α subunit with the sequences of the R2 protein of ribonucleotide reductase, stearyl-ACP desaturase, phenol hydroxylase, toluene-4-monooxygenase, and ruberythrin (adapted from ref. 45).

α subunit of the <i>M. capsulatus</i> hydroxylase	143	D E I R H T	242	D E I R H M
α subunit of the <i>M. trichosporium</i> hydroxylase	143	D E I R H T	242	D E I R H M
R2 protein of ribonucleotide reductase	114	S E T I H S	237	D E A L H L
stearyl-ACP desaturase	175	E E N R H G	261	D E K R H E
phenol hydroxylase	138	D E L R H V	233	D E A R H M
toluene-4-monooxygenase	140	D E L R H G	239	D E S R H A
ruberythrin	52	Q E R E H A	127	A E E F H E

BIOGRAPHICAL NOTE

The author was born in Pittsburgh, Pennsylvania, and received the Bachelor of Arts degree from Amherst College in 1988. She initiated graduate studies at the Massachusetts Institute of Technology in 1989. In November of 1993, she was married to Kenneth M. Comess. She has received a National Institutes of Health Postdoctoral Fellowship for study at the Harvard Medical School, in the Department of Biological Chemistry and Molecular Pharmacology.